FATIGUE STRENGTH ANALYSIS OF OFFSHORE TUBULAR WELDED JOINTS UNDER CONSTANT AMPLITUDE LOADING: LOCAL STRAIN AND FRACTURE MECHANICS APPROACH

DANIEL IHEANACHO NWOSU

FATIGUE STRENGTH ANALYSIS OF OFFSHORE TUBULAR WELDED JOINTS UNDER CONSTANT AMPLITUDE LOADING: LOCAL STRAIN AND FRACTURE MECHANICS APPROACH

by

© Daniel Iheanacho Nwosu, B.Sc. (Hon.), M.Sc.

A thesis submitted to the School of Graduate
Studies in partial fulfillment of the
requirements for the degree of
Doctor of Philosophy

Faculty of Engineering and Applied Science
Memorial University of Newfoundland
February 1993

St. John's Newfoundland Canada

To my wife and daughters,
Opry, Roisin and Andrea.

Acknowledgements

I am much indebted to my supervisor Dr. A.S.J. Swamidas for his guidance and encouragement throughout the course of this study. His active support and continued interest is highly appreciated. My sincere appreciation to Association of Universities and Colleges of Canada for the award of a Canadian Commonwealth Scholarship during the entire period of this research. Additional support from my supervisor Dr. A.S.J Swamidas from his grants and Dr. J. Malpas, Dean of Graduate studies are gratefully acknowledged.

My sincere gratitude to Dr. R.T. Dempster, Chairman Department of Mechanical Engineering, for giving me a term eight finite element analysis course to teach and my sincere gratitude to Dr. J.J. Sharp, Associate Dean of Engineering who allowed me to teach this course while I was still in the graduate program.

My special thanks to Dr. K. Munaswamy and Dr. R.E. Baddour, members of the supervisory committee, for their constructive criticisms and useful suggestions after reading the manuscript. Sincere appreciation are due to Dr. G.R. Peters, former Dean, Dr. J.J Sharp, Associate Dean and Dr. T.R. Chari, former Associate Dean, Faculty of Engineering and Applied Science for providing the facilities.

I would like to extend my sincere appreciation to Mr. D. Press, Manager, Centre for Computer Aided Engineering Memorial University of Newfoundland, St. John's, who helped me with an ever increasing computer core space and thus assisted in the completion of this research. I also would like to acknowledge Mr. L. little, Mr.

T. Galway and Ms. V. Fortier, for their patience, cooperation and attention to many of my complaints in the Centre for Computer Aided Engineering.

Finally, my truly unbounded thanks to my wife Opry and my two daughters, Roisin and Andrea, for their understanding, love and patience throughout the course of this study.

Abstract

The main components of steel offshore structures, whether fixed or floating, are generally tubular members. Large stress concentrations arise due to the abrupt geometric discontinuities at the intersections of these welded tubular members, called joints or nodes. The varying environmental loads acting on these joints cause fatigue crack initiation, growth and their final catastrophic failure. This thesis presents a numerical study of the total fatigue life of offshore tubular welded joints under the action of axial, in-plane and out-of-plane bending loads, using local stress-strain and linear elastic fracture mechanics approaches. The study includes the development of a computer program for the automatic generation of meshes for tubular joints and a contact program for the prevention of crack surface penetration.

Stress analysis to determine the possible location of the crack initiation on the tubular joint has been carried out using eight noded degenerate isoparametric shell elements. The influence of geometric parameters on the stress distribution around the joint as well as through the joint thickness has been investigated, and the results obtained therein compared with experimental results; they also have been compared with established parametric equations. Good comparisons have been obtained with the experimental values.

The local stress-strain approach, using the Manson-Coffin rule, is utilized for the study of the crack initiation. Using experimental investigations on crack initiation life of tubular welded T-joints, fatigue strength exponent b and fatigue ductility exponent c have been determined empirically and used to compute crack initiation

life of the tubular joints analyzed in this study.

The weld toe crack influence on the through thickness and surface stress distribution has been studied using the line spring element in conjunction with the degenerate eight node shell elements to model the crack. The stress intensity factors determined, from this study, were compared with available theoretical studies and found to give good results.

Using the stress intensity factors obtained from the line spring model, the through-thickness crack propagation lives of the tubular joint under consideration were predicted using Paris crack growth law. The propagation lives for each loading conditions were predicted, on an incremental cycle basis, up to 90% of the chord thickness cracking. The estimated fatigue lives were compared with experimental investigations carried out at Memorial University of Newfoundland St. John's (for axial loading) and University of Waterloo (for in-plane loading) under the Canadian Cooperative Offshore Tubular Joint Program and found to give good results.

Contents

Acknowledgements iii

Abstract v

List of Figures xii

Tables xxvi

List of Symbols xxx

1 Fatigue of Tubular Welded Joints 1

1.1 Introduction 1

1.2 Crack Initiation and Growth in Fatigue Analysis 10

1.3 Scope of the Thesis 17

1.4 Organization of the Thesis 18

2 Literature Review 21

2.1 General 21

2.2 Stress Analysis of Stiffened and Unstiffened Tubular Welded Joints 23

2.2.1 Parametric Equations 29

2.3 Fatigue of Tubular Welded Joints 33

2.3.1 Fatigue Crack Initiation 35
2.3.2 Linear Elastic Fracture Mechanics 39
2.3.3 Finite Element Crack Modelling for SIF Evaluation 43
2.3.4 Application of Linear Elastic Fracture Mechanics to Fatigue Crack Propagation 52
2.3.5 Thickness, Size and Geometry Effect 58
2.4 Analytical and Numerical Studies on Fatigue Life Estimation 60
2.5 Summary 65

3 Theoretical Background **67**
3.1 Finite Element Formulation 67
3.2 Degenerated Isoparametric Elements 72
3.2.1 General 72
3.2.2 Coordinate Systems 72
3.2.3 Element Geometry Definition 77
3.2.4 Displacement Field 80
3.2.5 Definition of Strains and Stresses 85
3.2.6 Element Properties and Transformations 88
3.2.7 Element Assembly and Equation Solution Procedure 96
3.3 Life Prediction Formulation 97
3.3.1 Crack Initiation Life Prediction 98
3.3.2 Fatigue Crack Growth Formulation 100
3.3.3 Line Spring Model for Stress Intensity Factor Evaluation . . 102
3.3.4 Finite Element Implementation of the Line Spring Model . . 110
3.3.5 Fatigue Crack Growth model 113

4 Stress Analysis of Unstiffened Tubular Joints 116

4.1 General 116

4.1.1 Stresses in Tubular Joints 121

4.1.2 Boundary Conditions 127

4.1.3 Processing of Results 135

4.1.4 Convergence Test 139

4.1.5 Results and Discussion 141

5 Stress Analysis of Stiffened Tubular T-Joints 182

5.1 General 182

5.2 Joint Modelling for the Stiffeners 183

5.3 Loading and boundary conditions 187

5.4 Results and Discussion 195

5.4.1 Effect of the Stiffener Location 195

5.4.2 Effect of the Number of Stiffeners 203

5.4.3 Effect of the Stiffener Size 209

5.4.4 Effect of the Thickness (τ) and Thinness (γ) Ratios 212

5.4.5 Stress Concentration in the Stiffener 219

5.5 Summary 222

6 Fatigue Crack Initiation Life Prediction 224

6.1 General 224

6.2 Initiation Life Prediction Procedure 226

6.2.1 Weld Toe Strain Analysis 226

6.2.2 Stress-Strain and Manson-Coffin Equations 227

6.2.3 Determination of Fatigue Properties 229
6.3 Results and Discussion 230
6.3.1 Summary 231

7 Fatigue Crack Growth Life Prediction **242**
7.1 General 242
7.1.1 Finite element Model of the Cracked Joint 244
7.1.2 Joint Modelling for Crack 247
7.1.3 Tubular Joint Crack Shape 247
7.2 Stress Intensity Factor Evaluation 248
7.3 Fatigue Crack Growth Life Prediction 252
7.3.1 Fatigue Crack Growth Rate (da/dN) and the SIF Range (ΔK)253
7.3.2 Material Constants C and m 256
7.3.3 Fatigue Life Prediction 258
7.3.4 Propagation Life Calculation 261
7.3.5 Results and Discussions 262
7.4 Summary 284

8 Conclusions and Recommendations **285**
8.1 Conclusions 285
8.2 Recommendations 290

A Shape Function Generation **304**

B Elastic Constitutive Relationships **307**
B.1 The Generalized Hooke's law 307

C Stress Intensity Factors 312

List of Figures

1.1 A jacket type platform. 3

1.2 Environmental loadings on an offshore structure. 4

1.3 Tubular welded structure showing possible crack sites. 5

1.4 Typical tubular joint connections showing some of the many possible geometries. 7

1.5 Types of stiffeners used in offshore tubular joints. 9

1.6 Total strain-life plot. 12

1.7 Elastic stress field distribution ahead of a crack. 14

1.8 The three basic modes of crack surface displacements. (a) Mode I: opening mode, (b) Mode II: shearing mode, and (c) Mode III: tearing mode. 15

2.1 Triangular element with singularity at node 1. 45

2.2 Quadaratic isoparametric elements with midside nodes at quarter points. 47

2.3 2-D triangular element with midside nodes at quarter points. 47

2.4 3-D brick element with midside nodes at quarter points. 48

2.5 3-D prism with midside nodes at quarter points. 48

2.6 Schematic growth rate curve showing the sigmoidal variation of fatigue crack propagation rate da/dN with stress intensity factor range (ΔK). 54
2.7 Schematic representation of asymptotic crack growth equation [Liu, 1964]. 56
2.8 Schematic representation of three component crack growth equation [Saxena et al., 1979]. 57
3.1 Three-dimensional hexahedral elements of parabolic and cubic types. 70
3.2 (a) Quadratic solid three-dimensional element, (b) and (c) the corresponding degenerated shell elements. 73
3.3 Coordinate system: (a) nodal and curvilinear systems, (b) local system of axes. 75
3.4 Nodal vectors. 79
3.5 Nodal configuration of the two quadratic shell elements used: (a) rectangular parent, (b) isoparametric counterpart. 81
3.6 (a) Schematic cross-section of a surface crack with varying depth a(x) and projected length 2c in a shell of thickness t. (b) Schematic idealization of through-cut shell (plate) mid-surface with distributed stiffnesses along the crack line. 101
3.7 Single-edge notched specimen subject to combined tension and bending. 106
3.8 Schematic representation of surface crack in a tubular joint. 109
3.9 Shematic illustration of the intersection of an 8-node shell and a 6-node line-spring element in a cylindrical shell. 111

3.10 Line spring models showing flags for positive and negative cracks. . 112
4.1 Geometric notations for tubular T-joints. 118
4.2 Modes of loading used for the finite element analysis: (a) Axial, (b) IPB and (c) OPB. 120
4.3 Deformation stresses in a T joint under brace tension load. 122
4.4 Maldistribution of nominal stress at the intersection. 124
4.5 Subdivision of the tubular joint into a number of regions suitable for mesh generation. 125
4.6 Typical computer mesh generation for unstiffened tubular T-joints: (a) half joints, (b) detail showing the brace, chord and plug. 128
4.7 Structural configuration considered for analysis: (a) quarter-joint, (b) half-joint (see Table 4.2 for boundary conditions). 131
4.8 SCF comparison between half- and full-joint meshes: (a) brace, (b) chord (OPB). ($\alpha = 7.02$, $\gamma = 24$) 131
4.9 Original and deformed mesh for Axial loading. 136
4.10 Original and deformed mesh for IPB loading. 137
4.11 Original and deformed mesh for OPB loading. 138
4.12 Variation of SCF in brace for fixed and simply supported end conditions (Axial) ($\alpha = 7.02$, $\gamma = 24$). 145
4.13 Variation of SCF in chord for fixed and simply supported end conditions (Axial) ($\alpha = 7.02$, $\gamma = 24$). 145
4.14 Variation of SCF in brace for fixed and simply supported end conditions (IPB) ($\alpha = 7.02$, $\gamma = 24$). 146

4.15 Variation of SCF in chord for fixed and simply supported end conditions (IPB) (α = 7.02, γ = 24). 146
4.16 Variation of SCF in brace for fixed and simply supported end conditions (OPB) (α = 7.02, γ = 24). 147
4.17 Variation of SCF in chord for fixed and simply supported end conditions (OPB) (α = 7.02, γ = 24). 147
4.18 Variation of SCF along brace/chord intersection (Axial) (α = 7.02, τ = 1.0, β = 0.5, γ = 24.). 148
4.19 Variation of SCF along brace/chord intersection (IPB) (α = 7.02, τ = 1.0, β = 0.5, γ = 24). 148
4.20 Variation of SCF along brace/chord intersection (OPB) (α = 7.02, τ = 1.0, β = 0.5, γ = 24). 149
4.21 Comparison of SCF between PS and MUN results (Axial). IPB and OPB of PS included (α = 7.02, τ = 1.0, β = 0.5, γ = 24). 149
4.22 Comparison of SCF along brace/chord intersection between Axial, IPB and OPB loading in brace (α = 7.02, τ = 1.0, β = 0.5, γ = 24). 151
4.23 Effect of specified thickness either in chord or brace (Axial) (α = 7.02, γ = 24.). 151
4.24 Effect of specified thickness either in chord or brace (IPB) (α = 7.02, γ = 24.). 153
4.25 Effect of specified thickness either in chord or brace (OPB). (α = 7.02, γ = 24.). 153
4.26 Variation of SCF with β ratio (Axial). (α = 7.02, γ = 24.0, τ = 1.0) 154
4.27 Variation of SCF with β ratio (IPB). (α = 7.02, γ = 24.0, τ = 1.0) 154

4.28 Variation of SCF with β ratio (OPB). (α = 7.02, γ = 24.0, τ = 1.0) 155

4.29 Variation of SCF with τ ratio (Axial). (α = 7.02, β = 0.5, γ = 24.0) 155

4.30 Variation of SCF with τ ratio (IPB). (α = 7.02, β = 0.5, γ = 24.0) 156

4.31 Variation of SCF with τ ratio (OPB). (α = 7.02, β = 0.5, γ = 24.0) 156

4.32 Variation of SCF with γ ratio (Axial). (α = 7.02, β = 0.5, τ = 1.0) 158

4.33 Variation of SCF with γ ratio (IPB). (α = 7.02, β = 0.5, τ = 1.0). 158

4.34 Variation of SCF with γ ratio (OPB). (α = 7.02, β = 0.5, τ = 1.0). 159

4.35 Principal stress distribution along brace surface from the saddle point (Axial) (α = 7.02, τ = 1.0, γ = 24.0) 159

4.36 Principal stress distribution along chord surface from the saddle point. (Axial) (α = 7.02, τ = 1.0, γ = 24.0) 160

4.37 Principal stress distribution along brace surface from the crown point. (IPB) (α = 7.02, τ = 1.0, γ = 24.0) 160

4.38 Principal stress distribution along chord surface from the crown point. (IPB) (α = 7.02, τ = 1.0, γ = 24.0) 161

4.39 Principal stress distribution along brace surface from the saddle point. (OPB) (α = 7.02, τ = 1.0, γ = 24.0) 161

4.40 Principal stress distribution along chord surface from the saddle point. (OPB) (α = 7.02, τ = 1.0, γ = 24.0) 162

4.41 Ratio of membrane stress to total stress vs. ϕ (Axial) (α = 7.02, τ = 1.0, γ = 24.0) 162

4.42 Ratio of bending stress to total stress vs. ϕ (Axial) (α = 7.02, τ = 1.0, γ = 24.0) 164

4.43 Ratio of membrane stress to total stress vs. ϕ (IPB) (α = 7.02, τ = 1.0, γ = 24.0) 164
4.44 Ratio of bending stress to total stress vs. ϕ (IPB) (α = 7.02, τ = 1.0, γ = 24.0) 165
4.45 Ratio of membrane stress to total stress vs. ϕ (OPB) (α = 7.02, τ = 1.0, γ = 24.0) 165
4.46 Ratio of bending stress to total stress vs. ϕ (OPB) (α = 7.02, τ = 1.0, γ = 24.0) 166
4.47 SCF vs. β: comparison between empirical equations and PS (Axial). (α = 7.02, γ = 24.0, τ = 0.4) 166
4.48 SCF vs. β: comparison between empirical equations and PS (Axial). (α = 7.02, γ = 24.0, τ = 0.6) 168
4.49 SCF vs. β: comparison between empirical equations and PS (Axial). (α = 7.02, γ = 24.0, τ = 0.8) 168
4.50 SCF vs. β: comparison between empirical equations and PS (Axial). (α = 7.02, γ = 24.0, τ = 1.0) 169
4.51 Effect of τ ratio on location of peak SCF (Axial) (α = 7.02, τ = 0.4, γ = 24.0) 169
4.52 Effect of τ ratio on location of peak SCF (τ = 0.6) 170
4.53 Effect of τ ratio on location of peak SCF (τ = 0.8) 170
4.54 Effect of τ ratio on location of peak SCF (τ = 1.0) 171
4.55 SCF comparison between PS and Burdekin et al. (1992) 3-D and shell element results (Axial) 173

4.56 DoB comparison between PS and Burdekin et al. (1992) 3-D and shell element results (Axial) 173
4.57 Variation of SCF in brace for T-joint with and without plug (Axial) ($\alpha = 7.02$, $\tau = 1.0$, $\beta = 0.5$, $\gamma = 24.0$) 174
4.58 Variation of SCF in chord for T-joint with and without plug (Axial) ($\alpha = 7.02$, $\tau = 1.0$, $\beta = 0.5$, $\gamma = 24.0$) 174
4.59 Variation of SCF in brace for T-joint with and without plug (IPB) ($\alpha = 7.02$, $\tau = 1.0$, $\beta = 0.5$, $\gamma = 24.0$) 175
4.60 Variation of SCF in chord for T-joint with and without plug (IPB) ($\alpha = 7.02$, $\tau = 1.0$, $\beta = 0.5$, $\gamma = 24.0$) 175
4.61 Variation of SCF in brace for T-joint with and without plug (OPB) ($\alpha = 7.02$, $\tau = 1.0$, $\beta = 0.5$, $\gamma = 24.0$) 176
4.62 Variation of SCF in chord for T-joint with and without plug (OPB) ($\alpha = 7.02$, $\tau = 1.0$, $\beta = 0.5$, $\gamma = 24.0$) 176
4.63 Comparison between UCL parametric equations and PS results (Axial) 178
4.64 Comparison between UCL semi-loof thin-shell FEM data and PS results (Axial) 178
4.65 Comparison between UCL parametric equations and present study results (IPB) 179
4.66 Comparison between UCL semi-loof thin-shell FEM data and PS results (IPB) 179
4.67 Comparison between UCL parametric equations and PS results (OPB) ($\alpha = 9.0$, $\beta = 0.35$, $\tau = 0.2$, $\gamma = 9.0$) 180

4.68 Comparison between UCL semi-loof thin-shell FEM data and PS results (OPB) (α = 9.0, β = 0.35, τ = 0.2, γ = 9.0) 180

5.1 Details of the tubular T-joint used for stiffened joint analysis. . . . 184

5.2 Schematic representation of the locations of stiffeners. 185

5.3 Three types of stiffeners investigated. 185

5.4 Typical computer generated mesh for stiffened tubular joint (without the stiffners). 186

5.5 Brace SCF results for stiffened and unstiffened joint mesh (Axial) (α = 7.02, γ = 24) 191

5.6 Chord SCF results for stiffened and unstiffened joint mesh (Axial) (α = 7.02, γ = 24) 191

5.7 Brace SCF results for stiffened and unstiffened joint mesh (IPB) (α = 7.02, γ = 24) 192

5.8 Chord SCF results for stiffened and unstiffened joint mesh (IPB) (α = 7.02, γ = 24) 192

5.9 Brace SCF results for stiffened and unstiffened joint mesh (OPB) (α = 7.02, γ = 24) 193

5.10 Chord SCF results for stiffened and unstiffened joint mesh (OPB) (α = 7.02, γ = 24) 193

5.11 Computer mesh generation showing: (a) the half-joint with 3 internal ring stiffeners, (b) half-brace with one stiffener, (c) half-brace with two stiffeners, and (d) half-brace with three stiffeners 194

5.12 Effect of stiffener positions on SCF (Axial) (α = 7.02, γ = 24) . . . 201

5.13 Effect of stiffener positions on SCF (IPB) (α = 7.02, γ = 24) 201

5.14 Effect of stiffener positions on SCF (OPB) ($\alpha = 7.02, \gamma = 24$) . . . 202

5.15 Effect of number of stiffeners on the brace SCF (Axial) ($\alpha = 7.02, \beta = 0.5, \tau = 1.0, \gamma = 24$) 202

5.16 Effect of number of stiffeners on the chord SCF (Axial) ($\alpha = 7.02, \beta = 0.5, \tau = 1.0, \gamma = 24$) 204

5.17 Effect of number of stiffeners on the brace SCF (IPB) ($\alpha = 7.02, \beta = 0.5, \tau = 1.0, \gamma = 24$) 204

5.18 Effect of number of stiffeners on the chord SCF (IPB) ($\alpha = 7.02, \beta = 0.5, \tau = 1.0, \gamma = 24$) 205

5.19 Effect of number of stiffeners on the brace SCF (OPB) ($\alpha = 7.02, \beta = 0.5, \tau = 1.0, \gamma = 24$) 205

5.20 Effect of number of stiffeners on the chord SCF (OPB) ($\alpha = 7.02, \beta = 0.5, \tau = 1.0, \gamma = 24$) 206

5.21 SCF vs. number of stiffeners at the saddle (Axial) ($\alpha = 7.02, \gamma = 24$) 207

5.22 SCF vs. number of stiffeners at the crown (Axial) ($\alpha = 7.02, \gamma$) . . 207

5.23 SCF vs. number of stiffeners at the crown (IPB) ($\alpha = 7.02, \gamma = 24$) 208

5.24 SCF vs. number of stiffeners at the saddle (OPB) ($\alpha = 7.02, \gamma = 24$) 208

5.25 Effect of stiffener height (HS) on SCF in the brace (Axial) ($\alpha = 7.02, \gamma = 24$) 210

5.26 Effect of stiffener height (HS) on SCF in the chord (Axial) ($\alpha = 7.02, \gamma = 24$) 210

5.27 Effect of stiffener thickness (TS) on SCF in the brace (Axial) ($\alpha = 7.02, \gamma = 24$) 211

5.28 Effect of stiffener thickness (TS) on SCF in the chord (Axial) (α = 7.02, γ = 24) 211

5.29 Variation of brace SCF with angle ϕ, showing the effect of τ ratio (Axial) (α = 7.02, γ = 24, Position No. 2, TS = 19mm, HS = 120mm)213

5.30 Variation of chord SCF with angle ϕ, showing the effect of τ ratio (Axial) (α = 7.02, γ = 24, Position No. 2, TS = 19mm, HS = 120mm)213

5.31 Variation of brace SCF with angle ϕ, showing the effect of τ ratio (IPB) (α = 7.02, γ = 24, Position No. 2, TS = 19mm, HS = 120mm)214

5.32 Variation of chord SCF with angle ϕ, showing the effect of τ ratio (IPB) (α = 7.02, γ = 24, Position No. 2, TS = 19mm, HS = 120mm)214

5.33 Variation of brace SCF with angle ϕ, showing the effect of τ ratio (OPB) (α = 7.02, γ = 24, Position No. 2, TS = 19mm, HS = 120mm)215

5.34 Variation of chord SCF with angle ϕ, showing the effect of τ ratio (OPB) (α = 7.02, γ = 24, Position No. 2, TS = 19mm, HS = 120mm)215

5.35 SCF vs. τ ratio at the crown (Axial) (α = 7.02, γ = 24, Position No. 2, TS = 19mm, HS = 120mm) 216

5.36 SCF vs. τ ratio at the saddle (Axial) (α = 7.02, γ = 24, Position No. 2, TS = 19mm, HS = 120mm) 216

5.37 SCF vs. τ ratio at the crown (IPB) (α = 7.02, γ = 24, Position No. 2, TS = 19mm, HS = 120mm) 217

5.38 SCF vs. τ ratio at the saddle (OPB) (α = 7.02, γ = 24, Position No. 2, TS = 19mm, HS = 120mm) 217

5.39 Effect of thinness ratio (γ) on chord SCFs in stiffened and unstiffened tubular joints at the saddle (Axial) (α = 7.02, γ = 24, Position No. 2, TS = 19mm, HS = 120mm) 218

5.40 Effect of thinness ratio (γ) on brace SCFs in stiffened and unstiffened tubular joints at the saddle (Axial) (α = 7.02, γ = 24, Position No. 2, TS = 19mm, HS = 120mm) 218

5.41 Four critical stress regions in the stiffener 220

6.1 Strain-life curves showing total, elastic and plastic strain components for axial loading. 237

6.2 Strain-life curves showing total, elastic and plastic strain components for in-plane bending load. 238

6.3 Strain-life curves showing total, elastic and plastic strain components for out-of-plane bending load 239

6.4 Strain-life curves showing the upper and lower bounds of exponents b (fatigue stength exponent) and c (fatigue ductility exponent) used in this study 240

7.1 Typical computer generated mesh for crack growth analysis of the tubular joint under the action of brace axial and out-of-plane bending loads. 245

7.2 Typical computer generated mesh for crack growth analysis of the tubular joint under the action of brace in-plane bending load. . . . 246

7.3 Schematic illustration of a semi-elliptical surface crack. A point P on the semi-elliptical crack front is located by the angle ϑ on the inscribed circle. 249

7.4 Location of the line spring elements in the tubular joint. 251

7.5 Idealized crack growth rate (da/dN) vs. stress intensity factor range (ΔK), (log-log scale) 254

7.6 Typical crack growth rate (da/dN) vs. stress intensity factor range (ΔK) for thin specimens, (log-log scale) 254

7.7 Relation between m and C for steels tested in air at $R \approx 0$: •, structural steels; □, high strength steels; ×, weld metal; △, HAZ [Gurney (1979b)] 257

7.8 Influence of m on propagation rate. For structural steels, m usually lies between 2.4 and 3.6 [Gurney (1979b)] 257

7.9 Normalized stress intensity factor dependence on the crack front position (Axial load) (a_o = 1.00 mm, c = 62.71 mm) 263

7.10 Normalized stress intensity factor dependence on the crack front position (Axial load) (a_o = 2.50 mm, c = 62.71 mm) 263

7.11 Normalized stress intensity factor dependence on the crack front position (Axial load) (a_o = 3.80 mm, c = 62.71 mm) 264

7.12 Normalized stress intensity factor dependence on the crack front position (Axial load) (a_o = 5.70 mm, c = 62.71 mm) 264

7.13 Normalized tress intensity factor dependence on the crack front position (Axial load) (a_o = 7.60 mm, c = 62.71 mm) 265

7.14 Normalized stress intensity factor dependence on the crack front position (Axial load) (a_o = 9.50 mm, c = 62.71 mm) 265

7.15 Normalized stress intensity factor dependence on the crack front position (Axial load) (a_o = 11.40 mm, c = 62.71 mm) 266

7.16 Normalized stress intensity factor dependence on the crack front position (Axial load) (a_o = 12.54 mm, c = 62.71 mm) 266
7.17 Normalized stress intensity factor dependence on the crack front position (Axial load) (a_o = 14.25 mm, c = 62.71 mm) 267
7.18 Normalized stress intensity factor dependence on the crack front position (Axial load) (a = 16.00 mm, c = 62.71 mm) 267
7.19 Normalized stress intensity factor dependence on the crack front position (Axial load) (a_o = 17.10 mm, c = 62.71 mm) 268
7.20 SIF vs. ϑ comparison betwen the present study and that of Burdekin et al. (1992) using 3-D FE and combined equation (axial load) . . . 268
7.21 Normalized SIF (SIF/σ_{nom}) vs. a/T at the deepest points for axial, in-plane and out-of-plane bending loads. 272
7.22 Normalized SIF (SIF/$\sigma_{nom}\sqrt{\pi a_o}$) vs. a_o/T at the deepest points for axial, in-plane and out-of-plane bending loads. 272
7.23 Normalized SIF (SIF/$\sigma_{HS}\sqrt{\pi a_o}$) vs. a_o/T at the deepest points for axial, in-plane and out-of-plane bending loads. 273
7.24 SCF variation around the joint intersection at various crack depths (axial load) 273
7.25 SCF variation along the crack line at various crack depth. (axial load)275
7.26 SCF variation around the joint intersection, at various crack depths. (IPB load) 275
7.27 SCF variation along the crack line at various crack depths. (IPB load)276
7.28 SCF variation around the joint intersection, at various crack depths. (OPB load) 276

7.29 SCF variation along the crack line at various crack depths. (OPB load) 277

7.30 Crack depth vs cycles for propagating crack at saddle position; comparison between the present study (PS) and the earlier MUN experimental results (axial load) 277

7.31 Crack depth vs. cycles showing the effect of stress range on the fatigue life of tubular T-joints (Axial load) 278

7.32 Crack growth rate vs. crack depth comparison between the present study (Axial: FEM) and MUN (Axial:Experiment) results [Pates et al., (1989)]; present study (IPB: FEM) and University of Waterloo (IPB: Experiment) results [Pates et al., (1989)] 278

7.33 Comparison between the fatigue lives for axial, in-plane and out-of-plane bending loads for the present study (Note: University of Waterloo experimental results for in-plane bending load are also included) 280

A.1 Systematic generation of 'serendipity' shape functions. 306

List of Tables

4.1 Joint parameters 119

4.2 Details of boundary conditions 132

4.3 Comparison of SCF for half- and full-mesh for two T-joints under out-of-plane bending load 133

4.4 Comparison between results from coarse and fine meshes to show extent of convergence ($\alpha = 7.02$, $\beta = 0.5$, $\tau = 1.0$) 140

4.5 Comparison of SCFs obtained at Waterloo/Memorial Universities and National Engineering Laboratory with the present study: chord side ($\beta = 0.5$, $\tau = 1.0$) 142

4.6 Comparison of results obtained at Waterloo University and Memorial University Laboratories with the results of the present study 144

5.1 Comparison between two mesh types: (i) Unstiffened joint mesh; (ii) stiffened joint mesh. Axial loads 188

5.2 Comparison between two mesh types; (i) Unstiffened joint mesh; (ii) stiffened joint mesh. In-plane bending loads 189

5.3 Comparison between two mesh types: (i) Unstiffened joint mesh; (ii) stiffened joint mesh.Out-of-plane bending loads 190

5.4 Comparison of SCFs obtained at Waterloo/Memorial Universities and National Engineering Laboratory with the present study: Chord side 197

5.5 Geometric data of the stiffened model used for comparison between the present study and the National Engineering Laboratory experimental results and UCL semi-loof shell element and combined shell and brick elements 198

5.6 Comparison between SCFs obtained in the present study, National Engineering Laboratory experimental results and UCL semi-loof shell element and combined shell and brick elements - crown position (Axial) 198

5.7 Comparison between SCFs obtained in the present study, National Engineering Laboratory experimental results and UCL semi-loof shell element and combined shell and brick elements - crown position (Axial) 199

5.8 Stress analysis results of stiffened tubular joints subject to axial and out of plane bending loads; showing the values of SCFs at four critical point in the stiffener (α = 7.02, β = 0.5, γ = 24.0, τ = 1.0) 221

6.1 Fatigue crack initiation life of tubular T-joints under Axial, In-plane and Out-of plane bending loads: K′ = 1,500 MPa, σ'_f = 1,262 MPa, ε'_f = 1.28, n′ = 0.19, b = -0.209, c = -1.10 232

6.2 Comparison between experimental results of University of Waterloo and Memorial University with the present study (Pates et al., 1989) 233

6.3 Elastic and plastic strain amplitudes: K′ = 1,500 MPa, σ'_f = 1,262 MPa, ε'_f = 1.28, n′ = 0.19, b = -0.209, c= -1.10 (Axial) 234

6.4 Elastic and plastic strain amplitudes: K′ = 1.500 MPa, σ'_f = 1.262 MPa, ε'_f = 1.28, n′ = 0.19, b = -0.209, c= -1.10 (IPB) 235
6.5 Elastic and plastic strain amplitudes: K′ = 1.500 MPa, σ'_f = 1.262 MPa, ε'_f = 1.28, n′ = 0.19, b = -0.209, c= -1.10 (OPB). 236
7.1 Stress intensity factors for the deepest points of saddle and crown cracks (160 MPa) 259
7.2 Stress intensity factors for the deepest points of saddle and crown cracks (250 MPa) 260
7.3 Normalized stress intensity factors at the deepest point of a saddle crack (c = 62.71 mm) under brace axial load 270
7.4 Fatigue lives at 90% chord thickness cracking (Axial tension) 281
7.5 Fatigue lives at 90% chord thickness cracking (IPB) 282
7.6 Fatigue lives at 90% chord thickness cracking (OPB) 283
C.1 Stress Intensity Factors at Deepest and Surface points: 160 MPa (Axial Load) 313
C.2 Stress Intensity Factors at Deepest and Surface points: 170 MPa (Axial Load) 314
C.3 Stress Intensity Factors at Deepest and Surface points: 180 MPa (Axial Load) 315
C.4 Stress Intensity Factors at Deepest and Surface points: 190 MPa (Axial Load) 316
C.5 Stress Intensity Factors at Deepest and Surface points: 200 MPa (Axial Load) 317

C.6 Stress Intensity Factors at Deepest and Surface points: 210 MPa (Axial Load) 318
C.7 Stress Intensity Factors at Deepest and Surface points: 220 MPa (Axial Load) 319
C.8 Stress Intensity Factors at Deepest and Surface points: 230 MPa (Axial Load) 320
C.9 Stress Intensity Factors at Deepest and Surface points: 240 MPa (Axial Load) 321
C.10 Stress Intensity Factors at Deepest and Surface points: 250 MPa (Axial Load) 322
C.11 Stress Intensity Factors at Deepest and Surface points: 260 MPa (Axial Load) 323

List of Symbols

a	Crack depth
a_o	Deepest point in a semi-elliptical surface crack
$[\mathbf{B}']$	Matrix relating nodal displacements to element strains
b	Fatigue strength exponent
C	Crack growth constant, Paris law
c	Fatigue ductility exponent
$2c$	Semi-elliptical surface crack length
$[\mathbf{D}]$	Elasticity matrix
D	Chord diameter
d	Brace diameter
DoB	Degree of bending
DS	Distance between stiffeners
E	Modulus of elasticity
g	Gap between brace at intersection
G	Shear modulus
FEM	Finite element method

HAZ	Heat affected zone
HS	Stiffener height
IPB	In-plane bending
[J]	Jacobian matrix
da/dN	Crack growth rate
[K]	Element stiffness matrix
K	Stress intensity factor (SIF)
K_{min}	Minimum stress intensity factor
K_{max}	Maximum stress intensity factor
K_I	Mode I stress intensity factor
K_{II}	Mode II stress intensity factor
K_{III}	Mode III stress intensity factor
ΔK	Stress intensity factor range
$K_{I_{dpt}}$	Mode I stress intensity factor at deepest point
$K_{I_{spt}}$	Mode I stress intensity factor at surface point
K'	Cyclic strength coefficient
l	Brace length from the chord surface
L	Chord length
MUN	Memorial University of Newfoundland
N	Shape function

N_i	Shape function at node i
N_f	Fatigue crack initiation life (cycles)
N_p	Fatigue crack propagation life (cycles)
N_T	Total fatigue life
NEL	National Engineering Laboratory
n'	cyclic strain hardening exponent
OPB	Out-of-plane bending
PS	Present study
$CRSCF_{crl}$	Cracked tubular joint SCF at crack line
$CRSCF_{int}$	Cracked tubular joint SCF at intersection
SCF	stress concentration factor
SNCF	strain concentration factor
SCF_{crl}	Uncracked tubular joint SCF at crack line
SCF_{int}	Uncracked tubular joint SCF at intersection
T	Chord thickness
t	Brace thickness
t_i	Modulus of thickness vector $\vec{\mathbf{V}}_{3i}$
TS	Stiffener thickness
UCL	University College London
σ'_f	Fatigue strength coefficient

u, v, w	displacements in the global x, y, z directions
u_i, v_i, w_i	displacements in the global x, y, z directions at node i
u', v', w'	displacements in the local x', y', z' directions
V	Element volume
$\vec{v}_{1i}, \vec{v}_{2i}, \vec{v}_{3i}$	Unit vectors defining local x', y', z' directions at node i
$\vec{\mathbf{V}}_{3i}$	Thickness vector at node i
x, y, z	Global Cartesian coordinates
x', y', z'	Local Cartesian coordinates
x_i, y_i, z_i	Cartesian coordinates of node i
Y	SIF Geometric factor
$\{\delta\}$	Generalized nodal displacements for the element
$\{\delta'_i\}$	Generalized nodal displacements at node i
$\{\varepsilon'\}$	Local strain vectors
$[\theta]$	Cosine matrix of the local coordinate system
α_i, β_i	Rotations of normal at node i
α	2L/D
β	d/D
γ	D/2T
κ	Shear correction factor
ϕ	Angle around intersection

σ_B	Through chord wall thickness bending stress
σ_M	Through chord wall thickness membrane stress
σ_T	Total stress ($= \sigma_B + \sigma_M$)
σ_{HS}	Hot spot stress
σ_{nom}	Applied nominal stress
θ	Angle between brace and chord axes
ϑ	Crack front angle
ν	Poisson's ratio
ξ, η, ζ	Curvilinear coordinate set

Chapter 1

Fatigue of Tubular Welded Joints

1.1 Introduction

For more than a century it has been well understood that metal components and structures subjected to variable or repeated loads would fail in service, even though they are usually capable of withstanding considerably higher loads if the loads were of a static nature. This type of failure, which consists of the formation of a crack or cracks, under the action of varying loads, around highly stressed critical areas has come to be recognized and known as fatigue. It is however, virtually impossible to produce a complete list of the types of structures which may suffer from this type of failure.

Considering structures which are fabricated by welding in nich fatigue cracking have caused failure, those in the following list spring immediately to mind. They are conveniently classified under some of the typical forms of loading which may cause fatigue failure.

1. **Fluctuating live loads :** Bridges,cranes, gantry girders, diesel engine frames, locomotive underframes, lorry chassis, frames and axles, ships, earth-moving

equipment, farm machinery, rock crushers, presses etc.

2. **Pressure fluctuations :** Pressure vessels, pipework, containers etc.

3. **Temperature fluctuations :** Process equipment involved with hot or cold materials, liquid and gases.

4. **Vibrations :** Rotating machinery, grading equipment and conveyor.

5. **Environmental loadings :** Marine platforms and rigs.

The last item in the list forms the subject of this research. The active search for gas and petroleum has resulted in extensive offshore producing activities world-wide. Most of the rigs currently in operations are of the jacket type construction, comprising of a steel platform supported by a steel framework. These steel frame type structures are fabricated from tubular members that are joined together by welding the end of one tube (brace) to the undisturbed exterior surface of another tube (chord) at discrete points called the intersections. Figure 1.1 shows the sketch of a typical jacket type platform. Because of the abrupt discontinuity or change in geometry at these points coupled with the complex environmental loadings such as wind, wave and current loadings, as shown in Figure 1.2, they become sources of stress concentration and hence potential candidates for fatigue crack initiation and propagation sites (Figure 1.3). If fatigue cracks occur, they are initiated at these zones of large stress concentrations, and in fact the fatigue behaviour of these tubular structures depends primarily on the severity of these stress concentrations and reversals. It is therefore apparent, that in designing structures with welded

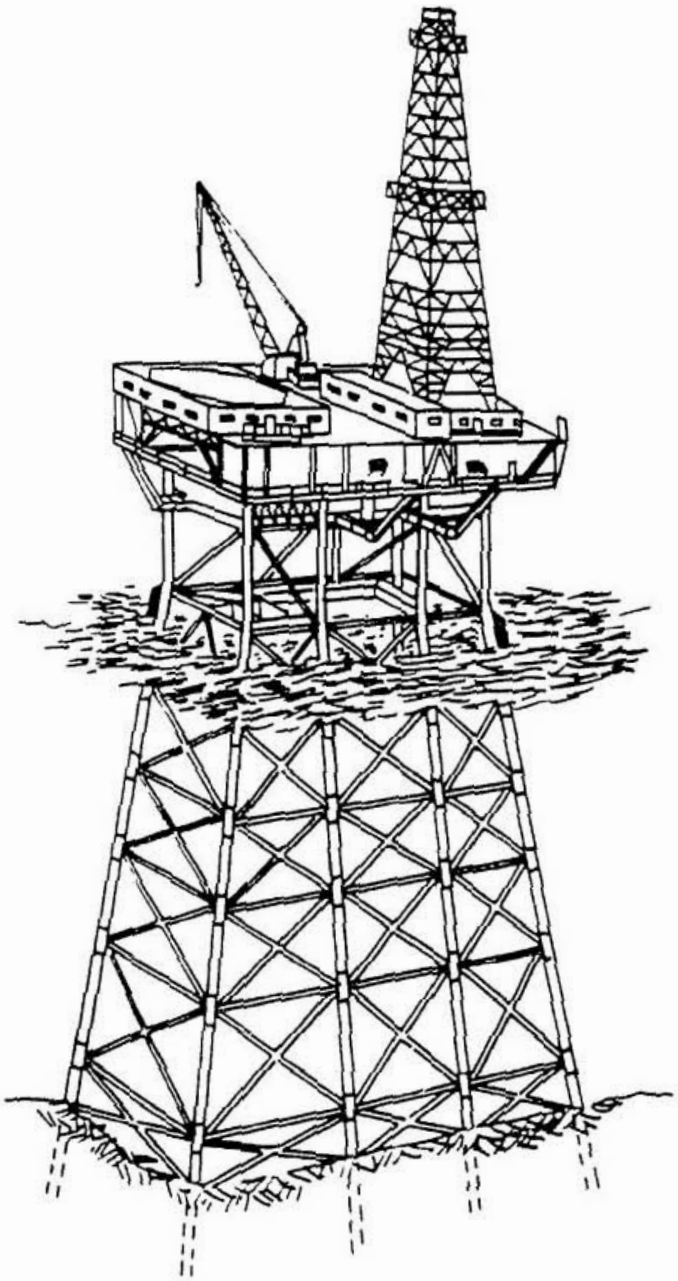

Figure 1. A jacket type platform.

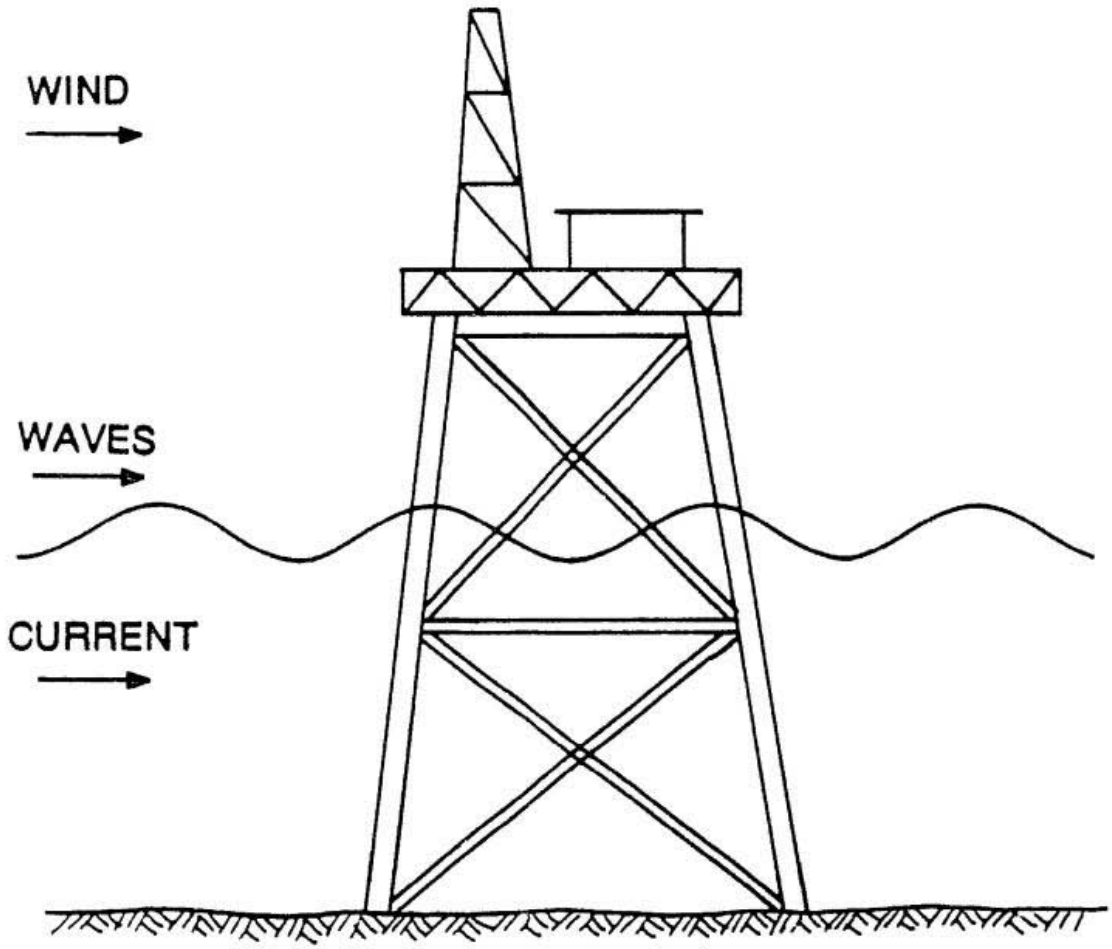

Figure 1.2: Environmental loadings on an offshore structure.

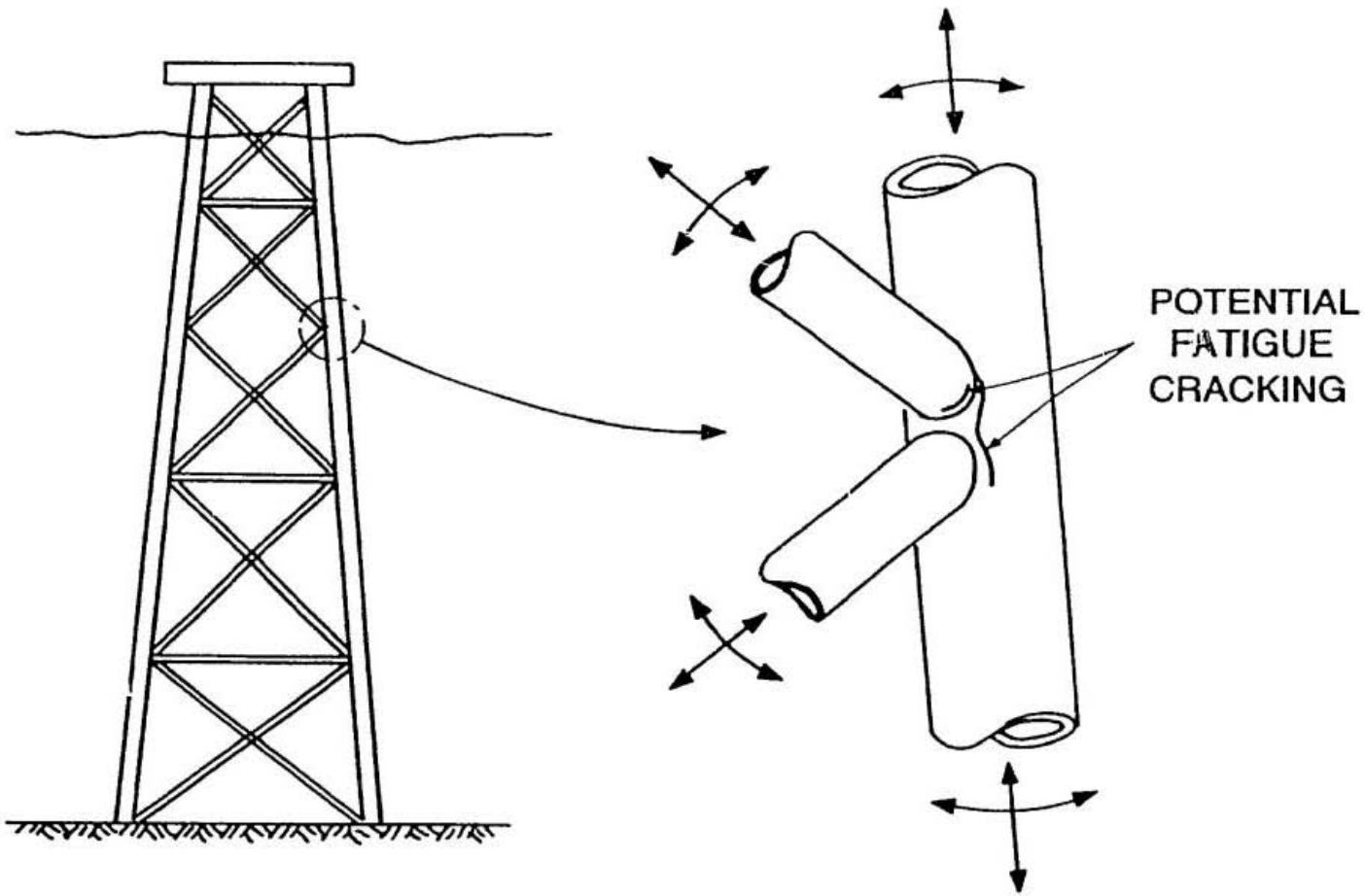

Figure 1.3: Tubular welded structure showing possible crack sites.

tubular joints, minimization of the number of joints should be of paramount importance from the fatigue point of view; in addition, an optimal joint configuration giving a large joint fatigue life should be determined. In the past, majority of criteria governing tubular welded structures dealt mainly with the static strength (load bearing) capabilities, because most operational and design experience of these type of structures had been gained in the relatively shallow and calm waters of the Persian Gulf and the Gulf of Mexico.

Tubular sections have high priority over open sections for structural use in offshore platform design because of their high-torsional rigidity, symmetry of sectional properties, simplicity of shape, and pleasing appearance. They possess great structural advantages as structural elements, but their use was for many years hampered by the difficulties in joining the members. This problem has been overcome in recent years by directly welding the contoured end of one tube onto the undisturbed outside of the other tube.

There are innumerable configurations for offshore tubular joints, if three-dimensional geometry is considered. Even restricting consideration to in-plane connections (where the axes of all the tubes lie in the same plane), there are still many configurations. In-plane offshore tubular joints are designated as T, double T, Y, K, N, etc., depending on the positions of the braces. Figure 1.4 shows some of the possible geometries of typical tubular joints. Regardless of the loading transmitted through the brace, large stress concentrations are produced at certain points along the brace/chord intersection. This effect can be attributed to two main reasons; (i) the presence of the weld and (ii) the abrupt change in geometry at intersection.

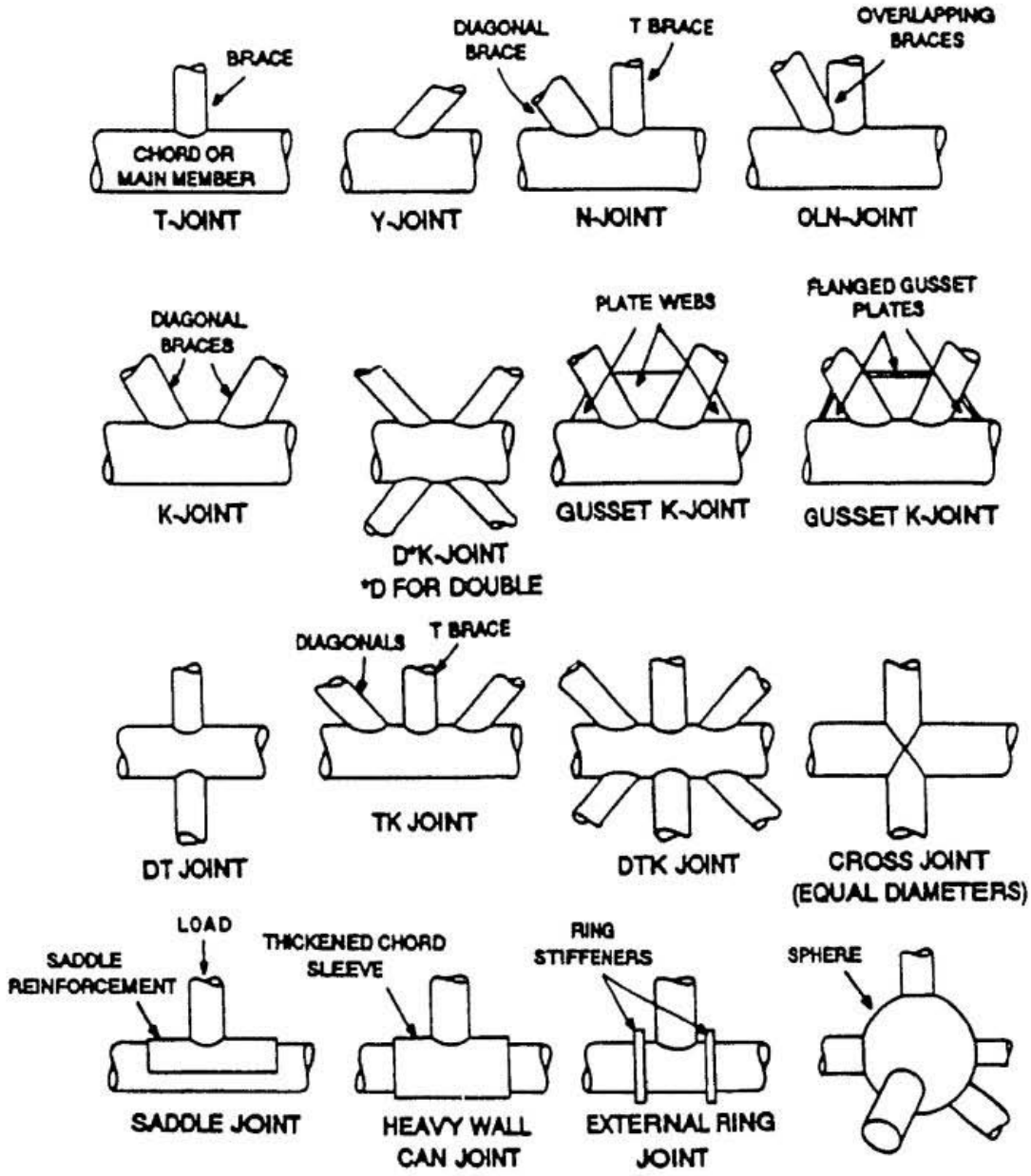

Figure 1.4: Typical tubular joint connections showing some of the many possible geometries.

The stresses at these critical locations can be several times higher than they would be if such effects as weld and change in geometry are not present. Cracks initiate first at these highly stressed regions, and depending on which side of the joint (chord or brace) this highly stressed region is located, the cracks first spread as multiple cracks along the weld and soon coalesce to form a single crack, and start growing through the thickness of the brace or chord.

Long before an all-out effort was made in the late 1960s to develop relevant offshore tubular joint design criteria, many design configurations have been implemented to strengthen the jacket joints. Gusset plates, welded in-between the brace ends and chords, were first tried. Sometimes pass-through gussets [Figure 1.5 (a)] were used. But it was not too long before it was discovered that gusset plates produced undesirable stress concentrations which shortened the fatigue life characteristics of the joint, and the general trend was towards the reinforcing of joints with external ring stiffeners [Figure 1.5 (b)]. These ring stiffeners were placed on the chord to strengthen the chord wall against collapse; sometimes they were added at intervals along the lengths of the brace to preclude ovalization of the cross section of the brace and subsequent buckling if the brace was loaded in compression. Use of internal ring stiffeners [Figure 1.5 (c)] has recently gained wide acceptance as one of the effective methods of reducing the stress concentration around the intersection of tubular joints, provided the tube is large enough to allow their placement.

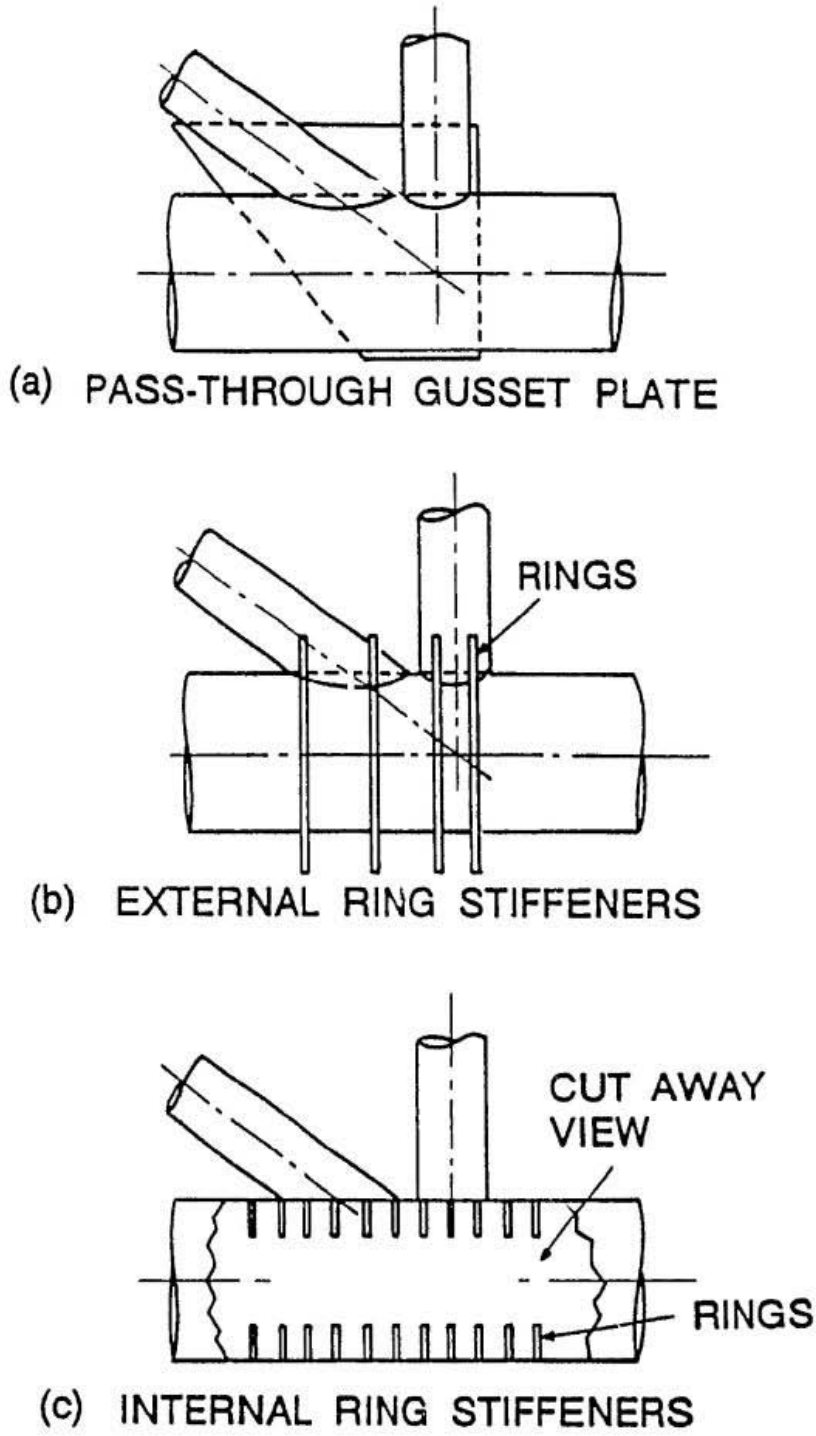

Figure 1.5: Types of stiffeners used in offshore tubular joints.

1.2 Crack Initiation and Growth in Fatigue Analysis

The fatigue strength of a structure, for general engineering purposes, is described as the number of stress cycles of a particular amplitude that a given component will withstand, before complete failure occurs. Fatigue failures are divided arbitrarily into two groups, viz., low cycle and high cycle fatigue failures. Where a component fails within 10^3 to 10^4 cycles or less, the failure is termed as a low cycle fatigue failure. If components survive more than 10^6 cycles then the process is termed high cycle fatigue. Structures such as submarines, pressure vessels, steam turbines etc., that are subjected to very low frequencies of loading are normally associated with low cycle fatigue failure. On the other hand, offshore structures such as oil rigs, are subjected to relatively high loading frequencies due to the passage of waves. Because of this, the stresses in oil rig structural members, have to be designed for the high cycle region (lives in the region of 10^6 cycles and above). Fatigue failure, whether of low or high cycle , consists of three distinct stages:

Stage I : crack initiation and nucleation;

Stage II : crack propagation; and

Stage III : ultimate failure.

For most practical design purposes, particularly for offshore steel structures, the last phase is ignored. In these cases, the design against fatigue does not allow cracks to propagate to a critical size where rapid brittle fracture can occur. Materials used in offshore structures are ductile enough to cause separation of the brace from the chord before brittle fracture can occur in the structure; thus brittle fracture is

prevented in offshore structures..

The evaluation of the crack initiation life by the local strain approach concept (strain life) is based on the observation that in many components the response of the material in critical locations is strain or deformation dependent. This approach to crack initiation recognizes the fact that fatigue is a localized process and, therefore, focuses on the regions of stress concentration in the structure where crack initiation is most likely to occur. Since these regions experience local plastic deformations, plasticity effects are explicitly treated. The fatigue resistance of the structure at the critical point is characterized by a strain-life curve obtained from the log-log plot of the total strain amplitude $\Delta\varepsilon/2$, versus reversals to failure, $2N_f$, which is given in the form:

$$\frac{\Delta\varepsilon}{2} = \frac{\sigma'_f}{E}(2N_f)^b + \varepsilon'_f(2N_f)^c \tag{1.1}$$

where

E = Elastic modulus,
σ'_f = Fatigue strength coefficient,
ε'_f = Fatigue ductility coefficient,
b = fatigue strength exponent,
c = fatigue ductility exponent, and
N_f = fatigue life of the specimen

and is schematically shown in Figure 1.6.

Assessment of the crack propagation life is generally based on linear elastic fracture mechanics principle which has received increasing attention during recent years in

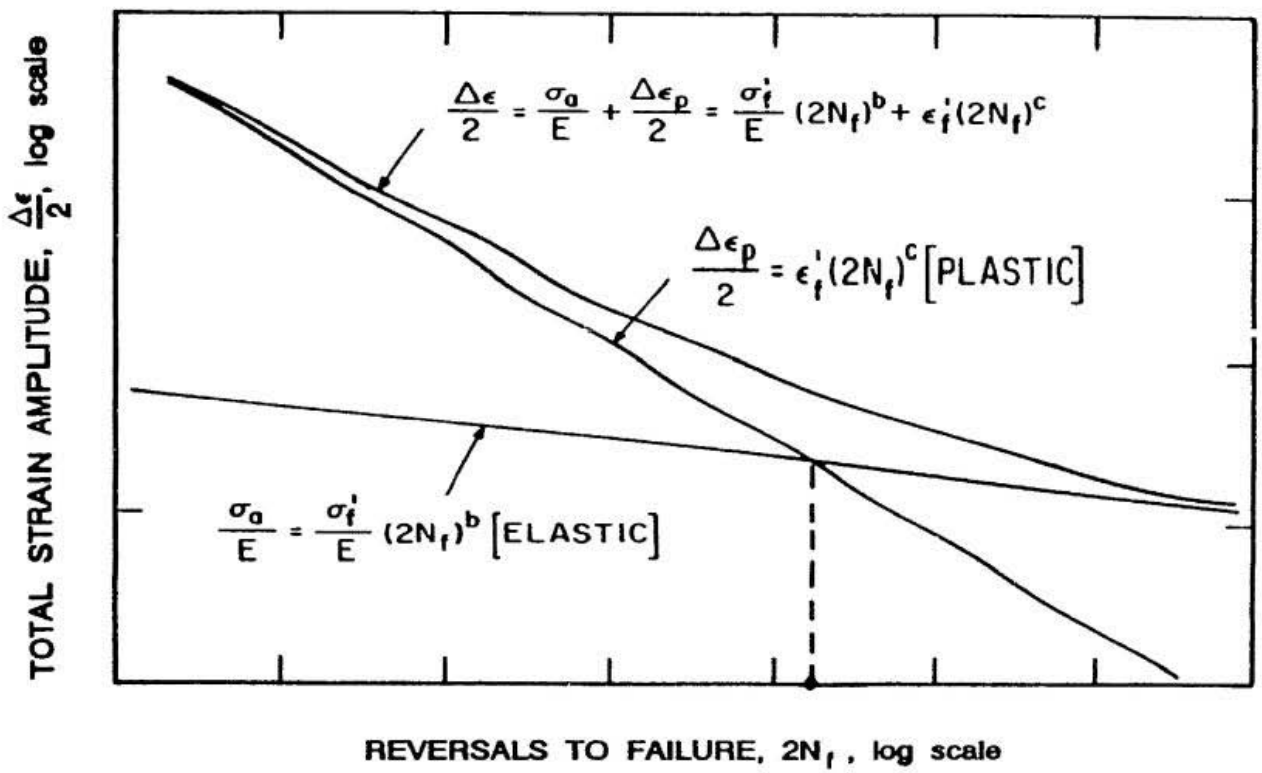

Figure 1.6: Total strain-life plot.

the fatigue analysis of tubular joints. Parameters such as nominal hot spot stress and crack size are used by this approach in characterizing the fracture behaviour of structures. Linear elastic fracture mechanics (LEFM) methodology uses an analytical procedure that relates the stress field magnitude (Figure 1.7) and its distribution in the vicinity of a crack tip to (i) the nominal stress applied to the structure, (ii) the size, shape, and orientation of the crack or crack-like discontinuity and (iii) the material properties. Any loading on a cracked body is accompanied by inelastic deformations in the neighbourhood of the crack tip due to stress concentration. Depending on the mode of loading on a cracked component, the relative movement of a crack surface is characterized by three basic modes of deformation and these are distinguished as:

1. The opening mode (Mode I), characterized by local displacements that are symmetric with respect to the xy - and xz-planes. The two fracture surfaces are displaced perpendicular to each other in opposite directions [Fig.1.8 (a)].

2. The sliding or shear mode (Mode II), characterized by local displacements that are symmetric with respect to the $x-y$ plane and skew symmetric with respect to the $x-z$ plane. The two fracture surfaces slide over each other in a direction perpendicular to the line of the crack tip [Fig.1.8 (b)].

3. The tearing mode (Mode III), is associated with local displacements that are skew symmetric with respect to both $x-y$ and $x-z$ planes. The two fracture surfaces slide over each other in a direction that is parallel to the line of the crack front [Figure 1.8 (c)].

Each of these modes of deformation corresponds to a basic type of stress field (see

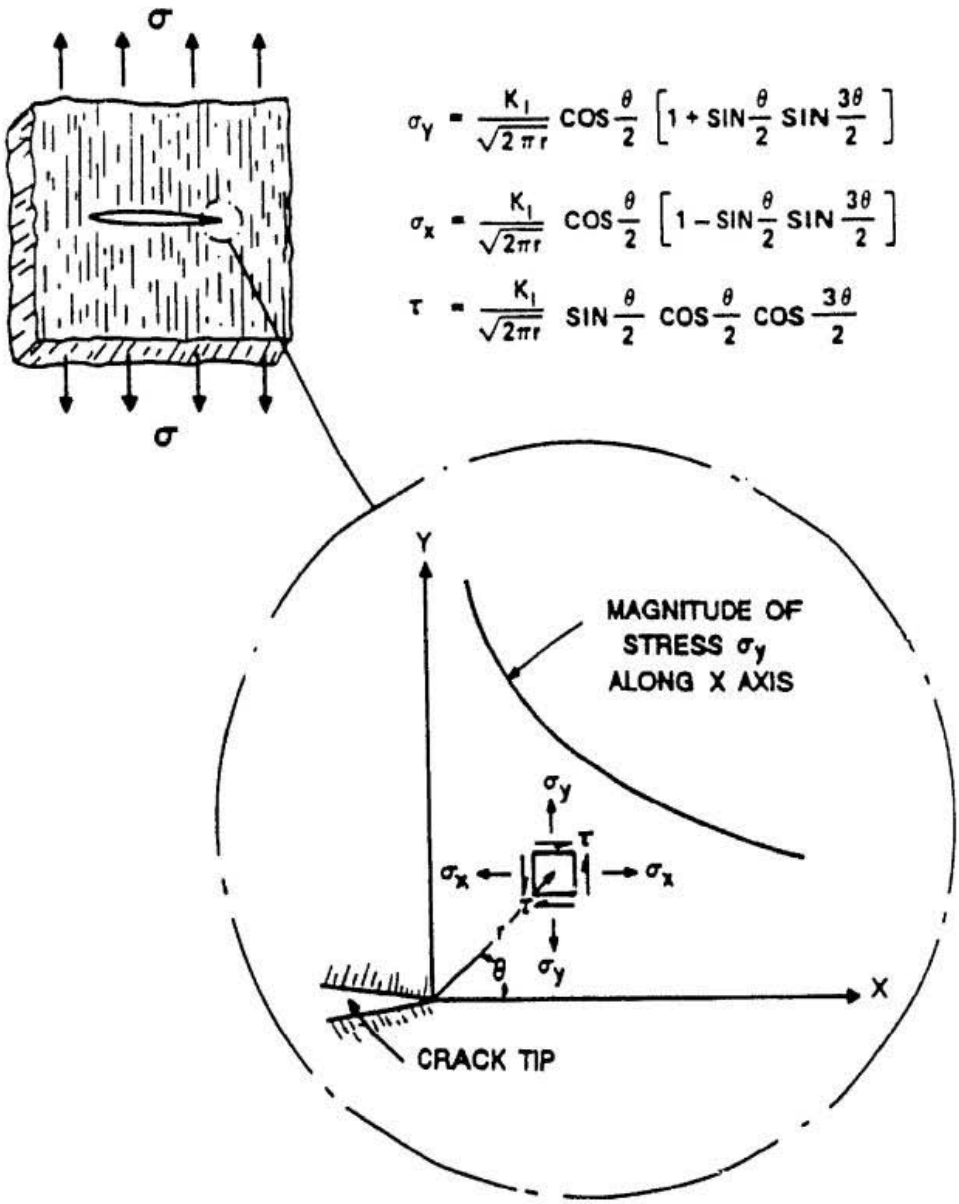

Figure 1.7: Elastic stress field distribution ahead of a crack.

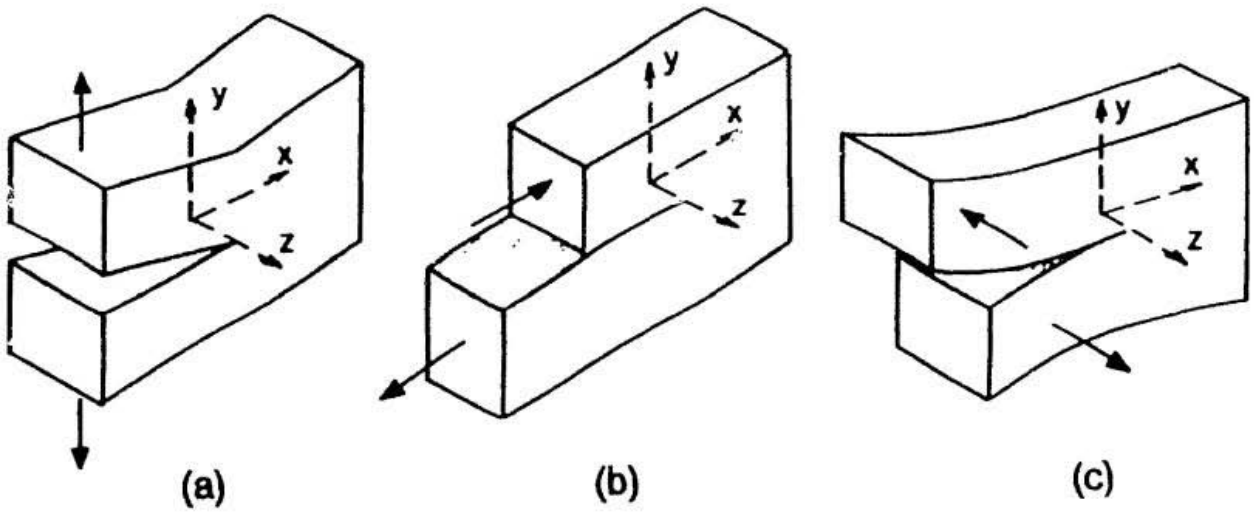

Figure 1.8: The three basic modes of crack surface displacements. (a) Mode I: opening mode, (b) Mode II: shearing mode, and (c) Mode III: tearing mode.

Figure 1.7) in the vicinity of the crack tip. Depending on the geometry and loading conditions, the deformations and stresses at the crack tip can be treated as one or a combination (mixed mode) of these local displacement modes. Figure 1.7 shows that the distribution of stresses and strains around the crack tip can be described by a single parameter K, designated as the stress intensity factor. Based on the Griffith's original analysis (1943) and the subsequent extension of that work to ductile materials, it has been established that the stress intensity factor in general is related to crack length and applied nominal stress as follows:

$$K = Y \sigma_{nom} \sqrt{\pi a} \tag{1.2}$$

where K is the stress intensity factor, σ_{nom} the applied nominal stress, Y a geometric factor and a the crack size. The geometric factor Y depends on the configuration of joint and the crack geometry and has been the subject of extensive investigations. As a result, various relationships for stress intensity factors of simple crack configurations with various crack sizes, orientations, shapes, and loading conditions have been published. Unfortunately limited number of studies have been made in this direction for welded tubular joints. Existing studies have always been carried out experimentally with the argument that the complexities of the geometry and the three dimensional stress distributions around the welded intersections have made it very difficult to determine, analytically, the function Y for tubular joints. Since present investigation is analytical, an attempt is made to study this problem in detail.

Many theories and empirical equations relating fatigue propagation rate (da/dN) to stress intensity factor range (ΔK) have been proposed; the most commonly used is the Paris power law:

$$\frac{da}{dN} = C(\Delta K)^m \tag{1.3}$$

where C and m are material constants

From Eqn. (1.3) the propagation life (N_p) can be calculated by integrating from the initial flaw size depth (a_i) to critical flaw size (a_c) as:

$$N_p = \int_{a_i}^{a_c} \frac{da}{C(\Delta K)^m} \tag{1.4}$$

In conclusion it is apparent that the fracture mechanics methodology offers the most comprehensive approach to fatigue life determination of offshore tubular joints. This methodology is used in this investigation to determine the fatigue crack propagation life of unstiffened tubular joints.

1.3 Scope of the Thesis

The purposes of this study is to estimate by numerical analysis the fatigue life of tubular joints which have been tested in the Strength Laboratory of Memorial University of Newfoundland, St. John's. The influence of various geometric parameters on the stress distribution around the intersection is examined and the results compared with the available parametric equations. The through thickness stress

distributions have been investigated by using a simple linear relationship between the through thickness bending stress and hot spot stress (degree of bending). The relative proportion of bending stress in the wall of the tube is investigated and its importance in fatigue life evaluation emphasized. The behaviour of the stiffened tubular joints with internal ring stiffener is investigated with a view to obtain the size and positions for which they are most efficient from fatigue point of view.

A numerically efficient method for determining the combined crack initiation and crack propagation life of offshore welded tubular joints is developed using finite element method. Fatigue life of offshore welded tubular joints have been determined from an entirely numerical point of view and compared with the experimental results obtained for tubular welded joints at the Faculty of Engineering and Applied Science, Memorial University of Newfoundland.

1.4 Organization of the Thesis

The following provides a brief description of the material covered in this thesis. The study mainly emphasizes the use of numerical methods for fatigue life assessment of full scale offshore welded steel tubular joints under the action of brace axial, in-plane and out-of-plane bending loads.

Chapter 2 covers the past, present and related review of literature concerning offshore welded tubular joints. Various numerical and theoretical backgrounds utilized in fatigue strength analysis are presented in Chapter 3. The formulation of the element (degenerate isoparametric shell element – 8-node serendipity and 9-node Lagrangian) used for the stress analysis of stiffened and unstiffened tubular joints,

in the present study, is given in this chapter. The 'line spring element' formulation developed by Parks et. al. (1981) have been utilized to model the crack and for SIF evaluation along the crack front. The basic concept of this element is also presented in Chapter 3. Finally the formulation of the local strain approach for crack initiation life and the integration technique of the Paris power law, for fatigue crack propagation are presented.

In order to predict the fatigue crack initiation life of any component susceptible to fatigue failure, the knowledge of the stress distribution in the vicinity of the stress concentration areas is required. The initiation life computation therefore, depends on the accuracy with which the stresses can be evaluated. Chapter 4, explicitly presents a comprehensive stress analysis of unstiffened tubular joints and the evaluation of the stress concentration factors for the determination of hot spot location where the crack is likely to initiate. Comparison of results obtained from the present study and experimental studies is also presented in this chapter.

In Chapter 5 the stress analysis and the behaviour of the tubular joints with internal ring stiffeners, under the action of the three loading (brace axial, in-plane and out-of-plane bending) cases, are given. The influence of stiffener locations, number (NS), height (HS) and thickness (TS) of stiffeners on the stress distribution around the intersection is provided; also comparisons with known experimental and analytical results have been made.

The crack initiation life prediction using the local stress approach is presented in Chapter 6 and Chapter 7 presents the application of linear elastic fracture mechanics

(LEFM) concept to fatigue crack propagation (FCP) life estimation of unstiffened tubular joints. Chapter 7 concludes with the evaluation of the total life of the joint (i.e., the sum of crack initiation life and the propagation life $N_T = N_f + N_p$) and the comparison with both experimental and analytical investigations.

Chapter 8 presents the summary, conclusions and the contribution of the present study. It also provides recommendations for future theoretical studies on offshore tubular joints.

Chapter 2

Literature Review

2.1 General

The state of deformation, stress and cracking in welded tubular joints, with complex geometric configurations, has been of great concern to the offshore engineers for many years and this has resulted in numerous developments. These developments have given rise to both analytical and experimental studies with many significant contributions made in the past few years.

The relative complexity of the geometrical configuration of the tubular joints, as well as the thin-shell theory governing their behaviour, have contributed immensely to the unreliable prediction of the stresses in such joints by analytical techniques. Hence numerical techniques such as the finite element method, have offered an alternative acceptable and reliable procedure for handling complex geometries and boundary conditions. Early attempts to apply the finite element method to the stress analysis of tubular joints were somewhat hindered by the computational demands generated by too many elements. The advances in the computer technology, with a larger central memory and faster computers in the recent years, have made

it possible to apply this powerful numerical technique not only to the stress analysis of tubular intersections, but also for studying the elastic behaviour of these intersections when they contain crack-like defects. However, some problems arise in modelling the near crack tip stress field using finite elements due to the singularity at the crack tip: the regular finite element shape functions when used for the analysis of a crack are unable to represent this crack tip singularity, and thus produce poor results when applied to fracture problems. Many attempts have been made to overcome the inability of the finite elements to represent the crack tip singularity by developing special elements which incorporate the required stress singularity in their formulation. The relevant literature pertaining to these developments are reviewed below to understand the state-of-the-art developments of fatigue and fracture of offshore tubular joints. While reviewing the state-of-the-art, a conscious decision has been made to neglect the large amount of experimental studies that are available on all types of tubular and other joints (T-joints, butt-welded joints, cruciform joints, etc.); in addition, the earlier numerical developments have also been left out for the major part except where it is found to be necessary to understand the thematic development of the topic.

Most analytical and experimental investigations, carried out to date on welded joints, have been done with a view to acquire significant information as to the life expectancy and fatigue performance of typical joints used in offshore construction. Two lines of approaches have been followed; the traditional S-N curve approach (stress-life) and the recent fracture mechanics approach (used in estimating the fatigue life spent in crack propagation), with the fracture mechanics approach receiving greater attention recently in the fatigue analysis of tubular joints.

2.2 Stress Analysis of Stiffened and Unstiffened Tubular Welded Joints

Offshore structures such as fixed platforms that are generally of tubular construction, experience high local stresses at the intersection of the chord and the brace adjacent to the connecting weld, where fatigue damage will generally occur. Therefore, fatigue analysis is highly dependent on the accuracy with which this high local stress at the hot spot can be calculated. The life determination is related to the nominal hot spot stress in the S-N diagram. Hence the first part of any fatigue study is the determination of the stress distribution, along the intersection as well as through the joint thickness, obtained experimentally, by strain gauging and, analytically by finite element method (FEM). For unstiffened tubular welded joints studies have shown that depending on the loading type (axial, in- and out-of-plane bending loads), geometry of the joint and the joint parameters (β, τ, α, γ, etc.) the hot spot may be located either on the chord side or the brace side. In addition, it may be at the crown or the saddle or in between the two points depending on the joint geometry, type of load and its combination. It is therefore apparent that a good design of offshore unstiffened tubular welded joints, from the fatigue cracking point of view, depends on the effort spent in the early stage to determine the magnitude and the location of the hot spot stress.

Two early methods, both very approximate, which have been summarized by Toprac et al.(1966) are usually referred to as the ring beam analogy and the Kellog (1956) method. Kellog method is based on the equations for a beam on elastic foundation. However, neither of these methods is now used. Of the theoretical techniques

thin shell finite elements have been used by several investigators, notably Dundrova (1965) and Scordelis (1970), but this method suffers from considerable limitations from the point of cost and of computational time. The finite element method, though suffering from the major disadvantage of being costly, particularly for complex joints, is really the only method which is capable of giving the local stress levels to the necessary degree of accuracy for fatigue strength calculations. Here, the assumption that members can be represented as thin shells is invoked and several types of shell elements have been used by different investigators.

Three distinct approaches, to the finite element representation of generally curved thin shells, have been employed based on (*i*) flat triangular or quadrilateral elements (*ii*) curved elements, formulated on the basis of various shell theories and (*iii*) three-dimensional isoparametric elements specialized to handle thin shells (degenerated isoparametric three-dimensional elements). These elements have been used by several investigators with reasonable results, notably among them being the studies of Rashid and Prince (1965) (flat triangular elements for the stress analysis of shell intersection), Greste (1970), Johnson (1967) (quadrilateral elements for the analysis of tubular K-joints), Yoshida et al. (1977) and Zienkiewicz (1977) (three-dimensional isoparametric elements for crack initiation prediction of tubular T-joints).

Kuang *et al.* (1975, 1977) carried out extensive and detailed studies on the stress concentration factors in welded tubular joints. Empirical formulae for estimating stress concentration factors for simple joints, commonly used in offshore structures, were derived from the results of this parametric study. Three types of simple non-

reinforced joints, viz., T, K, and TK-joints were considered. The finite element program used was that developed at the University of California, Berkeley, by Greste and Clough (1970). They modified existing stress analysis program to broaden the scope of its application and improved its efficiency and called it TKJOINT. They concluded that the parametric formulae presented by them would provide designers with sufficient information regarding the magnitude of hot spot stress in simple non-reinforced joints.

Welded tubular connections were analyzed by Liaw *et al.* (1976) using 20 noded three-dimensional isoparametric elements. The elements were found to provide more accurate modelling of the joints. The results of PMBSHELL and TKJOINT programmes were compared for an ungrouted K-joint and were found to give good agreement with their work except for some differences in the hot spot regions. They concluded that the small deviation was due to the assumptions made for using flat plate elements.

Gurney (1979) demonstrated that the stress concentration in tubular members can be reduced by controlling the weld shape; he observed that by increasing the weld leg length the fatigue strength of the joint could be increased, but found that this was relatively a minor effect. In his parametric study, Berge (1983) modelled the weld shape using the parameter θ, the weld toe angle, and ρ, the notch radius, and argued that the proper modelling of the radius ρ gave a more realistic model to the stress distribution at the weld toe and therefore had a significant effect on the fatigue strength of the joint.

The study by Hoffman and Sharifi (1980) have given a deeper insight into the stress concentration along the weld toe of the tubular T-joints. Two types of three-dimensional isoparametric elements were used in their studies (8-noded brick element and 16-noded thick shell element), with various "incompatible" modes introduced into the stiffness formulations to improve the flexural behaviour of the elements.

Gulati *et al.* (1982) conducted an analytical study of stress concentration effects in a multi-brace joint. Also studied were the simple T, K and TK joints subjected to isolated axial or in-plane bending loads. Loadings selected were only those that could lead to direct comparisons with stress concentration factors estimated by existing parametric equations. The comparisons showed good agreement between the computed and estimated values of the stress concentration factors. Majority of the finite element analyses were conducted by using MSC/NASTRAN computer program. The element types used included QUAD4, TRIA3, and BEAM elements and some analyses were conducted using the STARDYNE program. They concluded from their investigations that restricting attention to crown and saddle points for fatigue life evaluation can lead to erroneous results; hence they stated that fatigue life evaluation of a tubular joint should be carried out at eight points equally spaced at the chord-brace intersection. They argued that in computing stress concentration factors by using parametric equations for K and TK joints, both the joint geometry and the direction of loading should be properly considered.

Panagiotopoulos (1986) used a solid, incompatible element, at the intersection region of the T- and Y-joint connections, while using Ahmad *et al's* (1970) shell

element to model the rest of the structure. The transition between the two elements was accomplished by appropriately transforming the degrees-of-freedom of nodes, located on the mid-surface of the shell element, to be connected to the solid elements. Comparison between the numerical and experimental results demonstrated the efficiency of this type of idealization for predicting the stress gradients at the intersection region. It was concluded that this structural modelling leads to reliable results with no loss of essential features of the structural behaviour.

Dharmarvasan and Aaghaakouchak (1988) presented a finite element stress analysis of tubular joints stiffened by internal ring stiffeners of different sizes and at different locations in the chord. In order to study the behaviour of these set of tubular joints, a finite element parametric study was conducted. Semi-loof shell elements were used throughout the study with the explanation that these elements have a general curved shape and therefore model the geometry of the structure correctly. In their study, a T-joint with 15 different states of stiffening was analyzed under three loading cases: axial, in-plane bending and out-of-plane bending. Results of their analyses showed that in the case of axial and out-of-plane bending loading, adding the stiffeners to the chord at certain positions greatly reduced the stress concentration factors and gave a more uniform stress distribution around the intersection, especially on the chord side. The effect was found to be less significant in the case of in-plane bending. From the stiffener size point of view, it was observed that under the axial and out-of-plane bending loads, the stiffener height had the stronger effect in reducing the stress concentration factors (SCFs) compared to stiffener width. From the foregoing observations, they concluded that the moment of inertia of the stiffener is the main factor in controlling the level of SCFs. They

proposed that for the axial and out-of-plane bending cases the two quarters of the plug were the optimum positions. On the effect of the number of stiffeners, it was observed that as long as the stiffeners were located at the correct positions, increasing the number of the stiffeners resulted in increasing the chord moment of inertia and consequently in reducing the chord SCFs; but they have a smaller effect on the brace SCFs. They finally concluded: stiffening tubular joints at the middle half of the plug gives the optimum position for axial and out-of-plane bending (OPB) load cases. For the in-plane bending situation, adding the stiffeners to the two outer quarters of the plug was mo: efficient; the brace side may experience high SCFs due to the introduction of stiffeners. Stiffening reduces the ratios of bending to membrane stresses and produces a more uniform distribution of the stresses around the joint of the tubes. In this case it was stated that once the crack starts growing there may be a faster rate of crack growth through the thickness; hence if the existing definition of fatigue life in tubular joints is used it may not be safe to use the existing S-N curves for stiffened joints.

Aaghaakouchak and Dharmavasan (1990) presented an improved finite element technique for the determination of stress distribution around the welded intersection of stiffened and unstiffened tubular joints: a combined model of three dimensional and shell elements was considered in their study. Three dimensional isoparametric elements were used to model the welded intersection of the tubular joint and semi-loof thin shell elements were used for the rest of the joint. The results of the stress analysis obtained from both stiffened and unstiffened tubular joints, using the combined model, was compared with the results obtained from experiments and other types of finite element analyses. For the unstiffened joints, it was observed

that the model gave the result very close to the experimental stress concentration factors obtained for steel tubular joints. For the stiffened joints, they concluded that the distribution of available experimental SCFs were in general agreement with the finite element analysis using shell elements; close to the stiffener position, finite element analysis, with shell elements, showed an increase on the brace and a decrease on the saddle. The reduction of the SCFs at these positions on the chord, obtained experimentally, were found to be more significant than that predicted by finite element results. For the combined model of brick and shell elements, it was observed that around the stiffener positions due to the presence of significant shear and through-the-chord-thickness stresses, the direction of the principal stresses changed. The maximum difference between the principal and normal stresses were found to occur in the vicinity of the stiffener position on the chord. Comparing with available experimental results, they suggested that for the case of heavier stiffeners, a higher percentage of the loads were transferred to the chord around the stiffener position. They finally concluded, that, the through-the-chord-thickness transfer of loads may be a factor in this more significant reduction, and therefore, the strain measurements carried out on the tubular surfaces during the experiments on stiffened joints may not be able to represent the maximum principal stress at the chord weld toe and that care should be taken in interpreting the results.

2.2.1 Parametric Equations

Based on the results of numerical and experimental analyses, by several researchers, parametric equations have been developed, for determining the stress concentration

factors along the intersection of offshore tubular joints, and presented, in the familiar form of parametric equations

$$SCF = C\alpha^{n1}\beta^{n2}\tau^{n3}\gamma^{n4}\zeta^{n5}sin\theta^{n6} \tag{2.1}$$

where C is a constant, α = 2L/D, β = d/D, γ = D/2T, $\tau = t/T$, ζ = g/D are the non-dimensional joint parameters, and $n1$, $n2$, $n3$, $n4$, $n5$, $n6$ are exponents and θ is the intersection angle between members.

In addition to the work of Kuang et al's (1975, 1977) mentioned earlier, Gibstein (1978, 1981) also carried out parametric stress analysis of T and K (non-overlap and stiffeened) joints using the finite element program NV332. In the first study, seventeen T-joints were analyzed with both chord ends rigidly fixed. To investigate the effect of fixity, additional analysis of a T-joint with the chord ends simply supported was carried out. All the three loading cases — axial, in-plane and out-of-plane bending loads — were investigated. It was stated that there was a difference of 5% for axial loads and no difference in the bending ones, for the two boundary conditions. The influence of α, which was not investigated, was taken from the Kuang analysis. The SCF formulae for the brace had to be modified, by a factor of 0.8, to allow for differences between the predicted and experimental SCFs. In the second study nineteen models of K-joints, with β = 1.0, were analyzed and parametric equations presented for the chord and brace.

Wordsworth and Smedley (1978) presented empirical formulae for SCFs in T, Y, KT and X-joints, based on acrylic model test results. It was suggested that a

correction factor for the weld be applied as a multiplier to the SCFs obtained for T and DT joints for the chord side. Due to lack of data, no correction factor was given for Y and X-joints. The performance of the two semi-empirical equations given above (Kuang's and Wordsworth and Smedley) was compared by Irvine (1981). It was concluded that the stress concentration factors obtained using Wordsworth and Smedley's equation were more conservative than those of Kuang.

A set of equations, to predict these stress distributions for simple joints (T and Y), was proposed by Dhamarvasan and Dover (1984) and has been used to predict mixed mode stress concentration factors. The results obtained from a complex K joint was also examined in detail and the importance of the stress state, when predicting the mixed mode stress concentration factors, demonstrated. Three methods were used for their studies, viz., finite element analysis, strain-gauged steel models and strained-gauged acrylic models. The results from these techniques and the formulae obtained from them were compared with the available analytical, experimental and stress distribution equations. In conclusion it was observed that only the parametric equations by Wordsworth and Smedley (1978) could be assessed from the data base. They stated that these equations were on an average 7% higher and fall within a scatter band of +29% and -15%; the acrylic model gave comparable accuracy to the Wordsworth and Smedley equations. It was also shown that Dharmavasan and Dover's (1984) new stress distribution formulae were more accurate than previous formulations. It was shown that these new formulae can be used to predict mixed mode SCF's to within +20%.

Connolly et al. (1990) carried out a thin shell finite finite element parametric

study of the through-thickness bending to membrane stress ratios in tubular Y- and T-joints. In their study, nearly 900 finite element runs were performed for a wide range of joint geometries for axial, in-plane bending and out-of-plane bending loads. The validity of their approach was demonstrated by comparing the thin shell finite element results with data obtained from strain-gauged acrylic model tests and other finite element analyses utilizing thick shell or brick elements to model the intersection. The results were then used to construct semi empirical equations which related the relative proportions of bending and membrane stresses to a parametric equation of the joint. They concluded that the only important feature of the raw results which could not be directly incorporated into the parametric equations was that for small values of the brace angle θ (typically below 45°) together with either small β (= d/D) or small τ (= t/T); the proportion of membrane stress was typically much higher than would be expected from trends in the rest of the data. They suggested that in such cases it was probably wise to assume conservatively that the through thickness stresses are wholly tensile.

A statistical method for identifying the probable SCF regimes was developed by Dover et al. (1991); they compared five sets of SCF parametric equations that gave various levels of prediction and determined the best parametric equations that could be used for design purposes. The five parametric equations used in their study were those due to Kuang et al. (1977), Wordsworth and Smedley (1978), modified UEG (1985), Efthymiou and Durkin (1988), and Hillier et al. (1990). They concluded that the currently available steel SCF database was adequate for some categories (particularly, crown and saddle of T-joints) but insufficient for many. They also observed that some equations have normalized mean values close to unity, whereas

others give conservative values and hence advocated accountability in overall safety assessment where mean values were close to one.

Ramachandra et al. (1991) conducted an analytical and experimental investigation on internally stiffened steel tubular joints. Based on finite element analysis of T and Y stiffened joints, optimum stiffener positions were proposed for reducing the stress concentration factor. Parametric equations for calculating the maximum stress concentration factors (SCFs) for these joints under different loading conditions were also developed. The experimental and analytical results were compared. On assessing the influence of stiffener parameters (stiffener width/chord diameter ratio, $\chi = B/D$; stiffener thickness/chord thickness ratio, $\omega = T_s/T$), it was observed that there was a reduction in SCFs when the stiffener width/chord diameter ratio increased. However, they found that the reduction in SCF was not significant when the stiffener width/chord diameter ratio increase beyond 0.2. A reduction in the SCF was similarly observed when the value of stiffener thickness/chord thickness ratio increased. It was, however, observed again that the reduction in SCF was not significant when the stiffener thickness/chord thickness ratio increased beyond 0.75. The error in estimating the maximum stress concentration factor using the parametric formulae was given to be between +24% and −16.8%.

2.3 Fatigue of Tubular Welded Joints

From an engineering point of view, the total fatigue life of offshore tubular joints comprise of cycles required for crack to initiation (fatigue crack initiation life) as well as those required for crack propagation (fatigue crack propagation life); that

is:

$$N_T = N_f + N_p \tag{2.2}$$

where

N_T = total cycles to failure;

N_f = cycles to crack initiation; and

N_p = cycles for crack in propagation.

The relative magnitudes of N_f and N_p in Eqn. (2.2) can vary greatly from structure to structure, depending on the fabrication history, magnitude of applied loads, and severity of stress concentrations. It has generally been viewed that for large complex structures fabricated by welding, N_f, is relatively small compared to N_p. For example results from a full scale test of welded tubular joint, typical of that in an offshore structure, carried out by Wylde and McDonald (1981) demonstrated that engineering-sized cracks of 1 to 3 mm were present at less than 10% of the total life of the welded tubular joint. The results of recent experimental investigations reported by Pates et al., (1989) have shown that the concept of neglecting the crack initiation life of large scale structures, fabricated by welding may lead to erronous determination of the total fatigue life of such structures. For axial loading, it was observed that the crack initiation life was about 34.6% of the total life, in air at 250.0 MPa (hot spot nominal stress) and 46.6% in synthetic seawater at 160.0 MPa (Swamidas et al., 1988)

The local stress-strain approach have been applied successfully in the evaluation of fatigue crack initiation of welded joints. The procedure is based upon the earlier pioneering work in fatigue of notched members by Neuber (1969) and Peterson (1971) and later investigations by Lawrence (1978, 1980) and Fuchs (1980). The initiation life of the welded joint, which is assumed to contain a small notch, is related to the life of small unnotched specimens cycled to the same strains as the material at the weld notch root. The initiation period is defined as the time (in terms of cycles) required for a small, but detectable, fatigue crack to develop. For many years, this definition has been of great concern to many researchers. It has been difficult to quantitatively define the size of a crack to the end of the initiation and the beginning of propagation periods. For the crack propagation stage the fracture mechanics approach has proven to be an efficient and powerful tool for this aspect of fatigue life evaluation.

2.3.1 Fatigue Crack Initiation

Dowling (1979) and Lawrence (1979) have shown, in their respective studies, that reasonable success can be achieved by combining the local stress-strain approach to crack initiation and the fracture mechanics approach to crack propagation. Although this combined initiation and propagation approach to fatigue life prediction is both physically correct and generally applicable, the relative magnitudes of N_f, and N_p in Eqn. (2.2) can vary from structure to structure, depending on fabrication history, magnitude of applied loads, severity of stress concentration and environmental influence (corrosion). During the past, since the introduction of fracture mechanics approach for evaluating the fatigue life of offshore tubular welded joints,

it has been argued generally that for large complex structures like the tubular joints, fabricated by welding, N_f is relatively small compared to N_p.

Socie et al. (1979) presented a model for combining strain cycle fatigue and fracture mechanics concepts to estimate the total fatigue life of notched and cracked members. In their study the strain-life approach was employed by using the relationship between strain amplitude, $\Delta\varepsilon/2$, and reversals to failure, $2N_f$, which was expressed in the form:

$$\frac{\Delta\varepsilon}{2} = \varepsilon'_f (2N_f)^c + \frac{\sigma'_f}{E} (2N_f)^b \tag{2.3}$$

where σ'_f = fatigue strength coefficient, b = fatigue strength exponent, ε'_f = fatigue ductility coefficient, c = fatigue ductility exponent and E = elastic modulus. Their model provided a nonarbitrary definition of fatigue crack initiation length. A working definition for crack initiation length was proposed as the depth of the initiated fatigue crack when the fatigue damage due to crack propagation mechanisms exceeded that due to crack initiation or strain cycle fatigue mechanisms. Crack initiation length, and the total fatigue life, for center notched aluminium plates subjected from zero to maximum tensile loading were determined using their model. Theoretical elastic stress range, ΔS_x, at a distance x from a notched root was employed in conjunction with Neuber's rule (1969) to approximate the product of actual stress range, $\Delta\sigma_x$, and the strain range, $\Delta\varepsilon_x$, along the potential crack path part as:

$$\Delta\sigma_x \, \Delta\varepsilon_x = \frac{(\Delta S_x)^2}{2E} \tag{2.4}$$

From the various combinations of stress levels and notch acuity analyzed in their tests, to show the validity of their model, it was observed that the relative portion of the life spent in crack propagation increased with decreasing stress levels as also observed earlier by Hunter and Fricke (1957) and Dowling (1968). They concluded that crack initiation lengths, in typical engineering materials, appeared to be between 0.001 and 0.010 in. It was also observed that the greater the notch acuity, the larger is the portion of life spent in propagation.

An energy based method of calculating elastic-plastic strain and stresses near notches and cracks was presented by Glinka (1985). It was assumed that the strain energy density in the plastic zone, ahead of a notch, can be calculated on the basis of the elastic stress-strain solution. The application of this method for notches under tension and bending, including the effect of stress multiaxiality near the notch tip, was also presented. The concept developed by Hutchinson (1968), for cracks, and Walker (1974), for deep sharp notches (that in the case of localized plastic yielding the energy density distribution in the plastic zone is almost the same as in linear elastic material) was used in his study. For plane stress condition, using Ramberg-Osgood stress-strain relationship, he proposed that the energy density should be calculated as in the presence of localized yielding at the notch tip.

$$K_t^2 \frac{S_n^2}{2E} = \underbrace{\frac{\sigma_y^2}{2E}}_{elastic} + \underbrace{\frac{\sigma_y}{n+1}\left(\frac{\sigma_y}{K}\right)^{1/n}}_{plastic} \tag{2.5}$$

and that if the nominal stress S_n is beyond the proportionality limit, then the energy density should take the form

$$K_t^2 \left[\frac{S_n^2}{2E} + \frac{S_n}{n+1}\left(\frac{S_n}{K}\right)^{1/n}\right] = \underbrace{\frac{\sigma_y^2}{2E}}_{elastic} + \underbrace{\frac{\sigma_y}{n+1}\left(\frac{\sigma_y}{K}\right)^{1/n}}_{plastic} \tag{2.6}$$

For plane strain conditions, a biaxial state of stress exists at the notch tip. But it was however, stated that the energy density was made up of σ_y only because the components σ_x, σ_{xy}, ε_z vanish. Consequently expressions analogous to Eqns (2.5) and (2.6) were presented, for this case, by using the suggestions and relationships given by Dowling et. al. (1979) for the translation of the uniaxial stress-strain curve into the biaxial "plane-strain" relationship. It was pointed out that in the case of sharp, deep notches and cracks, the stress components σ_x and σ_z were relatively higher than ahead of the blunt notches, and that the stress distribution was also larger owing to the more intensive plastic yielding ahead of the crack tip. It was demonstrated that the method, which was based on the assumption that the strain energy density distribution (we will call it as Glinka's method) in the plastic zone ahead of a notch is the same as that determined on the basis of the pure elastic stress-strain solution, was the same as the Neuber's equations. Therefore, the difference between these two methods was higher for materials with large plastic zones and higher stress concentration factors. It was observed that in all analyses

performed the difference between calculated (using Glinka's method) and measured notch strains were smaller than 10%.

The predicted fatigue crack initiation lives of welded plated T-joints in air and seawater environment, was reported by Bhuyan and Vosikovsky (1987). Their approach was based on the local stress-strain approach. The effects of plate thickness on predicted fatigue crack initiation lives were also presented. The predicted lives were compared with the experimental data from Canadian offshore steel research program (Vosikovsky et. al., 1985/1987; Mohaupt et. al 1987).

2.3.2 Linear Elastic Fracture Mechanics

Linear Elastic Fracture Mechanics (LEFM) is a branch of applied mathematics which has developed as a result of studies into the phenomenon of brittle fracture. It is the field of analysis that deals with the stress and strain distributions at the tips of cracks in ideally elastic solids. The approach is based on the fact that the crack-tip stress intensity factor, K, defined by linear elasticity, uniquely characterizes the stress-strain field at the crack tip and thereby provides a measure of the "driving force" for crack propagation.

Inglis (1913) published the earliest theoretical work on the elastic stress distribution surrounding a crack in a stressed plate, but Griffith (1920) in a classic paper, for the first time, identified the weakening effect of cracks in materials. The results of both Inglis and Griffith show that stress gradients in the vicinity of the crack tip are quite steep with the stresses ultimately tending to infinity as the crack tip is ap-

proached. In order to ascertain why most materials fail well below their theoretical cohesive strengths, Griffith carried out further investigations, and concluded that the weakening effect was due to the existence of sharp ended flaws or cracks within the material leading to high local stress concentrations. His work with glass fibre showed the sensitivity of brittle materials to the presence of surface flaws. Applying the theoretical results due to Inglis, Griffith then attempted to quantify the weakening effect of the surface cracks. Using the results from Inglis work, he showed that for a given crack size, there is a critical value of stress $\sigma_{crit.}$ above which unstable fracturing of the material will occur. To complete the energy balance, Griffith made the assumption, that the energy required to create new surfaces in the material is proportional to the fracture area from which energy is released. This energy balance theory is known as the Griffith fracture criterion and is normally written in the form

$$\sigma\sqrt{a} = \left(\frac{2\gamma_e E}{\pi}\right)^{\frac{1}{2}} \tag{2.7}$$

which indicates that the extension of a crack, in ideally brittle materials, is governed by the product of the applied nominal stress σ and the square root of the crack length, a. The right handside of Eqn. (2.7) is equal to a constant value that is characteristic of a given brittle material. Consequently, Eqn. (2.7) indicates that crack extension in such materials will occur when the product $\sigma\sqrt{a}$ attains a constant critical value. Eqn. (2.7) has been expressed in another form as

$$\frac{\pi\sigma^2 a}{E} = 2\gamma_e \tag{2.8}$$

where the left-hand side has become known as the energy-release rate, G, and represents the elastic energy per unit crack surface area that is avaliable for infinitesimal crack extension. The right-hand side of Eqn. (2.8) represents the material's resistance R to crack extension. In general the Griffith criterion has been formulated for both plane stress and plane strain situations as

$$\begin{aligned} \sigma_{crit.} &= \sqrt{\frac{2E\gamma_e}{\pi a}} && \text{Plane stress} \\ \sigma_{crit.} &= \sqrt{\frac{2E\gamma_e}{\pi a(1-\nu^2)}} && \text{Plane strain} \end{aligned} \tag{2.9}$$

where E is the Young's Modulus, γ_e is the surface energy per unit crack area, ν is the Poissons ratio and a is the half crack length.

Irwin (1948) suggested that the Griffith fracture criterion, for ideally brittle materials, could be modified and applied to brittle materials and to metals that exhibited plastic deformation. Consequently Eqn. (2.8) was modified to

$$\frac{\pi\sigma^2 a}{E} = 2\left(\gamma_e + \gamma_p\right) \tag{2.10}$$

and Eqn. (2.9) became

$$\begin{aligned} \sigma_{crit.} &= \sqrt{\frac{2E\left(\gamma_e + \gamma_p\right)}{\pi a}} && \text{Plane stress} \\ \sigma_{crit.} &= \sqrt{\frac{2E\left(\gamma_e + \gamma_p\right)}{\pi a(1-\nu^2)}} && \text{Plane strain} \end{aligned} \tag{2.11}$$

where γ_p was the plastic work per unit crack area.

The inability of the Griffith fracture criterion to determine the surface energy terms, γ_e and γ_p, when applied to ductile materials, lead to the recasting of the Griffith equations in terms of parameters that were more readily measurable. Irwin (1957) therefore introduced the concept of fracture toughness, given the symbol G_c, and defined it as the energy released from the surrounding stress field per unit increase of the crack area which would be required just to maintain the propagation of the unstable crack. By using the semi-inverse method of Westergaard (1939), Irwin (1957) showed that the primary stress components in the crack region correspond to the three displacement modes (Opening Mode I, Shearing Mode II, Tearing Mode III: see Figure. 1.7. in Chapter 1), could be expressed in the following form:

$$\begin{aligned} \sigma_y &= \frac{K_I}{(2\pi r)^{\frac{1}{2}}} f(\theta) \\ \sigma_{xy} &= \frac{K_{II}}{(2\pi r)^{\frac{1}{2}}} f(\theta) \\ \sigma_{yz} &= \frac{K_{III}}{(2\pi r)^{\frac{1}{2}}} f(\theta) \end{aligned} \tag{2.12}$$

In the above expression, r, is the radial distance from the crack tip and the terms $f(\theta)$ are the functions of the polar angle θ. From this Irwin observed that the stress field possessed a singularity of strength $1/\sqrt{r}$ at the crack tip. The parameters K_I, K_{II}, and K_{III} were called the ' stress intensity factors' (SIFs) corresponding to the three cracking modes. He further concluded that these parameters characterize the magnitudes of the crack tip stress field.

From the foregoing review it is evident the linear elastic fracture mechanics is an immensely powerful tool for crack analysis. It is also clear that, provided a fracture mechanics solution can be obtained for a structure or component, a safe prediction for fatigue life can be made for that structure based on data from simple specimen tests and from numerical/analytical results. This methodology, if well developed, would tend to eliminate the expensive and time consuming large scale tests.

2.3.3 Finite Element Crack Modelling for SIF Evaluation

For the past decade or so, the finite element method has become firmly established as the standard technique for the solution of practical fatigue fracture problems. Several techniques have been suggested for evaluating stress intensity factors from finite element results but adequate representation of the crack tip singularity is a problem common to most of the proposed methods. From the very outset, the most appealing approach to finite element fatigue fracture mechanics analysis was that which took explicit account of the crack tip singularity. Initial efforts with the use of conventional elements [e.g., Chan et al. (1970) and Kobayashi (1969)] demonstrated clearly that hundreds, or perhaps thousands, of simple elements were required to achieve a solution accuracy within 5%. In line with the importance of adequately representing the crack tip stress singularity, both in linear elastic and elastic-plastic fracture mechanics, special two and three dimensional elements were developed. Different approaches were utilized by several investigators to determine the stress intensity factors along the crack front in a structural component containing a flaw.

One of the earliest attempts at introducing a $\frac{1}{\sqrt{r}}$ singularity into a finite element was presented by Tracey (1971). This approach, employing a simple polynomial

displacement field within a triangular element, was subsequently generalized by Tracey and Cook (1977) to give a family of elements. A singularity of order r^{-p} (where r is the radial distance from node 1, Figure 2.1) was achieved when the displacement field within the element was interpolated as

$$u = (1-\xi^p)\,\delta_1 + \xi^p\,(1-\eta)\,\delta_2 + \xi^p \eta \delta_3 \tag{2.13}$$

The local coordinates ξ and η were defined such that $\xi = 1$ along the edge 2-3 of the element and $\xi = 0$ at node 1. The radial edges 1-2 and 1-3 correspond to $\eta =$ 0 and 1 respectively. The element that resulted from this technique was, however, unable to represent the constant strain conditions.

Henshell and Shaw (1975) recognized that by placing the mid-side node at the quarter point in a quadratic isoparametric quadrilateral or triangular two dimensional element, a singularity in strain results at the nearest corner node. The singularity was found to be of order $1/\sqrt{r}$ as required by the Westergaard solution (1939) for stress distribution around a sharp crack.

A different approach to crack tip singularity modelling by finite element methods was introduced by Barsoum (1976). The idea proposed used the 8 noded isoparametric element for plane strain, plane stress and axisymmetric analyses and the 20 noded isoparametric for three dimensional crack tip analyses. The singularity in all the element was achieved by placing the mid-side node near the crack tip at the quarter point. For the two and three dimensional elements studied, four cases of crack tip singularity were investigated, viz., (a) Eight noded quadrilateral

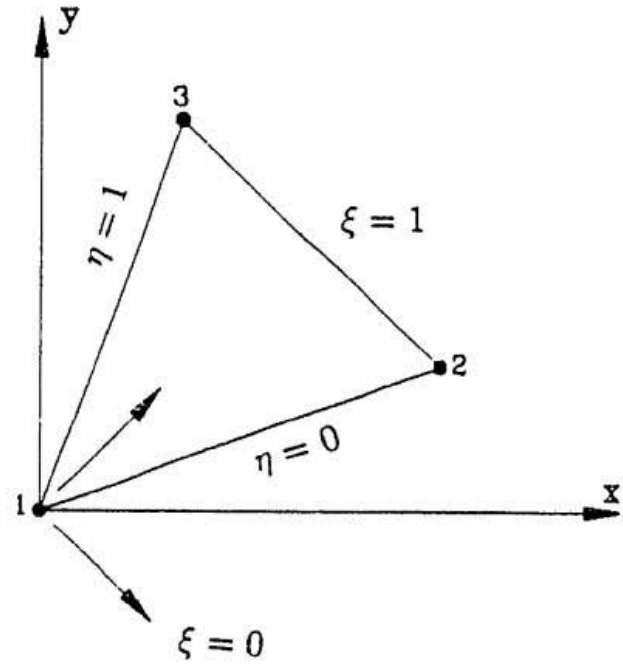

Figure 2.1: Triangular element with singularity at node 1.

with midside nodes of the two sides at quarter points (Figure 2.2); (b) Six noded triangle with mid-side nodes at the quarter points (Figure 2.3). This triangle was generated by collapsing the side 1-4 of the quadrilateral in Figure 2.3; (c) Three dimensional twenty noded cubic element with four midside nodes at the quarter points (Figure 2.4); and (d) Three dimensional prism with four midside nodes at the quarter points (Figure 2.5). This was achieved by degenerating a cube with one face collapsed. It was observed that the collapsed elements [cases (a) and (d)] were easier to use in generating mesh and they gave somewhat better results.

For a semi-elliptical surface crack, in a plate of finite thickness, Smith and Alavi (1971), Smith and Sorensen (1974) and Kobayashi *et al.* (1975), used the alternating finite element method to obtain the stress intensity factor variations along the crack front for various crack shapes. The same information was obtained by Kathiresan (1976) and Raju and Newman (1977, 1979) by using the finite-element method. Raju and Newman (1981) went further in presenting an empirical stress intensity factor equations for a surface crack as a function of parametric angle, crack depth, crack length, plate thickness and plate width for tension and bending loads. The stress-intensity factors, used to develop the equation, were obtained from their previous three-dimensional finite-element analysis of semi-elliptical surface cracks, in finite elastic plates, subjected to tension and/or bending loads.

The simplicity of the line spring element, developed earlier by Rice and Levy (1972 a,b), in effectively reducing a three-dimensional problem to one in a plate and shell theory was demonstrated by Parks et al. (1981a). Results for a number of plates and axially cracked cylindrical shells were presented; these compared favorably with

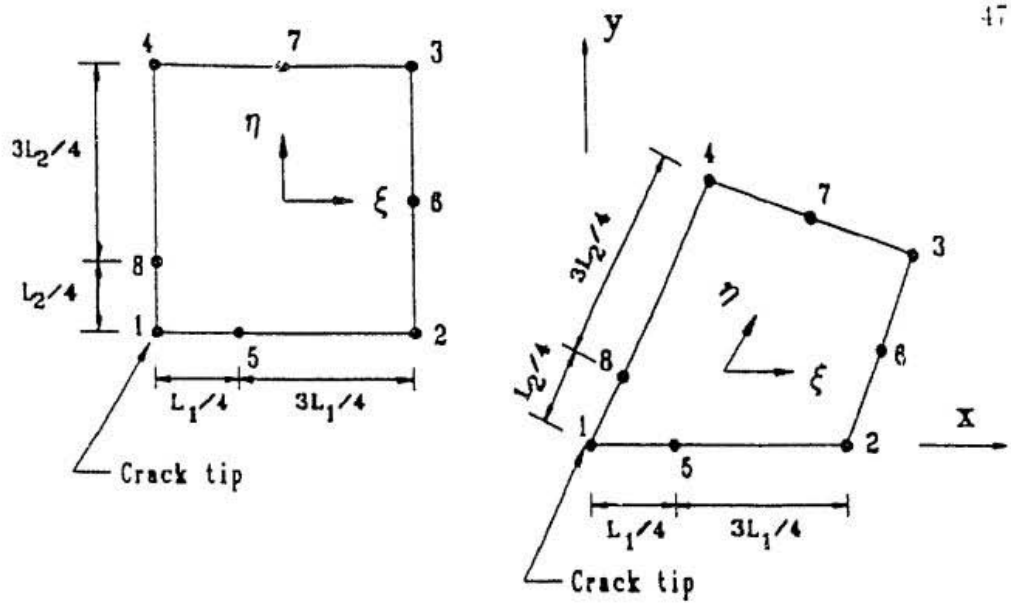

Figure 2.2: Quadaratic isoparametric elements with midside nodes at quarter points.

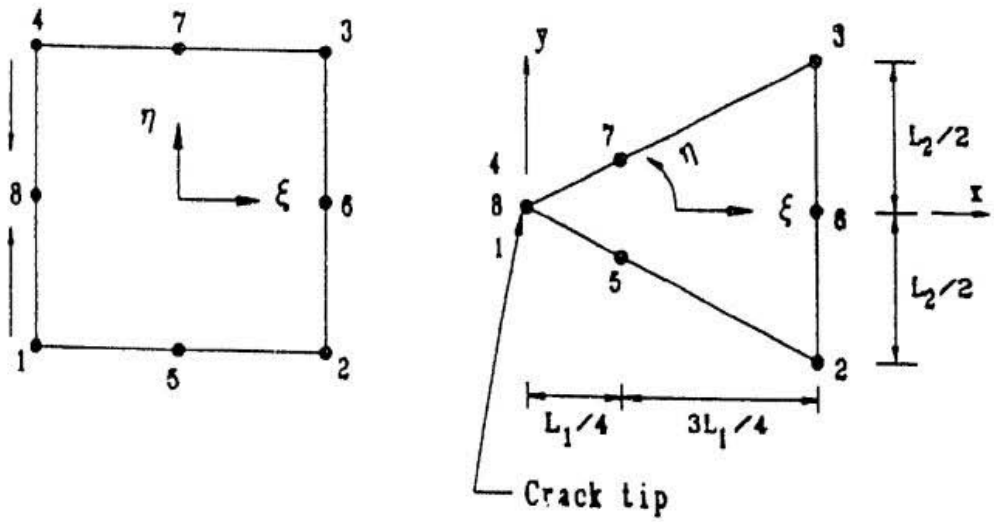

Figure 2.3: 2-D triangular element with midside nodes at quarter points.

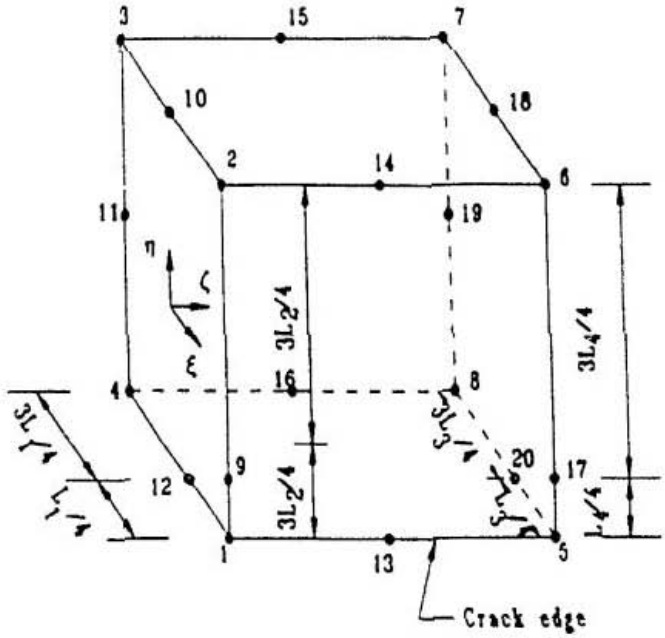

Figure 2.4: 3-D brick element with midside nodes at quarter points.

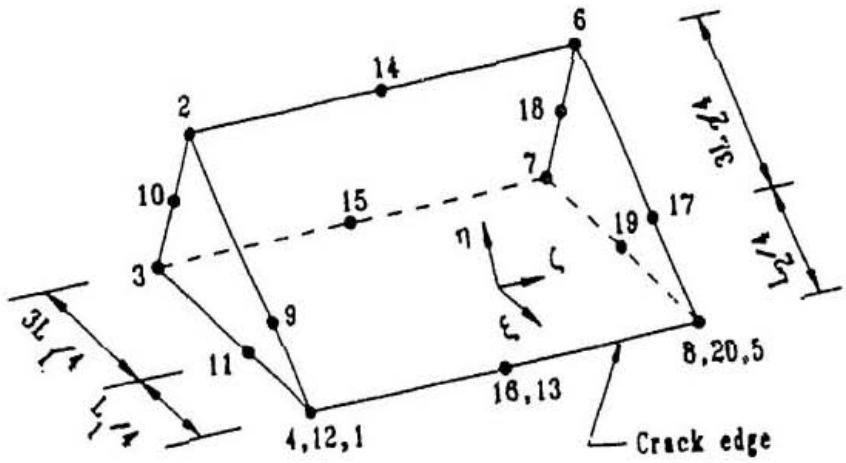

Figure 2.5: 3-D prism with midside nodes at quarter points.

the existing, detailed three-dimensional solutions. They observed that the results were generally somewhat better for plates than for the shells. In conclusion they argued that the above phenomenon may be a general feature of the line spring element as independently explained by Parks (1981b). Line-spring model results were obtained by Delale and Erdogan (1981) by embedding the model within singular integral equation formulations of isotropic elastic plate or shell theory. It was observed that the computational efficiency of the (one-dimensional) singular integral equations, when applied to structural components, greatly exceeded even that obtained with the line-springs embedded in a finite element model of the (two-dimensional) shell middle surface. In a recent paper Fröhling (1992) has used the line spring elements and weight function approach to verify the SIFs obtained for an X-joint.

Niu and Glinka (1987) presented a method for the determination of weight functions relevant to welded joints and the subsequent calculation of stress intensity factors. The weight function for edge cracks emanating from the weld toe in a T-butt welded joint was derived using the Petroski and Achenbach (1978) crack opening displacement function. Parametric equations were derived for the weight functions; these equations make it possible to calculate stress intensity factors for a variety of tension and bending combinations. The stress analyses and the stress intensity factor calculations revealed that the geometric parameters such as the weld toe radius ϱ affect the stress intensity factors more than the stress distributions $\sigma_y(x)$. Finally their comparison of the stress intensity factors, calculated using the derived approximate weight function with the finite element calculations, revealed the satisfactory accuracy of the weight function.

A procedure was developed by Rhee (1989a,b) to calculate the stress intensity factors from the displacements along any arbitrary crack tip radial line on a quarter-point singular finite element boundary. The developed procedure was validated by analysing an angled edge crack in a flat plate under tension and a weld toe surface flaw in an X-shaped tubular joint under tension and bending loads. He stated that, depending on the objective of an analysis (deterministic or probabilistic), the most suitable stress intensity factor solutions can be selected from those given for various locations. He concluded that the method developed herein, could provide analysts with a means to assess the accuracy of the stress intensity factor solution of complex geometries without resorting to other means, such as experiments. In a later paper Rhee (1991) presented a reliable method for the calculation of stress intensity factor solutions for weld toe surface crack. Two topics were explicitly dealt with in the study: (i) identification of a reliable approach to fracture mechanics defect assessment; and (ii) the use of fracture mechanics method for design analyses. Empirical stress intensity factor formulas for T-joints, which were developed from the solution obtained by the identified method, were presented; these formulae were developed from the SIF results obtained for, 40 different T-joints with cracks. Three type of loading were considered; axial , in- and out-of-plane bending loads. It was recommended that for SIF empirical formulas to be applicable to general problems of fracture mechanics and in-service structural integrity assessment, many sets of SIF formulas have to be developed; the SIF empirical formulas presented by him were only a starting point of such a development.

Haswell (1992) presented a general fracture mechanics model for tubular joints based on the results of extensive parametric finite element studies of a range of

uncracked and cracked joint geometries. The finite element study included over 70 tubular joints containing chord saddle cracks subjected to axial and out-of-plane bending loads. The fracture mechanics model related, in a general sense, the crack tip parameter (SIF) to the uncracked stress field parameters (degree of bending (DoB), and stress concentration factor (SCF)); Parametric study was conducted to investigate a range of tubular joint conditions. The finite element models were constructed using 8 noded shell elements. The PATRAN graphics software (PDA Engineering, 1989) was utilized for the mesh generation, while the model analysis was performed with ABAQUS finite element software (Hibbitt et al. 1989). Part-through wall cracks were modelled by including the line spring elements of Parks and White (1982) along the weld toe position, which was assumed to be radially offset 25 mm from the brace mid-shell surface. Cracks of constant aspect ratio (a/2c = 0.1) were modelled by mapping a planar semi-elliptical crack front shape onto the weld toe curve. A simple model relating the stress intensity factor (SIF), stress concentration factor (SCF) and the degree of bending (DoB) at each discrete crack depth was proposed as

$$\frac{SIF}{SCF.\sigma_{nom}} = A - B.DoB \tag{2.14}$$

where

SIF = K_I at the deepest point on the crack front,

σ_{nom} = Nominal stress in brace,

$$\text{SCF} = \frac{\text{Maximum principal stress at weld toe}}{\sigma_{nom}}$$

It was observed that the absolute scatter in the data varied from 8% at crack depth $a/T = 0.2$ to 16% at crack depth $a/T = 0.8$. It was finally concluded that (i) the model required only a stress analysis of the uncracked joint, as it used the linear relationships between SIF and SCF, and SIF and DoB at discrete crack depths between 2% and 80% of wall thickness; (ii) the model could be applied to any tubular joint within the limits of the parametric study using only the results of an uncracked shell analysis; and (iii) that the effect of complexity and structural restraints can be quantified in terms of the reduction in crack site SCF and DoB due to the addition and restraint of in- and out-of-plane braces.

2.3.4 Application of Linear Elastic Fracture Mechanics to Fatigue Crack Propagation

Safety of structural components that contain cracks, or that develop cracks early in their lives such as offshore welded tubular joints, may be governed by the rate of subcritical crack propagation. Many attempts were made in the 60's to quantify the growth stage of fatigue crack by means of fatigue crack propagation laws.

Paris and Erdogan (1963) suggested that the crack propagation depended on the crack tip stress intensity factor range, ΔK, which is a proper measure of the "driving force" for the rate of fatigue crack growth, da/dN. Furthermore, an analysis of available fatigue crack growth rate data at that time suggested that the functional relationship between da/dN and $f(\Delta K)$ could be expressed in the form

$$\frac{da}{dN} = f(\Delta K) \tag{2.15}$$

When the experimental results were plotted in the form of $\log(\Delta K)$ versus $\log(da/dN)$ a straight line was obtained suggesting a power law relationship. The slope of the line m was found to be 4 and they suggested a law of the form

$$\frac{da}{dN} = C(\Delta K)^m \tag{2.16}$$

In the 29 years since Eqn. (2.16) was established, extensive studies of the fatigue crack growth resistance of a wide range of materials have established that da/dN is also sensitive to load ratio and environment, the latter giving rise to additional loading and environmental variables. It also became clear during this time that, in general, Eqn. (2.16) was only valid over two to three orders of magnitude in growth rate. For example, da/dN vs ΔK in inert environments, examined over a broad range of growth rates, generally exhibited the sigmoidal shape with three distinct regions shown in Figure 2.6. Following this realization, da/dN vs ΔK relationships have been in a state of continual evolution.

The results from Paris law Eqn. (2.16) show that at all values of K a positive growth rate will occur. However the results due to Liu (1964) demonstrated that below a certain minimum value of K no growth occurs. This value of K was referred to as the threshold value K_{th}. Liu therefore introduced the fatigue crack growth threshold, ΔK_{th}, to create a lower asymptote to the da/dN vs. ΔK curve, thereby representing rates in region I by:

$$\frac{da}{dN} = C(\Delta K - \Delta K_{th})^m \tag{2.17}$$

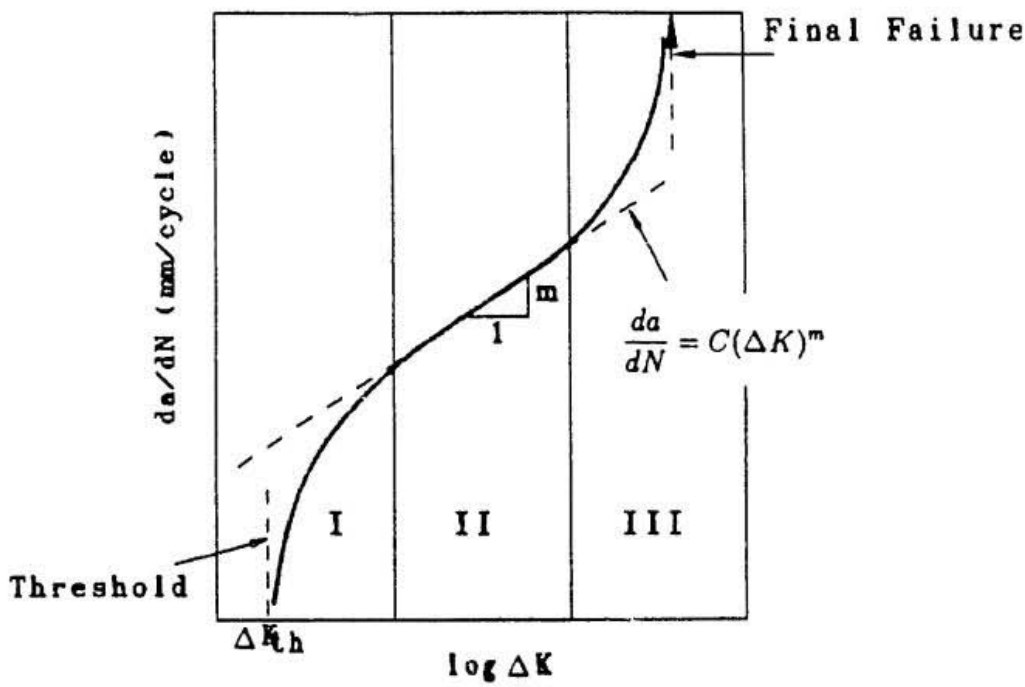

Figure 2.6: Schematic growth rate curve showing the sigmoidal variation of fatigue crack propagation rate da/dN with stress intensity factor range (ΔK).

Figure 2.7 provides a graphical representation of Eqn. (2.17) and serves to define the parameters of this equation and illustrate its asymptotic nature.

An attempt to model the transition from stable to unstable crack growth was presented by Forman et al. (1967). They proposed the following modification to Equation (2.16) to account for the upturn in the (ΔK) curve in Region III as K_{max} approaches the fracture toughness (K_c) of the material.

$$\frac{da}{dN} = \frac{C(\Delta K)^m}{(1-R)K_c - \Delta K} \tag{2.18}$$

where R is the stress or load ratio ($\sigma_{min}/\sigma_{max}$).

Numerous equations of added complexity followed the above simple representations. Several of these utilized common mathematical functions which possess the characteristic sigmoidal shape of the da/dN vs. ΔK curve; for example, the hyperbolic sine and inverse hyperbolic tangent functions of Miller and Gallagher (1981).

Saxena et al. (1979) pointed out that the equations which are asymptotic in Region I tend to select asymptotes which are about 10% below the lowest ΔK value contained in a data set, regardless of the fact that cracks could propagate significantly below this value. In order to avoid the above problem, the so-called "three-component model" was developed which does not contain an asymptote in Region I. This model is based on adding the material's resistance to fatigue growth, that is $(da/dN)^{-1}$, in the three commonly observed regions of crack growth, Figure 2.8. The characteristic equation describing da/dN as a function of ΔK is given by:

$$\frac{da}{dN} = C(\Delta K - \Delta K_{th})^m$$

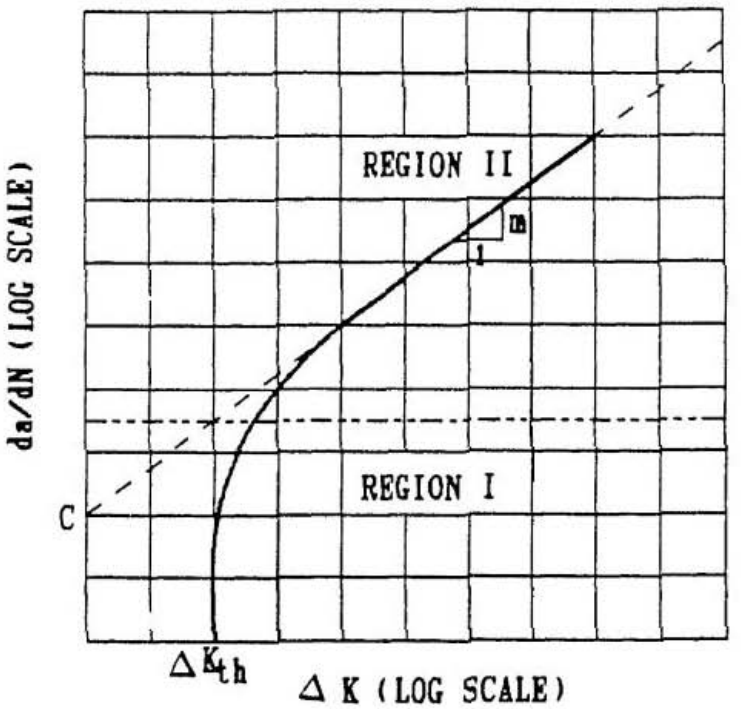

Figure 2.7: Schematic representation of asymptotic crack growth equation [Liu, 1964].

$$\frac{1}{da/dN} = \frac{A_1}{\Delta K^{m_1}} + \frac{A_2}{\Delta K^{m_2}} - \frac{A_2}{[(1-R)K_c]^{m_2}}$$

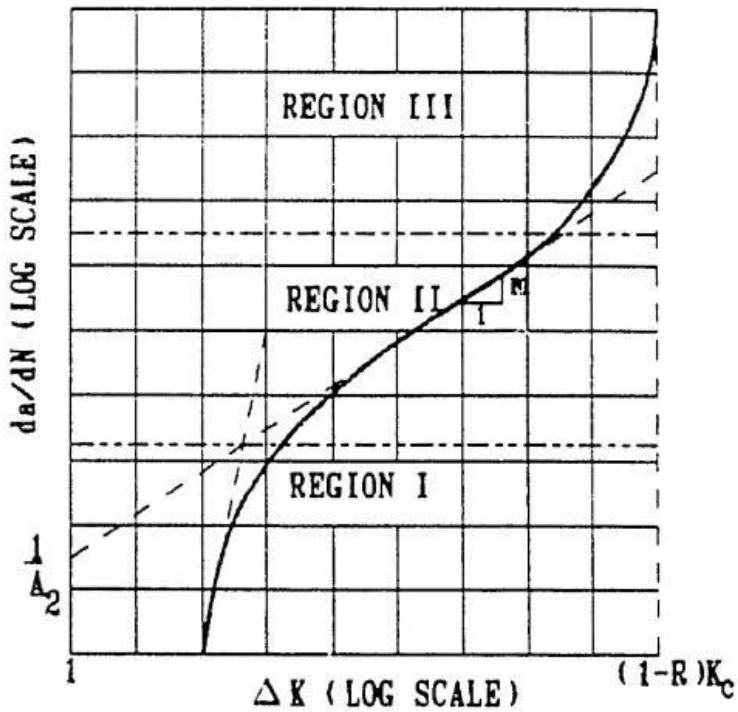

Figure 2.8: Schematic representation of three component crack growth equation [Saxena et al., 1979].

$$\frac{1}{da/dN} = \frac{A_1}{\Delta K^{m_1}} + \frac{A_2}{\Delta K^{m_2}} - \frac{A_2}{[(1-R)K_c]^{m_2}} \tag{2.19}$$

where A_1, m_1, A_2, m_2 and K_c are empirical constants which are defined as illustrated in Figure 2.8. Each term in Eqn. (2.19) was represented by a given region shown in Figure 2.8; for transition regions, combination of adjacent terms are used. The exponents m_1 and m_2 are slopes in Regions I and II, respectively; the constants A_1 and A_2 are the reciprocals of the intercepts (at $\Delta K = 1$) in Regions I and II, respectively. It was argued that the form of the three-component model facilitates the representation of load ratio effects by expressing A_1 and A_2 as functions of R since these effects are known to be specific to Regions I and II.

In conclusion it is evident that fatigue crack growth rates can be characterized and predicted using elastic stress intensity factor. This implies that as long as a stress intensity factor solution can be obtained for a cracked body or structure, the life of the structure can be predicted using fracture mechanics concepts.

2.3.5 Thickness, Size and Geometry Effect

It had long been known that plate thickness was likely to be a relevant variable for fatigue cracking under bending stresses. This was due to the fact that the stress gradient through the thickness of a 'thin' specimen would be steeper, and as such will be less damaging than in a 'thick' specimen. However only in the recent past numerous tests and theoretical investigations have been carried out on welded joints under bending loads considering thickness effects.

Gurney (1977), on the basis of theoretical fracture mechanics calculations, observed that the fatigue strength of welded joints could be affected by plate thickness, even when they were subjected to axial loading.

Gurney (1989) reviewed the research work carried out in Britain on the influence of thickness on the fatigue strength of welded joints by using both theoretical fracture mechanics and experimental approach. The results of tests under axial loading carried out by Johnston (1978), on specimens with transverse nonload-carrying fillet welds fabricated from plates of various thicknesses, indicated that there was a general tendency for fatigue strength to decrease as the plate thickness increased. Several investigators such as Booth (1987), Haibach et al. (1978) and Dijkstra and Hartog (1978), in their combined European Offshore Fatigue Programs, also found a tendency for fatigue strength to decrease as the thickness increased. Booth (1983) investigated bending fatigue life of transverse K butt welds, Haibach et al. (1978) the bending fatigue resistance of transverse nonload-carrying fillet welds, and Dijkstra and Hartog (1978) the axial fatigue strength of tubular T joints. Reported at the same time was the work of Wildschut (1978); but surprisingly the tests on 40 mm and 70 mm thick transverse nonload-carrying fillet welds in bending exhibited no obvious effect of thickness. The results obtained and expressed in terms of relative fatigue strength normalized to a thickness of 32 mm, were summarized by Gurney (1989). On the basis of these data, he proposed an empirical thickness correction for fatigue strength as follows:

$$S = S_B \left(\frac{T_B}{T}\right)^{\frac{1}{4}} \tag{2.20}$$

where S is the fatigue strength of the joint under consideration, T its thickness, S_B the fatigue strength of the joint using the basic S-N curve and T_B the thickness corresponding to the basic S-N curve, with the S-N relationship given by:

$$N(S)^m = \text{constant} \tag{2.21}$$

The corresponding thickness correction for fatigue life (with $m = 3$) was given by Gurney as:

$$N = N_B \left(\frac{T_B}{T}\right)^{\frac{1}{4}} \tag{2.22}$$

On the basis of Gurney's work, the thickness correction was included in the revised 1984 UK Department of Energy Guidance notes for offshore structures (1984). The reference plate thickness T_B for plate joints was taken as 22 mm, and 32 mm for tubular joints. Below the reference thickness T_B, the fatigue strength was to be taken as the strength at T_B. No upper limit existed on the range of the thickness correction.

2.4 Analytical and Numerical Studies on Fatigue Life Estimation

The present design method for offshore jacket employs the S-N design curve approach. These curves are derived from experimental tests carried out on small and large scale tubular joints. Although this approach will continue to remain the primary method of design for some time, the effort geared towards finding analytical

and numerical approaches to fatigue crack evaluation is rapidly increasing among many investigators. It is beginning to be clear, that development of an efficient and reliable analytical/numerical approach to fatigue assessment of offshore tubular joints may alleviate the costly and time consuming exercise encountered when tubular joints are to be tested for this purpose. Some analytical and numerical studies have already been conducted in this area and from the comparison of results obtained with experimental approach, it looks that analytical/numerical approach has a promising future for fatigue evaluation and consequently for the design of offshore welded tubuar joints.

Becker et al. (1970) compared their theoretical and experimental studies on the fatigue behaviour of tubular welded joints. Theoretical fracture mechanics analytical crack models, using two-dimensional notch cracks and three-dimensional semi-elliptical cracks were utilized. In order to check the analytical crack models against their experimental results, fracture mechanics coupons from actual tubular joints, used in the study, were tested. The material constants obtained were numerically different; however when they applied it to failure prediction of the analytical notch crack, comparative results in the low range of $4x10^3$ to 10^4 cycles was obtained. In their final summation they concluded that linear elastic fracture mechanics approach may be used to approximate fatigue crack propagation behaviour of structural steels and proposed that effective stress be utilized in interpreting the range of the stress intensity factor when macro-plasticity occurred around the crack tip.

Dover and Dharmavasan (1982) carried out random load fatigue tests on T- and

Y- joints using an 'Inherent Flaw' model, capable of using fracture mechanics in a simple way, to predict the fatigue life of tubular welded joints. Observations during the studies suggested that fatigue cracks present in the tubular joints grew steadily through the wall thickness at a fairly constant rate, and fatigue crack depth during the tests on the Y joints was found to be similar to that measured in the T plate joints. Experimental stress intensity factor $\Delta K_{exp.}$ was determined using the following crack growth expression obtained from specimen tests by Dover and Holdbrook (1979):

$$da/dN = 1.5 \times 10^{-12} (\Delta K_{exp.})^{3.3} \tag{2.23}$$

and the stress intensity factor expression was taken as

$$K = Y_s \, Y_\sigma \, \sigma_{nom} \sqrt{\pi a} \tag{2.24}$$

where Y_s is a factor dependent on crack shape and Y_σ is dependent on the loading, joint geometry and local geometry. Y_s was assumed as unity and since the two factors will vary during the course of the life, in the early stages Y_s would dominate whereas for most of remaining life Y_σ would control the crack growth. With the assumption that Y_s was unity, Y_σ was given by,

$$Y_\sigma = \frac{\Delta K_{exp.}}{\sigma_{nom} \sqrt{\pi a}} \tag{2.25}$$

The plot of this factor against a/t for the Y joint was compared with the results of T joints and a K joint tested by Gibstein (1981) and Gibstein and Moe (1981); this exhibited good agreement.

Bhuyan (1986) presented the results of an analytical and experimental investigation on the fatigue behaviour of welded tubular T-joints. Linear fracture mechanics approach was used. Analytical study included the development of a finite element computer program for tubular joints with or without weld toe crack, while the experimental investigation consisted of quantification of sea water, temperature, frequency, load ratio and wave form effects on fatigue crack growth rates in the base steel material (CT tests) that has been proposed for the Canadian offshore. The fatigue crack growth rates for tubular joints were determined using the stress intensity factors corresponding to a 50% of thickness crack and the material coefficients C and m were obtained from small scale specimen CT tests. It was observed that at higher hot spot stress ranges, the estimated lives showed good agreement with experimental results available in the literature.

Rhee (1986) and Rhee and Tyson (1987) presented analytical solutions that explicitly considered the effects of both flaw depth and length near the saddle point of X- and K-joints under brace tension and in-plane bending loads using TUSTRA (1985). In the analysis the warped crack surfaces, along the brace-chord intersection, were modelled using quarter-point crack tip singularity elements. For crack growth simulation, the three component crack growth model by Saxena (1975) was used. He concluded in his studies (using axial, in-plane/out-of-plane bending loads) that depending on the loading conditions, the crack tip behaviour of a weld

toe surface flaw can be predominantly mixed-mode, even for a simple tubular joint geometry. It was observed that under a brace tension loading condition, the crack growth rate on the surface decreased as the crack grew. This he stated was due to the stress reduction along the crack growing path. Comparison with laboratory results showed good agreement with his analytical solutions.

Bell et al. (1987) presented the development and testing of a fracture mechanics model for prediction of the fatigue growth life of welded plate joints. The finite element technique was adopted for the stress intensity factor evaluation using both two and three dimensional analyses. The joints were modelled using quadratic isoparametric elements, with singular elements around the crack tip. The crack shape development was achieved through the assumption that initially the small cracks were semi-circular; then the crack shape development could be described by an exponential relationship

$$\frac{a}{c} = e^{-ka} \tag{2.26}$$

the parameter k according to their study decribed the variation of mean aspect ratio of the crack with the depth, and was shown to be described by an equation having the same form as that of Gurney (1979a) for fatigue strength. With the above explanation they presented the equation relating the parameter k to the stress range and plate thickness as

$$k = k_B \left[\frac{\Delta\sigma}{\Delta\sigma_B}\right]^2 \left[\frac{t}{t_B}\right]^{1/2} \tag{2.27}$$

where t_B is a reference thickness and $\Delta\sigma_B$ is the associated stress range, t is any thickness and $\Delta\sigma$ is its stress range. The number of cycles N, to propagate an initial size a_i to final size a_f, was computed using Runge-Kutta numerical integration technique on a cycle by cycle basis. From the three crack growth procedures examined, viz., single crack (SC) solution, straight fronted crack (SFC) solution and multiple crack (MC), the multiple crack case, which accounted for the multiple nucleation and coalescence of cracks, gave a good prediction, while the straight fronted crack (SCF) and single crack (SC) solutions were, respectively, conservative and over predicted the life.

2.5 Summary

The relevant literature pertaining to the stress analysis, development of parametric equations, fatigue crack initiation, linear elastic fracture mechanics principles, developments in finite element modelling for stress intensity factor evaluation, application of linear elastic fracture mechanics principles to fatigue crack propagation, thickness/size and geometry effect and the available numerical/analytical studies on fatigue life estimation of stiffened and unstiffened tubular joints have been reviewed in this chapter. Inspite of the numerous developments available in the area, not a single study has examined the whole range of stress analysis, crack initiation and crack propagation in a detailed manner and tied together these results with the results of experimental investigations. Since a detailed experimental investigation was carried out in the Faculty of Engineering and Applied Science, Memorial University, St. John's, Newfoundland, on tubular T-joints it was felt necessary and relevant to carry out a detailed theoretical investigation of tubular T-joints with a

view to compare the results. The subsequent chapters outline the efforts made in this direction and the results obtained in the process.

Chapter 3

Theoretical Background

The results of the stress analysis, reported in this thesis, was obtained using the general purpose computer program ABAQUS marketed by Hibbit, Karlsson and Sorensen (1989); certain smaller programs were written for the purpose of generating the proper data input to ABAQUS. In order to clarify the essential issues involved in the modelling and analysis of the problem and to appreciate the validity and applicability of the results given herein, relevant theoretical background is given in this chapter.

3.1 Finite Element Formulation

The complex geometrical configurations of tubular joints coupled with their behaviour as shell structures, have created increasing difficulties in finding a universally accepted approach for evaluating the stress distribution along the intersection, when they are subjected to simple or complex loads. Analytical solution to shell structures are limited in scope, and in general, are not applicable to arbitrary shapes, load conditions, irregular stiffening and support conditions as would be encountered in welded tubular joints. In addition, if the thickness of the shell structure

is sufficiently large so that shear deformation is significant, then the applicability of classical approaches becomes questionable. Two approaches are at present possible, viz., (i) testing of structural models of smaller/medium/large scale size and (ii) numerical finite element analysis using computers. Although both of these methods present their own difficulties, clearly the latter is more convenient for design and evaluation of structural integrity.

For a displacement method of analysis, wherein displacements are chosen as the primary unknowns, the finite element technique is based on the assumption that a structure can be divided into a finite number of elements tied together at a finite number of points so that continuity can be maintained between neighbouring elements. A simple power series displacement is considered in order to compute the element stiffness matrix and the corresponding loads and displacements for each node. The stiffness matrix and load vector of the individual elements are transformed from their respective local coordinate systems into the global structural system by appropriate transformation matrices. Finally they are assembled into the structural stiffness matrix by superposition and solved to obtain the structural displacements and member forces.

In the past three types of elements have been used for the finite element analysis of welded tubular joints, viz., (i) flat triangular or quadrilateral elements, (ii) curved elements formulated on the basis of various shell theories, and (iii) elements derived from three-dimensional elements by the degeneration concept.

The first approach involves replacing the curved shell by an assembly of flat tri-

angular or quadrilateral elements. This simplification leads to the use of a large number of elements, and any advantage that could be gained by more sophisticated elements (which despite reduction in number could yield improved accuracy) is lost (Zienkiewicz and Cheung, 1967; Zienkiewicz et al., 1968; Clough and Johnson, 1968). The earliest numerical studies of shell problems involved discretizing the shell by plane triangular plate bending elements, onto which the membrane stiffness was added. The results obtained were found to be satisfactory. A number of difficulties and shortcomings arise when these flat elements are applied to curved shells such as the presence of discontinuous bending moments, which do not appear in the actual continuous curved structure (Gallagher, 1976). Thus the need for elements which can take up curved shapes becomes obvious.

The second approach uses a classical concept, whereby a shell theory is used as the starting point in the finite element formulation. Using the variety of classical shell theories that have been developed in the past, a number of finite elements with different degrees of complexity have been formulated for both deep and shallow shells. Although these curved elements based on the Kirchhoff-Love hypothesis, guarantee a high solution accuracy, their usage in finite element analysis is complicated by convergence and compatibility requirements.

The third approach, derived from a three dimensional finite element analysis concept (Figure 3.1), makes it possible to circumvent the difficulties outlined in the first two approaches; in addition the shear deformation, neglected in the first two approaches on the assumption of thin shell theory, can easily be incorporated.

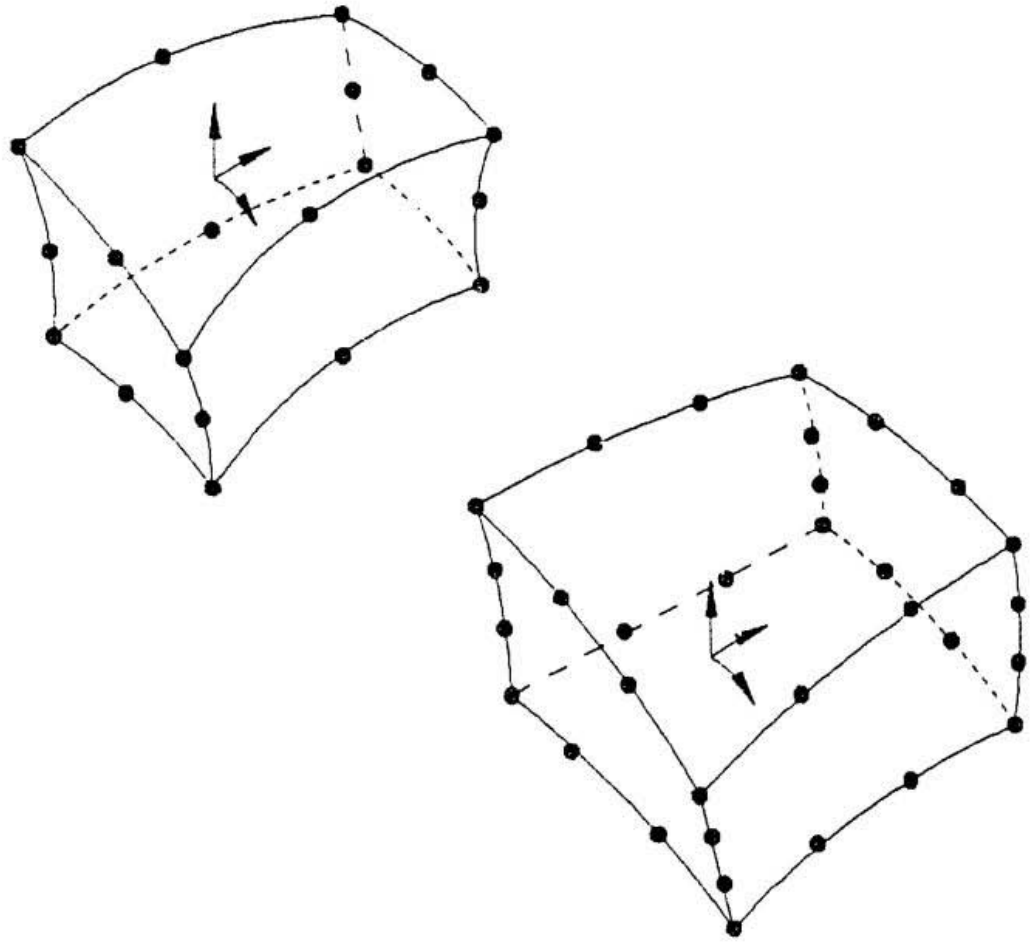

Figure 3.1: Three-dimensional hexahedral elements of parabolic and cubic types.

Isoparametric elements [1] of the type shown in Figure 3.1. have been used for some years with success for three-dimensional analysis purposes. The starting point for the development of the third approach (i.e., shell finite elements obtained from three-dimensional formulation) was the realization by many investigators that the three-dimensional elements could be made thinner by the degeneration process so that they represented shell segments.

This degeneration concept originally introduced by Ahmad *et al.* (1970), for linear analysis of moderately thick shells, avoids the Kirchhoff-Love assumptions, which limit the range of applicability to thin shells, and at the same time permits the representation of curved geometries with no extra computational effort. It therefore appeared to be a very attractive candidate for use in finite element procedure for a general shell structure. Although the element seemed promising when it was introduced, difficulties later arose, due to the degenera ion procedure, as the thickness of the element was reduced. These difficulties were due to the presence of large bending stiffness, which may be traced to the fact that the assumed displacement interpolation functions impose large amounts of shearing strain in the development of simple bending deformation. The phenomenon has been referred to by many investigators as 'shear lockiing' (Doherty et al., 1969, Zienkiewicz et al., 1971 and Pawsey and Clough, 1971). They have pointed out that the element performance could be improved greatly by evaluating the shear strain energy in the element by a lower order integration procedure (reduced integration) than was used for the normal strain energy. This lower order integration neglects the large extraneous

[1] Elements in which the number of nodes used to define the element shape is equal to the number of nodes used to define the interpolation function.

shear strain introduced by the assumed displacement functions, and tends to relax the overstiffness of the element.

3.2 Degenerated Isoparametric Elements

3.2.1 General

Figure 3.2(a) shows a solid three-dimensional element based on a quadratic displacement field and Figures 3.2(b) and (c) illustrate the corresponding quadratic degenerated shell element. Two basic assumptions are adopted in the degeneration process: First it is assumed that, 'normals' to the middle surface remain straight after deformation (this also includes thick shells). Secondly, the strain energy corresponding to the stresses perpendicular to the middle surface is degenerated, that is, the stress components normal to the shell middle plane are constrained to be zero in the constitutive equations. For each nodal point of the element, five degrees of freedom are specified, viz., three displacements and two rotations of the 'normal' at the node. It is important to note at this point, that, the two assumptions introduced correspond only to part of the usual assumptions of the shell theory; also the use of independent rotational and displacement degrees of freedom permits transverse shear deformation to be taken into account, since rotations are not tied to the slope of the mid-surface.

3.2.2 Coordinate Systems

In order to understand the basic concept of the type of finite element employed in the present study, it is expedient to start by introducing the coordinate systems used. Different coordinate system have to be used when formulating the degener-

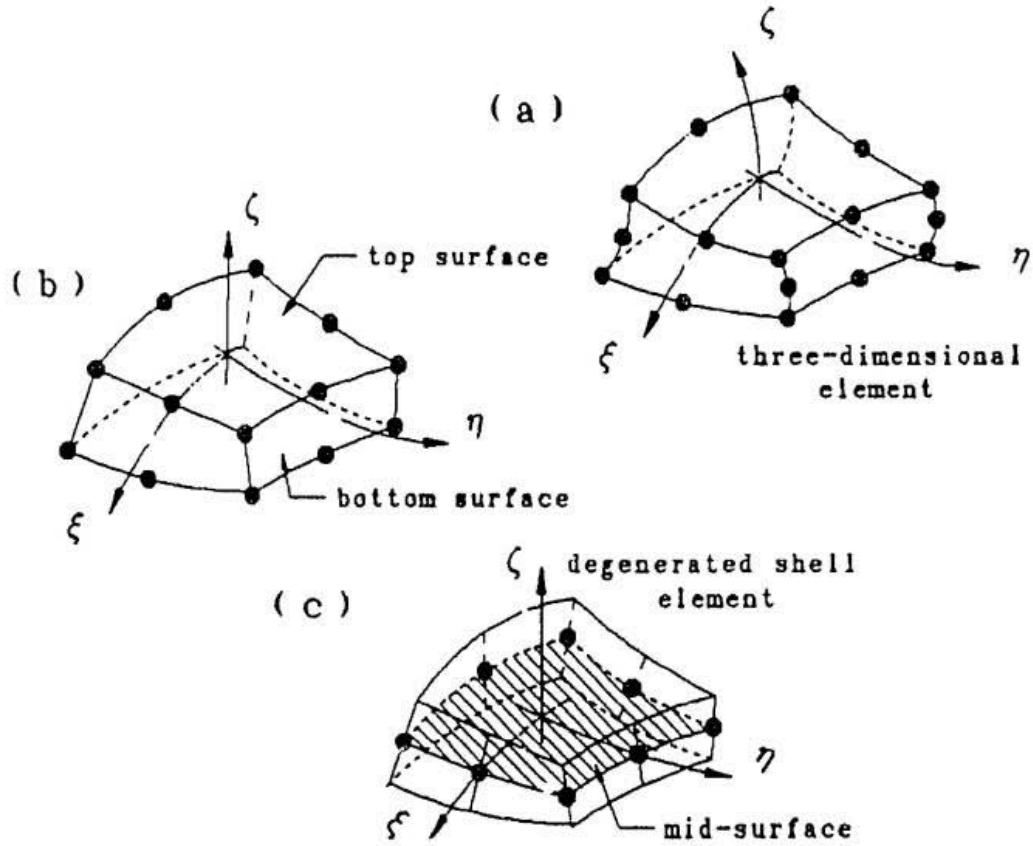

Figure 3.2: (a) Quadratic solid three-dimensional element, (b) and (c) the corresponding degenerated shell elements.

ated curved shell elements. For the presented study, four different coordinates have been chosen in order to adequately describe the general characteristics of these type of elements. These coordinate systems are schematically shown in Figures 3.3(a) and 3.3(b) and are briefly described below.

1. Global coordinate set – x, y and z

   A cartesian coordinate system, freely chosen in relation to the structure geometry in space. Nodal coordinates and displacements, as well as the global stiffness matrix and the applied load vectors are referred to this system.

2. Nodal coordinate set – $\vec{\mathbf{V}}_{1i}$, $\vec{\mathbf{V}}_{2i}$ and $\vec{\mathbf{V}}_{3i}$

   A nodal coordinate system defined at each nodal point with origin at the reference surface (mid-surface). For node i in the mid-surface, it is convenient to construct a vector $\vec{\mathbf{V}}_{3i}$ connecting the upper and the lower points (i.e., a vector of length equal to the shell thickness, t) through the mid-surface coordinates. This vector is achieved in the present study as follows:

$$\vec{\mathbf{V}}_{3i} = \begin{Bmatrix} x_i \\ y_i \\ z_i \end{Bmatrix}_{\text{top}} - \begin{Bmatrix} x_i \\ y_i \\ z_i \end{Bmatrix}_{\text{bottom}} \tag{3.1}$$

   The usefulness of this vector will be shown later in the element geometry formulation.

3. Curvilinear coordinate set – ξ, η and ζ

   In this coordinate system, ξ, η are two curvilinear coordinates in the middle

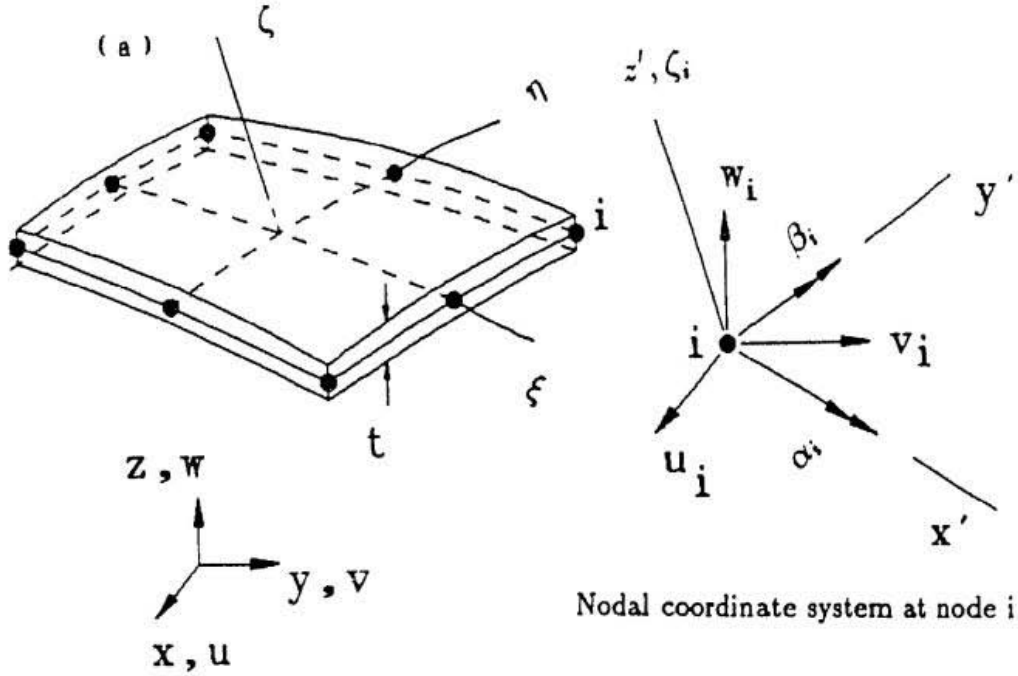

Nodal coordinate system at node i

Global coordinate system

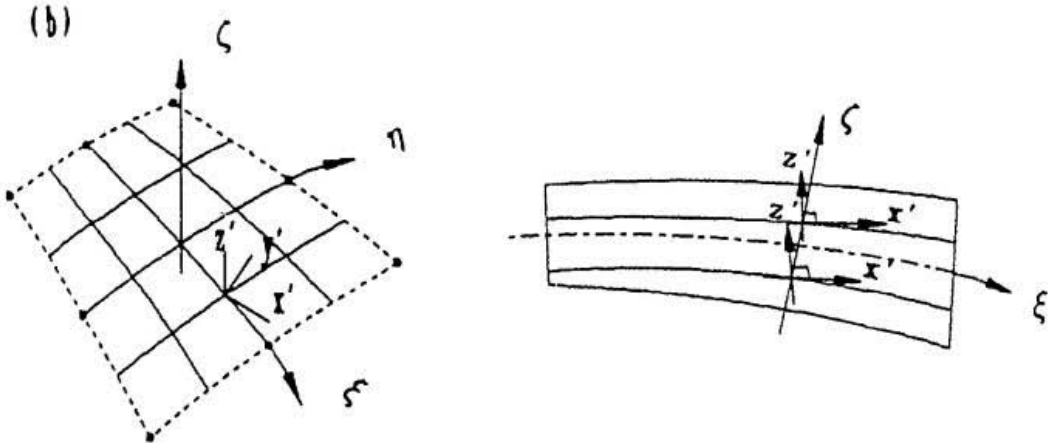

Surface η = constant

Surface ζ = constant

Local coordinate system

Figure 3.3: Coordinate system: (a) nodal and curvilinear systems, (b) local system of axes.

plane of the shell element and ζ is a linear coordinate in the thickness direction. It is assumed that ξ, η and ζ vary between -1 and +1 on the respective faces of the element. The relationship between the curvilinear coordinates (ξ, η and ζ) and the global coordinates (x, y and z) are given later while defining the element geometry. The direction of ζ is only approximately perpendicular to the shell mid-surface, since ζ is defined as a function of the unit vector $\hat{\mathbf{v}}_{3i}$

4. Local coordinate set – x', y' and z'

This is a Cartesian coordinate system defined at the sampling points where the stresses and strains are to be computed. A point is taken on the shell surface to construct three orthogonal axes x', y', z' [Figure 3.3(b)], such that z' is normal to the surface ζ = constant, and axes x' and y' lie in the tangent plane. The direction z' is obtained by the cross product of the ξ and η directions as

$$\vec{z}' = \begin{Bmatrix} \dfrac{\partial x}{\partial \xi} \\ \\ \dfrac{\partial y}{\partial \xi} \\ \\ \dfrac{\partial z}{\partial \xi} \end{Bmatrix} \times \begin{Bmatrix} \dfrac{\partial x}{\partial \eta} \\ \\ \dfrac{\partial y}{\partial \eta} \\ \\ \dfrac{\partial z}{\partial \eta} \end{Bmatrix} = \begin{Bmatrix} \dfrac{\partial y}{\partial \xi}\dfrac{\partial z}{\partial \eta} - \dfrac{\partial y}{\partial \eta}\dfrac{\partial z}{\partial \xi} \\ \\ \dfrac{\partial x}{\partial \eta}\dfrac{\partial z}{\partial \xi} - \dfrac{\partial x}{\partial \xi}\dfrac{\partial z}{\partial \eta} \\ \\ \dfrac{\partial x}{\partial \xi}\dfrac{\partial y}{\partial \eta} - \dfrac{\partial x}{\partial \eta}\dfrac{\partial y}{\partial \xi} \end{Bmatrix} \tag{3.2}$$

The direction x' is taken to be tangent to the ξ-direction at the sampling point. This can be expressed as

$$\vec{x}' = \begin{Bmatrix} \dfrac{\partial x}{\partial \xi} \\ \\ \dfrac{\partial y}{\partial \eta} \\ \\ \dfrac{\partial z}{\partial \xi} \end{Bmatrix} \tag{3.3}$$

while the direction y' is defined as the cross product of z' and x' directions,

$$\vec{y}' = \vec{z}' \times \vec{x}' \tag{3.4}$$

The local coordinate system varies along the thickness for any normal depending on the shell curvature and variable thickness. The direction cosine matrix $[\theta]$, that relates the transformations between the local and global system, is obtained by following the process which defines uniquely two orthogonal vectors, and is given as

$$[\,\theta\,] \;=\; [\,\hat{\mathbf{v}}_1, \hat{\mathbf{v}}_2, \hat{\mathbf{v}}_3\,] \tag{3.5}$$

where $\hat{\mathbf{v}}_1$, $\hat{\mathbf{v}}_2$, and $\hat{\mathbf{v}}_3$ are unit vectors in the x', y', and z' directions, respectively.

3.2.3 Element Geometry Definition

The global coordinates of pairs of points on the top and bottom surface at each node [Figure 3.3(a)] prescribes the shape of the element. Alternatively, the mid-surface nodal coordinates and the corresponding directional thickness can be used

to define the element geometry. Using the curvilinear coordinate set (ξ, η, ζ) with the curvilinear ξ and η in the middle plane, rectilinear ζ in the thickness direction and further remembering that ξ, η, ζ vary between -1 and 1 on the respective faces of the element, the coordinates of any point within the element are :

$$\begin{Bmatrix} x \\ y \\ z \end{Bmatrix} = \sum_{i=1}^{n} N_i(\xi,\eta)\frac{(1+\zeta)}{2}\begin{Bmatrix} x_i \\ y_i \\ z_i \end{Bmatrix}_{\text{top}} + \sum_{i=1}^{n} N_i(\xi,\eta)\frac{(1-\zeta)}{2}\begin{Bmatrix} x_i \\ y_i \\ z_i \end{Bmatrix}_{\text{bottom}} \tag{3.6}$$

or alternatively, using the mid-surface nodal co-ordinates and the corresponding directional thickness t_i,

$$\begin{Bmatrix} x \\ y \\ z \end{Bmatrix} = \sum_{i=1}^{n} N_i(\xi,\eta)\begin{Bmatrix} x_i \\ y_i \\ z_i \end{Bmatrix}_{\text{mid}} + \sum_{i=1}^{n} N_i(\xi,\eta)\zeta\frac{t_i}{2}\begin{Bmatrix} l_{3i} \\ m_{3i} \\ n_{3i} \end{Bmatrix} \tag{3.7}$$

The interpolation functions N_i appearing in these equations together with their derivatives are given in Table A.1 of Appendix I and Figure A.1 shows the systematic generation of these shape functions. The terms l_{3i}, m_{3i}, and n_{3i} are the direction cosine of the vector $\vec{\mathbf{V}}_{3i}$ normal to the middle surface and spans the thickness t_i of the shell element at node i (Figure 3.4): this can obtained from the following expression:

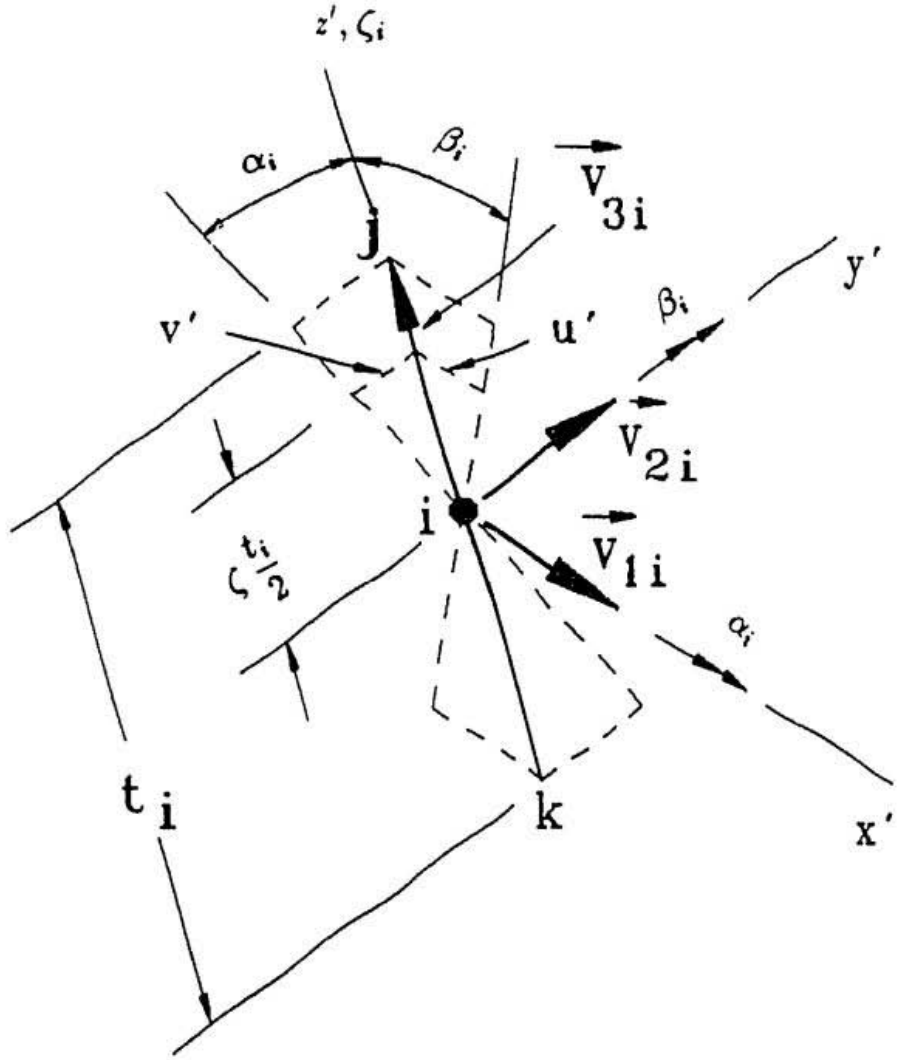

Figure 3.4: Nodal vectors.

$$\vec{\mathbf{V}}_{3i} = \left\{ \begin{array}{c} x_{top} - x_{bottom} \\ y_{top} - y_{bottom} \\ z_{top} - z_{bottom} \end{array} \right\} = \left\{ \begin{array}{c} l_{3i} \\ m_{3i} \\ m_{3i} \end{array} \right\} t_i \tag{3.8}$$

The subscripts *top* and *bottom* in Eqn. (3.6) represent the top and bottom surfaces of the shell, respectively. In the fortran subprogram written for this purpose, either the coordinates of the top and bottom points or the direction cosine for $\vec{\mathbf{V}}_{3i}$ are given as data.

The rectangular parent and the isoparametric counterpart of the nodal configuration for the two kinds of elements used in the present study (8-node serendipity and 9-node Lagrange) are shown in Figures 3.5(a) and 3.5(b). Since an isoparametric concept was adopted throughout the entire element formulation, the geometric interpolation functions were taken to be the same as the displacement shape functions. Physically, this means that the natural co-ordinates ξ and η are curvilinear, and all sides of the element become quadratic curves for the 8-node serendipity and 9-node Lagrange elements.

3.2.4 Displacement Field

Taking into consideration the thin shell assumptions of the degenerated element, the displacement throughout the element is taken to be uniquely described by the five degrees of freedom of a 'normal' at the node, viz., the three Cartesian components of the nodal displacements (u_i, v_i, w_i) and two rotations (α_i, β_i) of the nodal vector $\vec{V}_{3i}$ about orthogonal directions normal to it (see Figure 3.4). Generic displacement

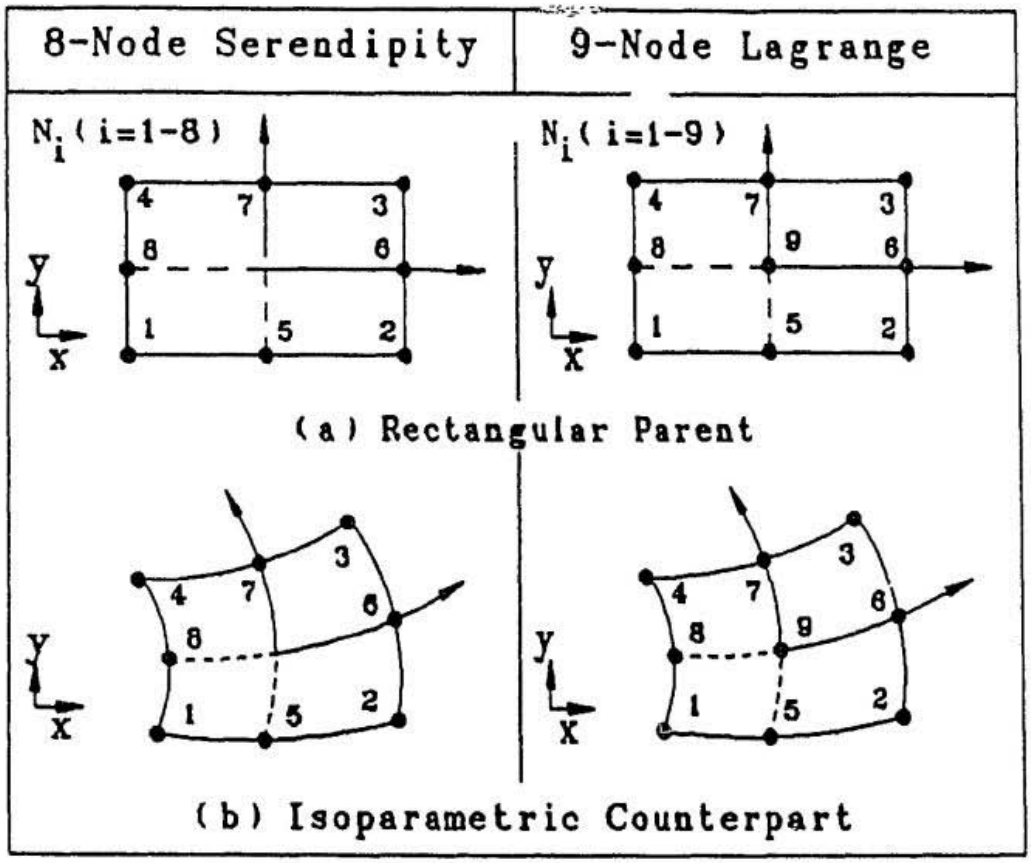

Figure 3.5: Nodal configuration of the two quadratic shell elements used: (a) rectangular parent, (b) isoparametric counterpart.

at any point in the shell element are taken to be in the directions of global axes. Thus,

$$\mathbf{u} = \begin{Bmatrix} u \\ v \\ w \end{Bmatrix} \tag{3.9}$$

On the other hand the nodal displacements consist of these same translations (in global directions) as well as two rotations α_i and β_i about the two local tangential axes x_i and y_i as indicated in Figure 3.3(a). Hence, the generic displacements in terms of nodal displacements are given as

$$\begin{Bmatrix} u \\ v \\ w \end{Bmatrix} = \sum_{i=1}^{n} N_i(\xi,\eta) \begin{Bmatrix} u_i \\ v_i \\ w_i \end{Bmatrix} + \sum_{i=1}^{n} N_i(\xi,\eta)\, \zeta \frac{t_i}{2}\, \mu_i \begin{Bmatrix} \alpha_i \\ \beta_i \end{Bmatrix} \tag{3.10}$$

where μ_i denotes the following matrix:

$$\mu_i = \begin{Bmatrix} -l_{2i} & l_{1i} \\ -m_{2i} & m_{1i} \\ -n_{2i} & n_{1i} \end{Bmatrix} \tag{3.11}$$

Column 1 in this array contains negative values of the direction cosines of the second vector $\vec{\mathbf{V}}_{2i}$, and column 2 has the direction cosines for the first vector $\vec{\mathbf{V}}_{1i}$ (Figure

3.4). These vectors are orthogonal to the vector $\vec{\mathbf{V}}_{3i}$, and to each other, but the choice for the direction of one of them is arbitrary. In order to settle the choice, we assume the following steps in this study. We let:

$$\vec{\mathbf{V}}_{1i} = \vec{\mathbf{e}}_y \times \vec{\mathbf{V}}_{3i}$$

In this $\vec{\mathbf{e}}_y$ is a unit vector in the direction of the y axis. Then the last vector to the other two is simply

$$\vec{\mathbf{V}}_{2i} = \vec{\mathbf{V}}_{3i} \times \vec{\mathbf{V}}_{1i}$$

(If for example $\vec{\mathbf{V}}_{3i}$ is parallel to $\vec{\mathbf{e}}_y$, the above scheme breaks down; this source is checked by a fortran subprogram incorporated into the finite element program used for this study. Whenever such break down of the scheme occurs, $\vec{\mathbf{e}}_y$ is replaced by $\vec{\mathbf{e}}_z$ which is a unit vector in the z direction).

Eqn. (3.10) can also be expressed more explicitly as

$$\begin{Bmatrix} u \\ v \\ w \end{Bmatrix} = \sum_{i=1}^{n} N_i(\xi,\eta) \begin{Bmatrix} u_i \\ v_i \\ w_i \end{Bmatrix} + \sum_{i=1}^{n} N_i(\xi,\eta)\zeta\frac{t_i}{2} \begin{Bmatrix} -l_{2i} & l_{1i} \\ -m_{2i} & m_{1i} \\ -n_{2i} & n_{1i} \end{Bmatrix} \begin{Bmatrix} \alpha_i \\ \beta_i \end{Bmatrix} \qquad (0.1)$$

The local generic translations are depicted in Figure 3.4 as u' and v' (in the directions of $\vec{\mathbf{V}}$, and $\vec{\mathbf{V}}_{2i}$) which are due to the nodal rotations β_i and α_i, respectively; these are evaluated using the following expressions:

$$u' = \zeta \frac{t_i}{2} \beta_i \qquad v' = -\zeta \frac{t_i}{2} \alpha_i$$

The contribution of these terms to the generic displacements at any point is given by the second summation in Eqn. (3.10). The contribution to the global displacements from a given node i is given by

$$\begin{Bmatrix} u \\ v \\ w \end{Bmatrix} = \begin{Bmatrix} N_i & 0 & 0 & -N_i\zeta\frac{t_i}{2}l_{2i} & N_i\zeta\frac{t_i}{2}l_{1i} \\ 0 & N_i & 0 & -N_i\zeta\frac{t_i}{2}m_{2i} & N_i\zeta\frac{t_i}{2}m_{1i}^{y} \\ 0 & 0 & N_i & -N_i\zeta\frac{t_i}{2}n_{2i} & N_i\zeta\frac{t_i}{2}n_{1i} \end{Bmatrix} \begin{Bmatrix} u_i \\ v_i \\ w_i \\ \alpha_i \\ \beta_i \end{Bmatrix} \tag{3.13}$$

or

$$\mathbf{u}_i = N_i \delta_i \tag{3.14}$$

For the complete element we have

$$\mathbf{u} = \mathbf{N}\delta \tag{3.15}$$

$\mathbf{u} = (u, v, w)$, $\mathbf{N} = [N_1, \ldots, N_i, \ldots, N_n]$ is the shape function matrix of the degenerate element, and $[\delta]^T = \left[\delta_1^T, \ldots, \delta_i^T, \ldots, \delta_n^T\right]$ is the vector of the element nodal variables. Here n represents the number of nodes per element.

3.2.5 Definition of Strains and Stresses

The solution to basic properties of any finite element analysis is achieved by appropriate derivation of the strains and stresses. The components in the directions of orthogonal axes related to the surface ζ = constant are essential; this is true if the basic shell assumptions are to be accounted for. Hence, to deal easily with the shell assumption of zero normal stress in the local z' direction ($\sigma_{z'}$), the strain components are expressed in terms of the local system of axes x', y', and z'. This local system of axes somewhat offers the most convenient and attractive system for expressing the stress components and their resultants for shell analysis. If at a point on the surface ζ = constant, we erect a normal z' with two other orthogonal axes x' and y' tangent to it, then the five strain components of interest are:

$$\{\varepsilon'\} = \begin{Bmatrix} \varepsilon_{x'} \\ \varepsilon_{y'} \\ \gamma_{x'y'} \\ \gamma_{x'z'} \\ \gamma_{y'z'} \end{Bmatrix} = \begin{Bmatrix} \dfrac{\partial u'}{\partial x'} \\ \dfrac{\partial v'}{\partial v'} \\ \dfrac{\partial u'}{\partial y'} + \dfrac{\partial v'}{\partial x'} \\ \dfrac{\partial u'}{\partial z'} + \dfrac{\partial w'}{\partial x'} \\ \dfrac{\partial v'}{\partial z'} + \dfrac{\partial w'}{\partial y'} \end{Bmatrix} \tag{3.16}$$

where u', v' and w' are the displacement components in the local x', y' and x' axes, respectively. The strain in the z' direction is neglected in order to be consistent with the shell assumption. It must be noted that in general none of these directions

coincide with those of the curvilinear co-ordinates ξ, η, ζ, although x' and y' are in the $\xi - \eta$ plane (ζ = constant).

The stresses corresponding to these strains are defined by a local matrix $\{\sigma'\}$ and are related by the elasticity matrix $[\mathbf{D}']$ which is given as

$$\{\sigma'\} = \begin{Bmatrix} \sigma_{x'} \\ \sigma_{y'} \\ \tau_{x'y'} \\ \tau_{x'z'} \\ \tau_{y'z'} \end{Bmatrix} = [\mathbf{D}']\,\{\varepsilon'\} \tag{3.17}$$

where $[\mathbf{D}']$ is a 5×5 elasticity matrix whose specific form varies depending on the material behaviour, namely isotropic, orthotropic or anisotropic material.

In the earlier portion of this chapter it was pointed out that the 'degenerated' shell element is a specialized form of the 20-node three dimensional element to handle the problems of thick, moderately thick and thin shell elements by curved finite elements. Furthermore, it was pointed out that in their thin shell form, the element exhibits some problem due to shear locking phenomena and that this problem could be rectified by either reduced integration and/or selective integration. The reduced integration is achieved by reducing the number of gauss points for numerical integration on the transverse shear strains, as well as on membrane strains; in the selective integration technique, bending (or bending and membrane) energies are

integrated using the normal rule, and the shear and membrane (or only shear) terms are computed using the reduced integration rule. It is to be noted that one major advantage of this element over the classical thin shell theory formulation, is the inclusion of the shear deformation terms. Most offshore tubular joints are fabricated with members whose thicknesses compared to the other dimensions are very small and consequently the shear deformation along the tube thickness is small compared to those due to bending; but in some situations, thick sections are used and in such cases the shear deformation need to be considered in addition to bending. Because of the foregoing explanation and the presence of the shear term in the 5×5 elasticity matrix $[\mathbf{D}']$, shear correction factors are applied to the last two shear terms in the $[\mathbf{D}']$ matrix defined as follows

$$[\mathbf{D}'] = \frac{E}{1-\nu^2}\begin{bmatrix} 1 & \nu & 0 & 0 & 0 \\ \nu & 1 & 0 & 0 & 0 \\ 0 & 0 & \frac{1-\nu}{2} & 0 & 0 \\ 0 & 0 & 0 & \frac{1-\nu}{2\kappa} & 0 \\ 0 & 0 & 0 & 0 & \frac{1-\nu}{2\kappa} \end{bmatrix} \tag{3.18}$$

in which E and ν are Young's modulus and Poisson's ratio, respectively. The factor κ is taken as 1.2, to improve the shear displacement approximation, which from the displacement definition given in Eqn. (3.10), shows that the shear distribution through the thickness is approximately constant, whereas in reality the shear dis-

tribution is approximately parabolic. Detailed derivation of the [D'] matrix is given in Appendix B.

3.2.6 Element Properties and Transformations

The stiffness matrix, and indeed all other element property matrices, involve, integrals over the volume of the element, which are generally of the form

$$\int_{vol.} [\mathbf{M}]\, dxdydz \tag{3.19}$$

where the matrix [M] is a function of the coordinates. In the expression for stiffness matrix, the matrix [M] is given as

$$[\mathbf{M}] = [\mathbf{B}]^T [\mathbf{D}][\mathbf{B}] \tag{3.20}$$

where the matrix [B] relates the strains to the nodal parameters in the form

$$\{\varepsilon\} = [\mathbf{B}]\,\{\delta\}^e \tag{3.21}$$

Thus in the present formulation, if the matrix [M] is expressed as an explicit function of the curvilinear coordinates (ξ, η, ζ) and the infinitesimal volume $dxdydz$ is also transformed accordingly, then a straightforward (numerical) integration will allow the properties to be evaluated. Hence, we require two sets of transformations

before the element can be integrated with respect to the curvilinear co-ordinates ξ, η, and ζ.

Firstly, from Eqn. (3.10) which relates the global displacements u, v and w to the curvilinear co-ordinates, we obtain the derivatives of these displacements with respect to the global x, y and z using the standard expression, viz.,

$$\begin{bmatrix} \frac{\partial u}{\partial x} & \frac{\partial v}{\partial x} & \frac{\partial w}{\partial x} \\ \frac{\partial u}{\partial y} & \frac{\partial v}{\partial y} & \frac{\partial w}{\partial y} \\ \frac{\partial u}{\partial z} & \frac{\partial v}{\partial z} & \frac{\partial w}{\partial z} \end{bmatrix} = [\mathbf{J}]^{-1} \begin{bmatrix} \frac{\partial u}{\partial \xi} & \frac{\partial v}{\partial \xi} & \frac{\partial w}{\partial \xi} \\ \frac{\partial u}{\partial \eta} & \frac{\partial v}{\partial \eta} & \frac{\partial w}{\partial \eta} \\ \frac{\partial u}{\partial \zeta} & \frac{\partial v}{\partial \zeta} & \frac{\partial w}{\partial \zeta} \end{bmatrix} \tag{3.22}$$

where the Jacobian matrix $[\mathbf{J}]$ is defined by the expression

$$[\mathbf{J}] = \begin{bmatrix} \frac{\partial x}{\partial \xi} & \frac{\partial y}{\partial \xi} & \frac{\partial z}{\partial \xi} \\ \frac{\partial x}{\partial \eta} & \frac{\partial y}{\partial \eta} & \frac{\partial z}{\partial \eta} \\ \frac{\partial x}{\partial \zeta} & \frac{\partial y}{\partial \zeta} & \frac{\partial z}{\partial \zeta} \end{bmatrix} \tag{3.23}$$

The elements of the Jacobian matrix can be found from the definition of the co-ordinates, Eqn. (3.7).

Secondly, the global derivatives of displacements are now transformed to the local

derivatives of the local orthogonal displacements, that is

$$\begin{bmatrix} \frac{\partial u'}{\partial x'} & \frac{\partial v'}{\partial x'} & \frac{\partial w'}{\partial x'} \\ \frac{\partial u'}{\partial y'} & \frac{\partial v'}{\partial y'} & \frac{\partial w'}{\partial y'} \\ \frac{\partial u'}{\partial z'} & \frac{\partial v'}{\partial z'} & \frac{\partial w'}{\partial z'} \end{bmatrix} = [\theta]^T \begin{bmatrix} \frac{\partial u}{\partial x} & \frac{\partial v}{\partial x} & \frac{\partial w}{\partial x} \\ \frac{\partial u}{\partial y} & \frac{\partial v}{\partial y} & \frac{\partial w}{\partial y} \\ \frac{\partial u}{\partial z} & \frac{\partial v}{\partial z} & \frac{\partial w}{\partial z} \end{bmatrix} [\theta] \tag{3.24}$$

Substituting Eqn (3.24) into Eqn. (3.26), we have

$$\begin{bmatrix} \frac{\partial u'}{\partial x'} & \frac{\partial v'}{\partial x'} & \frac{\partial w'}{\partial x'} \\ \frac{\partial u'}{\partial y'} & \frac{\partial v'}{\partial y'} & \frac{\partial w'}{\partial y'} \\ \frac{\partial u'}{\partial z'} & \frac{\partial v'}{\partial z'} & \frac{\partial w'}{\partial z'} \end{bmatrix} = [\theta]^T [\mathbf{J}]^{-1} \begin{bmatrix} \frac{\partial u}{\partial \xi} & \frac{\partial v}{\partial \xi} & \frac{\partial w}{\partial \xi} \\ \frac{\partial u}{\partial \eta} & \frac{\partial v}{\partial \eta} & \frac{\partial w}{\partial \eta} \\ \frac{\partial u}{\partial \zeta} & \frac{\partial v}{\partial \zeta} & \frac{\partial w}{\partial \zeta} \end{bmatrix} [\theta] \tag{3.25}$$

In order to compute the strains, as defined by Eqns. (3.21) and (3.25), the evaluation of the inverse of the Jacobian matrix given by Eqn. (3.23) is necessary. It is observed that by definition, this can in fact be written in terms of three vectors as follows

$$[\mathbf{J}] = \begin{bmatrix} \vec{\mathbf{S}} \\ \vec{\mathbf{T}} \\ \vec{\mathbf{V}}_3 \end{bmatrix} \tag{3.26}$$

In the above equation, the first two vectors are tangential to the reference surface (the mid-plane) while the vector $\vec{\mathbf{V}}_3$ is in the direction of the normal to the reference surface (it is considered that ζ is normal to the midside surface).

The inverse of the Jacobian matrix can now be written explicitly as

$$[\mathbf{J}]^{-1} = \frac{\left[\vec{\mathbf{T}} \times \vec{\mathbf{V}}_3,\ \vec{\mathbf{V}}_3 \times \vec{\mathbf{S}},\ \vec{\mathbf{S}} \times \vec{\mathbf{T}}\right]}{\|\mathbf{J}\|} \tag{3.27}$$

where the first two columns in the numerator of the adjoint of the Jacobian matrix are again vectors of the tangents to the reference plane and the third column is normal to it, and $\|\mathbf{J}\|$ represents the determinant of the Jacobian matrix $[\mathbf{J}]$.

In the expression for the direction cosine $[\theta]$ defined in Eqn. (3.5), that is

$$[\theta] = [\dot{\mathbf{v}}_1, \dot{\mathbf{v}}_2, \dot{\mathbf{v}}_3] \tag{3.28}$$

the third vector in the direction cosine expression [Eqn. (3.28)], has the same sense as the third vector in the Jacobian inverse expression [Eqn. (3.27)]. As a consequence of normal vector operations we can write

$$
\begin{aligned}
[\mathbf{A}] &= [\theta]^T [\mathbf{J}]^{-1} \\
&= \begin{bmatrix} \dot{\mathbf{v}}_1 \\ \dot{\mathbf{v}}_2 \\ \dot{\mathbf{v}}_3 \end{bmatrix} \left[\vec{\mathbf{T}} \times \vec{\mathbf{V}}_3,\ \vec{\mathbf{V}}_3 \times \vec{\mathbf{S}},\ \vec{\mathbf{S}} \times \vec{\mathbf{T}}\right] \div \|\mathbf{J}\| \\
&= \begin{bmatrix} \mathbf{A}_{11} & \mathbf{A}_{12} & 0 \\ \mathbf{A}_{21} & \mathbf{A}_{22} & 0 \\ 0 & 0 & \mathbf{A}_{33} \end{bmatrix}
\end{aligned}
\tag{3.29}
$$

By taking advantage of this special form of $\mathbf{A}$, Eqn. (3.26) is uncoupled into two parts:

$$
\left.
\begin{aligned}
[\mathbf{e}_1'] &= \begin{bmatrix} \mathbf{A}_{11} & \mathbf{A}_{12} \\ \mathbf{A}_{21} & \mathbf{A}_{22} \end{bmatrix} \begin{bmatrix} \dfrac{\partial u}{\partial \xi} & \dfrac{\partial v}{\partial \xi} & \dfrac{\partial w}{\partial \xi} \\ \dfrac{\partial u}{\partial \eta} & \dfrac{\partial v}{\partial \eta} & \dfrac{\partial w}{\partial \eta} \end{bmatrix} [\theta] \\
[\mathbf{e}_2'] &= \mathbf{A}_{33} \begin{bmatrix} \dfrac{\partial u}{\partial \zeta} & \dfrac{\partial v}{\partial \zeta} & \dfrac{\partial w}{\partial \zeta} \end{bmatrix} [\theta]
\end{aligned}
\right\}
\tag{3.30}
$$

The above technique is used during this study to reduce the number of operations in the program used in the study. The multiplications of zero terms are avoided during any run; this saves a substantial amount of computation time and computer CPU time.

It is also important to note that the elastic properties $[\mathbf{D}']$ and the strain vector

$\{\varepsilon'\}$ can be decomposed into two parts, viz., in-plane and transverse components, as

$$
\begin{aligned}
[\varepsilon'_1] &= \begin{bmatrix} \varepsilon'_m \\ \varepsilon'_s \end{bmatrix} \\
[\mathbf{D}'] &= \begin{bmatrix} \mathbf{D}'_m & 0 \\ 0 & \mathbf{D}'_s \end{bmatrix}
\end{aligned}
\tag{3.31}
$$

The energy expressions for an isotropic material are related to equations (3.18) to (3.21); hence after decomposing both the elastic properties $\mathbf{D}'$ and the strain vector ε' into two parts as shown in Eqn. (3.30), the strain energy can be expressed as

$$
dU' = \frac{1}{2}\left[\{\varepsilon'_m\}^T [\mathbf{D}'_m] \{\varepsilon'_m\} + \{\varepsilon'_s\}^T [\mathbf{D}'_s] \{\varepsilon'_s\}\right] \tag{3.32}
$$

where the strain vector $\{\varepsilon'\}$ is obtained from Eqn. (3.25) and takes the following form:

$$\{\varepsilon'\} = \begin{bmatrix} \frac{\partial}{\partial x'} & 0 & 0 \\ & \frac{\partial}{\partial y'} & 0 \\ \frac{\partial}{\partial y'} & \frac{\partial}{\partial x'} & 0 \\ \frac{\partial}{\partial z'} & 0 & \frac{\partial}{\partial x'} \\ 0 & \frac{\partial}{\partial z'} & \frac{\partial}{\partial y'} \end{bmatrix} \begin{Bmatrix} u' \\ v' \\ w' \end{Bmatrix} = [\mathbf{G}] \begin{Bmatrix} u' \\ v' \\ w' \end{Bmatrix} \tag{3.33}$$

Transforming the local displacement vector to global displacement vector we have

$$\{\varepsilon'\} = [\mathbf{G}] \left[\theta^T\right] \begin{Bmatrix} u \\ v \\ w \end{Bmatrix} \tag{3.34}$$

Expanding this equation using Eqn. (3.10) and (3.29) we have

$$\{\varepsilon'\} = [\mathbf{B}_i] \left[\theta^T\right] \begin{Bmatrix} u_i \\ v_i \\ w_i \end{Bmatrix} + \frac{t_i}{2} [\zeta[\mathbf{B}_i] + [\mathbf{C}_i]] [\theta]^T [-\hat{\mathbf{v}}_{2i}, \hat{\mathbf{v}}_{1i}] \begin{Bmatrix} \alpha_i \\ \beta_i \end{Bmatrix} \tag{3.35}$$

where i denotes the nodal number of an element, and

$$[\mathbf{B}_i] = \begin{bmatrix} B_1 & 0 & 0 \\ 0 & B_2 & 0 \\ B_2 & B_1 & 0 \\ 0 & 0 & B_1 \\ 0 & 0 & B_2 \end{bmatrix} ; \quad [\mathbf{C}_i] = \begin{bmatrix} 0 & 0 & 0 \\ 0 & 0 & 0 \\ 0 & 0 & 0 \\ C_1 & 0 & 0 \\ 0 & C_1 & 0 \end{bmatrix} \tag{3.36}$$

$$\left.\begin{aligned} B_1 &= A_{11}\frac{\partial N_i}{\partial \xi} + A_{12}\frac{\partial N_i}{\partial \eta} \\ B_2 &= A_{21}\frac{\partial N_i}{\partial \xi} + A_{22}\frac{\partial N_i}{\partial \eta} \\ C_1 &= A_{33}N_i \end{aligned}\right\} \tag{3.37}$$

Finally by minimizing the strain energy of the element domain with respect to nodal displacement parameters, the element stiffness matrix is obtained. From Eqn. (3.19), the infinitesimal volume is given in terms of the curvilinear co-ordinates as

$$dx\, dy\, dz = \|\mathbf{J}\|\, d\xi\, d\eta\, d\zeta \tag{3.38}$$

and

$$[\mathbf{K}]^e = \int_{-1}^{+1}\int_{-1}^{+1}\int_{-1}^{+1} [\mathbf{B}']^T\, [\mathbf{D}']\, [\mathbf{B}']\, \|\mathbf{J}\| d\xi d\eta d\zeta \tag{3.39}$$

Two special features of Eqns. (3.31) and (3.35), i.e., identical terms and sparseness of the matrices, were taken into account in performing the matrix multiplication during the construction of the element stiffness matrix Eqn. (3.39).

3.2.7 Element Assembly and Equation Solution Procedure

The direct stiffness method approach was essentially employed in the present study to assemble the stiffness matrix contributions from each element to form the global stiffness matrix and global load vector. The element stiffness matrices were assembled in their own coordinate systems (local coordinate system) and later transformed to the tubular joint coordinate system. This results in a set of simultaneous equations. The frontal solution technique was used for the direct solution of the equations. The main idea of this solution technique is to assemble the equations element by element and eliminate the variables at the same time. Although the frontal solution technique was used in preference to the banded solution, however, just as the banded technique demands a good node numbering system for keeping the computational costs down, the frontal technique needs a good ordering of the elements. Indeed, if the elements are not numbered carefully, the latter can even lose out to the former. Hence at every stage of the tubular joint generation in this investigation an attempt was made to minimize the frontwidth, by passing the mesh element numbers and their corresponding nodes through a fortran subprogram developed for this purpose.

In conclusion, by simply reducing the order of the integration for all stress com-

ponents the degenerate shell element concept has proved to yield accurate results for both thick and thin shells. The aspect ratio of the elements can be increased almost to any value without introducing stiffness effects. This element indeed is amongst the most accurate ones known and, by being able to render correctly shear deformations within the element, may be termed the most general shell element.

3.3 Life Prediction Formulation

Recent investigations into the constant amplitude load fatigue of welded tubular joints have clearly indicated that the assumption of the total fatigue life (which is the sum of the cycles required for crack initiation, N_i, and crack propagation, N_p) being controlled purely by the crack propagation life, may be misleading. Recent experimental investigation on the fatigue life of offshore welded tubular joints by Pates et al., (1989) have shown that the crack initiation life may be of the order of 25 to 30 percent of the total fatigue life in air tests and more for corrosion fatigue tests in water. Consequently estimation of fatigue life using only the crack propagation life for the entire life of the joint would be unrealistic. A realistic and better life estimation technique should, therefore, include both the initiation and the propagation lives of the joint.

The following techniques are combined in the present study to determine the total fatigue life:

1. The local stress-strain approach to crack initiation, and

2. The fracture mechanics approach to crack propagation.

Though reasonable success has been demonstrated in combining the local stress-strain approach and the fracture mechanics approach for prediction of the initiation and propagation lives, for small and large scale test specimens and relatively simple structures, little or no analytical/numerical literature is available for this combined approach in dealing with complex and large structures like offshore welded tubular joints. One of the main objectives of this investigation was to explore the use of purely numerical techniques for combining these different approaches in arriving at the total fatigue life of the joint. In what follows the formulation used for crack initiation is given first followed by that for crack propagation.

3.3.1 Crack Initiation Life Prediction

The local stress-strain approach, also known as the strain cycle fatigue concept, is used for determining the crack initiation life in this investigation. The basic hypothesis of the notch stress-strain approach to fatigue is that if the stresses and strains at a critical location of a component are known, then the life to crack initiation at this position can be related to the fatigue life of strain-controlled unnotched laboratory specimens. Hence, the analysis reduces to one of determining the local stresses and strains and relating these to the known strain-life fatigue behaviour.

The procedure for crack initiation, as used in this study, is briefly outlined below: Finite element analysis for stress and strain computation was first performed in order to locate the possible location for crack initiation. The stress and strain concentrations were also determined.

For a nominal loading in the elastic range, the local stress and strain ranges are related to the nominal stress range by using the modified Neuber's rule given as

$$K_f \, \Delta\sigma_{nom} \;=\; (\Delta\sigma \, \Delta\varepsilon \, E)^{1/2} \tag{3.40}$$

where $\Delta\sigma$ and $\Delta\varepsilon$ are the weld toe stress and strain ranges, $\Delta\sigma_{nom}$ the nominal stress range applied to brace, E the elastic modulus and K_f is the fatigue notch factor. One can also express Eqn. (3.40) as

$$\Delta\sigma \, \Delta\varepsilon \;=\; \frac{(K_f \, \Delta\sigma_{nom})^2}{E} \tag{3.41}$$

Also required in the crack initiation life prediction, are the material's fatigue properties, which can be computed from (a) cyclic stress-strain relationship, and (b) strain-life relationship. The cyclic stress-strain relationship for a material is expressed as

$$\frac{\Delta\varepsilon}{2} = \frac{\Delta\sigma}{2E} + (\frac{\Delta\sigma}{2K'})^{1/n'} \tag{3.42}$$

where $\Delta\varepsilon$ and $\Delta\sigma$ are the weld toe strain and stress ranges, respectively, K' the cyclic strength coefficient and n' the cyclic strain hardening coefficient.

By combining Eqn. (3.41) with Eqn. (3.42), we have

$$\frac{\Delta\sigma^2}{2E} + \Delta\sigma \left(\frac{\Delta\sigma}{2K'}\right)^{1/n'} = \frac{(K_f \, \Delta\sigma_{nom})^2}{2E} \tag{3.43}$$

The values of $\Delta\sigma$ and $\Delta\varepsilon$ are determined in this by solving Eqn. (3.43) using numerical techniques.

Finally the prediction method involves solving the Manson-Coffin equation for crack-initiation life, N_f. This equation which takes into account contributions of both plastic and elastic weld toe strain ranges, is expressed as

$$\frac{\Delta\varepsilon}{2} = \frac{1}{2}(\Delta\varepsilon_e + \Delta\varepsilon_p) = \frac{\sigma'_f}{E}(2N_f)^b + \varepsilon'_f(2N_f)^c \qquad (3.44)$$

where $\Delta\varepsilon_e$ and $\Delta\varepsilon_p$ are the weld toe elastic and plastic strain ranges, σ'_f and ε'_f the fatigue strength and ductility coefficients, and b and c the fatigue strength and ductility exponents, respectively.

3.3.2 Fatigue Crack Growth Formulation

Fracture mechanics method has recently become an important tool for offshore structural design, fabrication and integrity assessment. For tubular joints, surface flaws initiate at the weld toe of the tubular intersection areas and propagate under environmental loads along the weld toe and through the joint thickness (Figure 3.6). The shape of this propagating flaw is influenced both by the local stress state and material properties near the tubular intersection area. The sensitivity of inspection techniques used in recent times for in-service inspections has made possible the earlier detection of fatigue cracks in offshore welded tubular joints. The increasing requirements for longer service lives of these joints coupled with the current move by industries toward limit state design, has necessitated fitness for purpose assessment to evaluate the significance of this cracking phenomena in

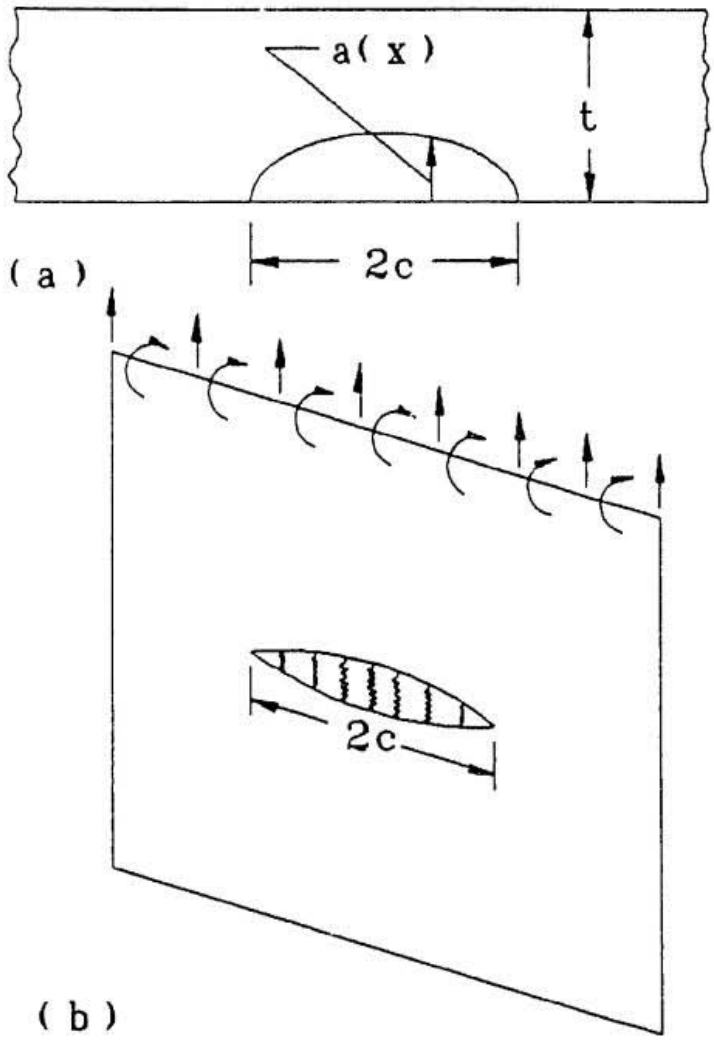

Figure 3.6: (a) Schematic cross-section of a surface crack with varying depth a(x) and projected length 2c in a shell of thickness t, (b) Schematic idealization of through-cut shell (plate) mid-surface with distributed stiffnesses along the crack line.

tubular welded joints (TWJ). Such assessment requires the application of fracture mechanics analysis, in which crack tip conditions are characterised using the stress intensity factors (SIF). Hence it is apparent that the fatigue crack growth life assessment of cracked components require information about the stress intensity factor.

Due to the nature of the special elements (line spring elements) employed in this study for stress intensity factor evaluation, which is an essential aspect for crack propagation life prediction, this section is divided into two parts: (i) Line spring element formulation and its implementation and (ii) Fatigue crack growth model.

3.3.3 Line Spring Model for Stress Intensity Factor Evaluation

Renewed interest has been shown recently in the use of simplified models for three-dimensional crack configurations which may be broadly termed "surface cracked plates and shells". The model termed the "line spring element" was originally introduced by Rice and Levy (1972) to estimate stress intensity factors for part-through surface cracks in large plates subjected to bending and tension. Extension of the simplified model to analysis of surface crack problems in cylindrical shells have been achieved by Rice and Levy (1972) and Parks (1980, 1981).

In order to determine the additional compliance introduced into the structure by a part-through crack, we start the formulation of this special model by considering a surface crack of length $2c$ and varying depth $a(x)$ in a shell wall thickness t as shown in Figure 3.6(a). By following the usual procedures of shell theory, the surface-

cracked structure is modelled by its midplane surface as a two-dimensional continuum, and the surface crack location is accordingly idealized as a one-dimensional cut as depicted in Figure 3.6(b).

If it is assumed that the surface crack is not present at the considered location, then the cut will carry a certain (uncracked) distribution of the shell generalized forces (the term "generalized force" is taken in this context to mean both forces and moments). If for example we assume now that the cut lies in a symmetry plane (this condition is assumed here to illustrate the line spring model development in it simplest form, a more general case is discussed later during the course of this formulation), the distribution of the shell forces will consist of a normal membrane force $N^0(x)$ and bending moment $M^0(x)$. These forces are sufficient to ensure that there is no discontinuity along the cut in the shell generalized displacements (translational and rotational) work-conjugate to these forces. These displacements consist of the jump in shell midsurface displacement, $\delta(x)$, in the shell tangent plane and normal to the cut and the small rotation, $\theta(x)$, of the tangent to the cut of the material line elements initially normal to the shell mid-surface.

The uncracked force and deformation distribution on the cut can thus be given by

$$[N(x), M(x)] = \left[N^0(x), M^0(x)\right] \tag{3.45}$$

$$[\delta(x), \theta(x)] = (0, 0) \tag{3.46}$$

Note that N^0, and M^0 are determined from the solution of the uncracked ($a(x) \equiv 0$)

problem.

Now consider the opposite extreme case where the crack has fully gone through the plate thickness (through crack), that is $[a(x)] \equiv t$ case, and denoting this case by superscript "t", we find that the discontinuous field terms, analogous to Eqns. (3.45) and (3.46), are

$$[N(x), M(x)] = (0, 0) \tag{3.47}$$

$$(\delta(x), \theta(x)) = (\delta^t(x), \theta^t(x)) \tag{3.48}$$

where again δ^t, θ^t are the opening and rotation discontinuities across the sides of the force-free "through-crack" cut.

If we now consider the true surface crack as having a surface depth distribution $a(x)$ intermediate between the two previous limiting cases, that is $0 < a(x) < t$ through most of the cut, then for this case, solution fields $[N(x), M(x)]$ and $[\delta(x), \theta(x)]$ which are intermediate in some sense to the uncracked and through-cracked limits are expected. Using the well known fact in engineering mechanics, that the extreme boundary conditions of zero displacement and zero traction can be conceptually considered as limiting cases of infinitely stiff and soft elastic foundations, respectively, we can then represent the intermediate part-through surface crack by some kind of generalized elastic foundation along the cut, with stiffness varying according to local crack depth $a(x)$. This foundation, then, consists of generalized springs distributed along the line of the cut.

For linear elastic behaviour, the constitutive relation for the springs which relates local loads (N, M) at each position x along the cut to their local work-conjugate displacements, (δ, θ), is symbolically expressed as

$$\begin{bmatrix} \delta(x) \\ \theta(x) \end{bmatrix} = \begin{bmatrix} C_{11} & C_{12} \\ C_{21} & C_{22} \end{bmatrix} \begin{bmatrix} N(x) \\ M(x) \end{bmatrix} \tag{3.49}$$

The above expression can be stated in an equivalent manner as

$$\begin{bmatrix} N(x) \\ M(x) \end{bmatrix} = \begin{bmatrix} K_{11} & K_{12} \\ K_{21} & K_{22} \end{bmatrix} \begin{bmatrix} \delta(x) \\ \theta(x) \end{bmatrix} \tag{3.50}$$

The matrices $[C]$ and $[K] = [C]^{-1}$ are the elastic compliances and stiffnesses, respectively. The model for choosing the above local compliances, $[C]$ is shown in Figure 3.7. If, in the far field, the axial force N and bending moment M per unit depth are simultaneously applied to the specimen, then the additional displacement δ_c and rotation θ_c at the load points due to the presence of the crack are expressed as

$$\begin{bmatrix} \delta_c \\ \theta_c \end{bmatrix} = \begin{bmatrix} P_{11} & P_{12} \\ P_{21} & P_{22} \end{bmatrix} \begin{bmatrix} N \\ M \end{bmatrix} \tag{3.51}$$

By using the energy compliance relations noted by Rice (1972), the matrix $[P]$ is determined from stress intensity factor calibration of the single-edge notched specimen. For plane strain condition, the elements of matrix $[P]$ are given as

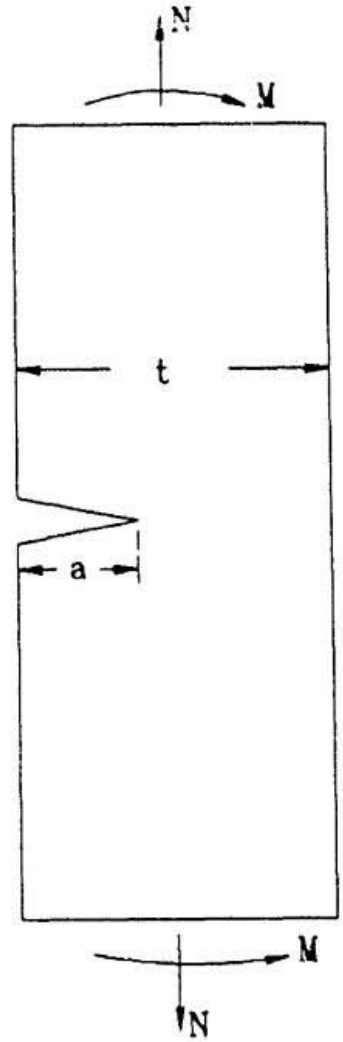

Figure 3.7: Single-edge notched specimen subject to combined tension and bending.

$$P_{11} = \frac{2\pi}{E/(1-\nu^2)}\,\gamma_{11} \tag{3.52}$$

$$P_{12} = P_{21} = \frac{12\pi}{E/(1-\nu^2)t}\,\gamma_{12} \tag{3.53}$$

$$P_{22} = \frac{72\pi}{E/(1-\nu^2)t^2}\,\gamma_{22} \tag{3.54}$$

where

$$\gamma_{ij} \;=\; \int_0^{\xi} \bar{\xi}\, F_i(\bar{\xi})\, F_j(\bar{\xi}) d\bar{\xi} \tag{3.55}$$

with $\bar{\xi}$ = a/t. The assumed calibration for stress intensity factor of this specimen is

$$K_1 \;=\; (\pi a)^{1/2} * [F_1(a/t)\frac{N}{t} + F_2(a/t)\frac{6M}{t^2}] \tag{3.56}$$

Tada *et al.* (1973) has given approximate formulae for F_is.

The integrals for γ_{ij} are usually numerically integrated using trapezoidal rule in steps of $\Delta\bar{\xi} = 0.01$. These values are stored for subsequent evaluation of γ_{ij} values for any particular local crack depth ratio, a/t, which can be obtained by interpolation between tabulated values.

The stiffness of the line spring foundation model is finally obtained by taking $[C] = [P]$, and hence evaluating $[K]$. It is important to note that in arriving at this result, we have assumed that the additional displacement and rotation, due to the presence of the crack in Figure 3.7, are obtained right on the surface of the crack line and it is lumped there as discontinuities across the cut.

The most important feature of the line spring model comes into play after the compliances have been obtained. If we now consider the surface cracked shell to be sectioned by a plane normal to the cut and containing the shell midsurface normal at some position x along the cut, it will locally bear a similar resemblance to the single-edge cracked specimen of Figure 3.7, with the interpretation that the crack length "a" is the local depth, $a(x)$, and the loads (N, M) are the local loads transmitted across the cut, $[N(x), M(x)]$. Then the line spring can be conveniently conceptualized as providing an estimate of the local stress intensity factor in the surface flaw from direct implementation of Eqn. (3.56).

Figure 3.8 shows the above situation now integrated into the present study. From this figure it is apparent that the concept employed for stress intensity factor evaluation in the case of the single-edge notched crack by employing the line spring model can be extended to the complex tubular joint case (which is the subject of this research) with some modifications. Some of the obvious modifications, in order to use the line spring model for the present study, are discussed in chapter 7.

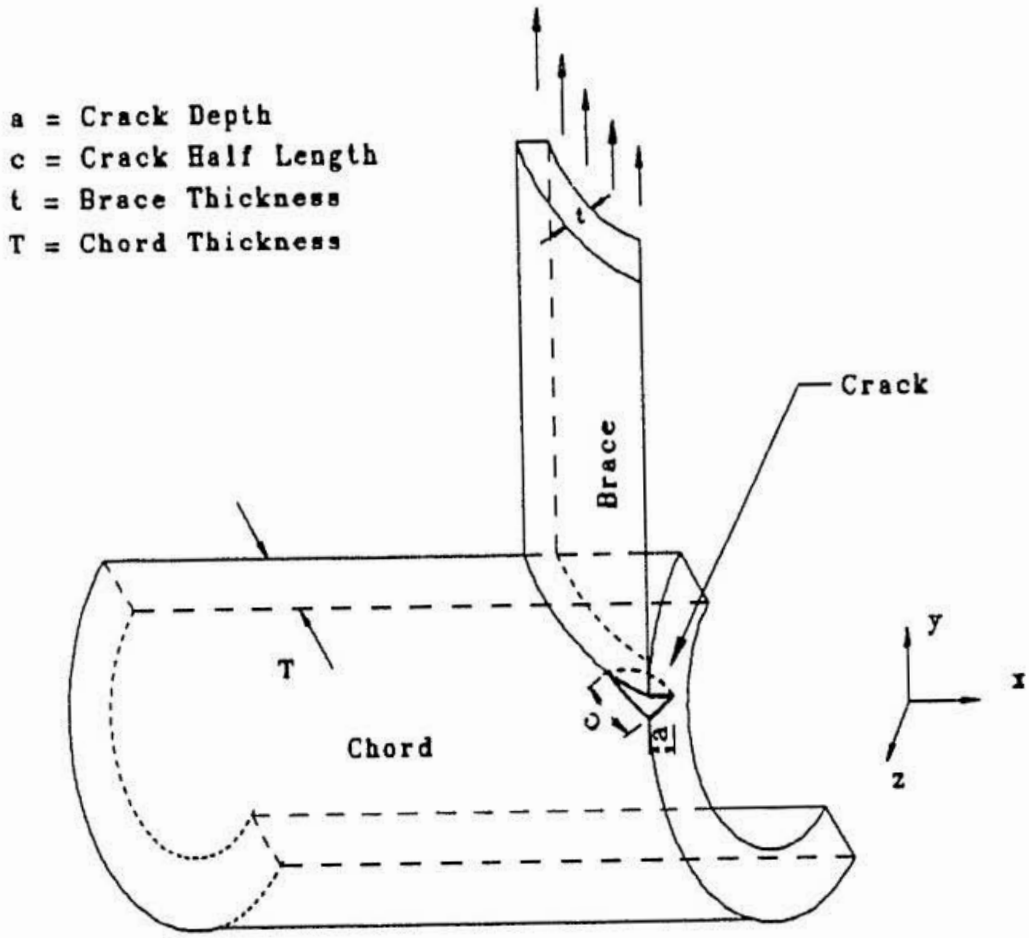

Figure 3.8: Schematic representation of surface crack in a tubular joint.

3.3.4 Finite Element Implementation of the Line Spring Model

The stress intensity factors, used in the evaluation of fatigue crack growth life in the present study, were obtained by incorporating the line spring element across the faces of the finite element model used in the study at the crack locations (see chapter 7).

Figure 3.9 schematically shows a shell/line-spring interface, in a particular local coordinate system (x,y,z). The 8-node shell element (nodes 1, 5, 2, 6, 3, 7, 4, 8) joins a 6-node line spring element (1, 5, 2, 10, 50, 20) along their common intersection of nodes 1, 5 and 2. As an input the line spring crack depth is specified at nodal locations along the cut, and interpolated to integration points. The crack depth contains a sign flag indicating whether the surface crack emanates from the positive or negative side of the shell (see Figure 3.10).

The line spring generalized displacements variables $[\delta(x),\theta(x)]$ along the cut, are given in local (x,y,z) coordinates by

$$\delta(x) = u_y(x, y = 0^+, z = R) - u_y(x, y = 0^-, z = R) \tag{3.57}$$

$$\theta(x) = \varphi_x(x, y = 0^+, z = R) - \varphi_x(x, y = 0^-, z = R) \tag{3.58}$$

where the field u_y and φ_x are interpolated from the nodal values. The sign of the right hand side of Eqn. (3.58) is changed if the crack emanated from the negative

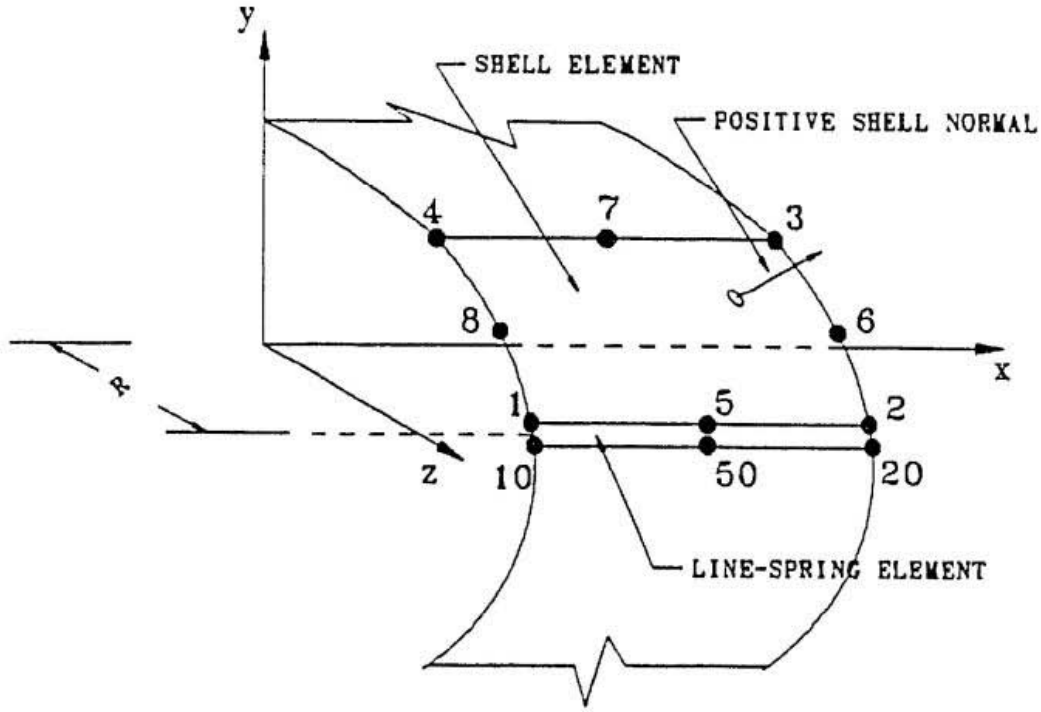

Figure 3.9: Schematic illustration of the intersection of an 8-node shell and a 6-node line-spring element in a cylindrical shell.

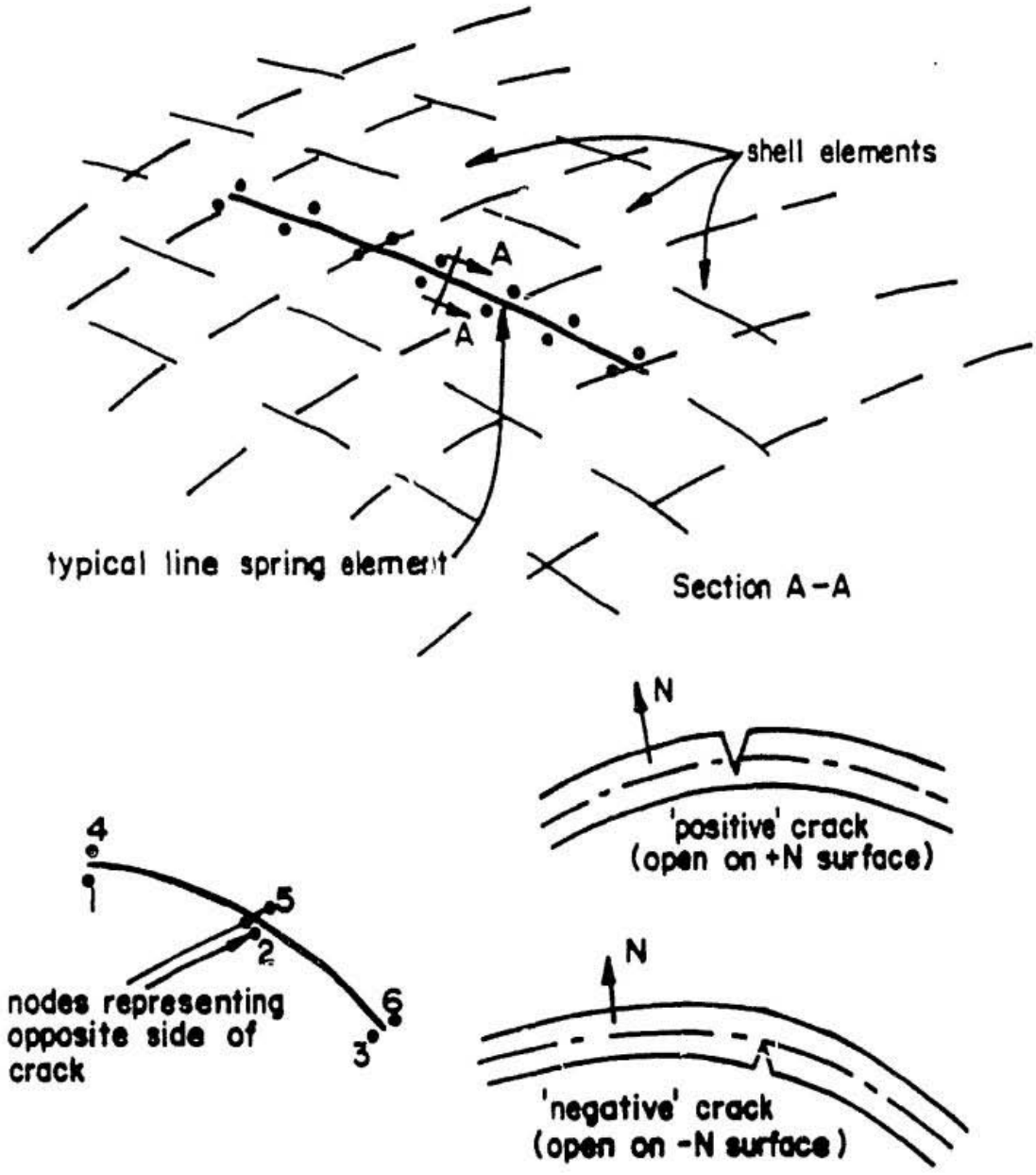

Figure 3.10: Line spring models showing flags for positive and negative cracks [ABAQUS (1989)].

shell surface.

By using the above equations and the matrix relationship given in Eqn.(3.50), the virtual work of the line spring element is given as:

$$V.W. = \int_{x_1}^{x_2} [\delta^*(x), \theta^*(x))] \begin{bmatrix} N(x) \\ M(x) \end{bmatrix} dx \tag{3.59}$$

where the virtual quantities δ^*, and θ^* are related to virtual nodal displacements in the standard manner, and x_1 and x_2 are the x coordinates of the two ends of the element. In the element stiffness matrix formulation obtained from Eqn. (3.59), a two point Gaussian integration is employed. After solution, the generalized displacements (δ, θ) and forces (N, M) are recovered at the integration points, and the stress intensity factors obtained from Eqn. (3.56).

In order to justify the use of this model for stress intensity factor evaluation in this study, the results obtained are compared with the results from recent line spring element application to tubular joints. Most of the available literature give stress intensity factors for the deepest part of the crack. The results presented in this study have been extended to compute all the stress intensity factors values along the crack front. In some instances a curve have been fitted to the data obtained from the finite element analysis. Details of this procedure are given in chapter 7.

3.3.5 Fatigue Crack Growth model

Once the stress intensity factors along the crack front have been obtained as outlined above, with the use of line spring element, they are then introduced into the crack

growth law for life calculation. The form of fatigue crack growth correlation for constant amplitude loading employed in this study is a log-log plot of fatigue crack growth rate, da/dN, in m/cycle, versus the stress intensity factor range ΔK, in $MPa\sqrt{m}$. The stress intensity factor range ΔK is obtained from

$$\Delta K = K_{max} - K_{min}$$

$$= Y\sigma_{max}\sqrt{\pi a} - Y\sigma_{min}\sqrt{\pi a} \tag{3.60}$$

The crack growth law, used in this study, is based on a linear relationship (on a log-log basis) developed by Paris *et al.* (1961), which is now known as Paris law. The growth law corresponds to region II (straight line) of the sigmoidal shape curve obtained when the crack growth rates, da/dN are plotted against the stress intensity factor ranges on a log-log plot. In it's simplest form this power law is expressed as

$$\frac{da}{dN} = C(\Delta K)^m \tag{3.61}$$

where da/dN is the change in the crack length or depth, a, per cycle, N, and C and m are constants determined from compact tension tests of the material of the tubular joint. The life can then be determined by integrating Eqn. (3.61):

$$N = \int_{a_f}^{a_i} \frac{da}{C(\Delta K)^m} \tag{3.62}$$

where a_i is the initial flaw size and a_f is the final flaw size. The above integration was carried out numerically in the present study. This numerical approach is discussed in greater detail in chapter 7.

In conclusion it can be seen, from the last three equations, that the fracture mechanics approach is considerably more complex than the S-N approach, since it requires knowledge of initial flaw sizes as well as that of the stress intensity factor solution. However, it must be emphasized, that in its simplest form, the fracture mechanics approach is consistent with the S-N approach, as both rely on a power law relationship between stress range and the propagation life.

Chapter 4

Stress Analysis of Unstiffened Tubular Joints

4.1 General

Owing to the cyclic wave loadings to which offshore welded tubular joints are subjected to, they become susceptible to fatigue damage. In the present study, interest is focused on the determination of total fatigue life of tubular welded joints, which includes the life spent in initiating cracks and the remaining life due to crack propagation. The strain life approach was employed in evaluating the former, while the latter was obtained through fracture mechanics technique. Conceptually it is evident that the first stage of the life predictions requires the knowledge of stress and strain distribution along the intersection without a crack, where the stresses are expected to be high, while the second stage requires both stress distribution along the intersection and through the thickness (with crack). Determination of stress and strain distribution along the intersection is aimed at finding the magnitude and the location of the problem stress level (hot spot stress), which invariably gives an insight as to where the crack(s) is (are) likely to initiate and also to determine the

stress concentration factors (SCFs) which are the measures of the amplification of the nominal brace stress as a result of member discontinuity and wall bending; the through thickness stress distribution on the other hand, is directed toward determining the relative proportion of the bending stress to the total stress (degree of bending DOB),

$$DOB = \frac{\sigma_b}{(\sigma_m + \sigma_b)} = \frac{\sigma_b}{\sigma_{total}} \tag{4.1}$$

This in fact gives an indication of the proportion of the stress (bending or membrane) that controls the fatigue life propagation as the crack grows through the joint thickness.

In order to carry out fracture mechanics calculations of the fatigue life it is necessary to determine the crack tip stress intensity factors and the corresponding crack growth rates. These calculations require information on the magnitude and distribution of the stress acting in the anticipated crack region. For most situations this means the computation of the magnitude and distribution of stresses through the thickness and around the intersection of the tubular members.

An extensive finite element analysis of tubular T-joints, covering various geometric joint parameters (see Figure 4.1), has been carried out to address the two aspects of stress distributions mentioned above. The range of the joint parameters investigated is shown in Table 4.1. The finite element study was carried out for three different type of loading cases, viz., axial tension, in-plane bending (IPB) and out-of-plane bending (OPB) loads. The three load cases are illustrated in Figure 4.2.

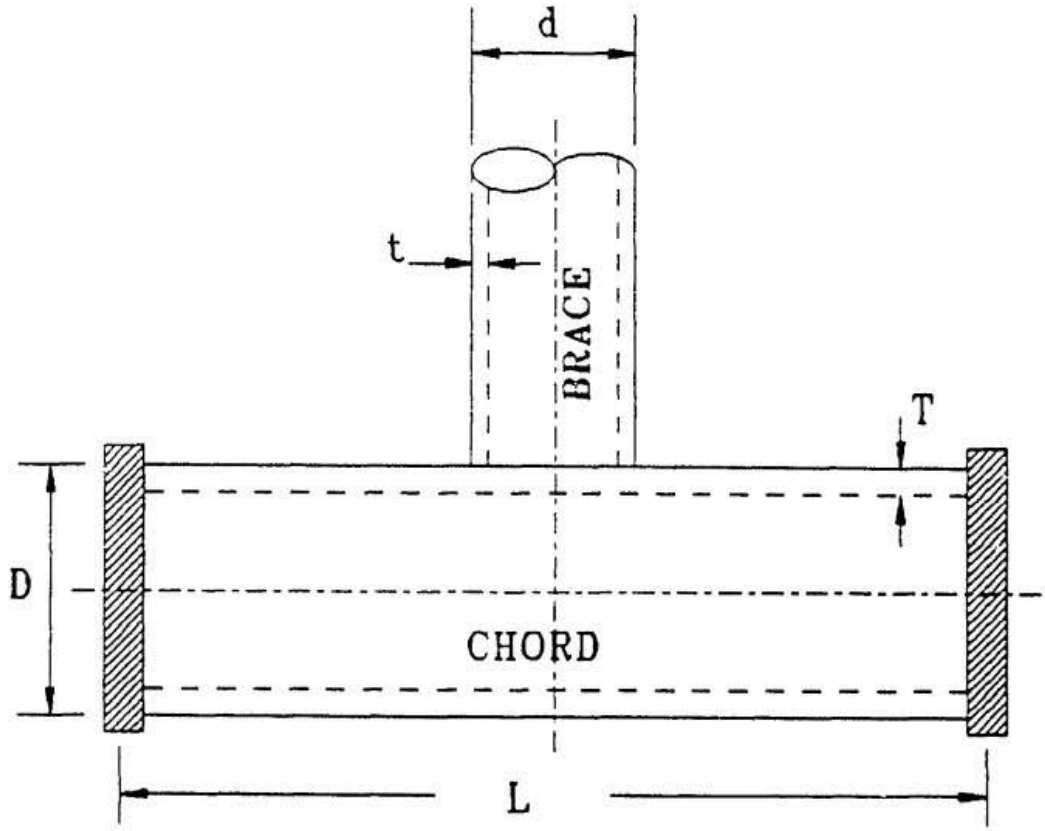

Distance between end restraints or point of contrflexure

Geometric ratios: $\alpha = \frac{2L}{D}$; $\beta = \frac{d}{D}$; $\gamma = \frac{D}{2T}$; $\tau = \frac{t}{T}$; $\zeta = \frac{g}{D}$;

Figure 4.1: Geometric notations for tubular T-joints.

Table 4.1: Joint parameters

Type of Joint	D (mm)	T (mm)	$\beta = \frac{d}{D}$	$\tau = \frac{t}{T}$	$\gamma = \frac{D}{2T}$	$\alpha = \frac{2L}{D}$
Tee	914	19 - 32	0.2 - 0.8	0.2 - 1.0	14 - 32	6.05 - 13.0

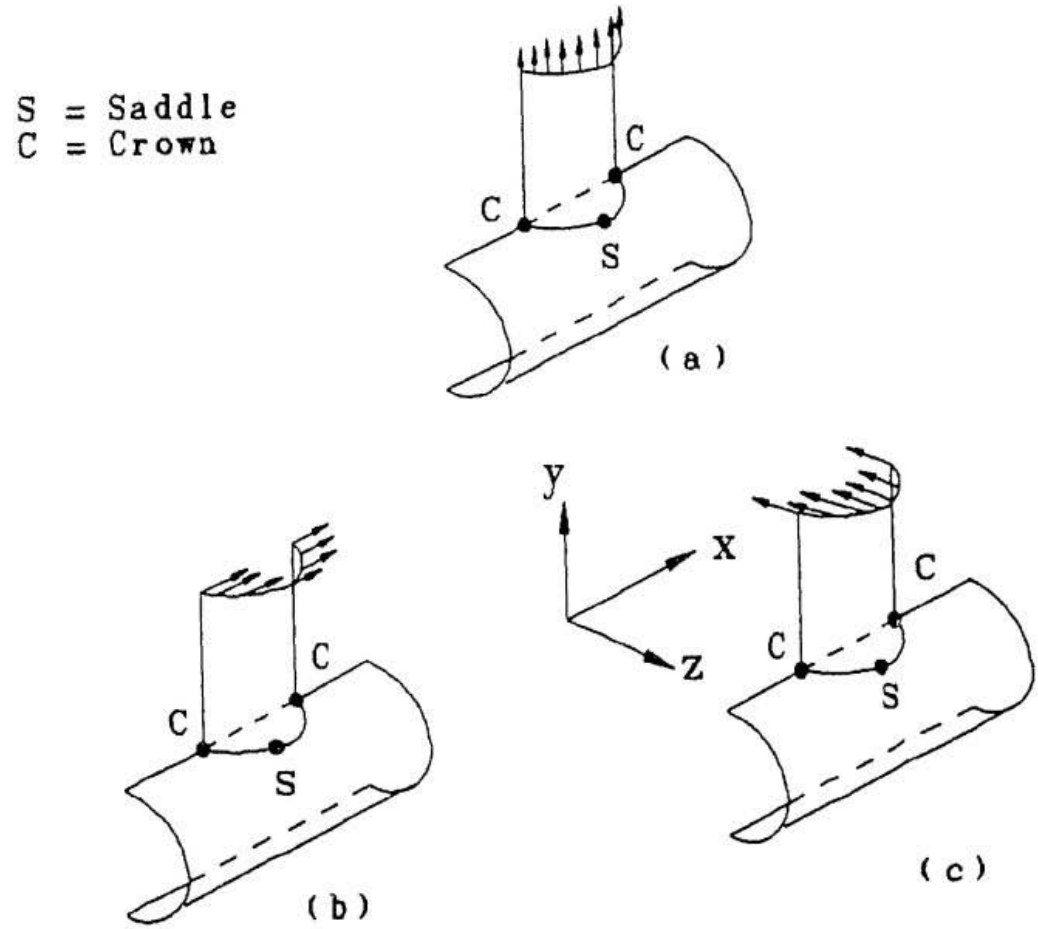

Figure 4.2: Modes of loading used for the finite element analysis: (a) Axial, (b) IPB and (c) OPB.

4.1.1 Stresses in Tubular Joints

Before any attempt can be made to determine the stress levels, it is important to have an understanding of the behaviour of joints and the factors which give rise to the complex nature of the stress distribution.

Stresses in tubular joints arise from three main causes classified as follows:

1. Basic structural response of the joint to the applied load on the structure is termed the nominal stress; generally this is referred to the stress level acting in the brace.

2. Deformation stresses, caused by the deformation of the tubular walls, while trying to maintain continuity at the intersection.

3. Notch stresses caused by the geometrical discontinuity due to the presence of the weld.

Nominal stresses are due to the framing action of the structure under applied external loads. Global analysis of the structure is required in order to compute these stresses. The deformation stresses are due to the deformation of the chord and brace while trying to maintain compatibility at the intersection of the brace and chord. For example Figure 4.3 shows how deformation stresses are developed in a T-joint under brace tension loading. Point 1 and 2 displace along the brace axis by similar amounts due to constant stiffness of the brace. The chord deforms in order to maintain compatibility, thereby introducing bending and membrane stresses in the chord wall. Since chord stiffness at the saddle (point 2) is greater than that at

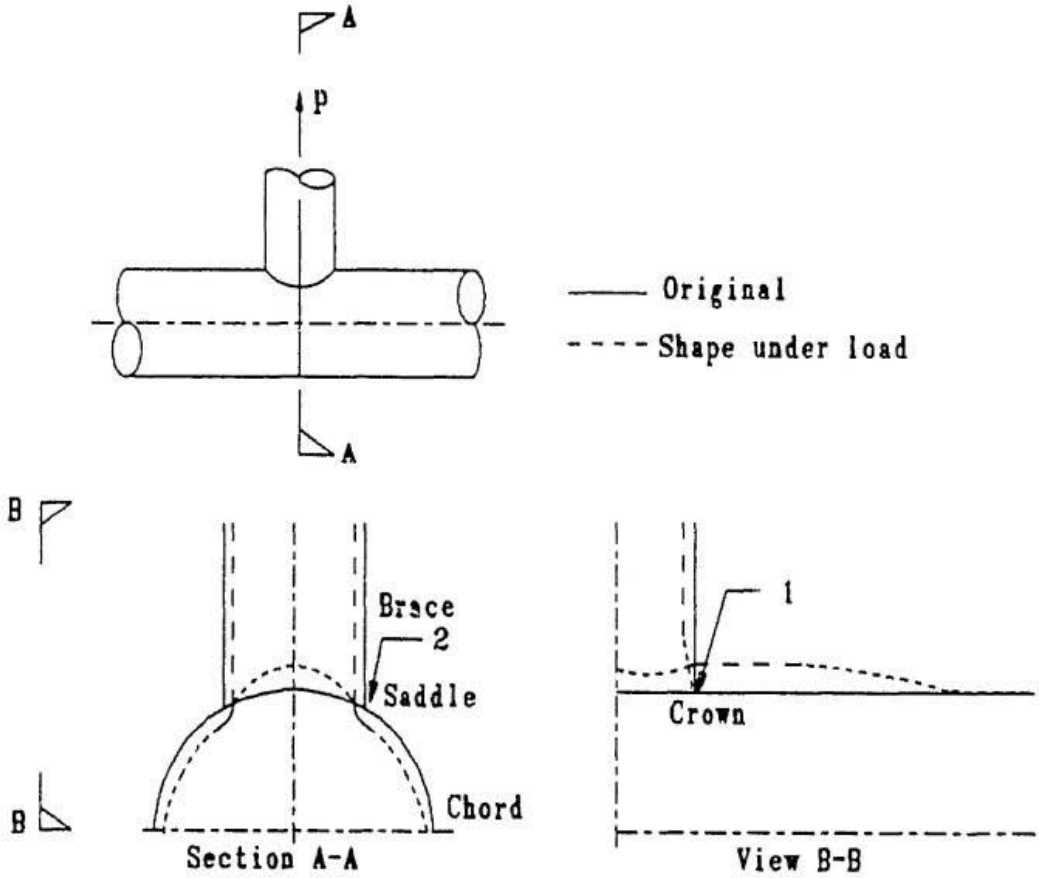

Figure 4.3: Deformation stresses in a T joint under brace tension load.

the crown (point 1), a larger force will be required at the saddle than at the crown. This results in maldistribution of the nominal stress near the intersection. Figure 4.4 illustrates this maldistribution. The bending and membrane stresses in conjunction with the maldistribution of the stress give rise to the deformation stresses. The notch stresses are the result of geometrical discontinuity of the tubular walls at the weld toes where an abrupt change of sections occur.

Mesh Generation

In order to carry out finite element stress analysis for the tubular joints investigated in this study, some form of automatic mesh generation is virtually essential. Any program that is developed for the purpose of tubular joint mesh generation should be cable of producing relatively fine elements in the vicinity of the brace/chord intersection where the stress gradients are large. Conversely, away from the intersection, for example, near the ends of the chord and the brace, where the stresses are more evenly distributed, the program should generate coarse elements in order to avoid unnecessary computational effort. In addition, for the best numerical conditioning of the stiffness equations and to ensure maximum numerical accuracy, the element aspect ratios, that is, the ratios between the lengths of element sides should be as close to unity as possible, and element sides should not be excessively distorted. Transition from the finer element region to the coarse element region should be gradual.

Generation of mesh for this study, to be consistent with the objectives mentioned above, necessitated dividing the chord and the brace into basic regions as shown in Figure 4.5.

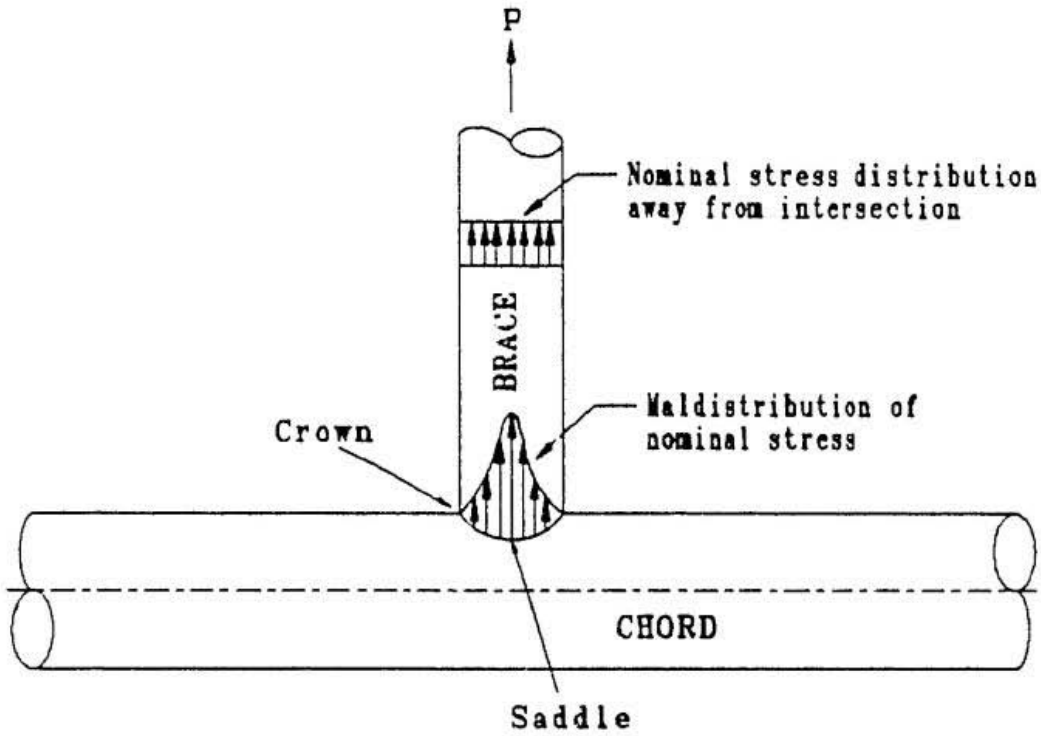

Figure 4.4: Maldistribution of nominal stress at the intersection.

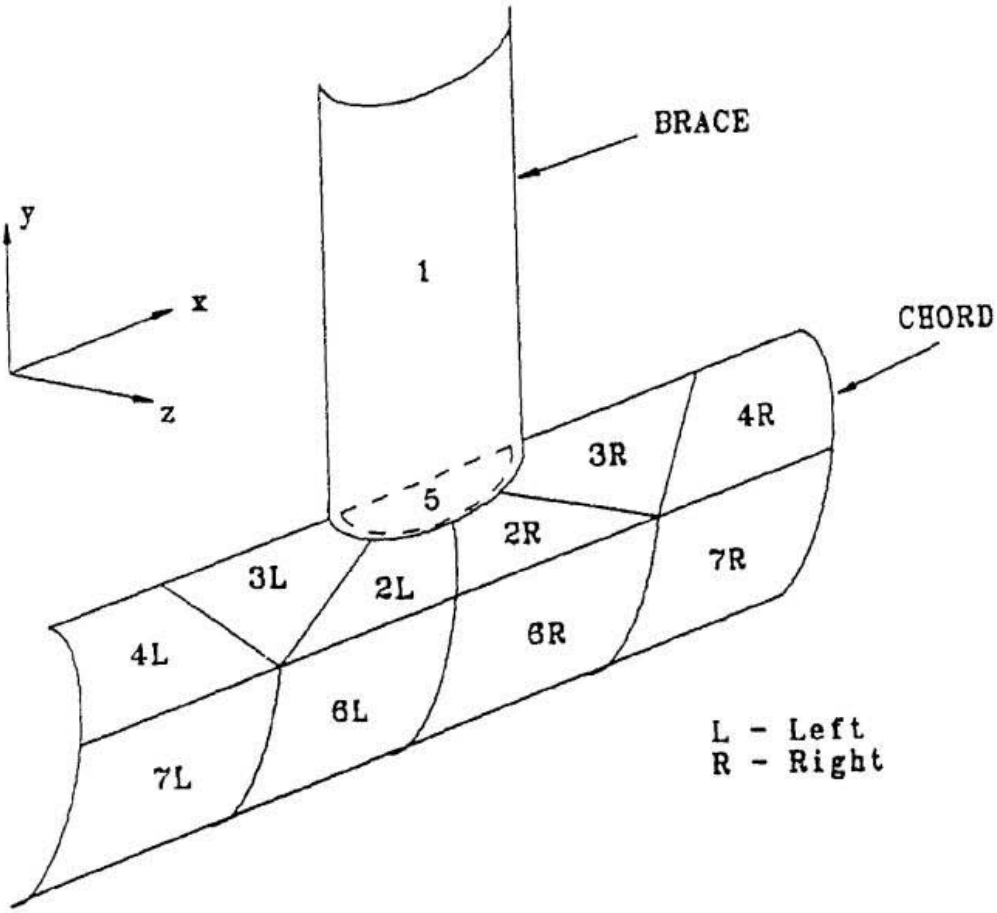

Figure 4.5: Subdivision of the tubular joint into a number of regions suitable for mesh generation

A Fortran subroutine that could be incorporated into any finite element mesh generation package was developed for the mesh generation of the tubular joints investigated in this study. Some of the powerful feature of this subroutine are; (*i*) ability to generate element nodal coordinates reliably for a wide range of geometrical parameters α, β, τ and θ with minimum effort, (*ii*) ability to make adjacent elements have a certain aspect ratio, such that the elements in the vicinity of the crack are finer and increase gradually away from the intersection. This ensures a smooth transition between the maldistribution stress area and the evenly distributed stress area and (*iii*) ability to generate the element nodal coordinates on a planar surface and then, using a mapping function, to map all the nodes onto the curved surface of the tube. This last feature was viewed in this study as one of the most powerful feature of this program, from the fracture mechanics stress intensity factor model (Line spring model) point of view. It was used extensively in the mesh generation for the tubular joint crack analysis.

It is important to note here that each of the subregions, shown Figure 4.5, represents a different level of mesh refinement in the program; the mesh could be refined anytime in the generation process whenever a generated mesh produced an undesirable shape. The subroutine has been written efficiently to have more flexibility and minimum user input. The sequence of steps executed in the generation of the mesh is summarized as follows. The intersection coordinates of the brace and chord junction (computed separately by another subroutine) were first used to generate region 1 of the brace with adjacent element aspect ratio (BIAS) of 0.75 and with flag direction from the intersection to the brace end. In a similar manner, regions 2L/2R, 3L/3R and 4L/4R were generated with the intersection coordinates. The

only difference here is that the nodes were first generated along the chord circumferential direction and then transferred to their appropriate locations on the tube surface. Next, coordinates of the plug region 5 were generated. Because of reasons of geometrical compatibility in this region (plug) the generation was performed in such a manner that from the intersection to a substantial distance away from it, quadrilateral elements were used and the remaining part of the plug was filled with triangular elements. Finally the remaining chord regions 6L/6R and 7L/7R were generated. A typical mesh, used for this study is shown Figure 4.6.

4.1.2 Boundary Conditions

Due to symmetry in axial loading and in-plane bending loading, only half of the joint geometry was modelled. Although no symmetry exists for the out-of-plane bending situation, it was however found that satisfactory results could be obtained with the same meshes used for the other two loads cases, if appropriate boundary condition can be found. All the degrees of freedom (u_x, u_y, u_z, ϕ_x, ϕ_y, ϕ_z) were restrained at the chord ends, where u_x, u_y, and u_z correspond to the displacements in the x, y and z directions, respectively, and ϕ_x, ϕ_y and ϕ_z the rotations about x, y and z. During preliminary modelling of the problem, separate analysis was performed for the axial and in-plane bending load cases using different joint meshes (quarter- and half-joint meshes, respectively). This led to large storage and computational requirements. Modeling the two load cases by a quarter-joint would have required two separate analyses with differing boundary conditions. It was later realized that modelling the two load cases with a half-joint mesh, using the same boundary conditions but as two separate load cases, resulted in computational and

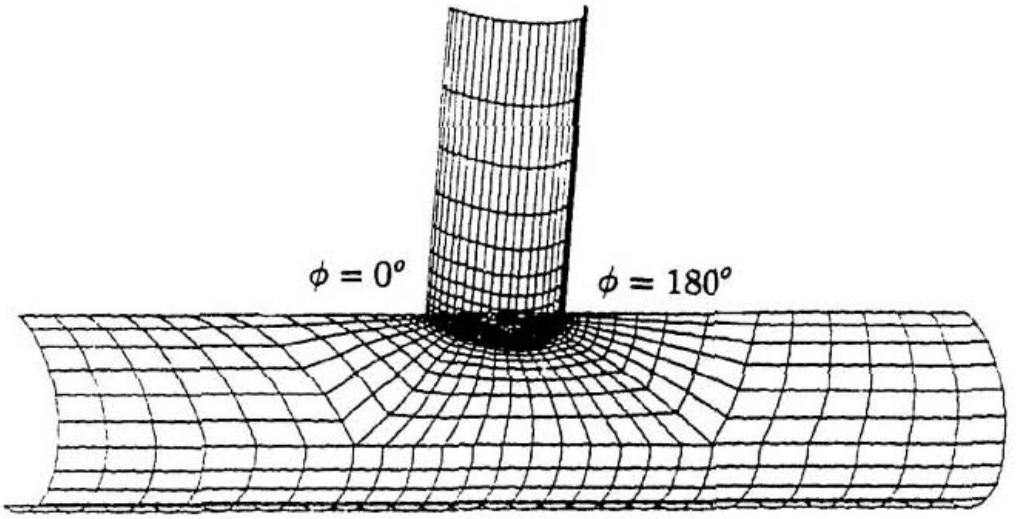

(a)

Figure 4.6: Typical computer mesh generation for unstiffened tubular T-joints: (a) half joints, (b) detail showing the brace, chord and plug

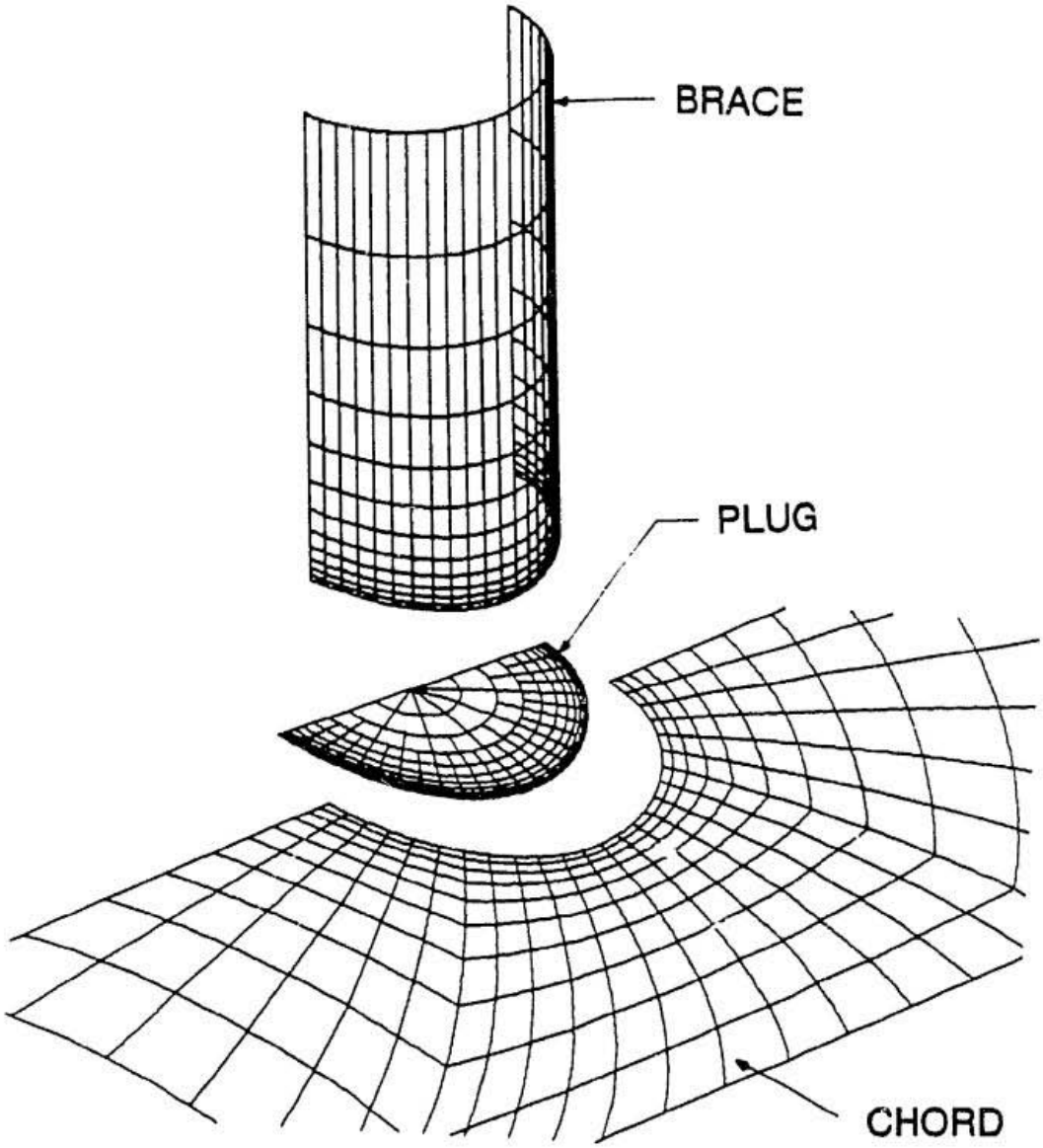

(b)

Figure 4.6 (continue)

storage economy. Hence for these two modes of loading, the joints were analyzed as two load cases of the same finite-element run. Figure 4.7 illustrates the quarter- and half- joint cases with alphabetic notations for the locations where boundary conditions are applied. Details of the boundary conditions, as applied in this study, are given in Table 4.2.

For the axial and in-plane bending load cases the xy plane constitutes a plane of symmetry (with the half-joint model), on which the displacements u_z and rotations ϕ_x and and ϕ_y must be restrained to correctly model the behaviour of the full joint. Using the half-joint mesh, the selection of the boundary conditions was not straight forward for the the out-of-plane bending case, because the symmetry about the xy plane through the origin no longer exists. Instead the problem becomes somehow close to skew symmetry and in order to simulate the full joint behaviour by the half joint mesh, the displacement components u_x and u_y and rotational component ϕ_z of all the nodes lying on the xy plane were restrained. The feasibility of this approach was demonstrated in this study by conducting analyses using the half- and full-joint meshes and comparison made between these two analyses. The stresses obtained and expressed in terms of the stress concentration factors, as a function of the angle around the intersection are given in Table 4.3 and Figures 4.8(a) and (b). The maximum difference between the half- and full-joint meshes, respectively were 2.2% (for both brace and chord) at the saddle, 4.5% (for chord) and 3.2% (for brace) at 45° and around 5.3% (for brace and chord) at 10° from the crown. Hence the use of the same half-joint modelling for out-of-plane bending was considered to be sufficient.

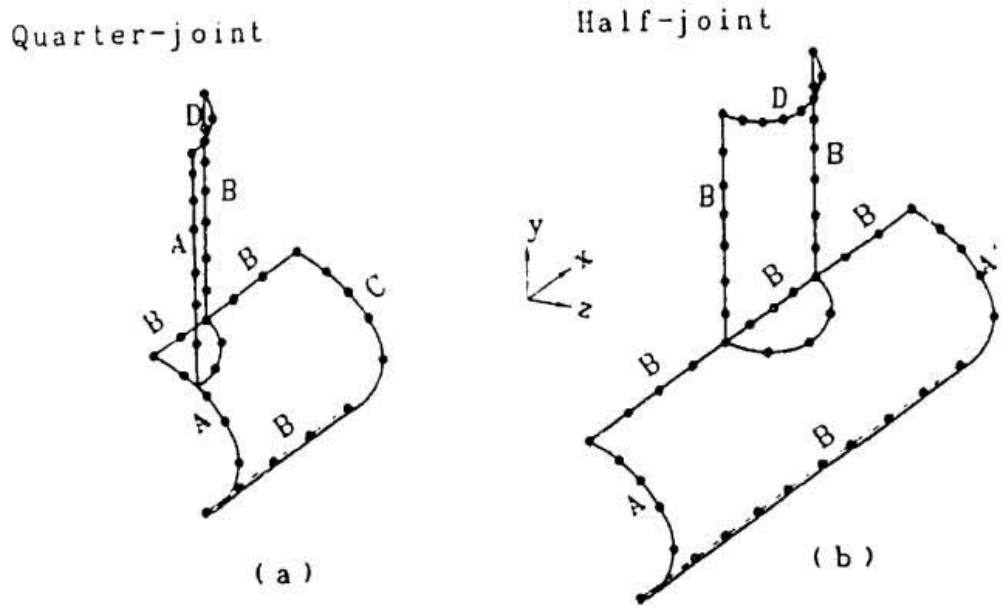

Figure 4.7: Structural configuration considered for analysis: (a) quarter-joint, (b) half-joint (see Table 4.2 for boundary conditions).

Table 4.2: Details of boundary conditions.†

Joint and loading type	Location of nodes	Restrained degrees of freedom
Quarter-Joint Axial Figure 4.7(a)	A	$u_x = \phi_y = \phi_z = 0$
	B	$u_z = \phi_x = \phi_y = 0$
	C	$u_x = u_y = u_z = \phi_x = \phi_y = \phi_z = 0$
	D	$\phi_x = \phi_y = \phi_z = 0$
Half-Joint Axial/IPB Figure 4.7(b)	A	$u_x = \phi_y = \phi_z = 0$* OR $u_x = u_y = u_z = \phi_x = \phi_y = \phi_z = 0$ ‡
	A′	$u_y = u_z = 0$ * OR $u_x = u_y = u_z = \phi_x = \phi_y = \phi_z = 0$ ‡
	B	$u_z = \phi_x = \phi_y = 0$
Half-Joint OPB Figure 4.7(b)	A	$u_x = \phi_y = \phi_z = 0$ * OR $u_x = u_y = u_z = \phi_x = \phi_y = \phi_z = 0$ ‡
	A′	$u_y = u_z = 0$ * OR $u_x = u_y = u_z = \phi_x = \phi_y = \phi_z = 0$ ‡
	B	$u_x = u_y = \phi_z = 0$

† see Figure 4.7

* A and A′ combination for simply supported chord end condition.

‡ A and A′ combination for fixed chord end condition.

Table 4.3: Comparison of SCF for half- and full-mesh for two T-joints under out-of-plane bending load

Joint Geometry $\tau = 1.0$; $\beta = 0.5$; $\alpha = 7.02$; $\gamma = 24$				
	Chord SCF		Brace SCF	
Angle around intersection ϕ (Deg.)	Half-Joint	Full-Joint	Half-Joint	Full Joint
0.00	-0.7135	-1.0452	-0.3741	-0.3122
11.25	1.1019	1.1610	0.9075	0.9531
22.50	1.7230	1.9118	1.6977	1.8192
33.75	3.4438	3.7732	3.0615	3.2422
45.00	6.7107	7.0580	5.1638	5.3380
56.25	11.1174	11.3389	7.9135	8.3380
67.50	15.9966	15.9969	10.9737	10.9486
78.75	20.0163	19.7596	13.5300	13.3340
90.00	21.5671	21.1268	14.5191	14.2076

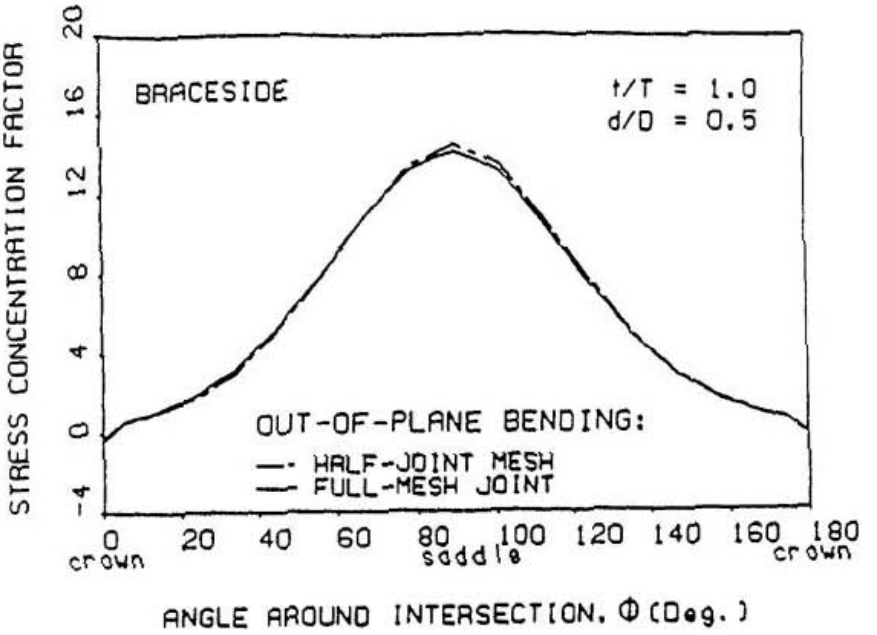

(a)

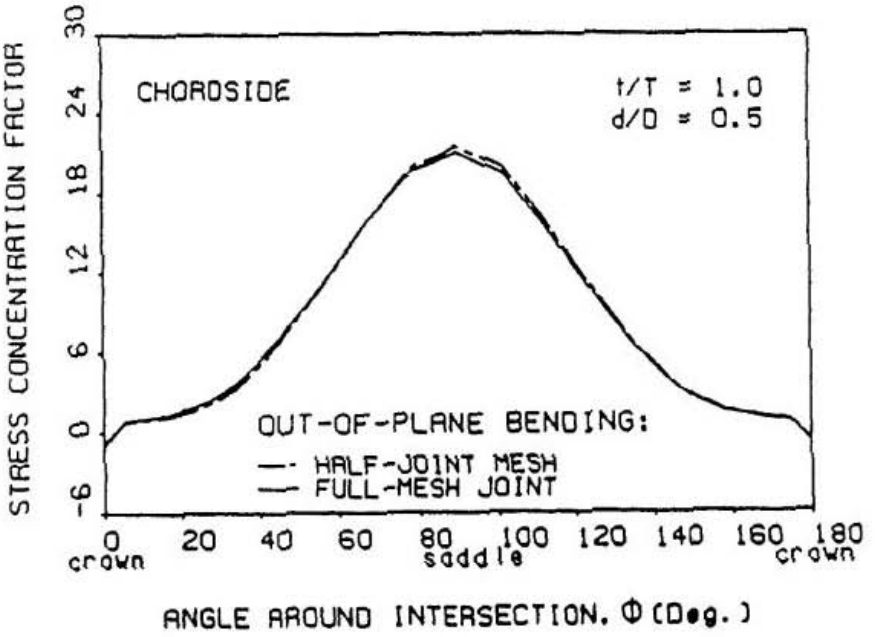

(b)

Figure 4.8: SCF comparison between half- and full-joint meshes: (a) brace, (b) chord. (OPB) ($\alpha = 7.02$, $\gamma = 24$)

4.1.3 Processing of Results

The stress analyses performed in this study was conducted for tubular T-joints with various joint parameters (α, β, τ, γ). The range of these parameters are already given in Table 4.1. At this stage of the study, a post processing program was developed. This program reads the stress output file from the analysis and automatically computes the maximum and the minimum principal stresses as well as the stress concentration factors around the intersection. The principal stresses at the inner and outer tube surfaces were used to determine the relative amounts of through-thickness bending and membrane stress. This choice was based on the fact that stress concentration factors (SCFs) are usually defined in terms of the principal stresses and thus the two sets of results should be compatible. Furthermore, from the cracking point of view, there is a considerable evidence that cracks, at their initial stage of development, are subjected to high shear stresses: hence at the initial stage, the initiated cracks open at an angle other than 90° to the tensile load, but they soon tend to grow perpendicular to the direction of the maximum tension. According to the reasons given above, the numerically greatest principal stresses on the outer tube wall was always chosen, even where this did not lie perpendicular to the intersection. The results of typical deformed shapes of tubular joints under these loads are shown in Figures 4.9 through 4.11.

In conducting analyses for the through-thickness stress distribution along the tubular joint intersection, a simple interpolation between the stresses on the inner and outer surfaces of the tubular joint chord wall was adopted. The simple linear interpolation was represented in terms of the ratio of the bending stress to the total

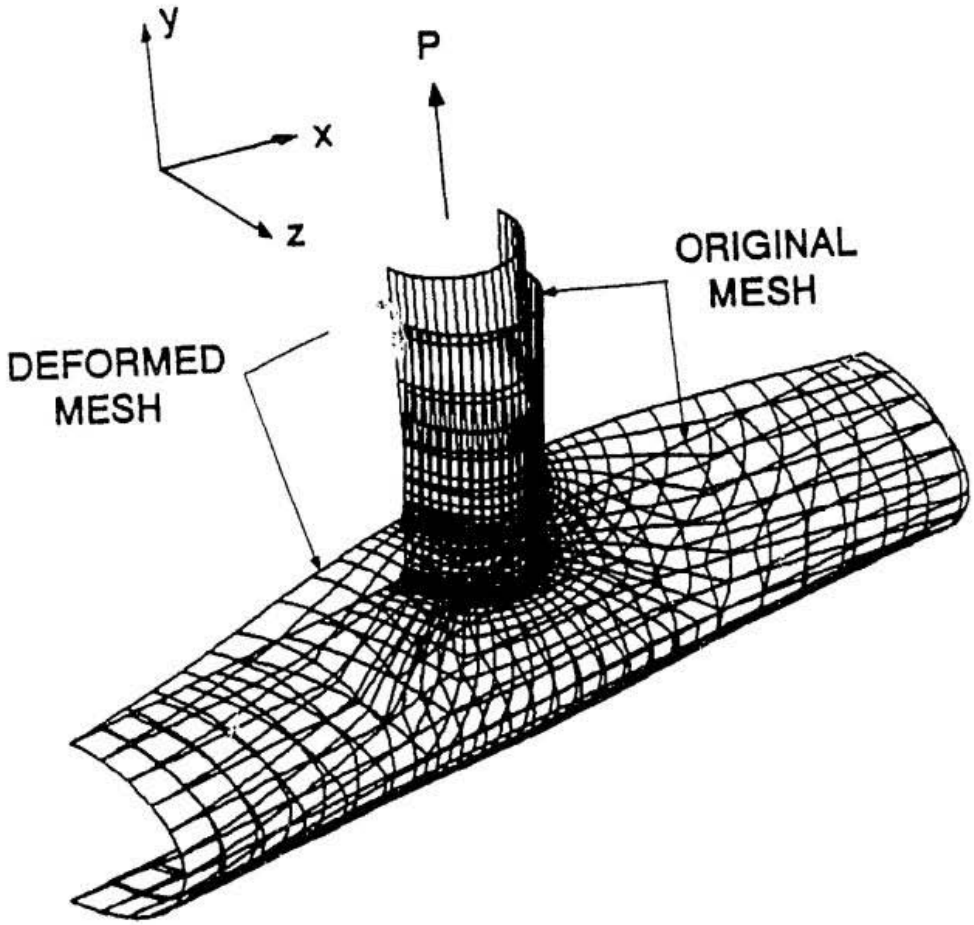

AXIAL TENSION

Figure 4.9: Original and deformed mesh for axial loading.

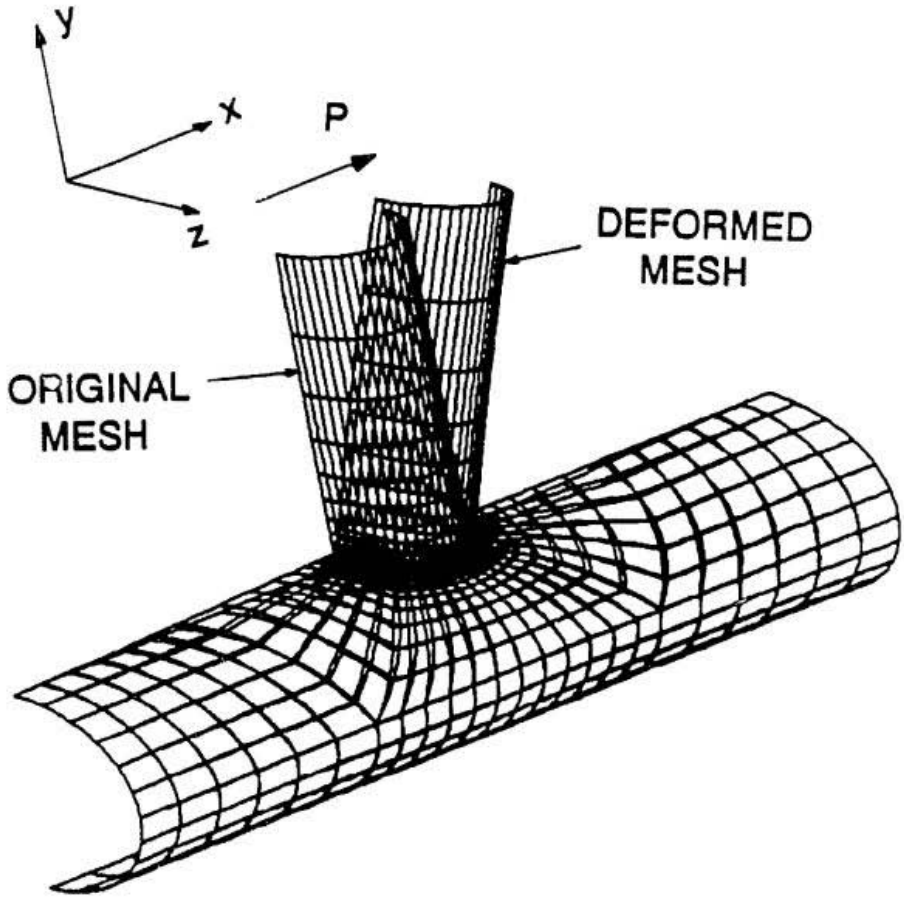

IN-PLANE BENDING

Figure 4.10: Original and deformed mesh for IPB loading.

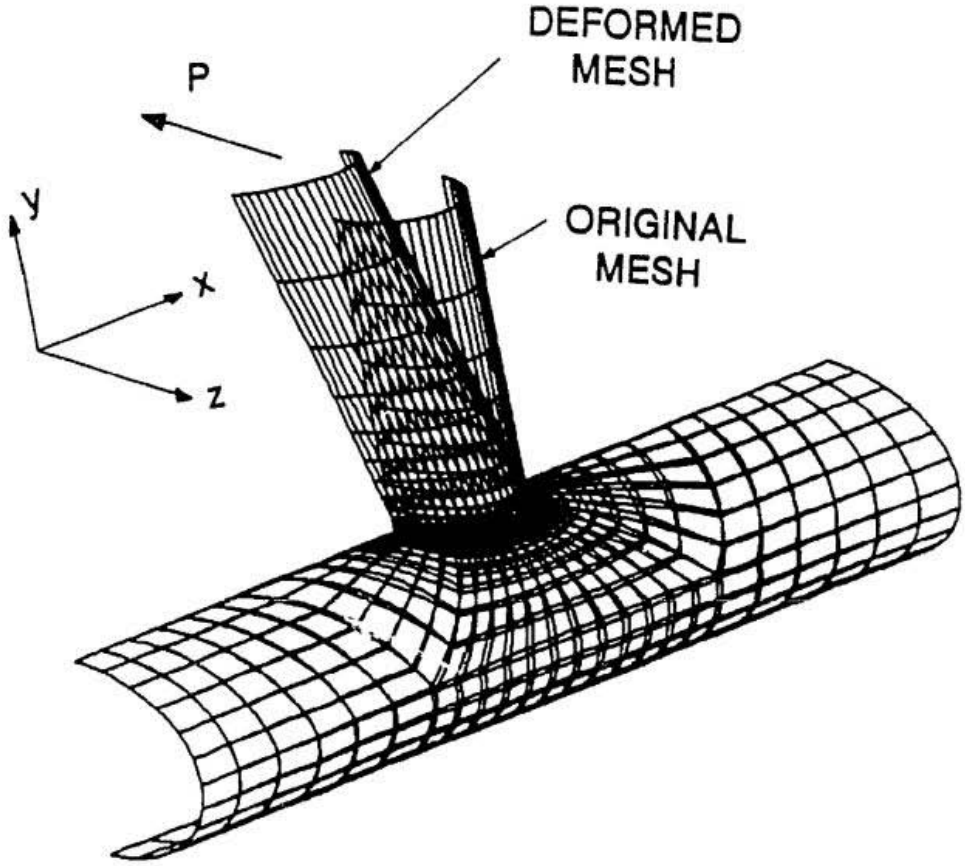

OUT-OF-PLANE BENDING

Figure 4.11: Original and deformed mesh for OPB loading.

stress as follows

$$\frac{\sigma_B}{\sigma_T} = \frac{\sigma_B}{(\sigma_B + \sigma_M)} \tag{4.2}$$

where σ_B and σ_M are the bending and membrane components of the total stress σ_T, respectively. The total stress corresponds to the total stress calculated on the outer surface of the tube. The membrane stress corresponds to the difference between the total stress and the bending stress on the outer surface. From the linear interpolation function Eqn. (4.2) it is evident that in cases where the membrane stresses are tensile the ratio σ_B/σ_T is less than one and greater than zero. For the other case where the membrane component is compressive the ratio σ_B/σ_T is greater than one. This equation is normally well behaved except where $\sigma_M = -\sigma_B$, when it becomes infinite. However, throughout this study, the latter result was not encountered.

4.1.4 Convergence Test

A convergence study was performed to check that the meshes used for this study were sufficiently fine to predict the stresses around the intersection and through the wall thickness with reasonable accuracy. For this part of the study the T-joint having 24 elements around half of the (weld toe) intersection (180°) was chosen. A coarse mesh of 16 elements around the intersection (180°) and a considerably finer mesh of 48 elements around the intersection (180°) were then analysed. The results of these three analyses are compared in Table 4.4. It can be seen that the SCF and the σ_B/σ_T values obtained from the meshes agree to within 0.25 - 0.98% in the

Table 4.4: Comparison between results from coarse and fine meshes to show extent of convergence ($\alpha = 7.002$, $\beta = 0.5$, $\tau = 1.0$)

	No. of elements around intersection	Chord				Brace			
		Crown		Saddle		Crown		Saddle	
		SCF	$\frac{\sigma_B}{\sigma_T}$	SCF	$\frac{\sigma_B}{\sigma_T}$	SCF	$\frac{\sigma_B}{\sigma_T}$	SCF	$\frac{\sigma_B}{\sigma_T}$
Axial loading	16	6.14	0.58	25.00	0.89	2.53	0.87	16.35	0.85
	24	6.22	0.58	24.48	0.88	2.55	0.86	16.10	0.85
	48	5.95	0.60	24.42	0.89	2.84	0.84	14.86	0.85
In-plane bending	16	6.46	0.78	0.	-	3.62	0.89	0.	
	24	6.56	0.79	0.	-	4.02	0.88	0.	-
	48	6.94	0.81	0.	-	4.31	0.82	0.	-
Out-of-plane bending	16	-0.71	-	21.57	0.90	-0.37	-	14.52	0.86
	24	-0.81	-	21.44	0.90	-0.33	-	14.52	0.87
	48	-0.73	-	21.23	0.90	-0.23	-	14.64	0.87

chord saddle, 4.3 - 13.56 % in the chord crown, 10.2 - 12.2% in the brace crown and 0.8 - 8.3% in the brace saddle between the 24 and 48 elements cases. Since chord stresses dominate the cracking behaviour, these differences were considered to be acceptable.

4.1.5 Results and Discussion

Since the discretization of the joint was done carefully, at the intersection and its vicinity, keeping the elements small and properly shaped, good results were anticipated. There is a gradual and smooth transition from the smaller and regular elements, concentrated around the intersection to those elements away from it. In order to reduce the complexities of the modelling procedure and also to save the computational time, different multi-point constraints were used. These constraints which are enforced boundary conditions in some sense reduce the number of unwanted, smaller sized, second order elements in the mesh zones that are not affected by the intersection behaviour.

Table 4.5 shows the comparison of the stress concentration factors, obtained from the present study, with the experimental values obtained at the University of Waterloo (UW), Memorial University (MUN) and the National Engineering Laboratory, England (NEL). While there is an excellent agreement for the axial loading between the experiments and analyses, the agreement is not so good for the bending situations. While there is a very good agreement between the Memorial and NEL results, the Waterloo results seem to underestimate the SCF values. NEL results for in-plane bending is 12.3% lower than the present analytical results while the Waterloo University results are lower by 35.4%. The probable reason for this may

Table 4.5: Comparison of SCFs obtained at Waterloo/Memorial Universities and National Engineering Laboratory‡ with the present study: chord side ($\beta = 0.5$, $\tau = 1.0$)

Mode of loading	Unstiffened T-joint						
	UW (Exp.)		MUN (Exp.)		NEL (Expt)	PS (Theo)	
	side 1	side 2	side 1	side 2		side 1	side 2
IPB CROWN	4.3	4.2	-	-		6.5	6.5
	Av.(4.2)		-		Av.(5.7)	Av.(6.5)	
OPB SADDLE	17.2	17.0	-	-		21.2	21.2
	Av.(17.1)		-		Av.(22.0)	Av.(21.2)	
AXIAL SADDLE	24.0	22.0	24.8	23.3		24.8	24.8
	Av.(23.0)		24.0		Av.(23.4)	Av.(24.8)	

‡ Pates et al., 1988

be due to the weld thickness effect at the crown. The ratios of the membrane and bending stresses to the total stress, and the ratio of the strain concentration factor to the stress concentration factor, obtained in this study, are compared with those of the Canadian Cooperative Tubular Fatigue Studies Program, carried out at Memorial and Waterloo Universities (1989), in Table 4.6. The agreement seems to be very good, except in the case of the membrane to total stress of in-plane bending tests where the difference is around 36.8% (Waterloo University results). Once again the difference could be attributed to the effect of weld thickness at the crown. The weld thickness could not be modelled by the plate elements used in this study due to the varying thickness of the weld around the intersection.

Figure 4.12 through 4.17 show the results obtained when additional analyses were performed to investigate the effect of chord end support , under the three loading conditions studied, on the stress distribution around the intersection on both chord and brace side. While the effect is obvious for the axial load case at the saddle point location (a difference of 10% was observed for chord stresses), very little difference was observed at the crown location (approx. 2%). The in-plane loading case exhibits a smaller influence (8%) while very little (approx. 2%) difference was observed for the out-of-plane loading case. Hence the length considered in the study was found to be insufficient for the case of the axial and in-plane loads.

Figures 4.18 through 4.20 compare the variation of SCF along the joint intersection for the three loading cases, viz., axial, and in-plane/out-of-plane (bending) loads. While there is a drastic decrease in the SCF values around the saddle region for the out-of-plane bending, the SCF changes for the in-plane bending are less prominent;

Table 4.6: Comparison of results obtained at Waterloo University and Memorial University Laboratories* with the results of the present study

mode of loading	Ratio of SCF/SNCF						Ratio of bending stress to total stress $\frac{\sigma_b}{\sigma_b + \sigma_m}$						Ratio of membrane stress to total stress $\frac{\sigma_m}{\sigma_b + \sigma_m}$					
	UW (Exp.)		MUN (Exp.)		PS (Fem)		UW (Exp.)		MUN (Exp.)		PS (Fem)		UW (Exp.)		MUN (Exp.)		PS (Fem)	
	side 1	side 2	side 1	side 2	side 1	side 2	side 1	side 2	side 1	side 2	side 1	side 2	side 1	side 2	side 1	side 2	side 1	side 2
IPB CROWN	1.2	1.2	–	–	1.2	1.2	0.73	0.75	–	–	0.80	0.80	0.27	0.25	–	–	0.19	0.19
	Av (1.2)		–		Av.(1.2)		Av.(0.74)		–		Av.(0.80)		Av.(0.26)		–		Av (0.19)	
OPB SADDLE	1.2	1.2	–	–	1.2	1.2	0.92	0.91	–	–	0.90	0.90	0.08	0.09	–	–	0.09	0.09
	Av (1.2)		–		Av.(1.2)		Av.(0.91)		–		Av.(0.90)		Av.(0.09)		–		Av (0.09)	
AXIAL SADDLE	1.2	1.2	1.148	1.140	1.13	1.13	0.880	0.880	0.837	0.907	0.89	0.89	0.12	0.12	0.163	0.093	0.11	0.11
	Av (1.2)		Av (1.144)		Av.(1.13)		Av.(0.880)		Av.(0.872)		Av.(0.890)		Av.(0.12)		Av (0.128)		Av (0.11)	

*Pates et al 1988

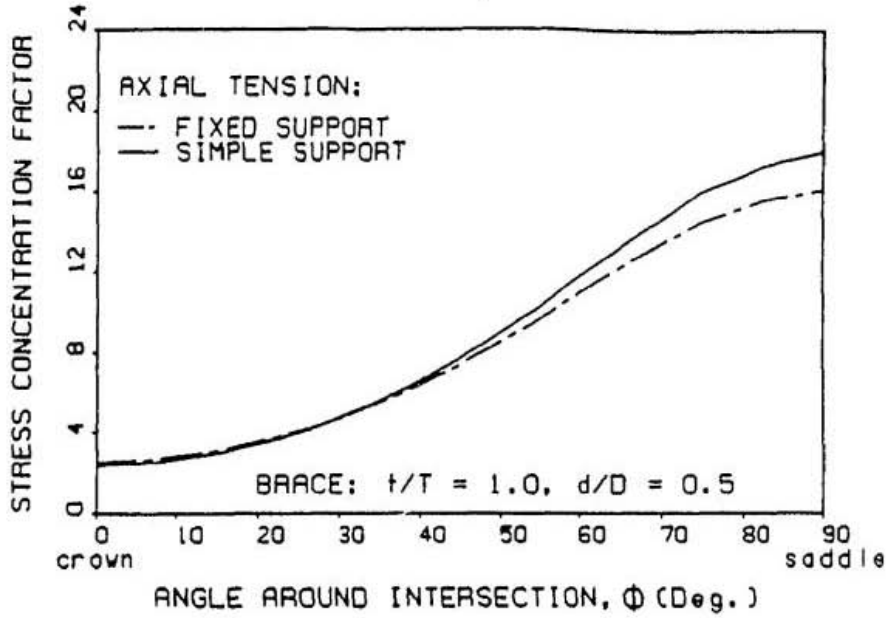

Figure 4.12: Variation of SCF in brace for fixed and simply supported end conditions (Axial) ($\alpha = 7.02$, $\gamma = 24$).

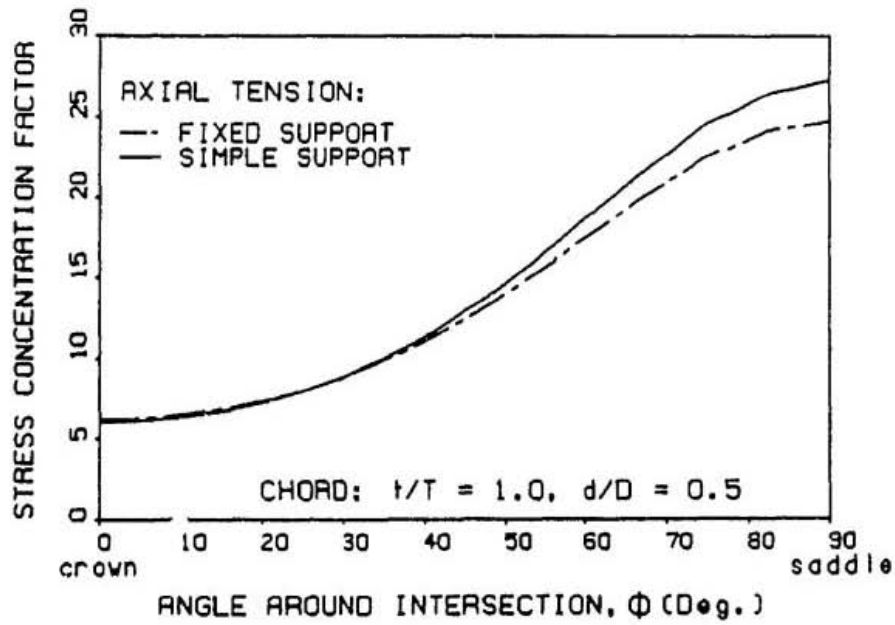

Figure 4.13: Variation of SCF in chord for fixed and simply supported end conditions (Axial) ($\alpha = 7.02$, $\gamma = 24$).

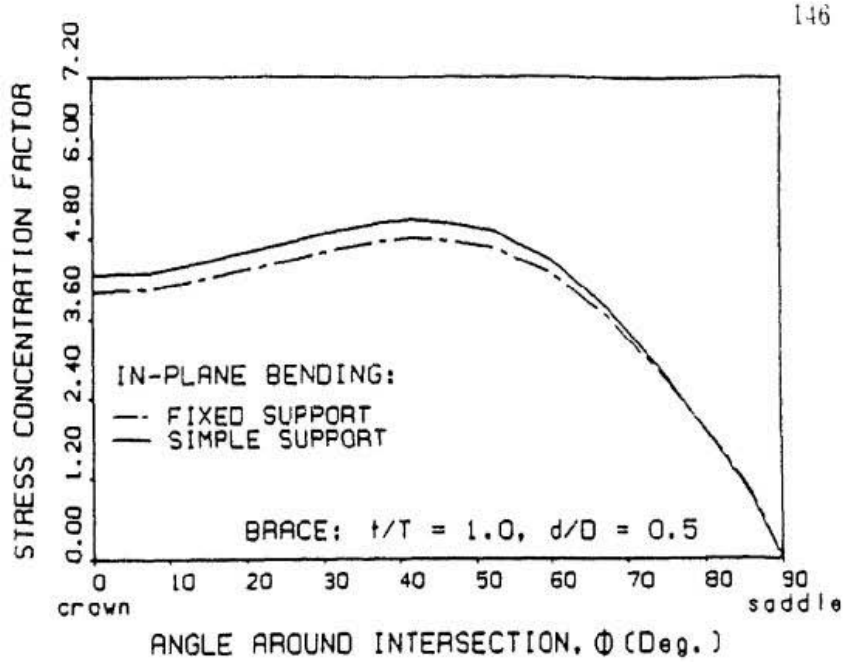

Figure 4.14: Variation of SCF in brace for fixed and simply supported end conditions (IPB) ($\alpha = 7.02$, $\gamma = 24$).

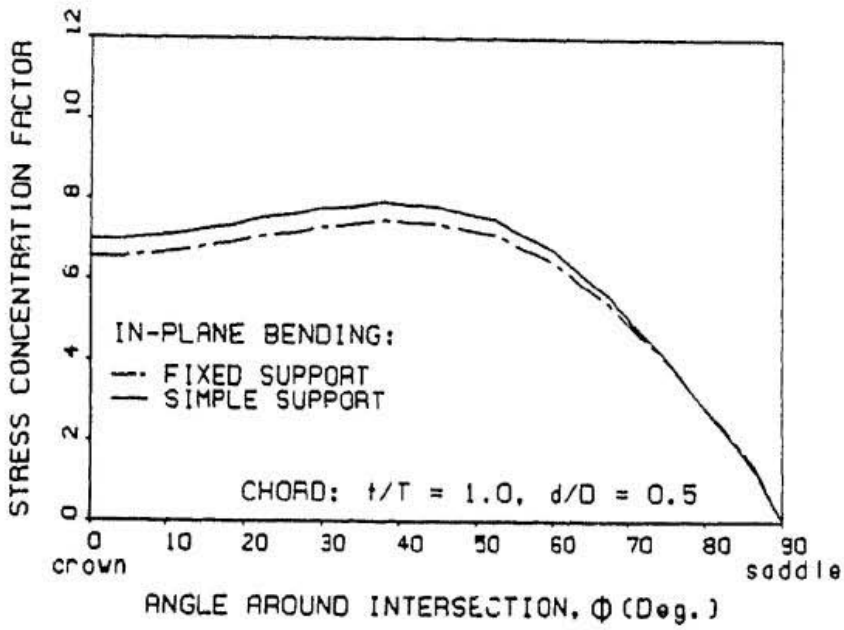

Figure 4.15: Variation of SCF in chord for fixed and simply supported end conditions (IPB) ($\alpha = 7.02$, $\gamma = 24$).

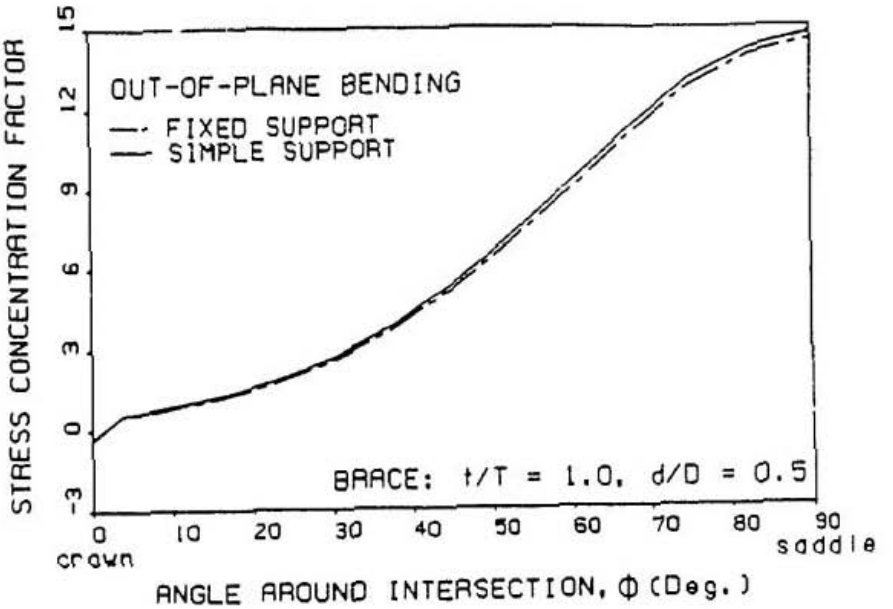

Figure 4.16: Variation of SCF in brace for fixed and simply supported end conditions (OPB) ($\alpha = 7.02$, $\gamma = 24$).

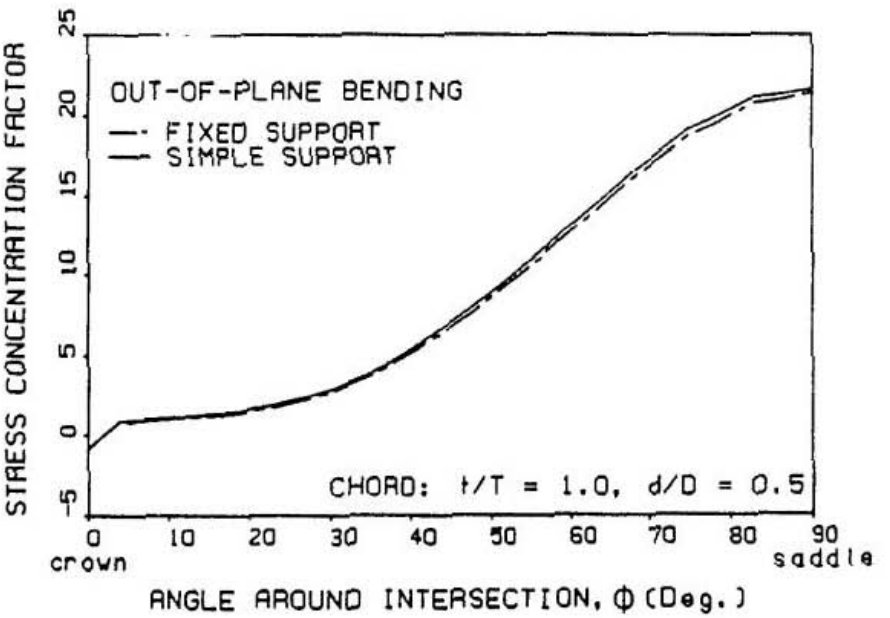

Figure 4.17: Variation of SCF in chord for fixed and simply supported end conditions (OPB) ($\alpha = 7.02$, $\gamma = 24$).

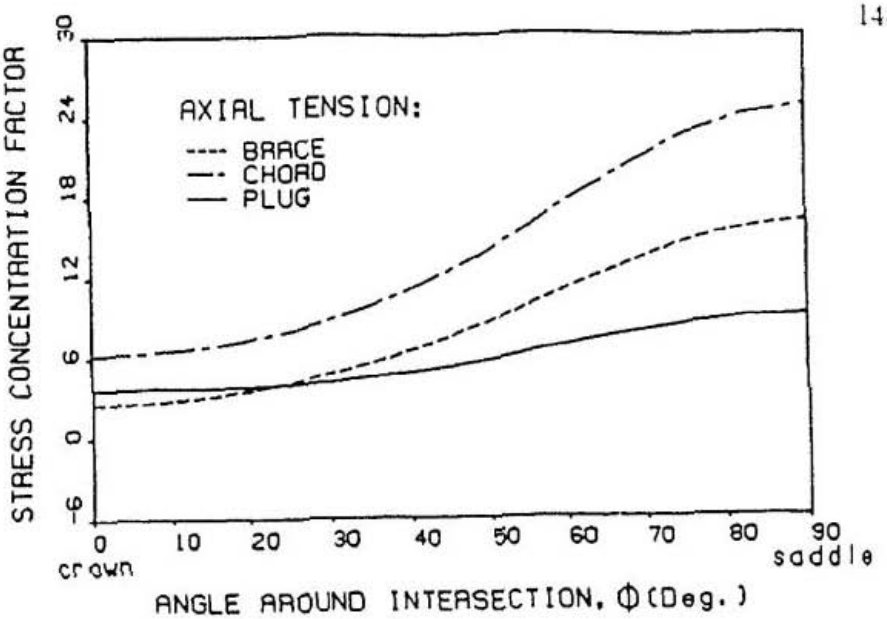

Figure 4.18: Variation of SCF along brace/chord intersection (Axial) ($\alpha = 7.02$, $\tau = 1.0$, $\beta = 0.5$, $\gamma = 24.$).

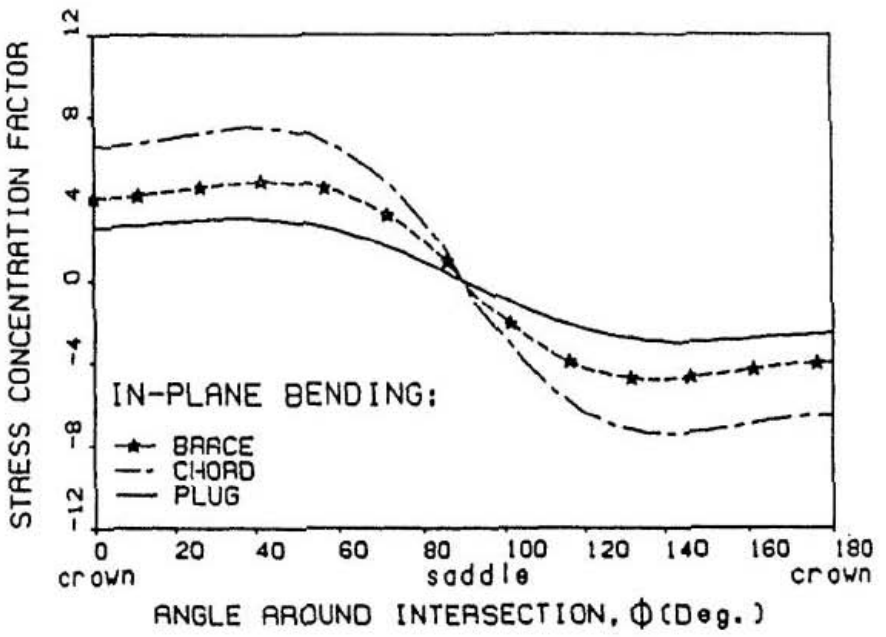

Figure 4.19: Variation of SCF along brace/chord intersection (IPB) ($\alpha = 7.02$, $\tau = 1.0$, $\beta = 0.5$, $\gamma = 24$).

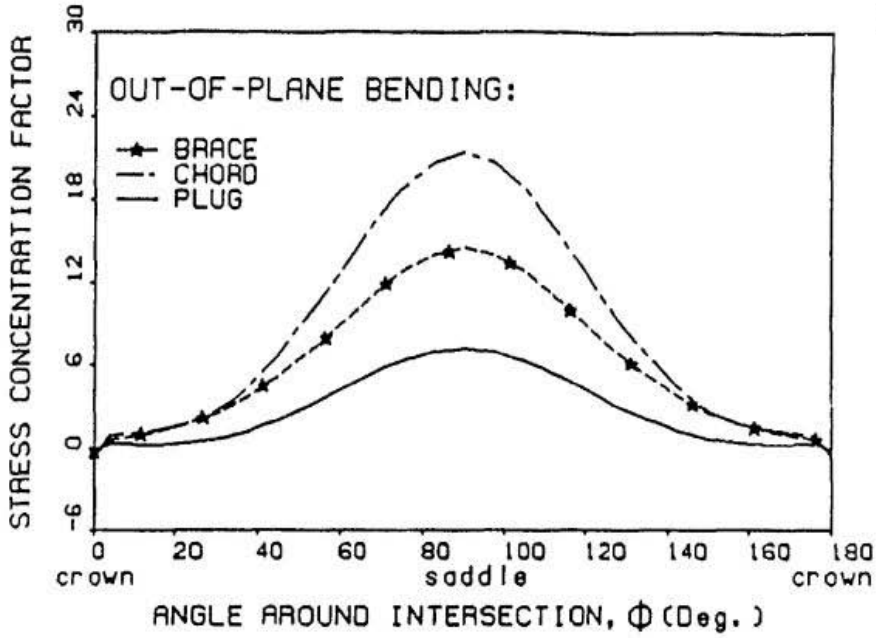

Figure 4.20: Variation of SCF along brace/chord intersection (OPB) ($\alpha = 7.02$, $\tau = 1.0$, $\beta = 0.5$, $\gamma = 24$).

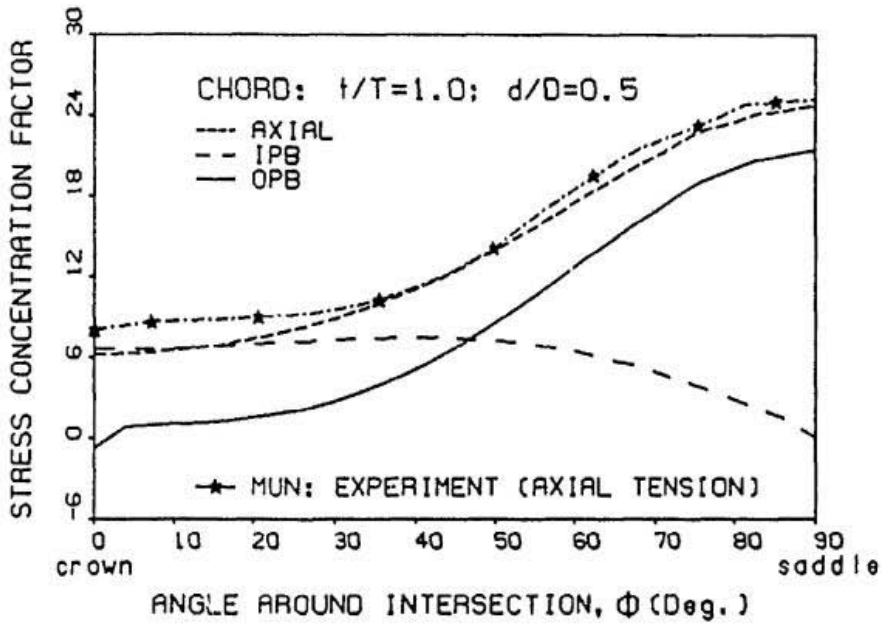

Figure 4.21: Comparison of SCF between PS and MUN results (Axial). IPB and OPB of PS included ($\alpha = 7.02$, $\tau = 1.0$, $\beta = 0.5$, $\gamma = 24$).

the axial SCF values come in between. For the in-plane bending case the maximum SCF occurs at an angular distance of 37° from the crown; the percentage difference between the chord crown SCF and the maximum value (at 37° from the crown) is 13.8%. This gives the possibility for the initiation of the fatigue cracking to occur early around this region rather than the crown. In actual experiments on in-plane bending cases, the cracking initiated first at an angular distance of 30 - 35° from the crown (Pates et al., 1989), validating the above conclusions.

Figure 4.21 shows the results obtained from the finite element model of the present study compared with the results of the experiment performed on a tubular T-joint at MUN under brace axial loading. Included also in this figure are the variations of SCF along the intersection for the other two loading cases (IPB and OPB). This shows that the finite element models used are of acceptable accuracy, with a difference between the two methods (experiment and analysis) of less than 2%, at the saddle. The figure also shows the nature of SCF drop around the hot spot for the three loading cases. It is observed that the in-plane bending load situation has a much flatter SCF distribution, around the weld toe, than the other two situations; this creates a plane strain condition over a larger region around the crown for the in-plane bending load. Probably this may be one of the primary reasons for the in-plane bending fatigue life of the joint being much lower than the other two. The out-of-plane bending has the sharpest drop in the SCF variation around the weld toe and often has the highest fatigue life for the joint. Similar results for the brace side for the three loading cases are shown in Figure 4.22; the results show that the nature of the stress distribution, between the chord and the brace, are similar.

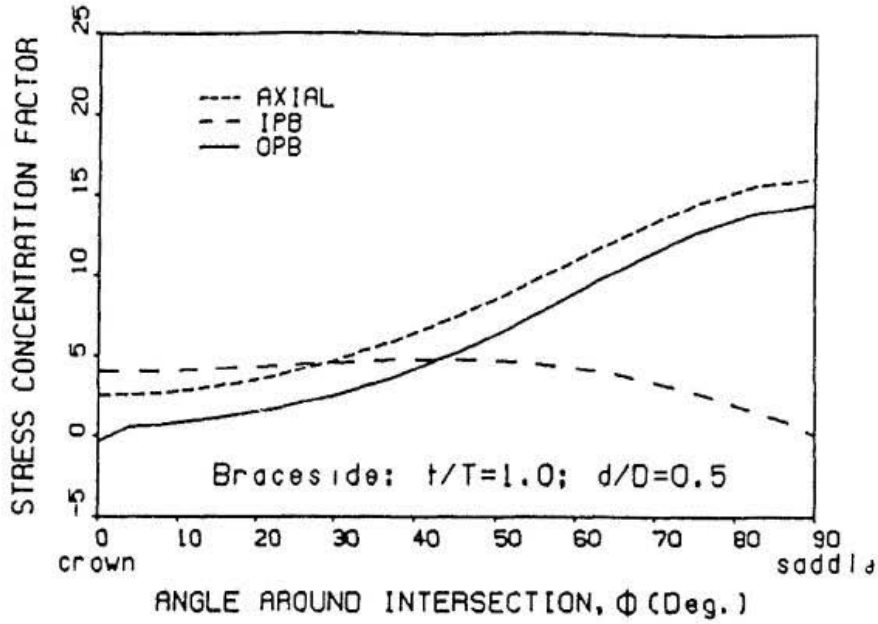

Figure 4.22: Comparison of SCF along brace/chord intersection between Axial, IPB and OPB loading in brace ($\alpha = 7.02$, $\tau = 1.0$, $\beta = 0.5$, $\gamma = 24$).

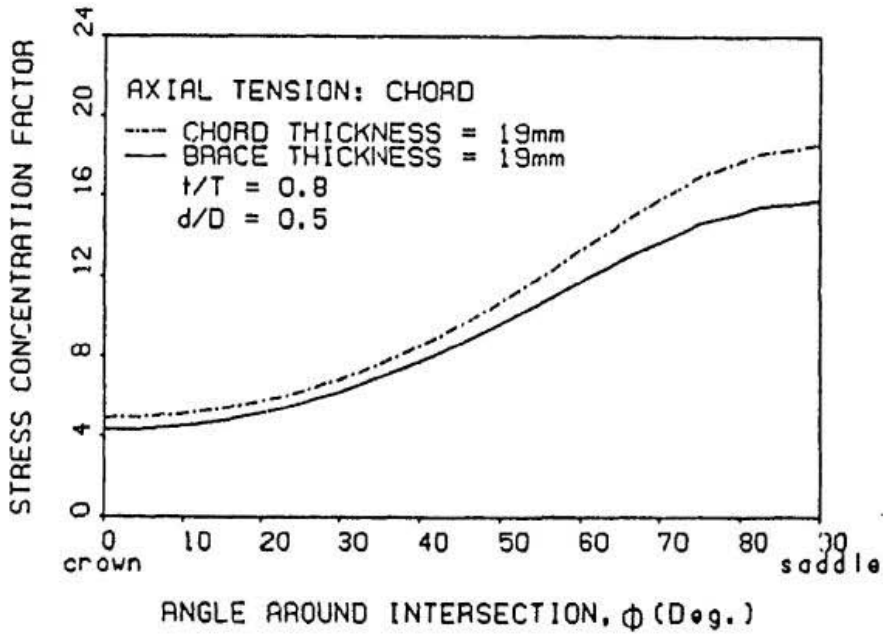

Figure 4.23: Effect of specified thickness either in chord or brace (Axial) ($\alpha = 7.02$, $\gamma = 24.$).

Figures 4.23 through 4.25 show the comparison between the SCF distribution along the intersection for the case when the brace thickness was kept constant at 19 mm, and the chord thickness was varied to achieve the various τ ratios, and the case when the the chord thickness was kept constant at 19 mm (standard situation, as per this study) with brace thickness varied to obtain various τ ratios. It can be seen that the effect of increasing the chord thickness with constant brace thickness (of 19 mm) is more beneficial to the axial and out-of-plane bending load cases and results in the reduction of the SCF at the saddle positions; a 16% reduction was observed for these load cases at their respective hot spot positions. This reduction is an indication of the thickness effect in welded tubular joints.

The variation of the SCF as a function of diametral (β = d/D), thickness (τ = t/T) and thinness (γ = D/2T) ratios are given in Figures 4.26 through 4.34, for axial and in-plane/out-of-plane bending load cases. Figures 4.26 to 4.28 show the influence of the diametral ratio (d/D) for the various loading cases. Three distinct characteristic behaviour patterns are observed for the three load cases. For the axial (brace) tensile loads, the chord SCF tends to level off for $\beta < 0.3$; the curve seems to be asymptotic at a SCF level of 28.0. For the in-plane bending load, the chord SCF seems to be almost a constant, varying between 6.0 to 7.0. This is probably due to the fact that the stiffness to in-plane bending is mainly dependent on the stiffness present in the brace diametral plane. For the case of out-of-plane bending, the maximum SCF of the intersection seems to occur when $\beta = 0.5$, for $0.5 < \beta < 0.5$, the SCF tends to be reduce.

From Figures 4.29 to 4.31 it can be stated that when $\beta = 0.5$, for τ less than 0.6,

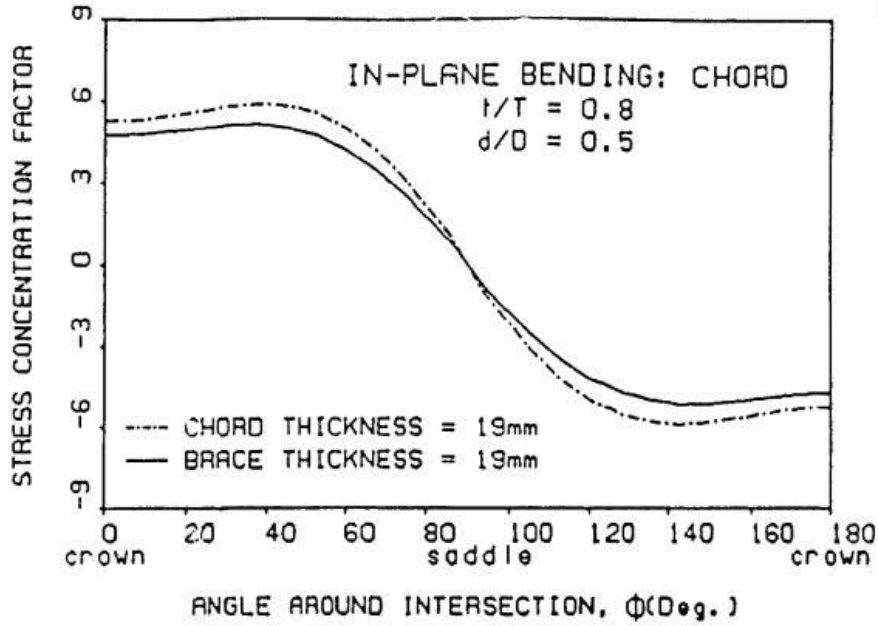

Figure 4.24: Effect of specified thickness either in chord or brace (IPB) ($\alpha = 7.02$, $\gamma = 24.$).

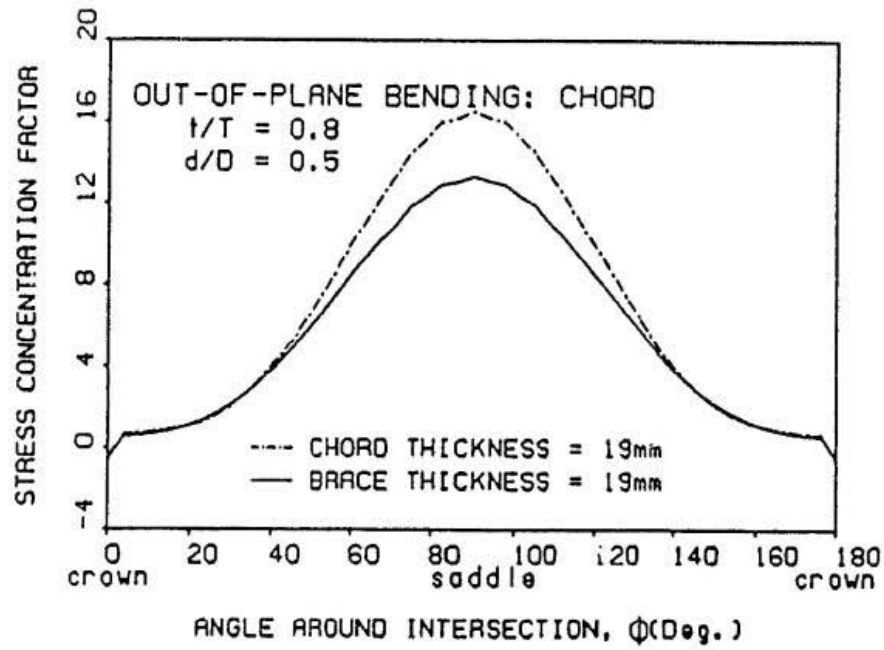

Figure 4.25: Effect of specified thickness either in chord or brace (OPB) ($\alpha = 7.02$, $\gamma = 24.$).

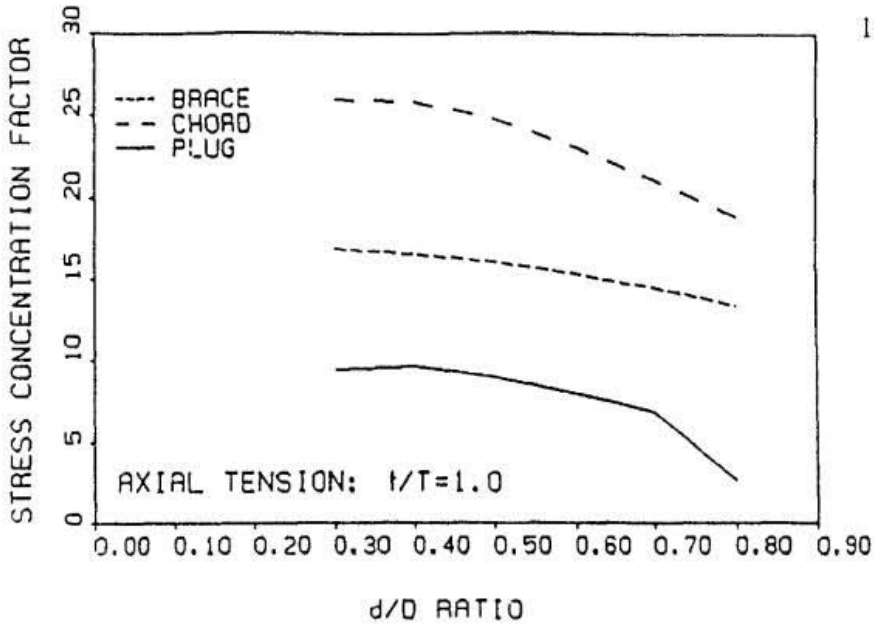

Figure 4.26: Variation of SCF with β ratio (Axial). (α = 7.02, γ = 24.0, τ = 1.0).

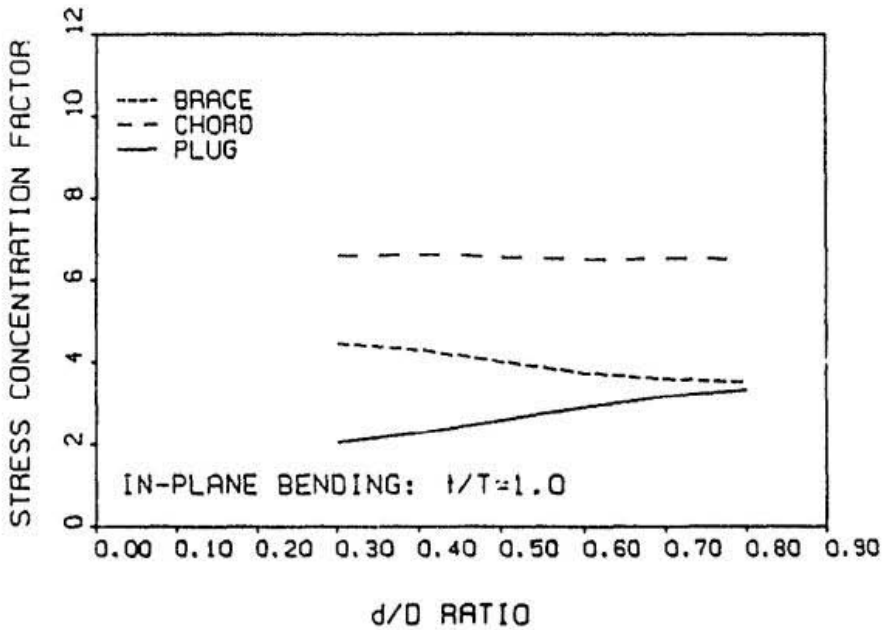

Figure 4.27: Variation of SCF with β ratio (IPB). (α = 7.02, γ = 24.0, τ = 1.0).

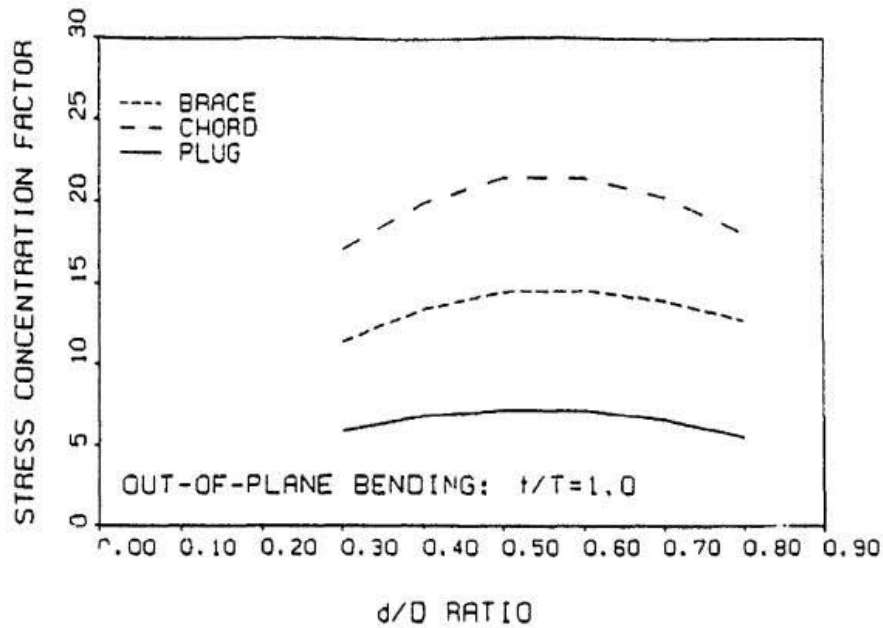

Figure 4.28: Variation of SCF with β ratio (OPB). (α = 7.02, γ = 24.0, τ = 1.0).

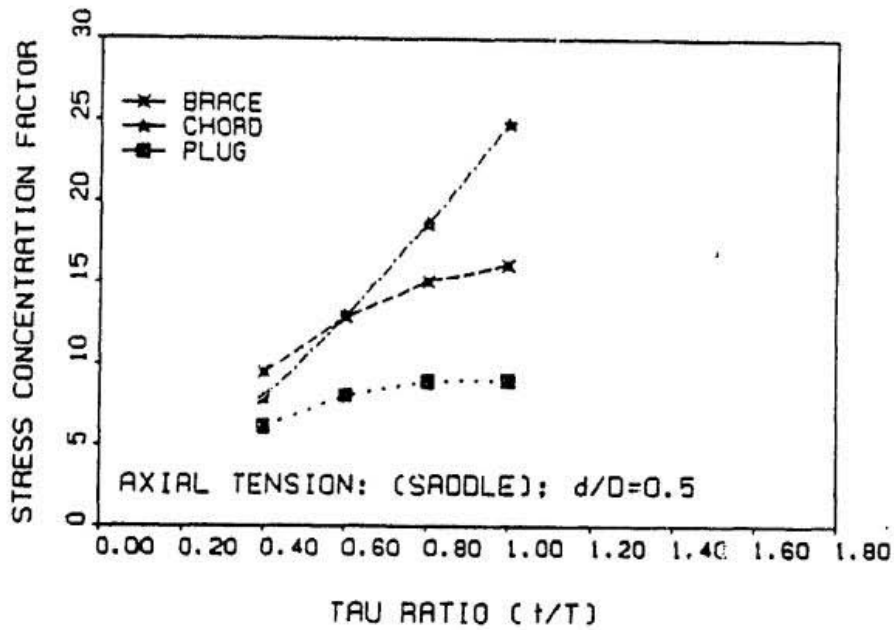

Figure 4.29: Variation of SCF with τ ratio (Axial). (α = 7.02, β = 0.5, γ = 24.0)

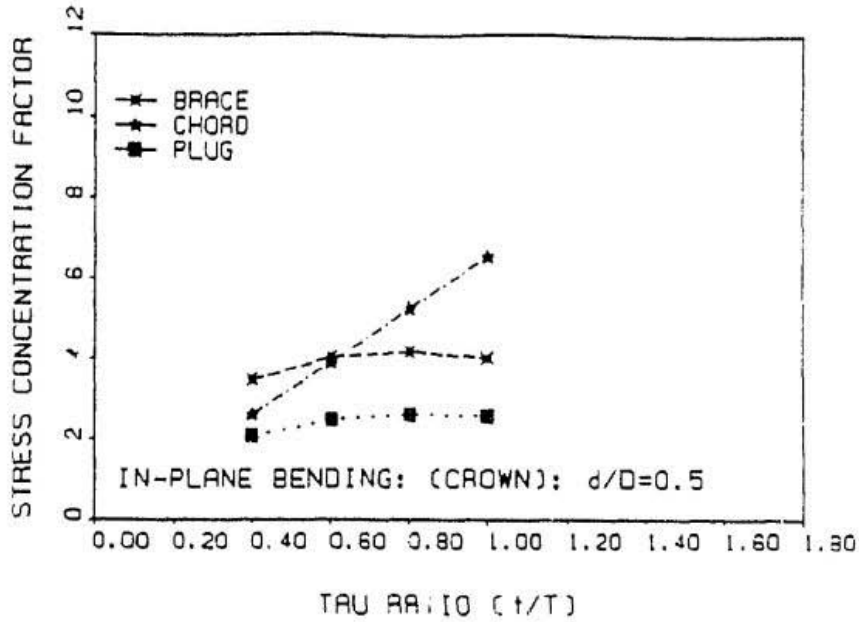

Figure 4.30: Variation of SCF with τ ratio (IPB). ($\alpha = 7.02$, $\beta = 0.5$, $\gamma = 24.0$)

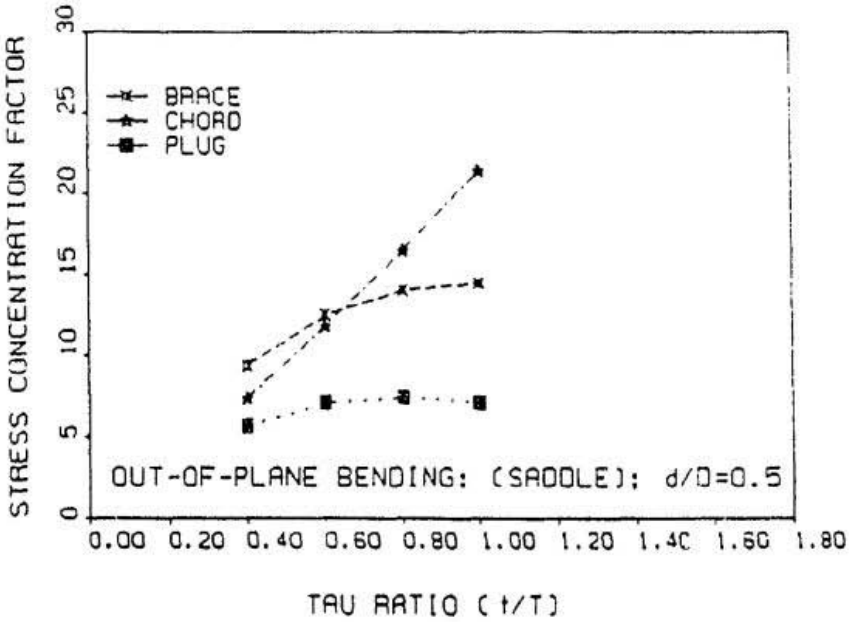

Figure 4.31: Variation of SCF with τ ratio (OPB). ($\alpha = 7.02$, $\beta = 0.5$, $\gamma = 24.0$)

there is a possibility for the peak stress at the weld toe to occur in the brace side; hence there is a possibility that the cracks may initiate on the brace side, since the brace *SCF* is higher than the chord *SCF*. This was observed to be the same for the axial, in-plane and out-of-plane load cases. Figures 4.32 to 4.34 give the influence of the thinness ratio (γ = D/2T) on the stress concentration factors of tubular joints. The SCFs in the chord tend to increase almost linearly as the thinness (or γ) ratios increase. The results of Figures 4.32 to 4.34 validate the results given in Figures 4.23 to 4.25 since larger *SCF* values are obtained for larger thinness (chord diameter to thickness) ratios and vice versa.

The maximum principal stress versus distance along the chord surface from the saddle and crown positions, for the three load cases, are given in Figures 4.35 to 4.40. In the computation of the SCF values, the extrapolation to the weld toe from standard distances were not carried out since (i) the weld was not modelled in the analysis by the shell elements and the stresses obtained were at the outer surface of the two intersecting shell elements; and (ii) even if extrapolation was used the SCF values would be affected only marginally since the variation of the stress is almost linear in this extrapolation region as could be seen from Figures 4.35 to 4.40. The region under the influence of joint discontinuity seems to be much larger in the brace than in the chord, for all the three load cases. While there is a zone of compression in the chord under axial and out-of-plane bending loads, for the in-plane bending cases, the zone of influence on the tensile stress region (of chord) is always tensile.

Comparing Figures 4.23 to 4.25 with Figures 4.35 to 4.40, it could be seen that

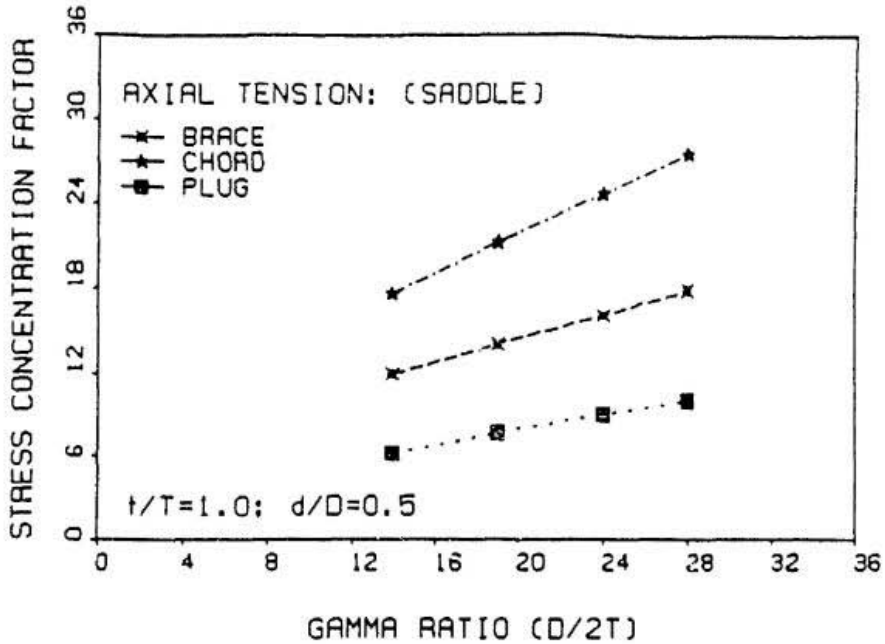

Figure 4.32: Variation of SCF with γ ratio (Axial). (α = 7.02, β = 0.5, τ = 1.0).

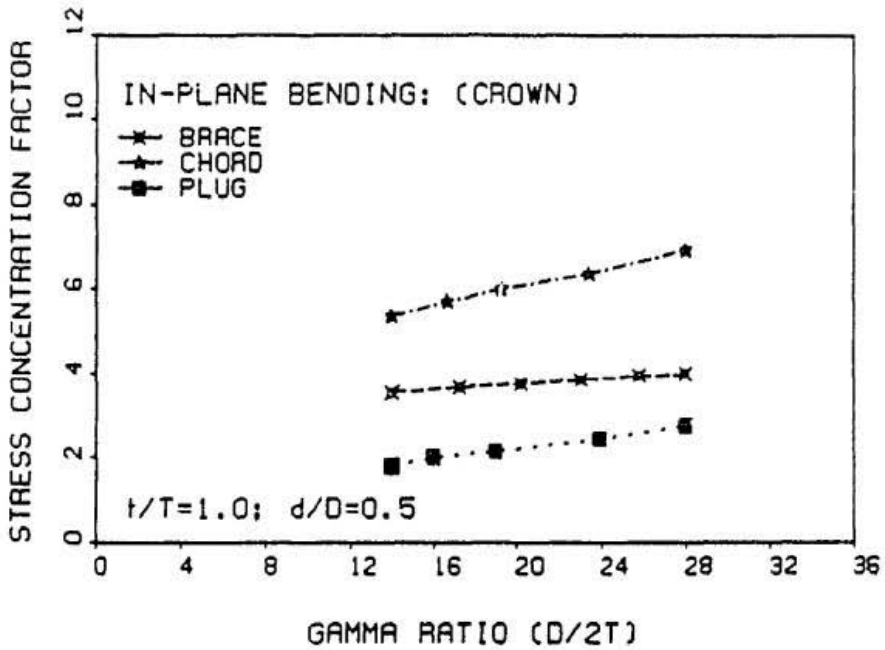

Figure 4.33: Variation of SCF with γ ratio (IPB). (α = 7.02, β = 0.5, τ = 1.0).

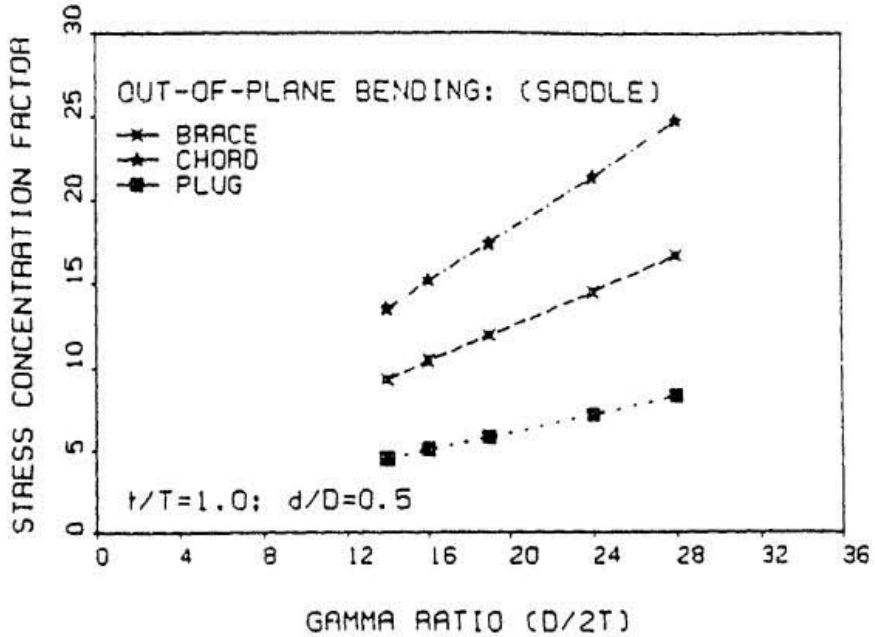

Figure 4.34: Variation of SCF with γ ratio (OPB). ($\alpha = 7.02$, $\beta = 0.5$, $\tau = 1.0$).

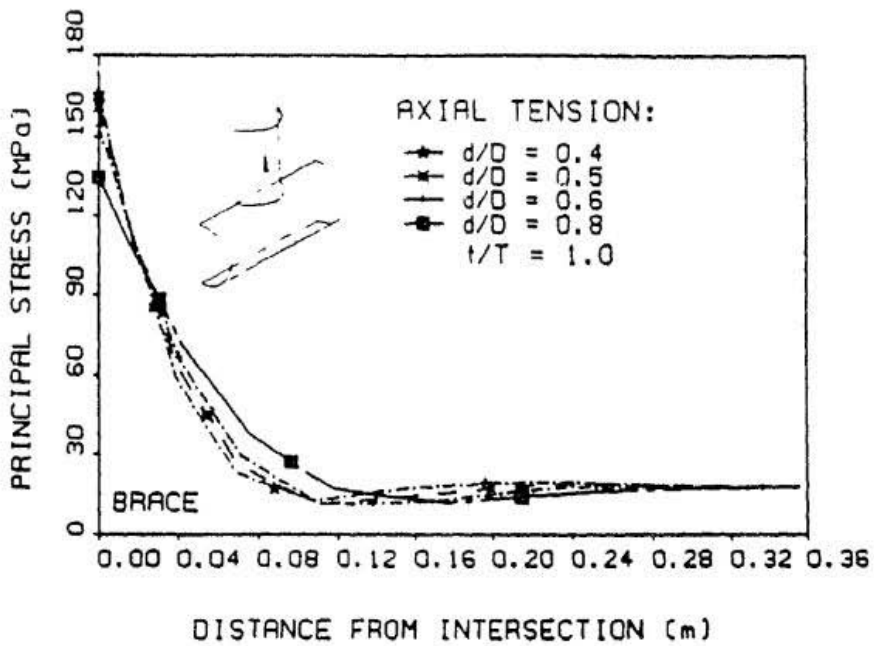

Figure 4.35: Principal stress distribution along brace surface from the saddle point. (Axial) ($\alpha = 7.02$, $\tau = 1.0$, $\gamma = 24.0$)

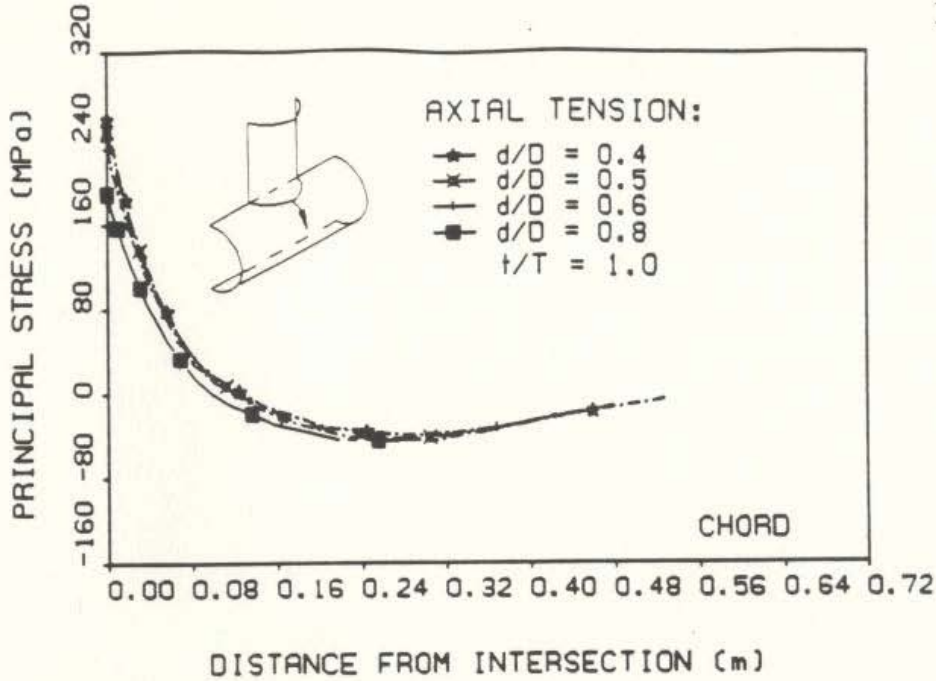

Figure 4.36: Principal stress distribution along chord surface from the saddle point. (Axial) ($\alpha = 7.02$, $\tau = 1.0$, $\gamma = 24.0$)

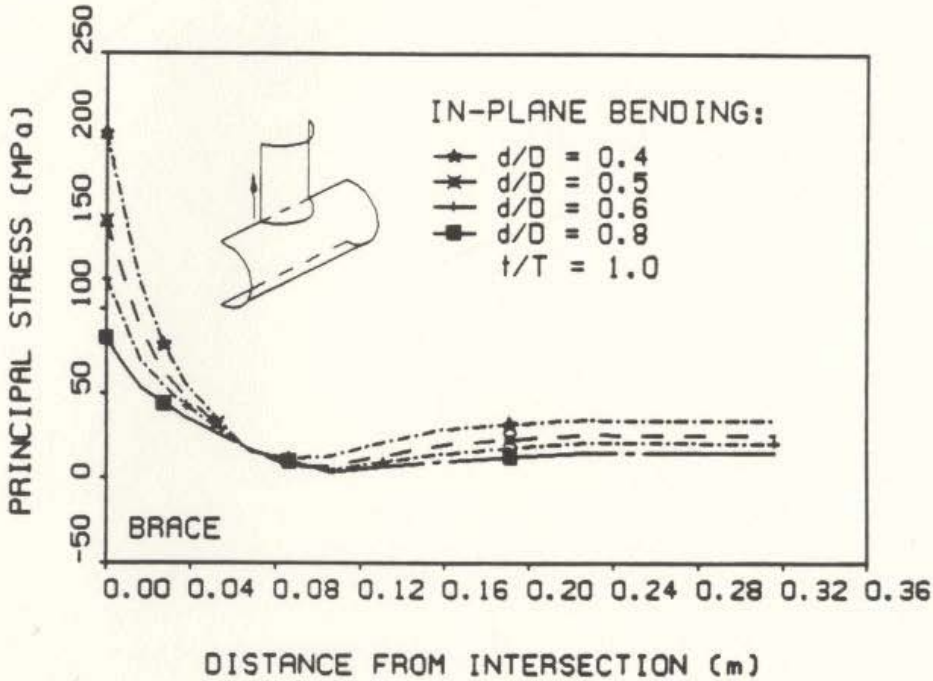

Figure 4.37: Principal stress distribution along brace surface from the crown point. (IPB) ($\alpha = 7.02$, $\tau = 1.0$, $\gamma = 24.0$)

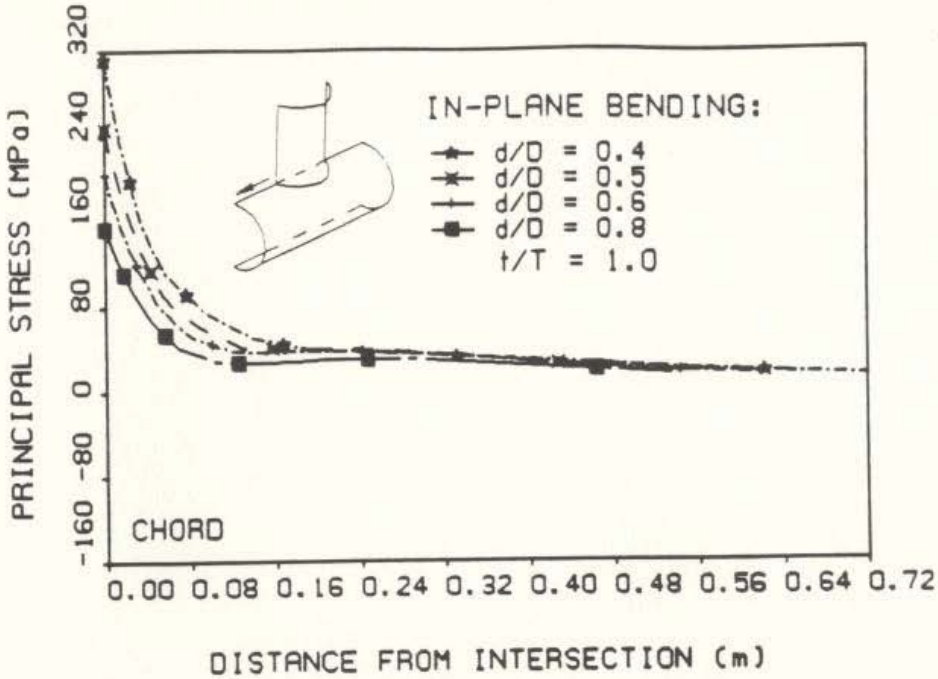

Figure 4.38: Principal stress distribution along chord surface from the crown point. (IPB) ($\alpha = 7.02$, $\tau = 1.0$, $\gamma = 24.0$)

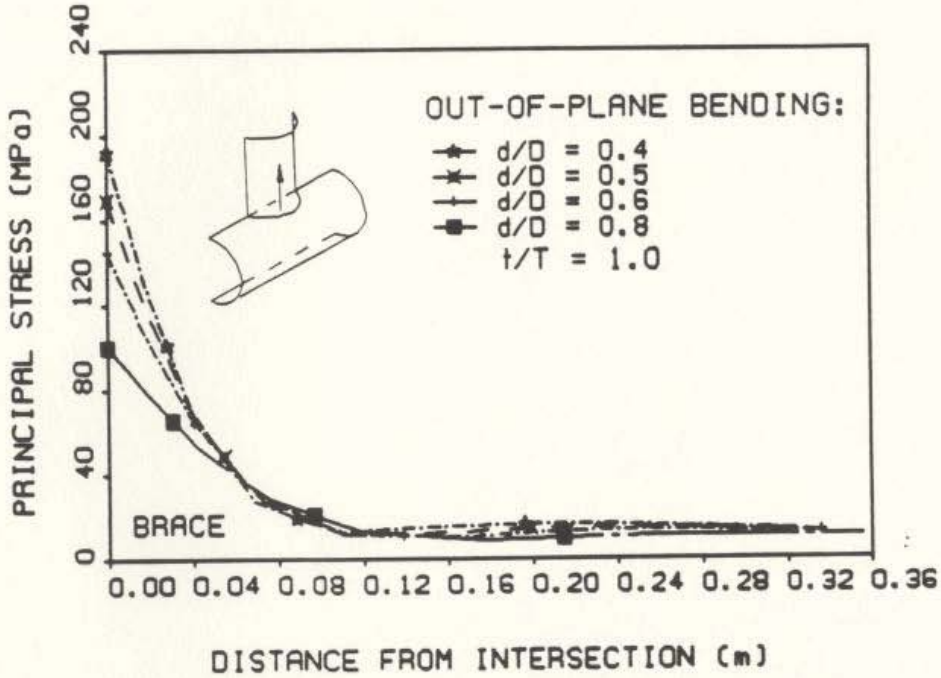

Figure 4.39: Principal stress distribution along brace surface from the saddle point. (OPB) ($\alpha = 7.02$, $\tau = 1.0$, $\gamma = 24.0$)

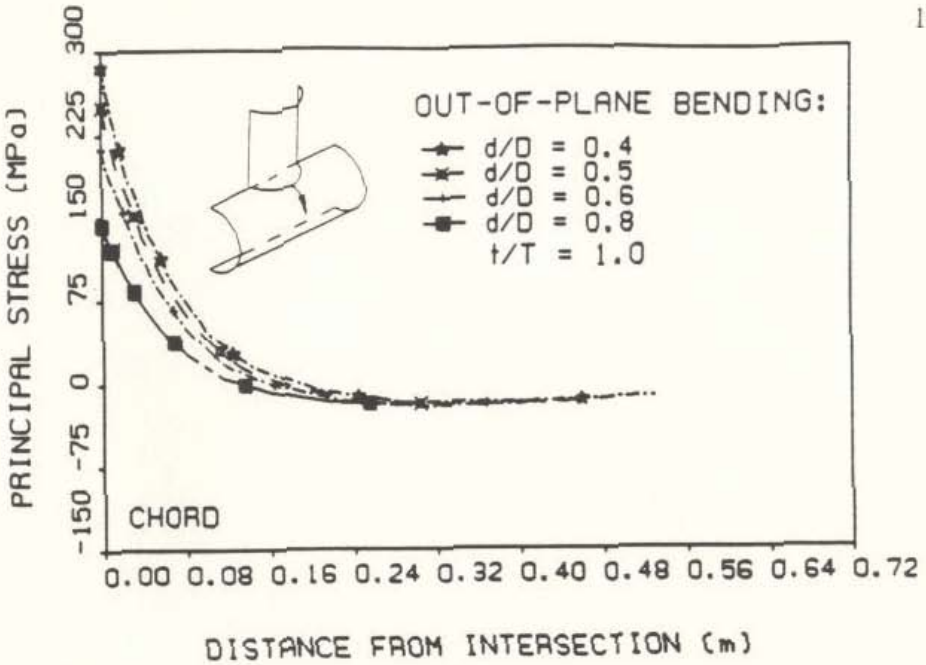

Figure 4.40: Principal stress distribution along chord surface from the saddle point. (OPB) ($\alpha = 7.02$, $\tau = 1.0$, $\gamma = 24.0$)

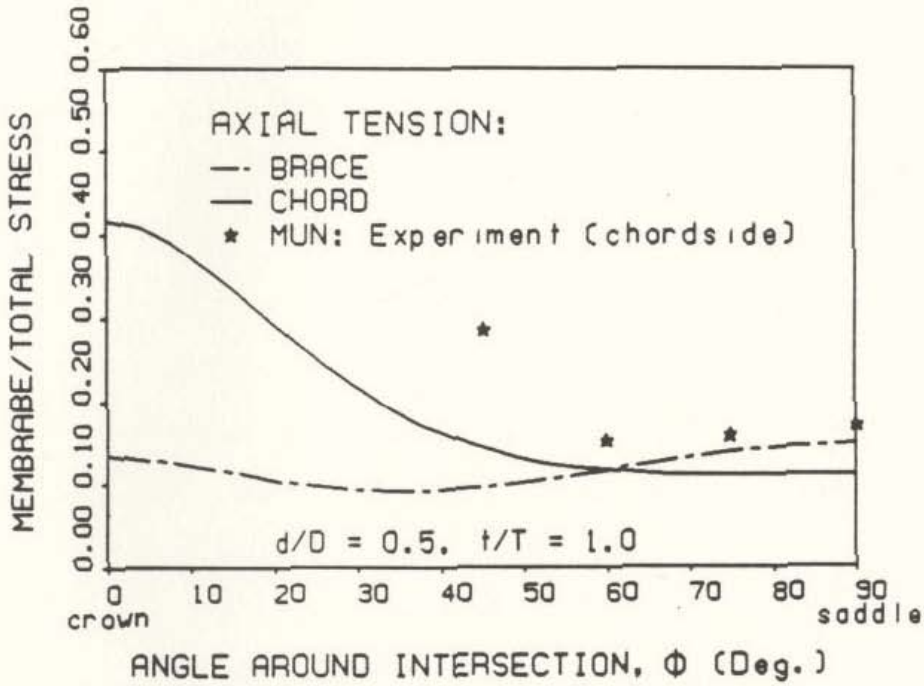

Figure 4.41: Ratio of membrane stress to total stress vs. ϕ) (Axial) ($\alpha = 7.02$, $\tau = 1.0$, $\gamma = 24.0$)

for the same stress level more work is done around the critical region for the in-plane bending load than for the axial and out-of-plane bending load cases. This may also be a reason for the lower fatigue life of the tubular T-joints subjected to in-plane bending loads. Also since the out-of-plane bending load would spend the lowest amount of energy around the weld toe during deformation this would have the largest fatigue life for the joint with the same stress level.

The variation of the ratios of the membrane/bending to total stresses, along the intersection, are given in Figures 4.41 and 4.46, for the axial in-plane and out-of-plane bending load cases. The results presented in these figures are those for the diametral ratio β and thickness ratio τ of 0.5 and 1.0, respectively. The same trend was observed for other ratios used in the present study. For the cases where the membrane stress is computed to be compressive, the bending stress to total stress ratio (degree of bending) is greater than one. In Figures 4.41 and 4.42 comparison between the results of the present study and the experimental data obtained at Memorial University of Newfoundland (Munaswamy et al., 1987) for a medium scale steel tubular joint under axial load is also presented. It is observed that the experimental values tend to fall away from the analytical values as the angle ϕ around the joint decreases from 90° to 0°; it must be stated that the MUN experimental results plotted radial stress values along the weld toe intersection, while the analytical values have plotted the principal stress values. It is also important to note that for in-plane bending, the ratio of bending to total stress could not be satisfactorily determined at locations between 60° and 90°. This is due to the difficulty in choosing the correct values of the principal stresses near the saddle; this might be due to the fact that this portion of the joint corresponds to the minimum

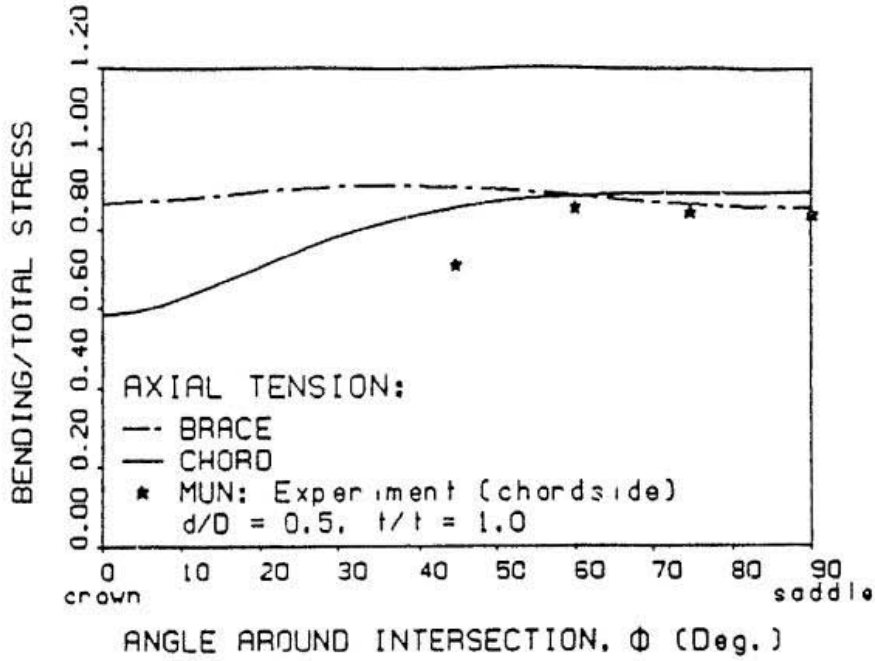

Figure 4.42: Ratio of bending stress to total stress vs. ϕ) (Axial) ($\alpha = 7.02$, $\tau = 1.0$, $\gamma = 24.0$)

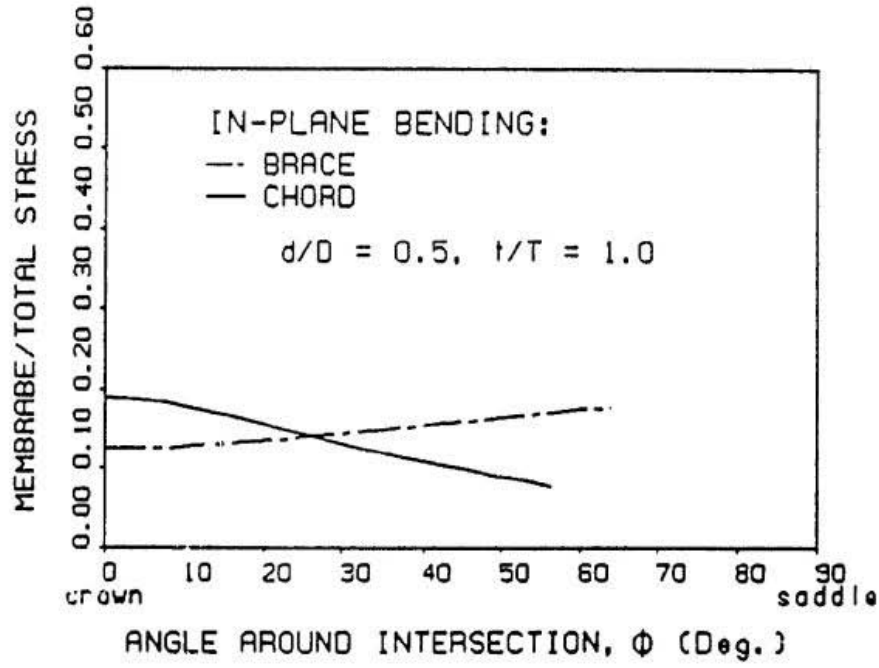

Figure 4.43: Ratio of membrane stress to total stress vs. ϕ) (IPB) ($\alpha = 7.02$, $\tau = 1.0$, $\gamma = 24.0$)

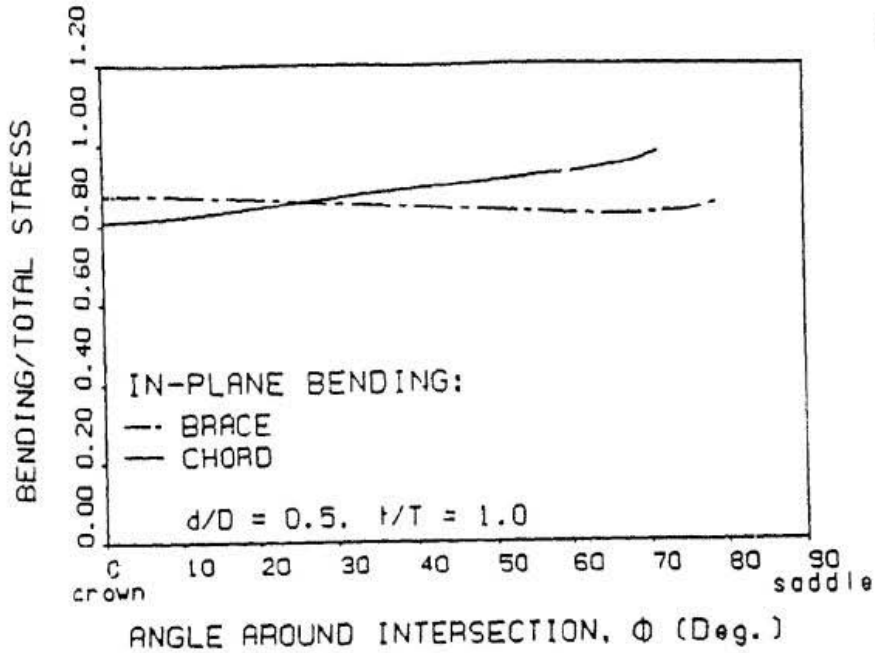

Figure 4.44: Ratio of bending stress to total stress vs. ϕ) (IPB) (α = 7.02, τ = 1.0, γ = 24.0)

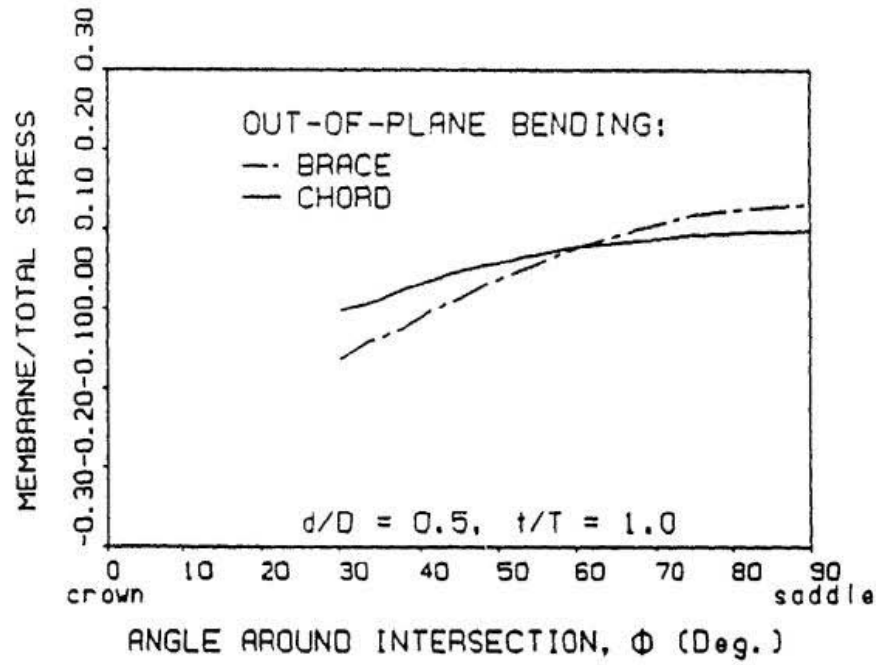

Figure 4.45: Ratio of membrane stress to total stress vs. ϕ) (OPB) (α = 7.02, τ = 1.0, γ = 24.0)

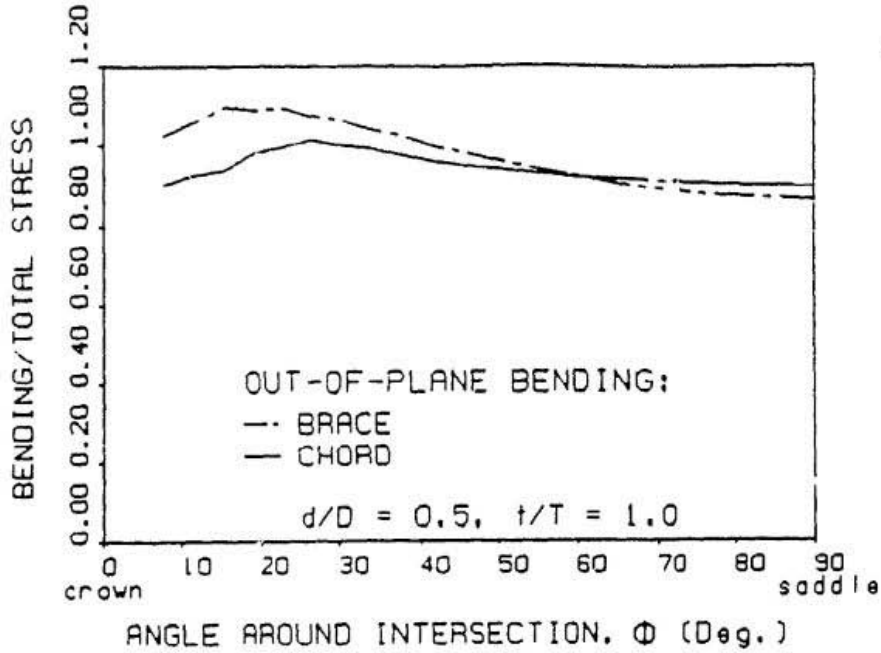

Figure 4.46: Ratio of bending stress to total stress vs. ϕ) (OPB) ($\alpha = 7.02$, $\tau = 1.0$, $\gamma = 24.0$)

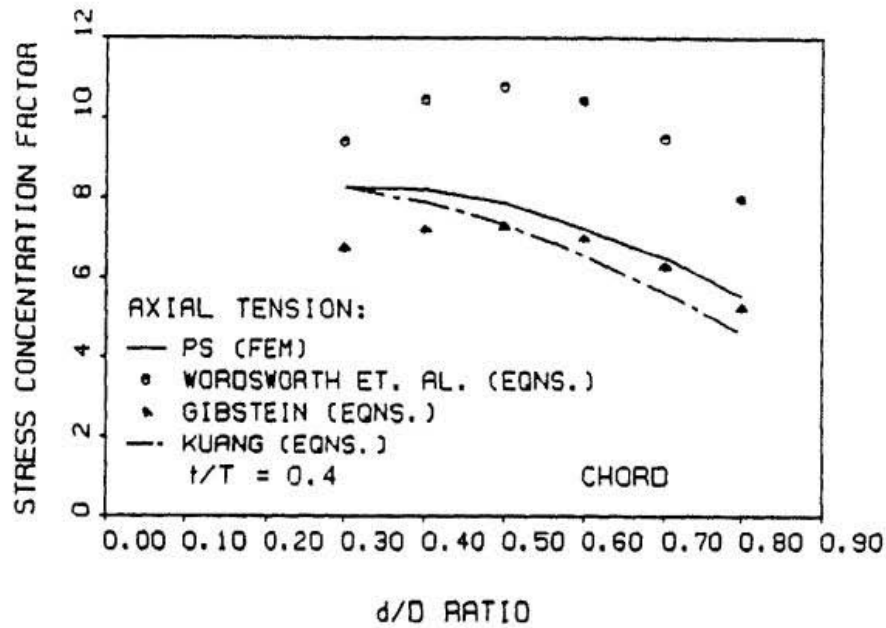

Figure 4.47: SCF vs. β; comparison between empirical equations and PS (Axial). ($\alpha = 7.02$, $\gamma = 24.0$, $\tau = 0.4$)

or zero stress position in the tubular joint.

The comparison of the present study, with some of the well established empirical parametric equations, available in the literature, are presented in Figures 4.47 through 4.50 for the case of axial tensile loads. The differences in the predicted equations and the finite element results of this study are evident, especially for the Wordsworth and Smedley equation. Good agreement is observed between the finite element results of the present investigation and Kuang's and Gibstein's equation for most of the thickness ratios shown in Figures 4.47 to 4.50. The experimental results obtained from the tests carried out at Memorial University are in good agreement with the results of this finite element analysis. As discussed by Dover et al. (1991) more effort needs to be put into the reliability of prediction by various parametric equations; also more efforts should be put in standardizing the mesh configuration for the SCF studies as well as in specifying the correct tubular length/diameter ratios to minimize the effect of end conditions in the chord.

Figures 4.51 to 4.54 show the stress distribution for the axially loaded tubular T-joints along the brace/chord intersection for various thickness ratios at β=0.5. These figures exhibit an important observation made in this study. The importance of the τ ratio of 0.6 for the alternation of the peak stress, between the chord and brace weld toe hot spot (saddle), is highlighted through these figures. This value of τ is observed to have an influence on whether the joint failure will initiate at the chord or brace side. It appears that for a value of τ less than 0.6, the failure would initiate on the brace side while for τ greater than 0.6, the failure would be on the chord side, with a 50% chance that it may either occur in the brace or the

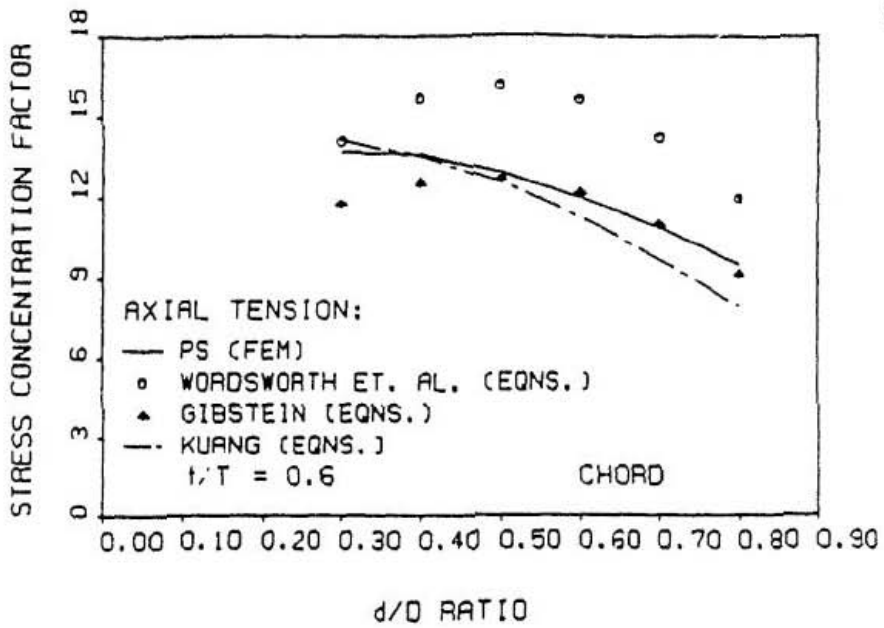

Figure 4.48: SCF vs. β: comparison between empirical equations and PS (Axial). ($\alpha = 7.02$, $\gamma = 24.0$, $\tau = 0.6$)

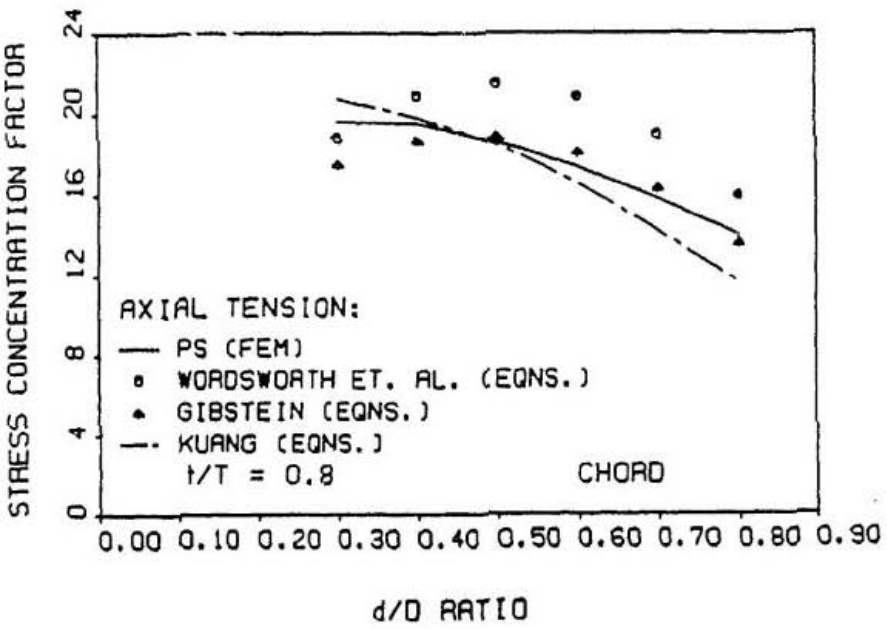

Figure 4.49: SCF vs. β; comparison between empirical equations and PS (Axial). ($\alpha = 7.02$, $\gamma = 24.0$, $\tau = 0.8$)

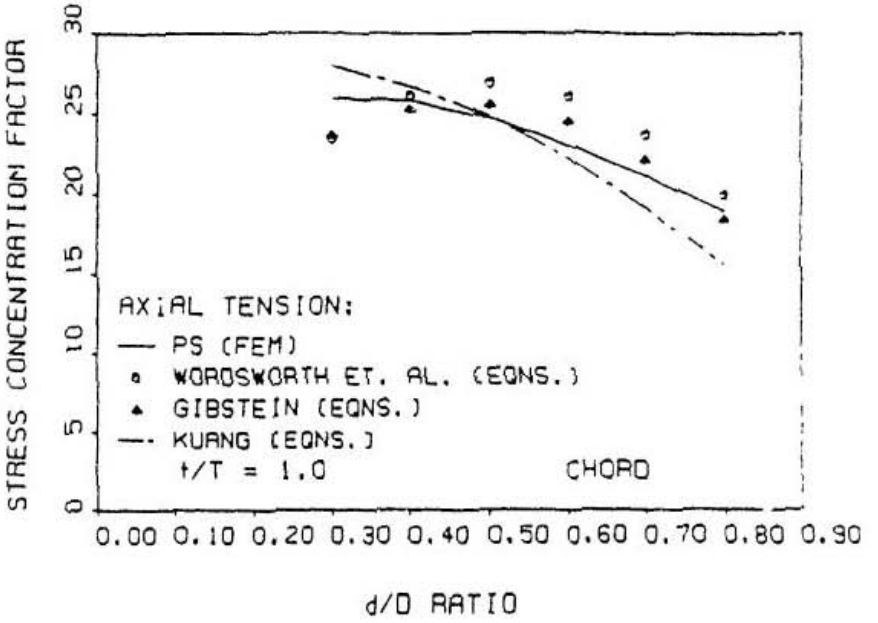

Figure 4.50: SCF vs. β: comparison between empirical equations and PS (Axial). (α = 7.02, γ = 24.0, τ = 1.0)

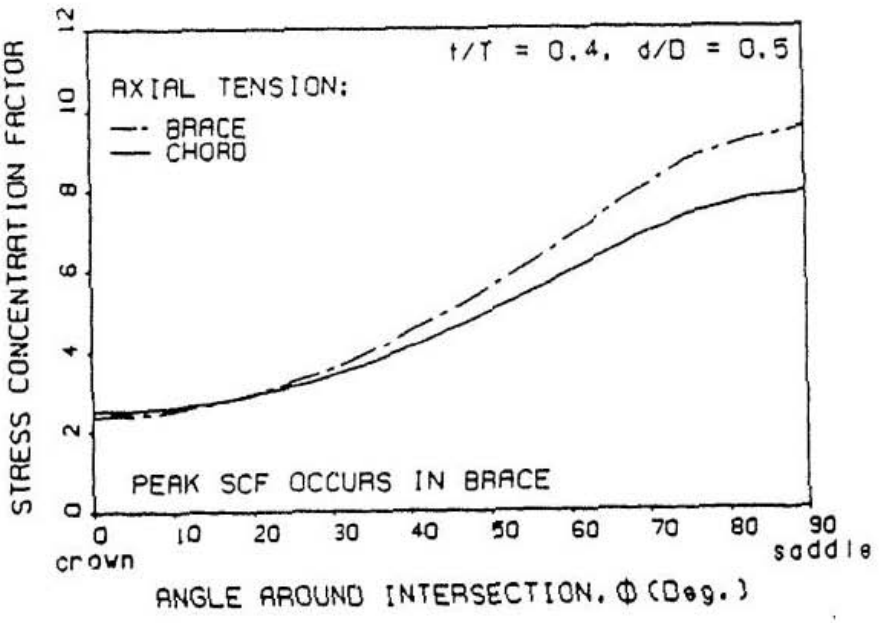

Figure 4.51: Effect of τ ratio on location of peak SCF (Axial) (α = 7.02, τ = 0.4, γ = 24.0)

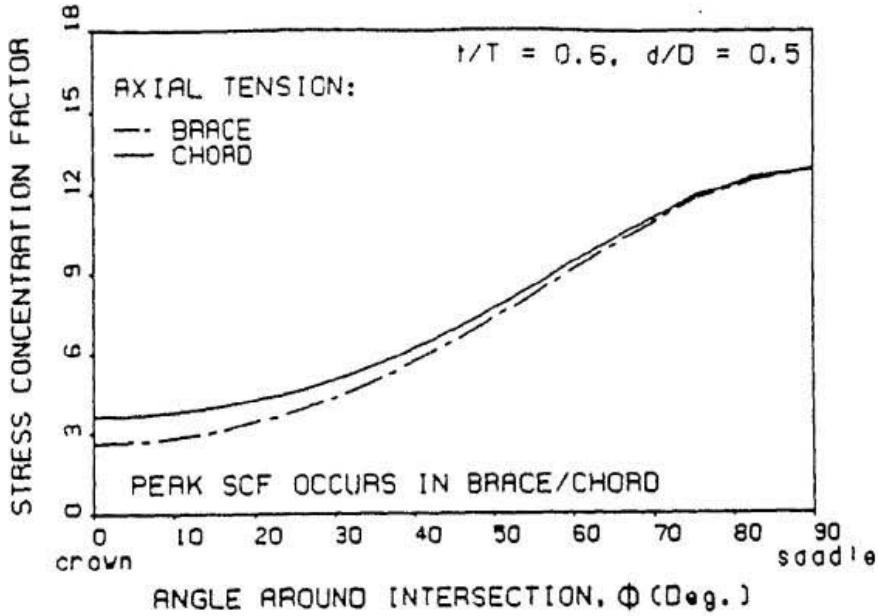

Figure 4.52: Effect of τ ratio on location of peak SCF ($\tau = 0.6$)

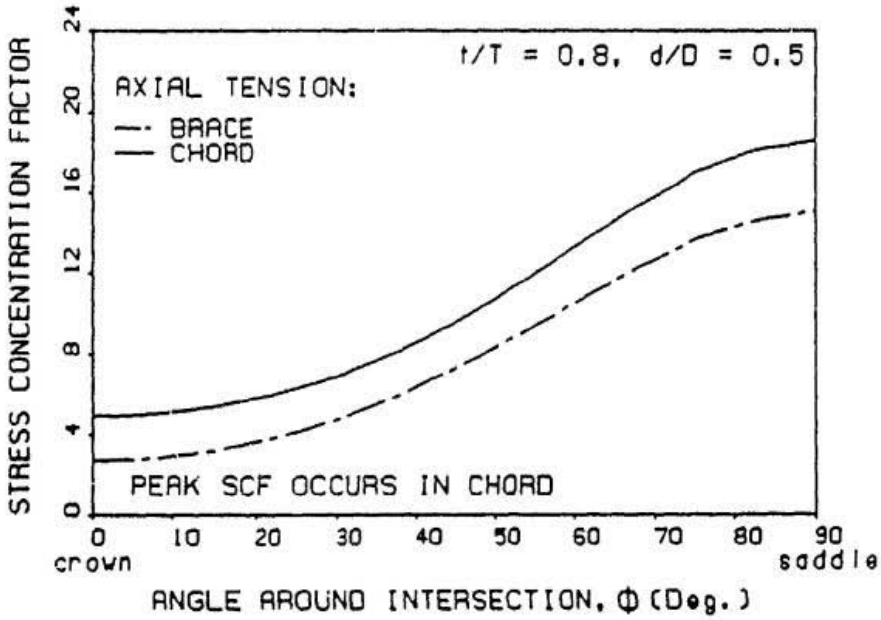

Figure 4.53: Effect of τ ratio on location of peak SCF ($\tau = 0.8$)

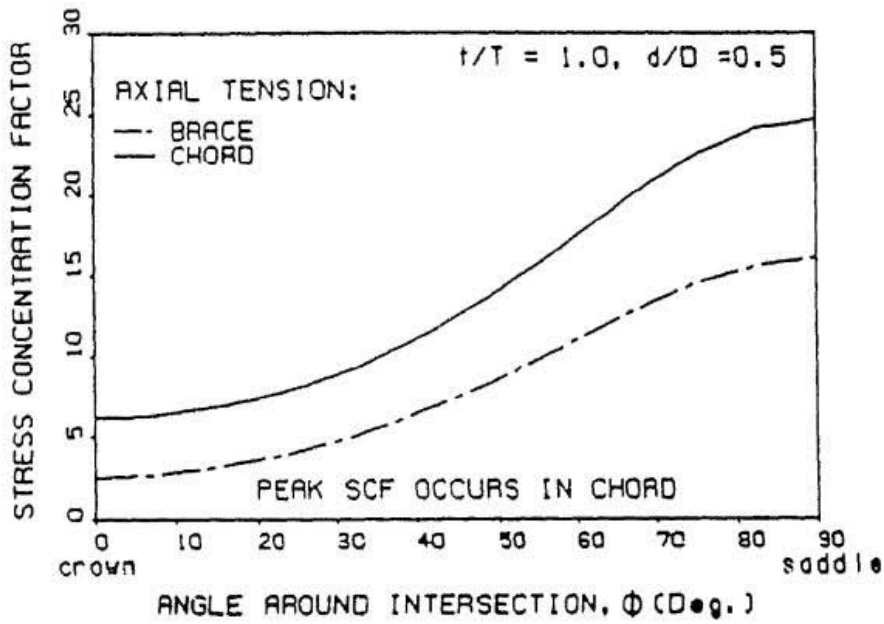

Figure 4.54: Effect of τ ratio on location of peak SCF ($\tau = 1.0$)

chord side when τ is 0.6. It must be emphasized here that the stress distribution may change depending on the local variation of the weld toe at the intersection. A similar behaviour is observed for in-plane and out-of-plane bending loads on tubular T-joints.

The results of the present study have also been compared with the most resent study on the stress distribution around the intersection and through thickness of a tubular T-joint. One such comparison was made between the present study and the results obtained by Burdekin et al. (1992) and is shown in Figures 4.55 and 4.56. It is observed that the SCF results of Burdekin et al. tend to be lower than those given by the present finite element study for the chord; but the trend is found to be the same. The results of the degree-of-bending seem to be agreeing very well.

Additional analyses were performed in this study to investigate the effect of the absence of the plug area on the stress concentration factor around the intersection; the results of these analyses are shown from Figures 4.57 through 4.62 for the three load cases investigated. Under axial tension loading there is a substantial difference between the stress concentration factors for the joint with plug and without plug on the brace side while no difference is observed on the chord side. The absence of the plug redistributed the loads so that the stiffness ratios for the axial tensile loads were almost the same for the chord and the brace. The same was true for the in-plane bending load except that on the chord side SCF reduced all around the weld toe. These results show that the failure may be catastrophic, especially on the brace side if the plug is eliminated from the joint. For the out-of-plane bending the absence of the plug redistributes the stresses at the joint between the

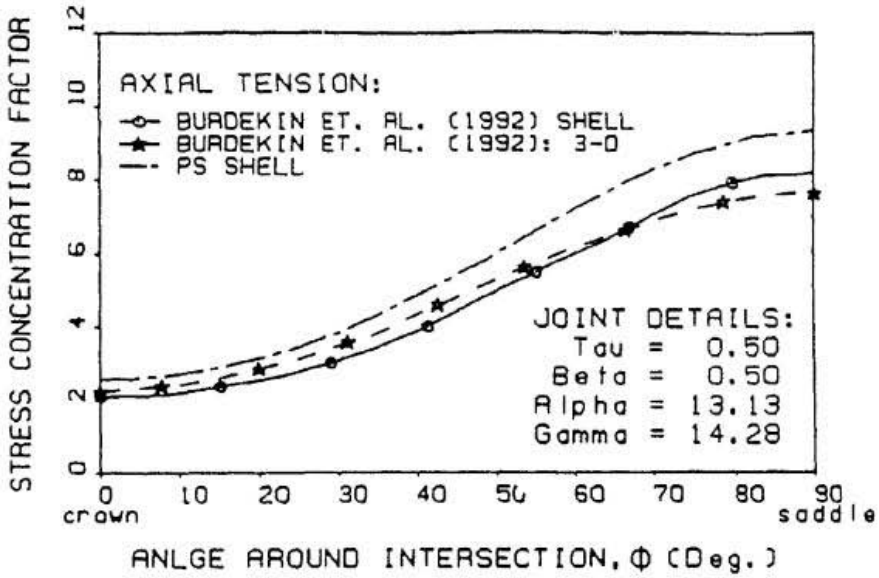

Figure 4.55: SCF comparison between PS and Burdekin et al. (1992) 3-D and shell element results (Axial)

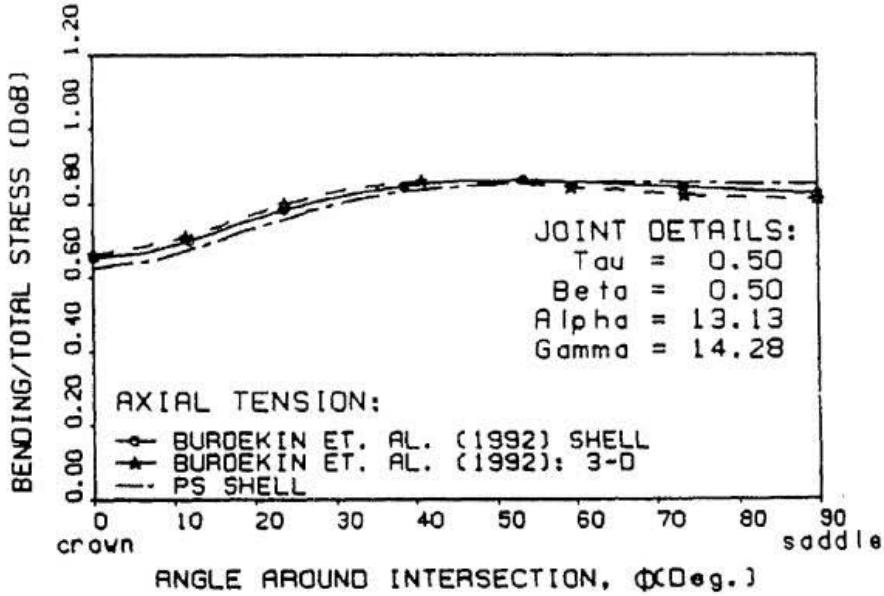

Figure 4.56: DoB comparison between PS and Burdekin et al. (1992) 3-D and shell element results (Axial)

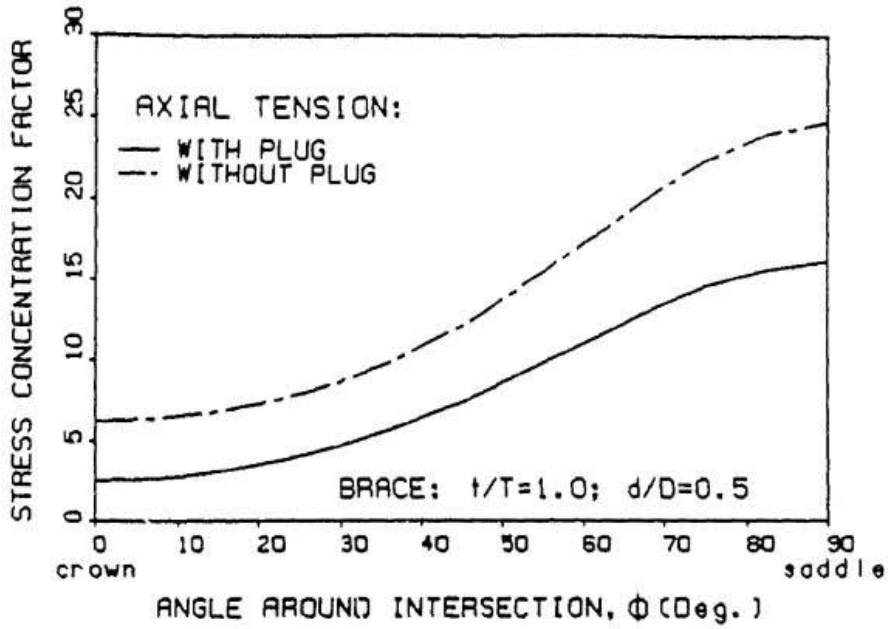

Figure 4.57: Variation of SCF in brace for T-joint with and without plug (Axial) ($\alpha = 7.02$, $\tau = 1.0$, $\beta = 0.5$, $\gamma = 24.0$)

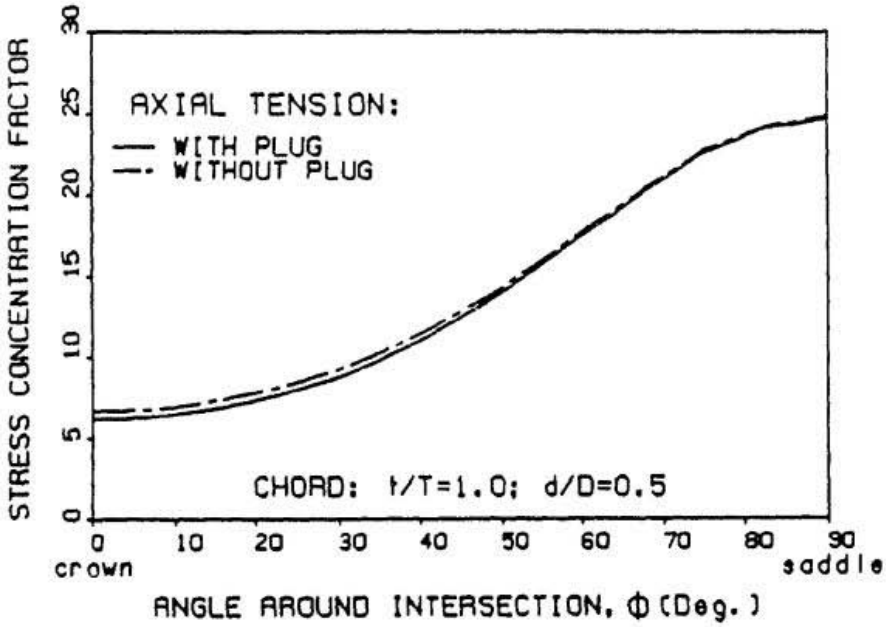

Figure 4.58: Variation of SCF in chord for T-joint with and without plug (Axial) ($\alpha = 7.02$, $\tau = 1.0$, $\beta = 0.5$, $\gamma = 24.0$)

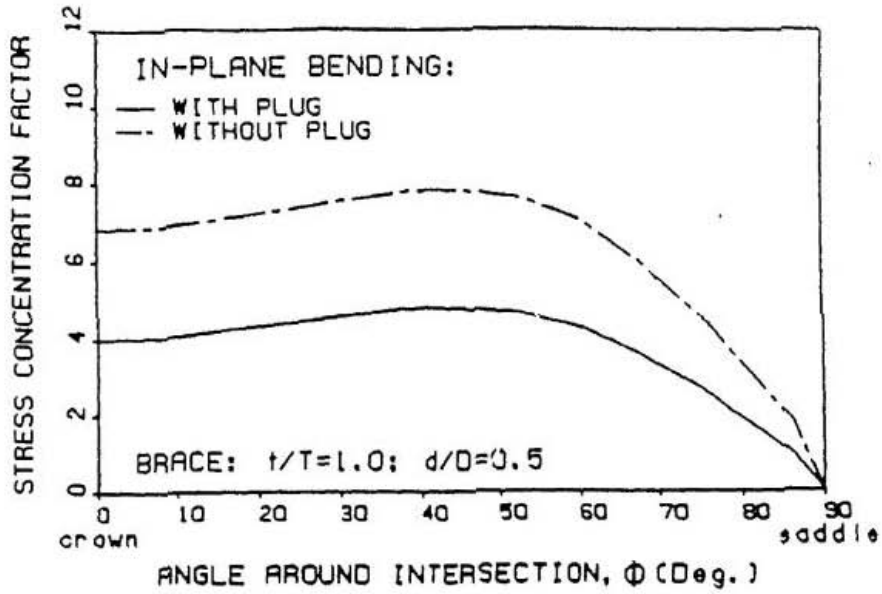

Figure 4.59: Variation of SCF in brace for T-joint with and without plug (IPB) ($\alpha = 7.02$, $\tau = 1.0$, $\beta = 0.5$, $\gamma = 24.0$)

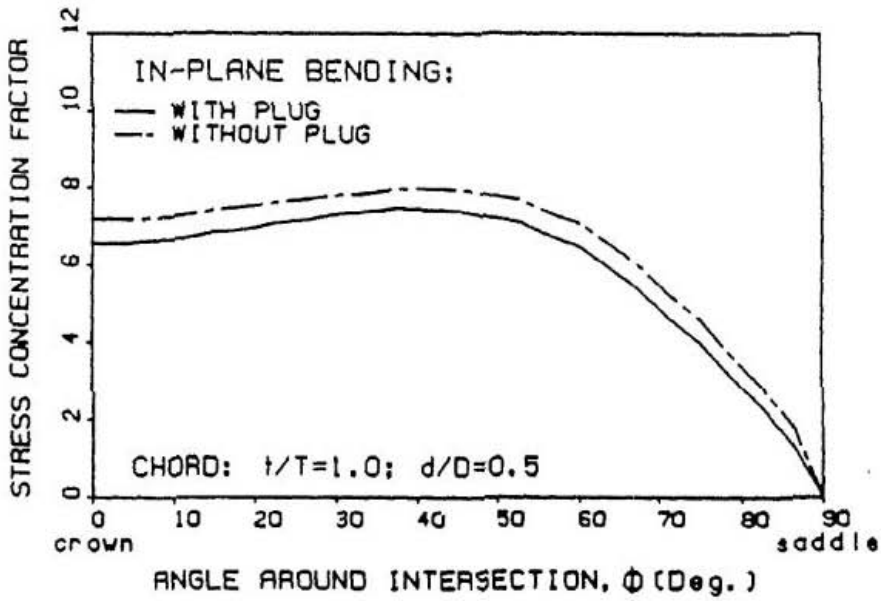

Figure 4.60: Variation of SCF in chord for T-joint with and without plug (IPB) ($\alpha = 7.02$, $\tau = 1.0$, $\beta = 0.5$, $\gamma = 24.0$)

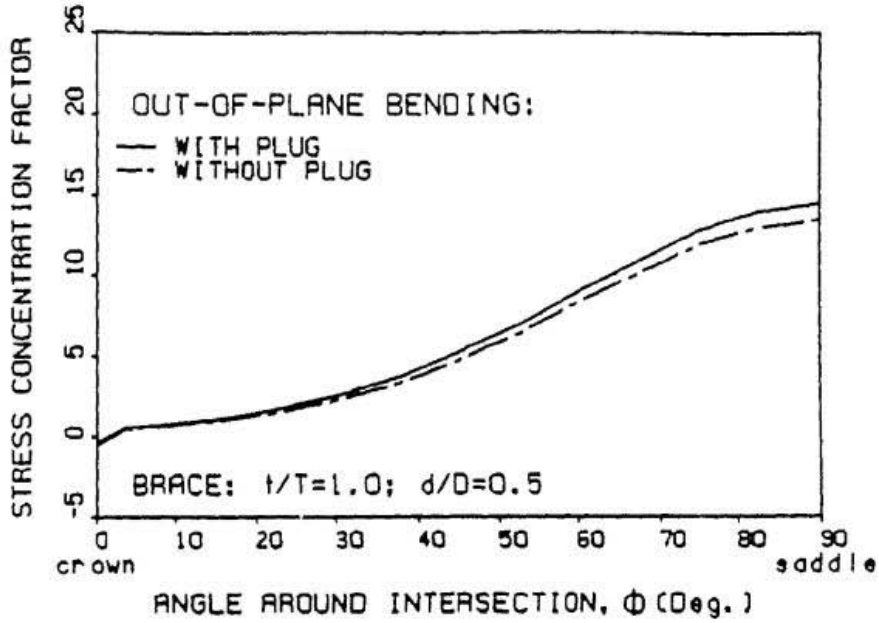

Figure 4.61: Variation of SCF in brace for T-joint with and without plug (OPB) ($\alpha = 7.02$, $\tau = 1.0$, $\beta = 0.5$, $\gamma = 24.0$)

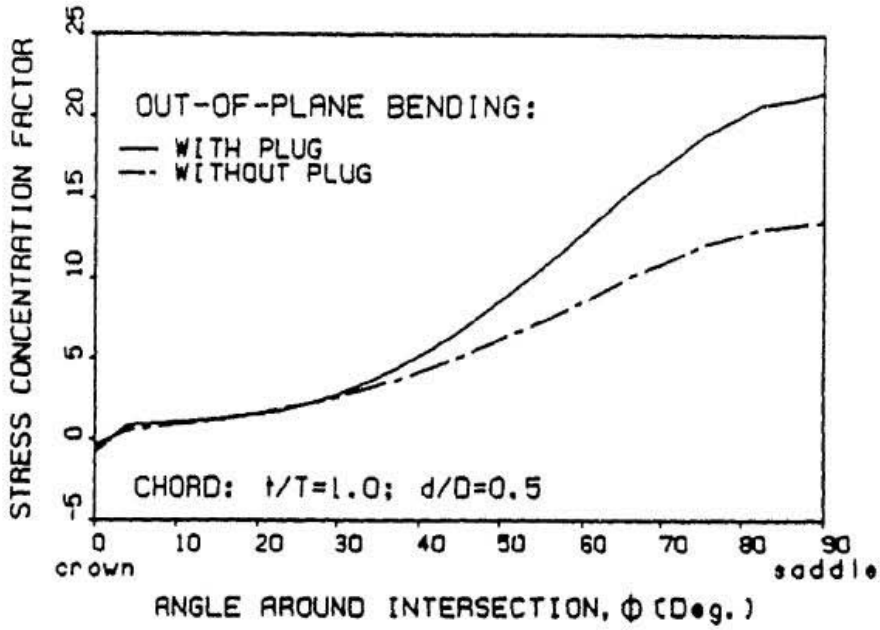

Figure 4.62: Variation of SCF in chord for T-joint with and without plug (OPB) ($\alpha = 7.02$, $\tau = 1.0$, $\beta = 0.5$, $\gamma = 24.0$)

chord and the brace; the SCFs in the chord and the brace tend to reduce rather than increase, as in the previous cases.

Finally a comparison between the finite element model (degenerated shell element) used in this study and the semi-loof finite-element (and parametric equations) study of the University College, London (UCL) (Hellier et al., 1990), was made. The results of these comparisons are presented in Figures 4.63 to 4.68. The results of the finite analysis show very good agreement between the MUN and UCL results for all the three loading cases. The results show a maximum difference between the two methods of less than 8% on the brace side. Hence the lower SCF obtained for in-plane bending cases in the University of Waterloo tests (Table 4.5) may be due to the presence of a thicker weld toe at the crown and due to the extrapolation errors of the experimental values to the weld toe region.

As mentioned earlier both the principal stress SCFs and radial stress SCFs have been used in the existing literature. Since crack initiation occurs on crystallographic slip planes in a shear mode (which depends on the principal planes), initially the cracks are oriented 45° to the maximum principal stress direction. Thereafter the initiated crack changes the mode of cracking and the growth direction is perpendicular to the largest principal cyclic stress. Hence the present researcher believes that only the principal stress SCFs must be used in the documentation of SCFs. The following conclusions are drawn from the finite element stress analysis of the welded tubular joints considered in this study:

1. From the numerical results, the location of the hot spot stress under axial and out-of-plane bending load cases is at the saddle position and is independent of the ratio of the diameters of the brace and the chord. However under in-plane bending this location shifts away from the crown position (away from crown

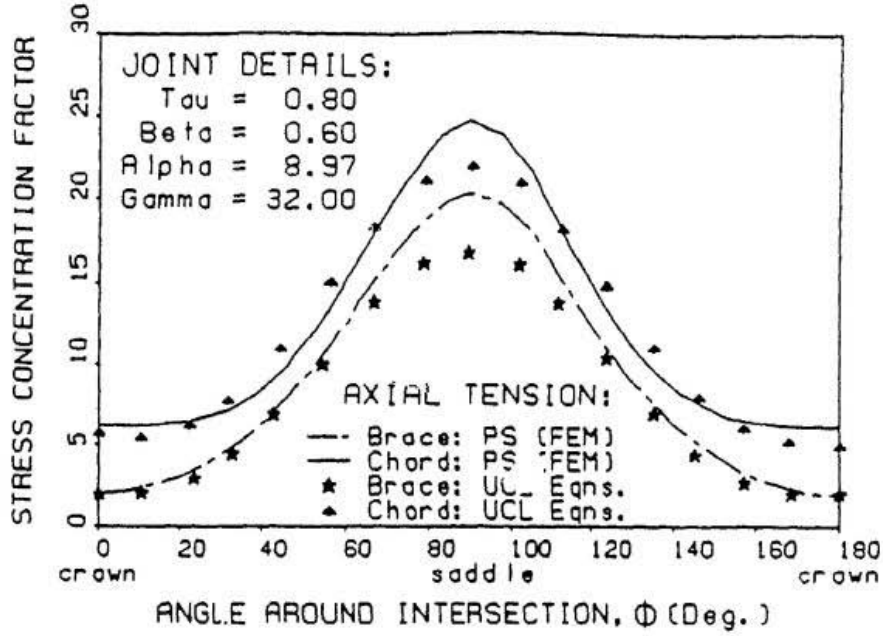

Figure 4.63: Comparison between UCL parametric equations and PS results (Axial)

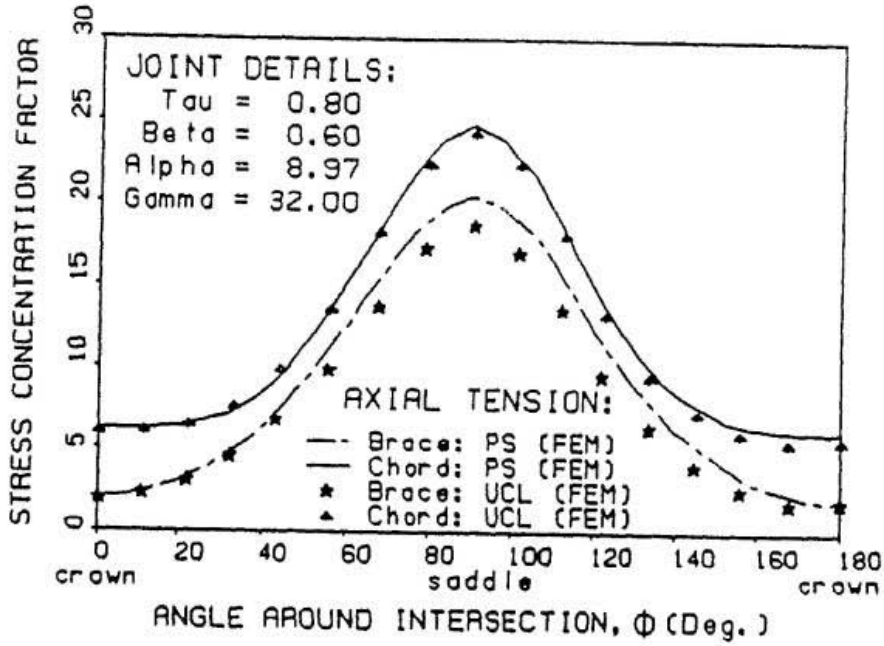

Figure 4.64: Comparison between UCL semi-loof thin-shell FEM data and PS results (Axial)

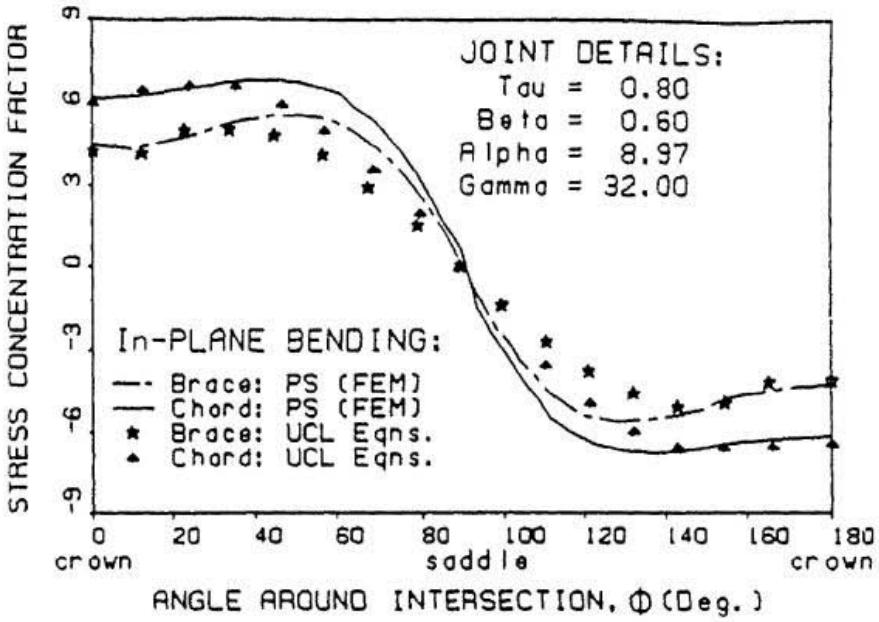

Figure 4.65: Comparison between UCL parametric equations and PS results (IPB)

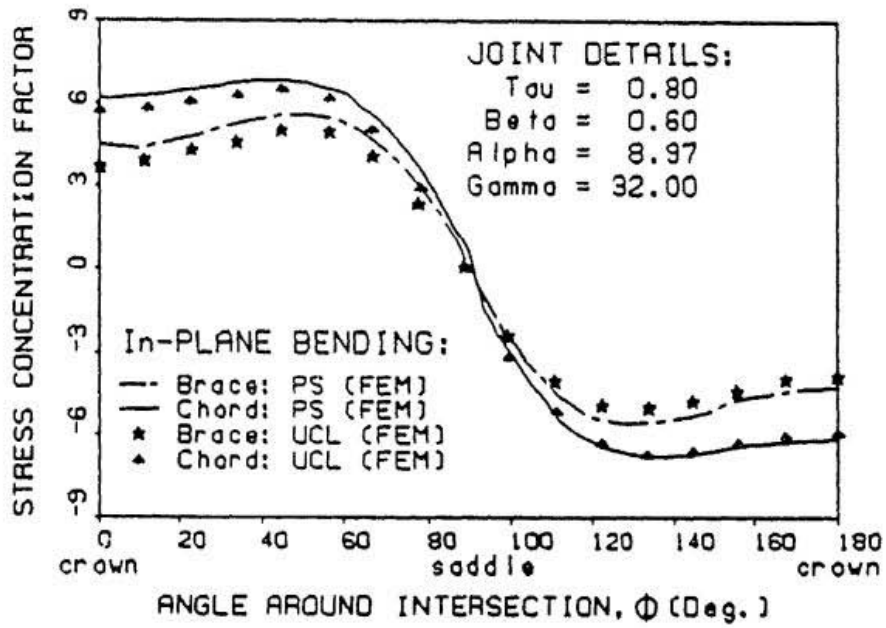

Figure 4.66: Comparison between UCL semi-loof thin-shell FEM data and PS results (IPB)

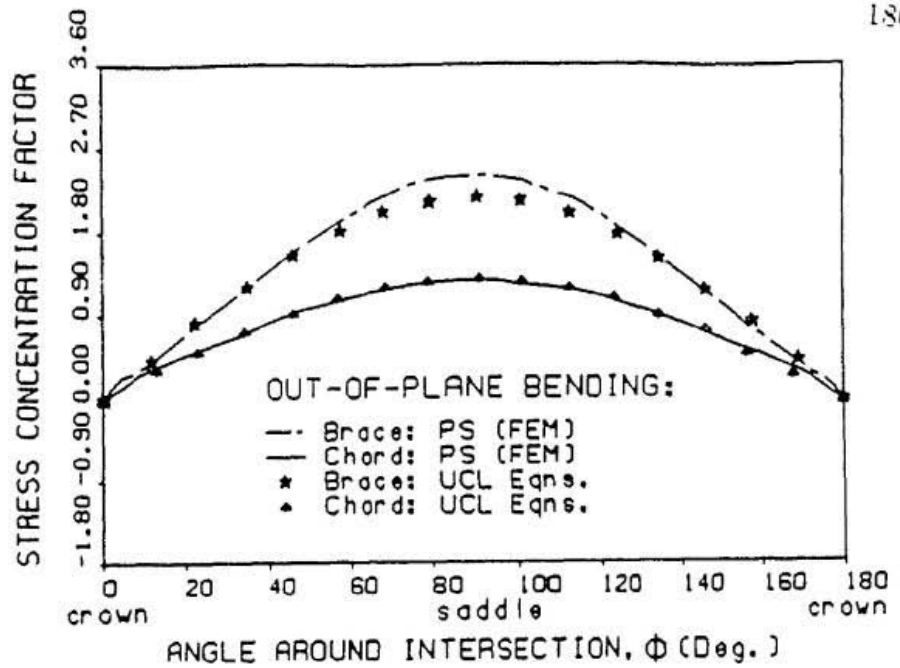

Figure 4.67: Comparison between UCL parametric equations and PS results (OPB) ($\alpha = 9.0$, $\beta = 0.35$, $\tau = 0.2$, $\gamma = 9.0$)

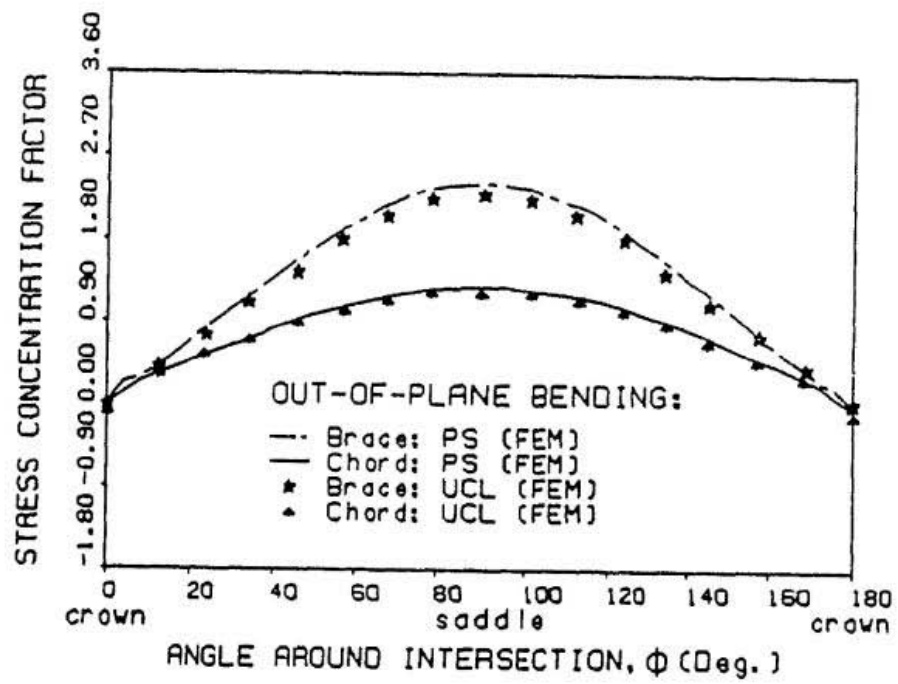

Figure 4.68: Comparison between UCL semi-loof thin-shell FEM data and PS results (OPB) ($\alpha = 9.0$, $\beta = 0.35$, $\tau = 0.2$, $\gamma = 9.0$)

at an angular distance of 25 - 37° as d/D increases and remains constant beyond a certain value of d/D.

2. The slight differences observed between the experimental and numerical results (of MUN, UW and NEL) are due to fabrication defects and the differences in the method of SCF computations between the experimental and numerical stresses (radial and principal stresses).

3. It is observed that when the τ ratio is less than 0.6, the brace hot spot stress is higher than the chord hot spot stress for all the three loading cases. Hence there is a possibility of the brace cracking occurring first below this τ ratio. The thickness effect of the tubular joint intersection tends to reduce the SCF values at the junction.

4. The nature of the stress distribution around the intersection and the amount of work done around the joint seems to determine the total life of joint. Since the in-plane load seems to spend the largest work during deformation, it would tend to have the lowest fatigue life and the out-of-plane load the highest fatigue life.

5. The absence of the plug tends to make the joint fail catastrophically and the failure may occur in the brace than in the chord.

6. The SCF values predicted by the Memorial University analytical computations match well with those given by the University College, London.

Since large amounts of data were available, the comparative results of 8-node serendipity elements and 9-node Lagragian elements are not given in this thesis. However it could be stated that both elements gave good results and the author opted for the 8-node serendipity elements because of their wider usage.

Chapter 5

Stress Analysis of Stiffened Tubular T-Joints

5.1 General

The stress field in the walls of intersecting tubes is one of the main factors which influences the fatigue life of the unstiffened tubular T-joints. The main governing parameter controlling the level of the stress concentration, around the intersection of the tubes, is the radial flexibility of the chord; hence it is of paramount importance that this parameter be controlled such that the stress distribution around and through the thickness of the joint be a minimum in order to improve the life of the joint. One of the methods, for decreasing the bending stresses in the tube walls, is by means of stiffening the chord by different types of stiffeners; the use of internal ring stiffeners is the most commonly employed technique. Hence, to design a tubular joint for a longer life, it is obvious that the primary task should be to find a method that will reduce the stress concentration factors, around the joint intersection, and the bending of the tube wall that induces high through thickness stress distribution.

It is generally accepted that the conventional S-N fatigue curve procedure can be used for stiffened tubular joints; however, results concerning the values for stress concentration factors for stiffened joints are few. Most of the available literature on this subject have investigated this experimentally; very few studies have been done to present analytical or numerical results. The present study has been carried out to evaluate the stress distribution in complex ring stiffened tubular joints and to validate them by comparing with available experimental results.

The geometric parameters of the tubular joints considered in this study are shown in Figure 5.1. Figure 5.2 shows how the stiffener positions were varied for the case of two stiffeners, while Figure 5.3 shows the positions for one, two and three stiffeners used for comparison purposes.

5.2 Joint Modelling for the Stiffeners

Typical mesh used for the analysis of the stiffened joint is shown in Figure 5.4. As can be seen from this figure, it is obvious that the discretization used in the unstiffened joint case has to be modified in order to use it for the stiffened joint study. In order to examine the usefulness of the above joint modelling, for stiffener placement, and, at the same time, to carry out a reasonable comparison between stiffened and unstiffened joints results, a convergence study was conducted. The convergence study involved the carrying out of a stress analysis on the joint discretization, to be used for stiffener study without the stiffeners in place. Figure 5.4 shows the typical mesh developed for the stiffened tubular joints; the figure illustrates the mesh without the stiffener in place. The results of the stress analysis,

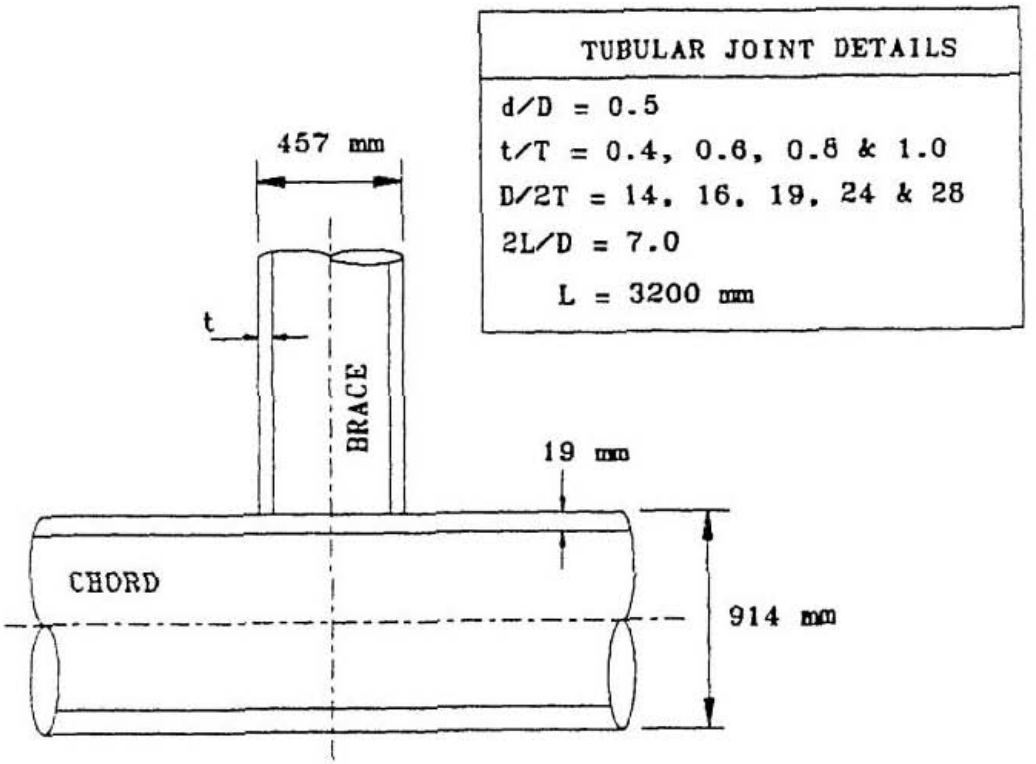

Figure 5.1: Details of the tubular T-joint used for stiffened joint analysis.

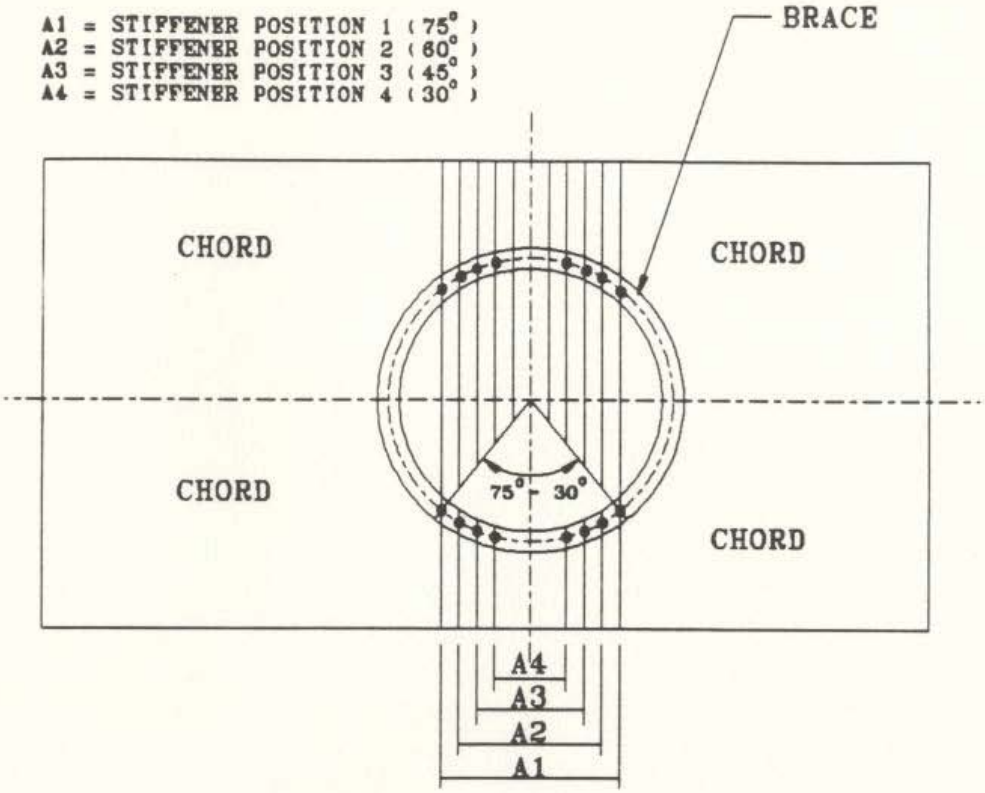

Figure 5.2: Schematic representation of the locations of stiffeners.

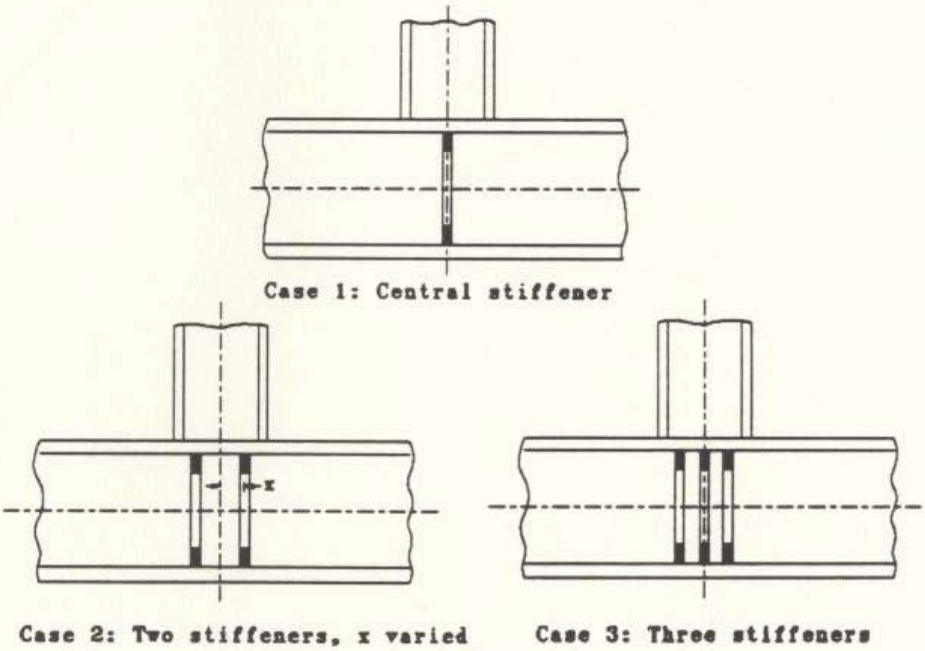

Figure 5.3: Three types of stiffeners investigated.

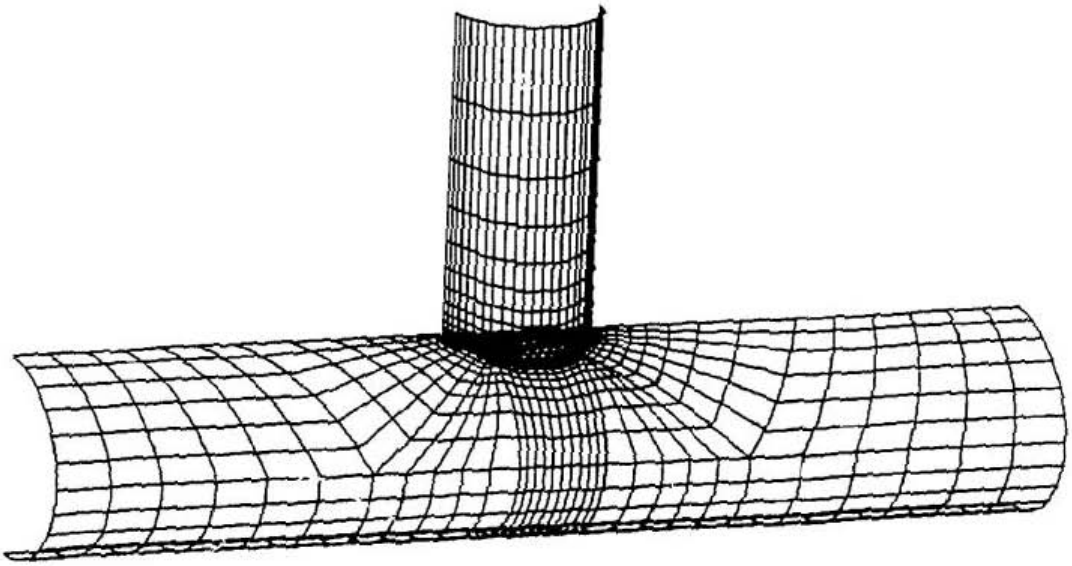

Figure 5.4: Typical computer generated mesh for stiffened tubular joint (without the stiffeners).

Table 5.4: Comparison of SCFs obtained at Waterloo/Memorial Universities and National Engineering Laboratory‡ with the present study: Chord side

Mode of loading		Stiffened T-joints					
		UW (Exp.)		MUN (Exp.)		NEL (Exp.)	PS (Fem)
		crack side	other side	side 1	side 2		
In-plane Bending CROWN	I	3.0	2.9				
	II	3.1	3.1				
	III	3.7	3.6	-	-	4.3	4.9
		Av. (3.2)		-			
SCF_{unst}†/SCF_{st}§		1.31		-		1.33	1.33
Out-of-plane Bending Saddle	I	4.7	4.7				
	II	4.4	4.5	-	-	5.2	5.1
		Av. (4.6)		-			
SCF_{unst}†/SCF_{st}§		3.72		-		4.23	4.16
Axial Saddle	I	6.1	6.1	6.4	5.9		
	II	6.4	6.1	7.0	6.3		
	III	5.6	6.3	6.0	6.3	7.0	7.3
	IV	5.4	6.0	6.7			
		Av.(6.0)		Av.(6.3)			
SCF_{unst}†/SCF_{st}§		3.83		3.81		3.34	3.40

‡Pates et al., 1988

† – SCF_{unst} = Unstiffened joint SCF

§ – SCF_{st} = stiffened joint SCF

Table 5.1: Comparison between two mesh types: (i) Unstiffened joint mesh; (ii) stiffened joint mesh. Axial loading

Joint Geometry $\tau = 1.0$; $\beta = 0.5$; $\alpha = 7.02$; $\gamma = 24$;; Axial Loading				
	Brace SCF		Chord SCF	
Angle around intersection ϕ (Deg.)	Unstiffened joint mesh	Stiffened joint mesh	Unstiffened joint mesh	Stiffened joint mesh
0.00	2.55	2.54	6.22	6.25
7.50	2.68	2.68	6.37	6.40
15.00	3.12	3.12	6.86	6.88
22.50	3.79	3.84	7.67	7.63
30.00	4.74	4.80	8.84	8.77
37.50	5.97	5.97	10.47	10.45
45.00	7.44	7.49	12.45	12.39
52.50	9.18	9.49	14.88	14.86
60.00	11.04	10.77	17.55	17.29
67.50	12.87	12.68	20.19	19.99
75.00	14.55	14.41	22.58	22.46
82.50	15.60	15.50	24,15	24.04
90.00	16.10	16.01	24.75	24.70

Table 5.2: Comparison between two mesh types; (i) Unstiffened joint mesh; (ii) stiffened joint mesh. In-plane bending loading

Joint Geometry $\tau = 1.0$; $\beta = 0.5$; $\alpha = 7.02$; $\gamma = 24$;; IPB Loading				
	Brace SCF		Chord SCF	
Angle around intersection ϕ (Deg.)	Unstiffened joint mesh	Stiffened joint mesh	Unstiffened joint mesh	Stiffened joint mesh
0.00	4.02	4.24	6.56	6.97
7.50	4.06	4.29	6.63	7.04
15.00	4.23	4.48	6.83	7.25
22.50	4.42	4.73	7.08	7.47
30.00	4.62	4.96	7.32	7.69
37.50	4.78	5.09	7.47	7.90
45.00	4.80	5.14	7.39	7.80
52.50	4.68	5.14	7.12	7.58
60.00	4.31	4.44	6.46	6.83
67.50	3.64	3.81	5.40	5.74
75.00	2.71	2.86	4.00	4.27
82.50	1.55	1.65	2.30	2.46
90.00	0.00	0.00	0.00	0.00

Table 5.3: Comparison between two mesh types: (i) Unstiffened joint mesh; (ii) stiffened joint mesh.Out-of-plane bending loading

Joint Geometry $\tau = 1.0$; $\beta = 0.5$; $\alpha = 7.02$; $\gamma = 24$;; OPB Loading				
	Brace SCF		Chord SCF	
Angle around intersection ϕ (Deg.)	Unstiffened joint mesh	Stiffened joint mesh	Unstiffened joint mesh	Stiffened joint mesh
0.00	-0.33	-0.42	-0.81	-0.75
7.50	0.72	0.73	0.96	0.97
15.00	1.12	1.13	1.23	1.25
22.50	1.72	1.72	1.72	1.75
30.00	2.56	2.56	2.71	2.75
37.50	3.71	3.70	4.41	4.44
45.00	5.19	5.20	6.74	6.75
52.50	6.97	7.14	9.58	9.65
60.00	8.95	8.78	12.78	12.56
67.50	10.95	10.79	15.95	15.74
75.00	12.79	12.64	18.81	18.63
82.50	13.97	13.97	20.70	20.52
90.00	14.52	14.52	21.44	21.28

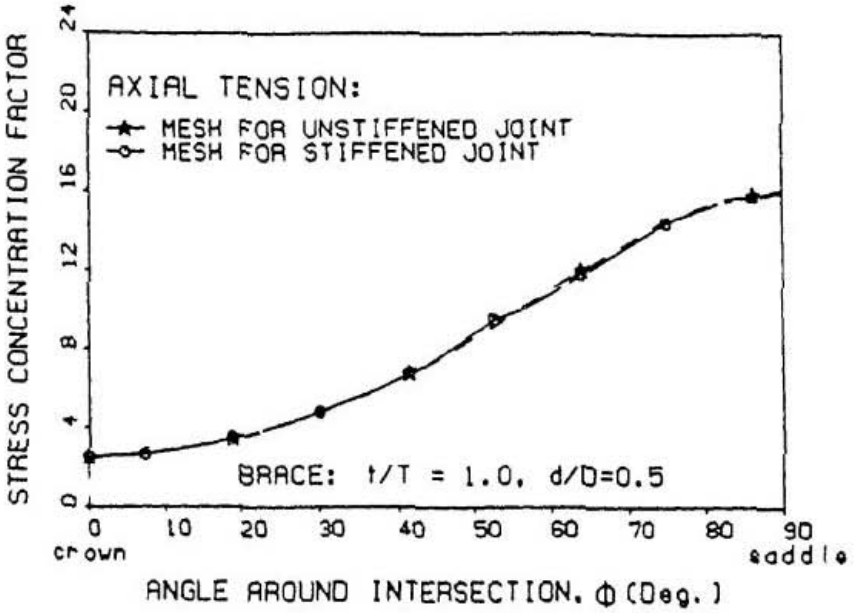

Figure 5.5: Brace SCF results for stiffened and unstiffened joint mesh (Axial) (α = 7.02, γ = 24)

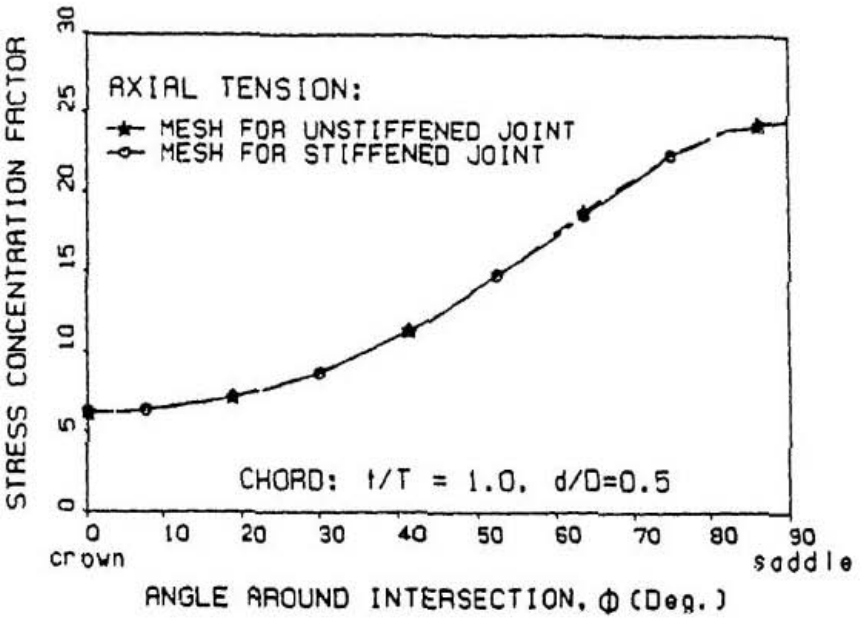

Figure 5.6: Chord SCF results for stiffened and unstiffened joint mesh (Axial) (α = 7.02, γ = 24)

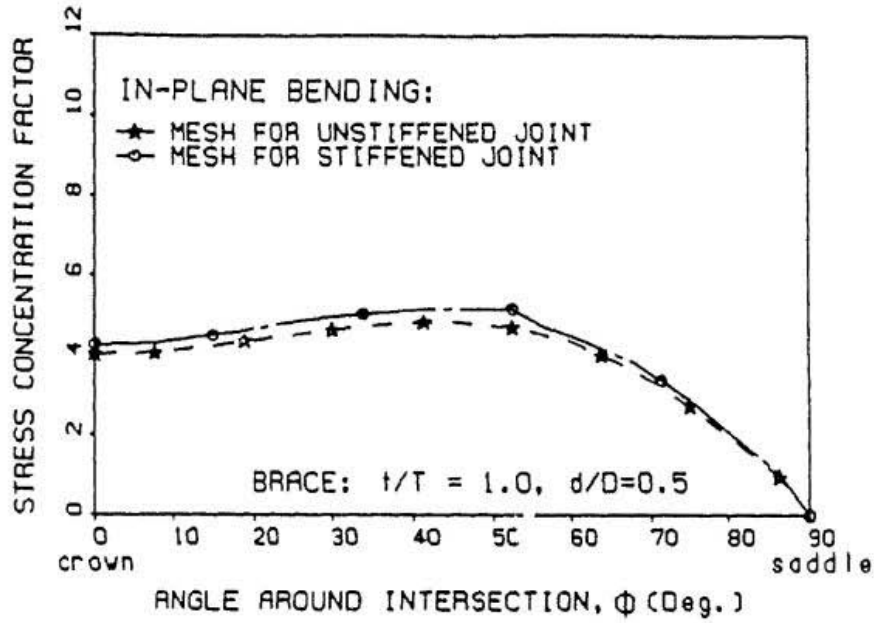

Figure 5.7: Brace SCF results for stiffened and unstiffened joint mesh (IPB) (α = 7.02, γ = 24)

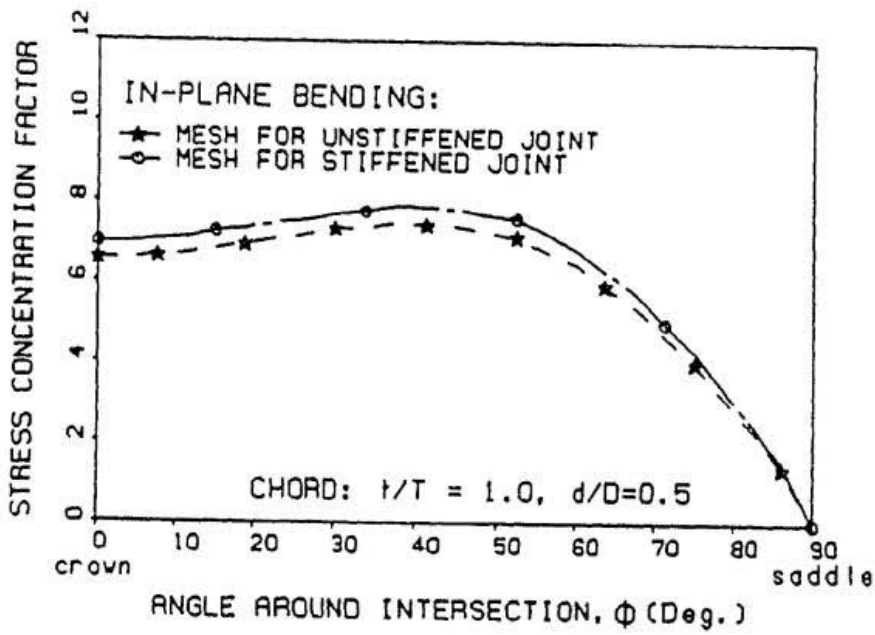

Figure 5.8: Chord SCF results for stiffened and unstiffened joint mesh (IPB) (α = 7.02, γ = 24)

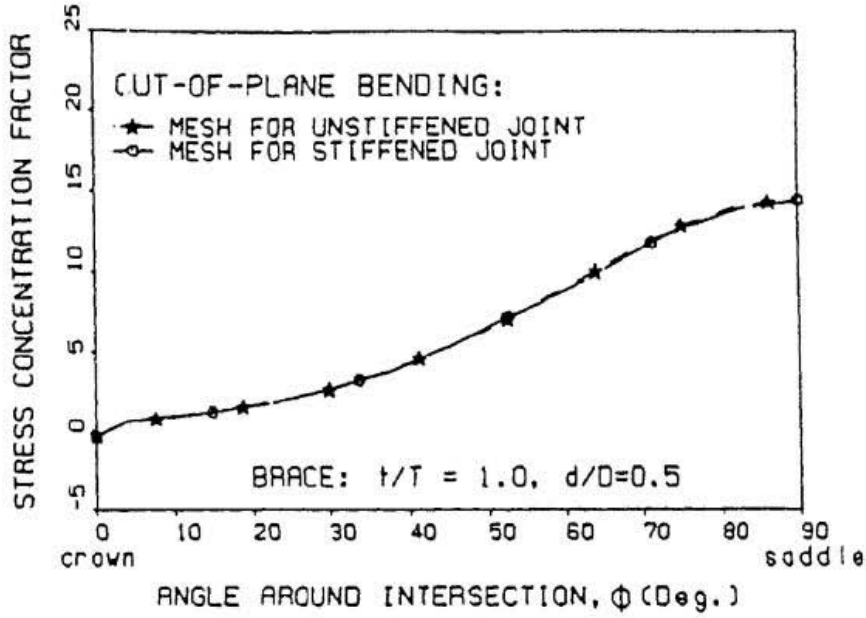

Figure 5.9: Brace SCF results for stiffened and unstiffened joint mesh (OPB) (α = 7.02, γ = 24)

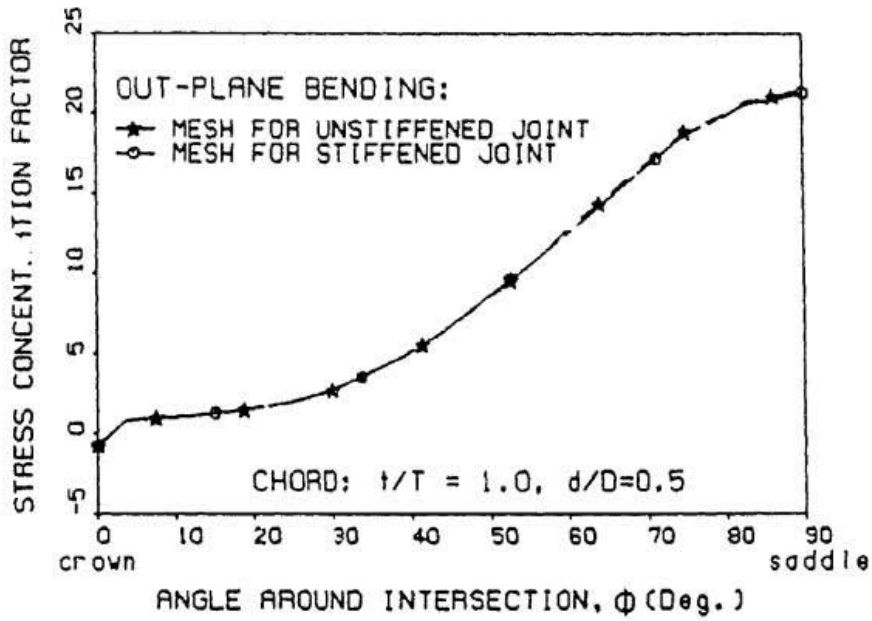

Figure 5.10: Chord SCF results for stiffened and unstiffened joint mesh (OPB) (α = 7.02, γ = 24)

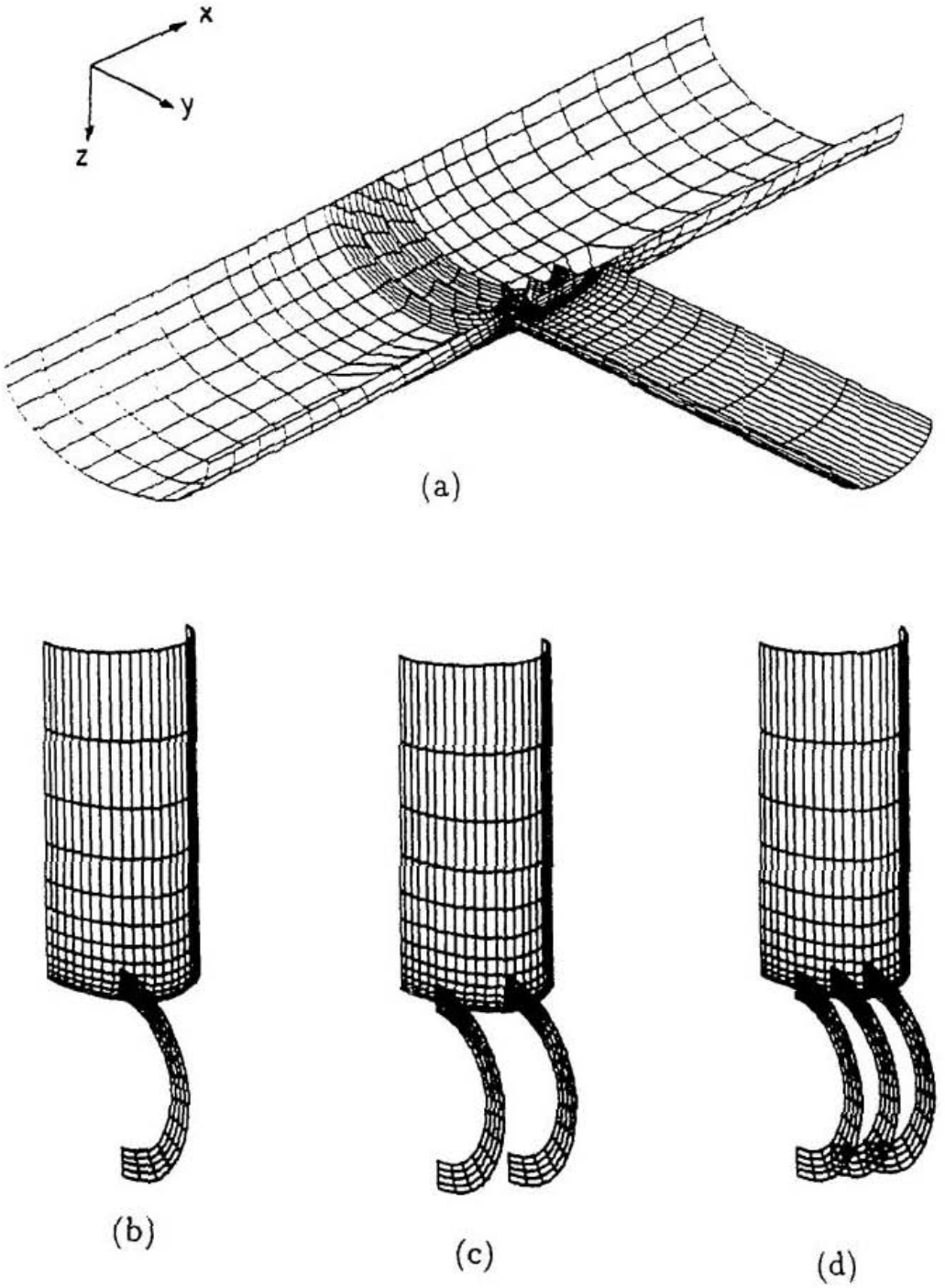

Figure 5.11: Computer mesh generation showing: (a) the half-joint with 3 internal ring stiffeners, (b) half-brace with one stiffener, (c) half-brace with two stiffeners, and (d) half-brace with three stiffeners.

5.4 Results and Discussion

This section describes the results obtained for the stiffened joints in the present study. As it is common in the context of tubular joints, the stress concentration factors (SCF) were calculated by dividing the principal stresses with the nominal stress in brace. The results from the stiffened joints analysis show that for the case of axial and out-of-plane bending load cases, addition of the stiffener to the chord at certain locations greatly reduces the stress concentration factors and gives a more uniform distribution of stresses on the chord side. No appreciable reduction in the SCFs was observed for the case of in-plane loading. On the brace side although the magnitudes of stress concentration factors were reduced at the saddle and the crown positions, generally it was observed that there was a sharp increase in the stress concentration factors at the stiffener locations. This sharp increase was more pronounced in the case of a single stiffener. This is especially so because of the stiffener location at the regions of high stress concentration (e.g., saddle for axial and out-of-plane bending loads). In the analysis, the maximum stress in the tubular joint was always found to be on the exterior surface of the tubes. However, it may be anticipated that there could be occasions when the maximum stress in the structure could occur in the stiffener; this case will be explored in a subsequent section.

5.4.1 Effect of the Stiffener Location

The comparison of the SCF results obtained in this study for two stiffeners at positions 2, with the experimental results of steel tubular T-joints carried out at the

University of Waterloo, Memorial University and National Engineering Laboratories are presented in Table 5.4. These values are at the saddle point location for the axial and out-of-plane bending loads cases and at the crown for the in-plane bending loads. It must be noted that in the MUN and Waterloo University SCF comparison results, the ratio of radial (radii emanating from the centre of the brace) tensile stresses to brace nominal stress was taken as SCFs, whereas in the finite element study, the SCFs were computed from the principal stresses. The results seem to indicate that in stiffened joints, even at the crown and saddle positions large tangential stresses are present which increase the principal stresses considerably above the radial stresses (around the chord intersection).

A steel tubular T-joint tested, as part of a study on stiffened joints, at the National Engineering Laboratory was analyzed using semi-loof shell elements and combination of shell elements and 3-dimensional brick elements by Aaghaakouchak and Dharmavasan (1990); this same tubular joint was analyzed in this study for comparison purposes. The joint was a T-joint stiffened by two ring stiffeners having the geometric data as shown in Table 5.5. The comparison of results obtained in the present study with the experimental and analytical studies using semi-loof shell elements and combined shell and brick elements are shown in Tables 5.6 and 5.7. It is observed that the results of the present study compare more favorably with the results of the experiments than the other two studies mentioned above.

Since the results presented by the MUN and University of Waterloo experimental studies on stiffened joints gave only the radial SCF values (radii emanating from the centre of the brace), detailed comparisons could not be made with the present

Table 5.4: Comparison of SCFs obtained at Waterloo/Memorial Universities and National Engineering Laboratory‡ with the present study: Chord side

Mode of loading		Stiffened T-joints					
		UW (Exp.)		MUN (Exp.)		NEL (Exp.)	PS (Fem)
		crack side	other side	side 1	side 2		
In-plane Bending CROWN	I	3.0	2.9				
	II	3.1	3.1				
	III	3.7	3.6	-	-	4.3	4.9
		Av. (3.2)		-			
SCF_{unst}†/SCF_{st}§		1.31		-		1.33	1.33
Out-of-plane Bending Saddle	I	4.7	4.7				
	II	4.4	4.5	-	-	5.2	5.1
		Av. (4.6)		-			
SCF_{unst}†/SCF_{st}§		3.72		-		4.23	4.16
Axial Saddle	I	6.1	6.1	6.4	5.9		
	II	6.4	6.1	7.0	6.3		
	III	5.6	6.3	6.0	6.3	7.0	7.3
	IV	5.4	6.0	6.7			
		Av.(6.0)		Av.(6.3)			
SCF_{unst}†/SCF_{st}§		3.83		3.81		3.34	3.40

‡Pates et al., 1988

† - SCF_{unst} = Unstiffened joint SCF

§ - SCF_{st} = stiffened joint SCF

Table 5.5: Geometric data of the stiffened model used for comparison between the present study and the National Engineering Laboratory experimental results and UCL semi-loof shell element and combined shell and brick elements.

	D	d	T	t	L	HS	TS	DS
Joint dimensions (mm)	914	457	16	16	2458	100	16	266

HS - stiffener height.
TS - stiffener thickness.
DS - Distance between stiffeners.

Table 5.6: Comparison between SCFs obtained in the present study, National Engineering Laboratory experimental results and UCL semi-loof shell element and combined shell and brick elements - crown position (Axial).

STIFFENED JOINT: BRACE							
CROWN				SADDLE			
NEL (exp.)	PS‡ (fem)	UCL† (fem)	UCL* (fem)	NEL (exp.)	PS‡ (fem)	UCL† (fem)	UCL* (fem)
1.83	2.67	3.10	2.26	4.25	4.20	4.50	3.42

‡ - Present study (Degenerated Shell Element)
† - Aaghaakouchak et al., 1990 (Semi-Loof Shell Element)
* - Aaghaakouchak et al., 1990 (Shell + 3-D Elements)

Table 5.7: Comparison between SCFs obtained in the present study, National Engineering Laboratory experimental results and UCL semi-loof shell element and combined shell and brick elements - *crown position (Axial)*

STIFFENED JOINT: CHORD							
CROWN				SADDLE			
NEL (exp.)	PS‡ (fem)	UCL† (fem)	UCL* (fem)	NEL (exp.)	PS‡ (fem)	UCL† (fem)	UCL* (fem)
4.43	4.00	4.02	3.69	7.30	7.30	7.92	6.69

‡ - Present study (Degenerated Shell Element)
† - Aaghaakouchak et al., 1990 (Semi-Loof Shell Element)
* - Aaghaakouchak et al., 1990 (Shell + 3-D Elements)

investigation which computed the principal stresses rather than radial stresses. Hence except the SCF comparisons no other detailed comparisons are made as in the case of unstiffened tubular T-joints. Moreover the presence of radial (to the weld toe) and tangential (to the weld toe) stresses at the intersection makes the fatigue cracking to be multimodal; hence no effort is made in correlating the fatigue lives of stiffened tubular T-joints in Chapters 6 and 7. The presence of significant mode II and/or mode III cracking would make the fracture mechanics analysis quite complex. Hence a conscious decision is made to exclude all stiffened tubular experimental results from fracture mechanics investigations.

The stress analysis results of one of the stiffened T-joints, under axial, in-plane and out-of-plane bending loads, with two stiffeners located at different positions (positions 1 to 4, Figures 5.2 and 5.3) are shown in Figures 5.12, 5.13 and 5.14. These figures show that the best positions for the stiffeners are the regions around the high stress concentration zones of stiffened tubular joints; the region is located near the saddle for the axial and out-of-plane bending cases and close to the crown for the case of in-plane bending load. It was observed in the final analysis that, for the four positions investigated in this study, position 2 and 3 gave the most optimum location for axial and out-of-plane bending load cases, with position 1 being the most favourable in the stress concentration reduction for the in-plane bending load. It can there be concluded that, as long as the stiffeners are located in these regions of high stress concentration (of unstiffened tubular joints), the maximum stress concentration values of stiffened tubular joints are not too sensitive to the exact location of the stiffener. The middle half of the plug seems to be the optimum positions for the axial and out-of plane bending loads; the remaining outer two

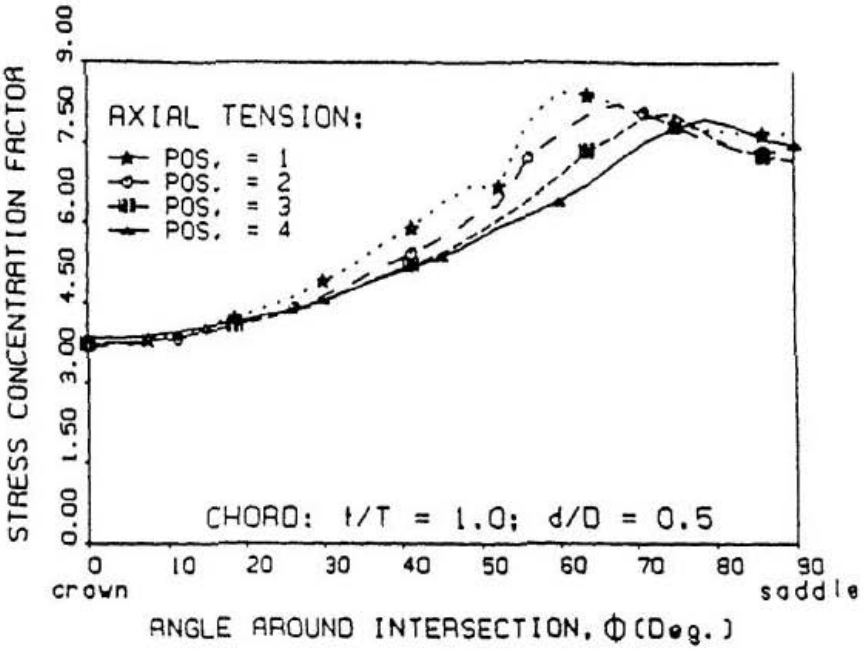

Figure 5.12: Effect of stiffener positions on SCF (Axial) ($\alpha = 7.02$, $\gamma = 24$)

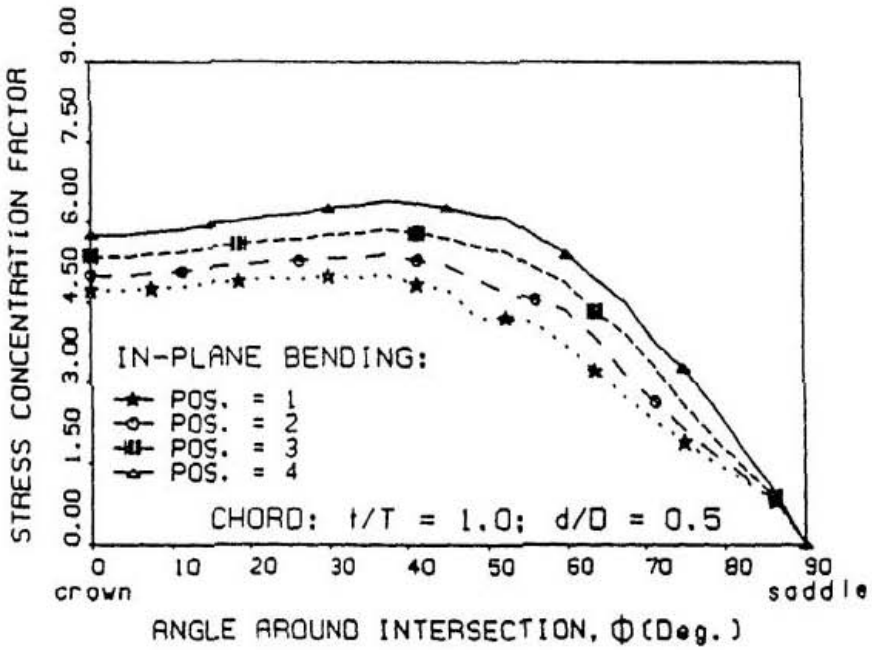

Figure 5.13: Effect of stiffener positions on SCF (IPB) ($\alpha = 7.02$, $\gamma = 24$)

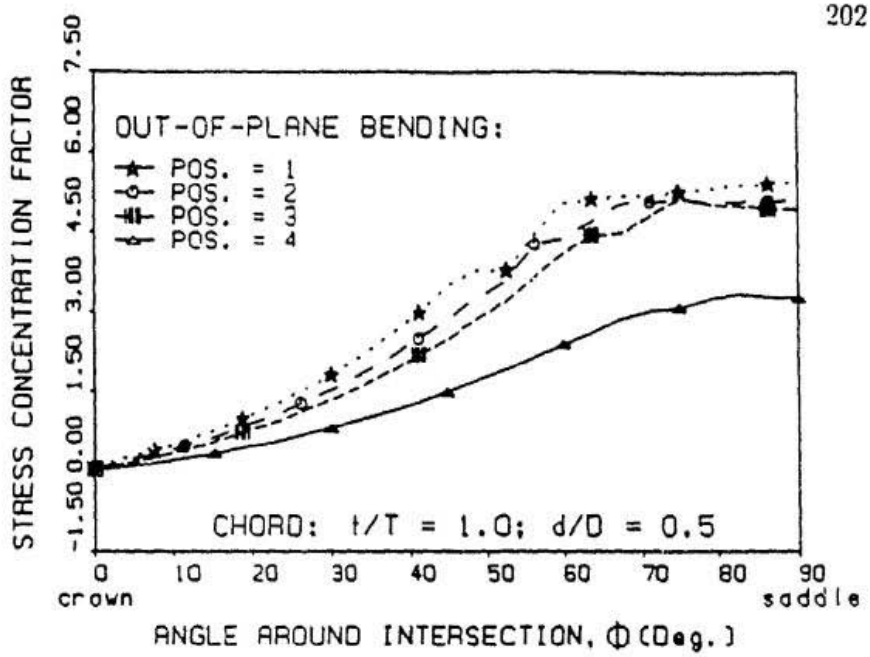

Figure 5.14: Effect of stiffener positions on SCF (OPB) ($\alpha = 7.02$, $\gamma = 24$)

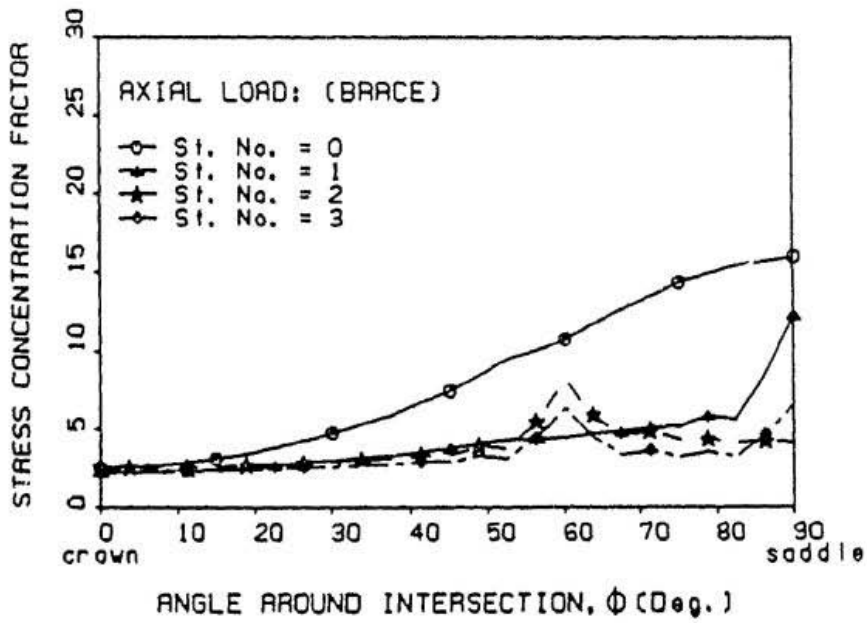

Figure 5.15: Effect of number of stiffeners on the brace SCF (Axial) ($\alpha = 7.02$, $\beta = 0.5$, $\tau = 1.0$, $\gamma = 24$)

quarters of the plug are recommended as optimum positions for in-plane bending case.

5.4.2 Effect of the Number of Stiffeners

Figures 5.15 to 5.20 illustrate the effect of the number of stiffeners on the stress distribution around the intersection. It is evident from these figures that as long as the stiffeners are located at the correct positions, increasing the number of stiffeners results in increasing the chord moment of inertia and consequently reduces the chord radial flexibility; this in turn reduces the stress concentration factor on the chord side. Their effect on the brace side is less than that on the chord side. It is also observed from these figures that when only one stiffener is used (at the saddle), there is a relatively higher stress concentration factor in the brace at the saddle and in the stiffener than in the chord. The cause of this is explained as follows: at locations around the single stiffener (saddle) the local chord stiffness is high and this causes a high proportion of the load to be transferred from the brace to the chord in this region. These results probably explain the experimental observations of Sawada et al. (1979), on the static and fatigue tests of T-joints stiffened by one internal ring at the saddle position, in which they reported crack initiation and growth in the brace and stiffener. This also confirms the finding of Dharmavasan and Aaghaakouchak (1988) using semi-loof shell element and combined shell and three dimensional brick elements, wherein similar results were given. Figures 5.21 to 5.24 show the above results put in another form to illustrate the effect of number of stiffeners on the stress concentration factors at the saddle and crown locations. For the axial and out-of-plane loads, the increase in the number of stiffeners progressively reduces the

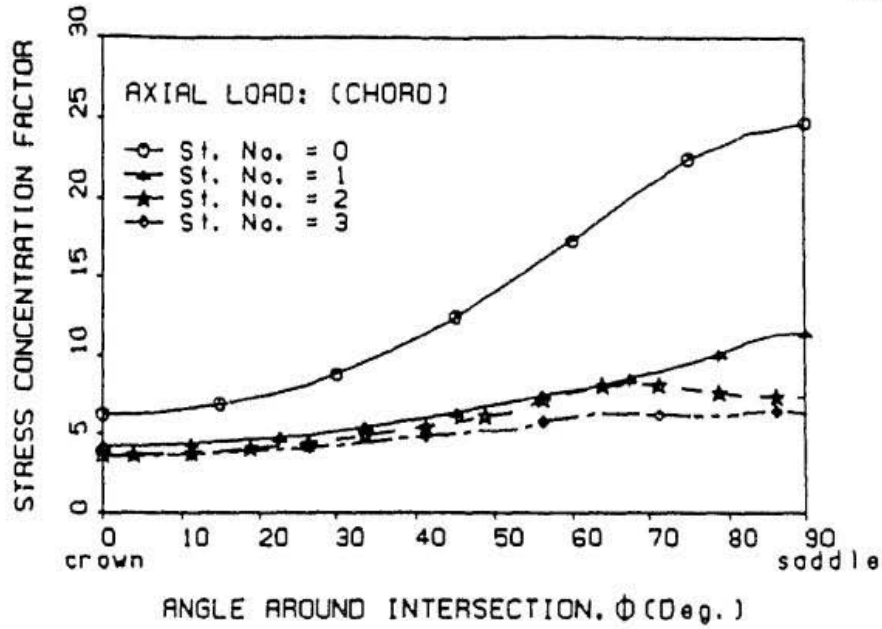

Figure 5.16: Effect of number of stiffeners on the chord SCF (Axial) (α = 7.02, β = 0.5, τ = 1.0, γ = 24)

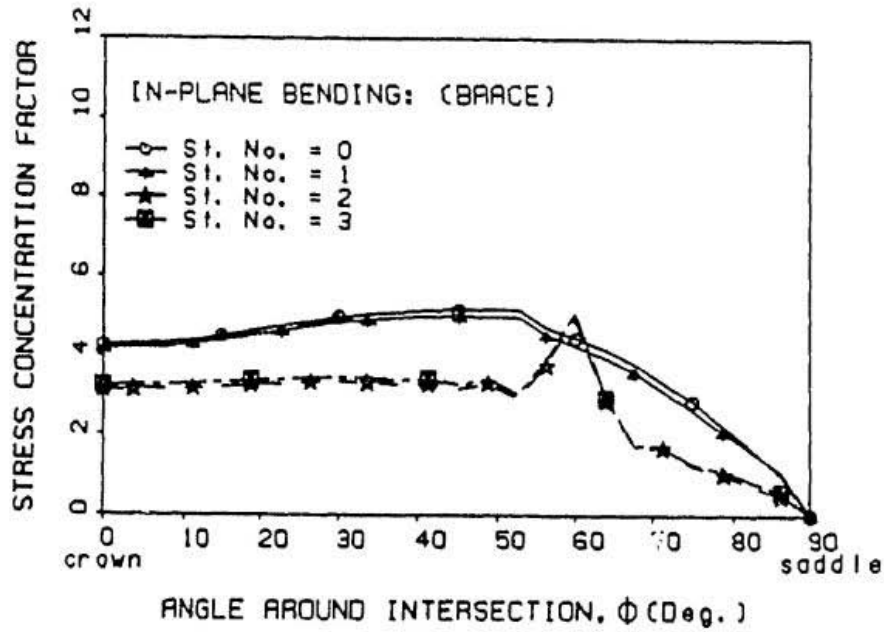

Figure 5.17: Effect of number of stiffeners on the brace SCF (IPB) (α = 7.02, β = 0.5, τ = 1.0, γ = 24)

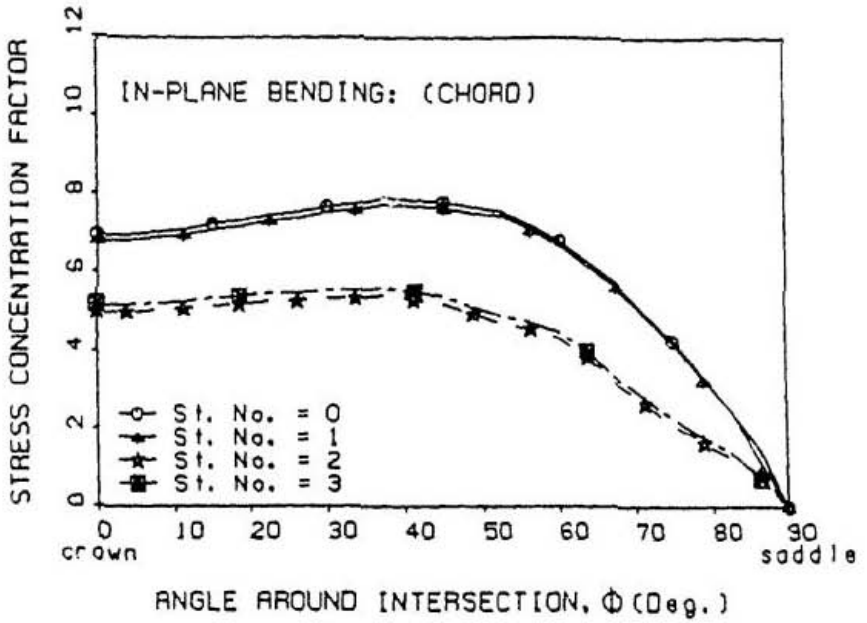

Figure 5.18: Effect of number of stiffeners on the chord SCF (IPB) (α = 7.02, β = 0.5, τ = 1.0, γ = 24)

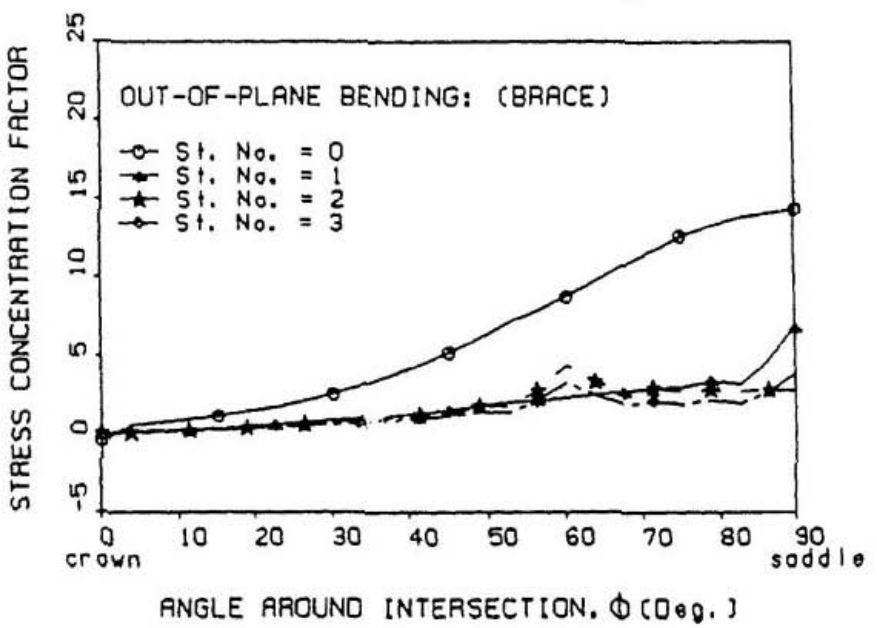

Figure 5.19: Effect of number of stiffeners on the brace SCF (OPB) (α = 7.02, β = 0.5, τ = 1.0, γ = 24)

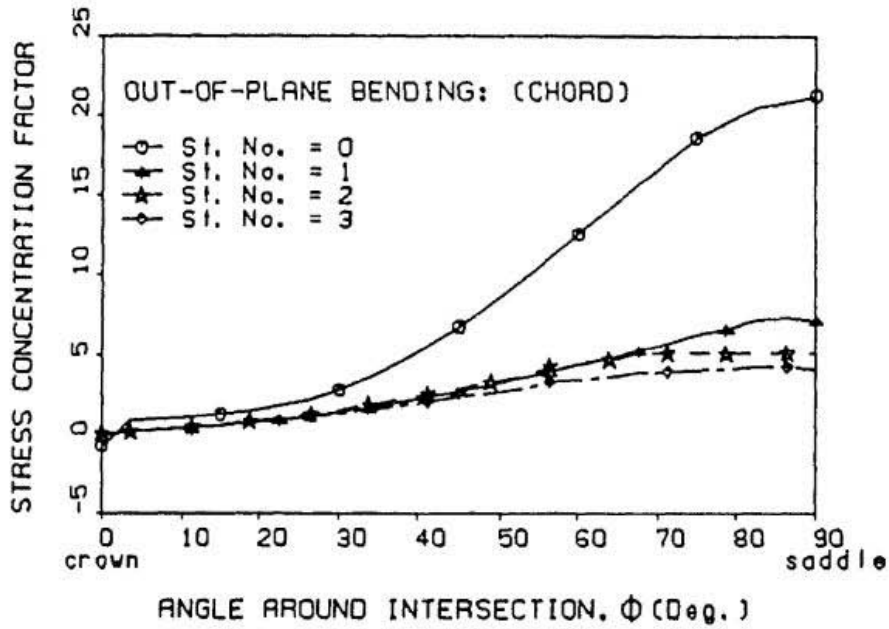

Figure 5.20: Effect of number of stiffeners on the chord SCF (OPB) (α = 7.02, β = 0.5, τ = 1.0, γ = 24)

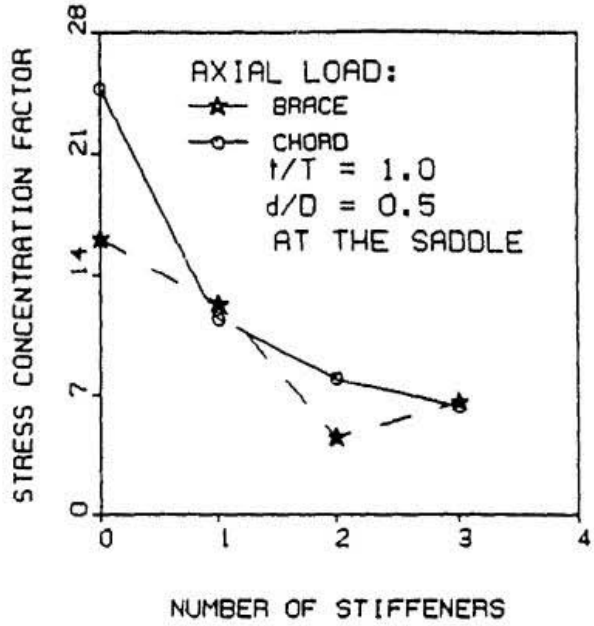

Figure 5.21: SCF vs. number of stiffeners at the saddle (Axial) ($\alpha = 7.02$, $\gamma = 24$)

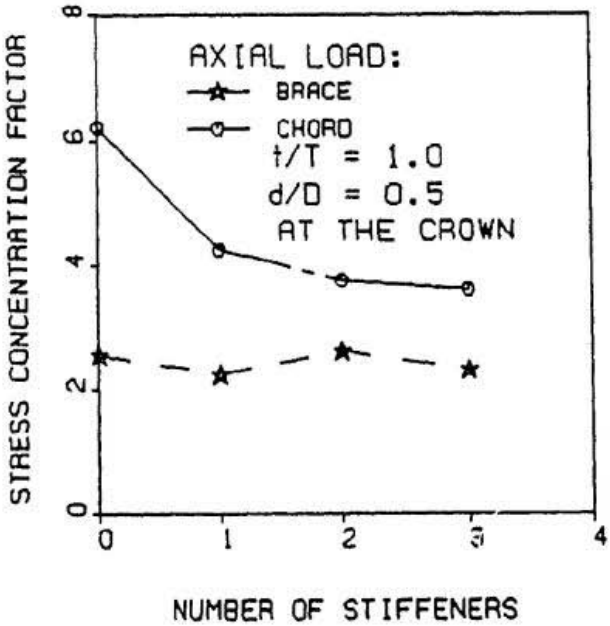

Figure 5.22: SCF vs. number of stiffeners at the crown (Axial) ($\alpha = 7.02$, $\gamma = 24$)

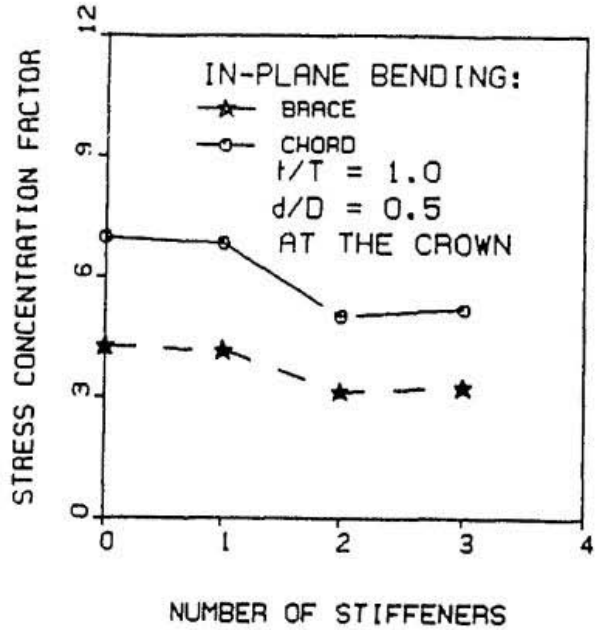

Figure 5.23: SCF vs. number of stiffeners at the crown (IPB) ($\alpha = 7.02$, $\gamma = 24$)

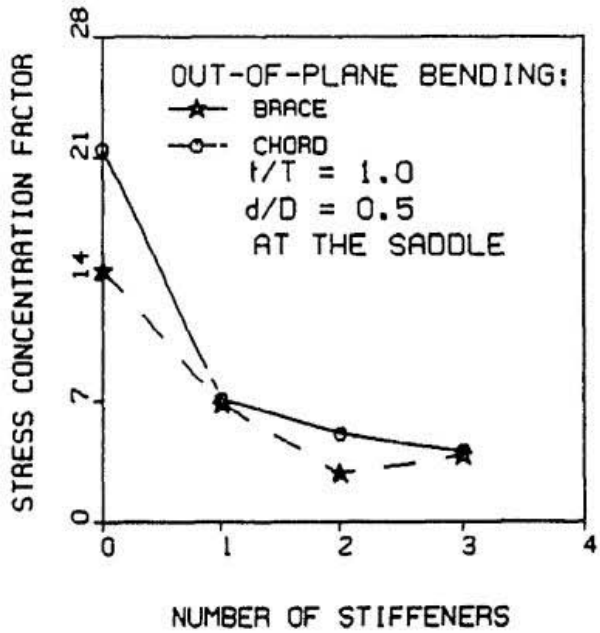

Figure 5.24: SCF vs. number of stiffeners at the saddle (OPB) ($\alpha = 7.02$, $\gamma = 24$)

stress concentration factor at the saddle and crown. For the in-plane bending the results of (0,1) and (2,3) stiffeners seems to be clustered in two separate groups: this is due to the fact of the stiffener located at the saddle being ineffective against bending loads. The single stiffener (located at the saddle) exhibits a sharp increase of the brace stress concentration factor at the brace saddle for both axial and out-of-plane bending load cases; for the in-plane loading, a single stiffener located at the saddle does not show any change from the no stiffener case.

5.4.3 Effect of the Stiffener Size

The effect of stiffener size was investigated by adding stiffeners of different sizes to the joint at position 2 (A2, see Figure 5.2). The results of this analysis for three different stiffener heights (HS) of 100mm, 120mm and 140mm and three different stiffener thicknesses (TS) of 19mm, 21mm and 24mm are shown in Figure 5.25 through 5.28 for the axial load case. These figures show that the change in the stiffener height has the stronger influence in reducing the stress concentration factor compared to the stiffener thickness. Similar results were obtained for out-of-plane and in-plane bending load cases. The conclusion that can be drawn from these results is that the moment of inertia of the stiffener, in the radial directions of the chord, is one of the main parameter which controls the level of stress concentration factor in a stiffened joint. These results at first glance may suggest that using thin tall stiffeners would lead to optimum SCF values; but this is not true. When the stress concentration of the stiffener is examined, it shows that this results in high stress concentration factors in the stiffener. The increase in the stiffener SCFs because of small thickness is significant, and it may therefore be wise to avoid the

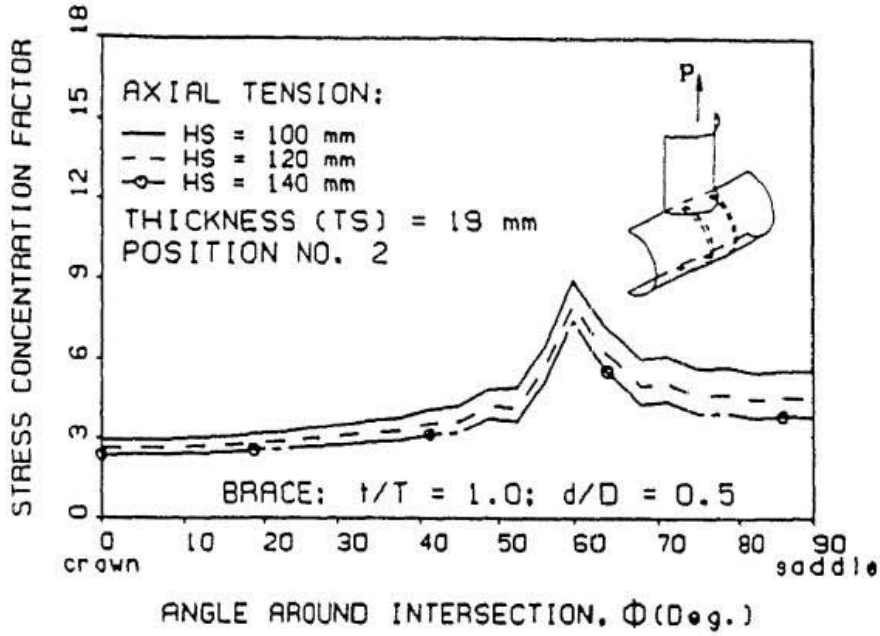

Figure 5.25: Effect of stiffener height (HS) on SCF in the brace (Axial) ($\alpha = 7.02$, $\gamma = 24$)

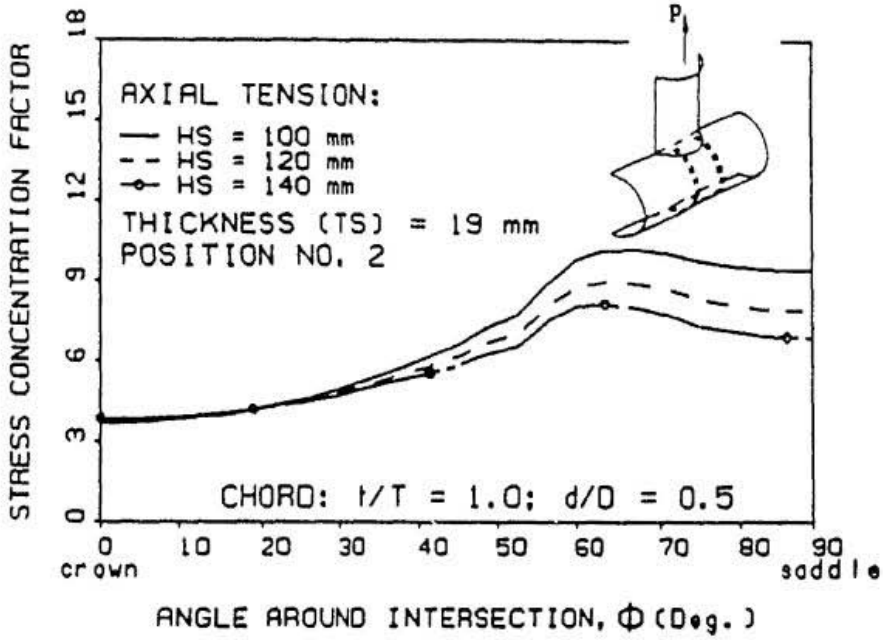

Figure 5.26: Effect of stiffener height (HS) on SCF in the chord (Axial) ($\alpha = 7.02$, $\gamma = 24$)

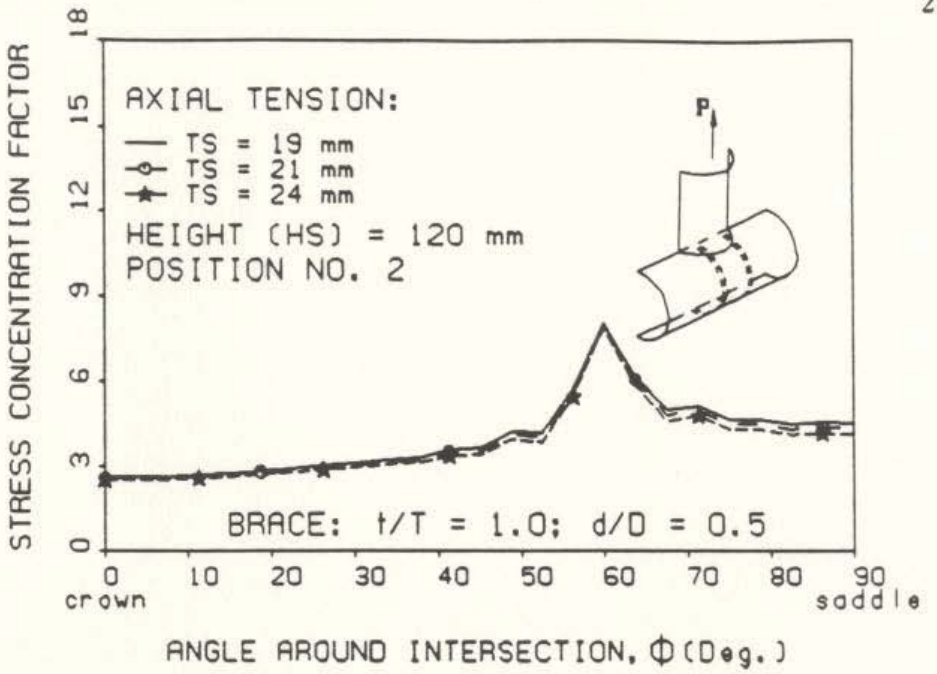

Figure 5.27: Effect of stiffener thickness (TS) on SCF in the brace (Axial) ($\alpha = 7.02$, $\gamma = 24$)

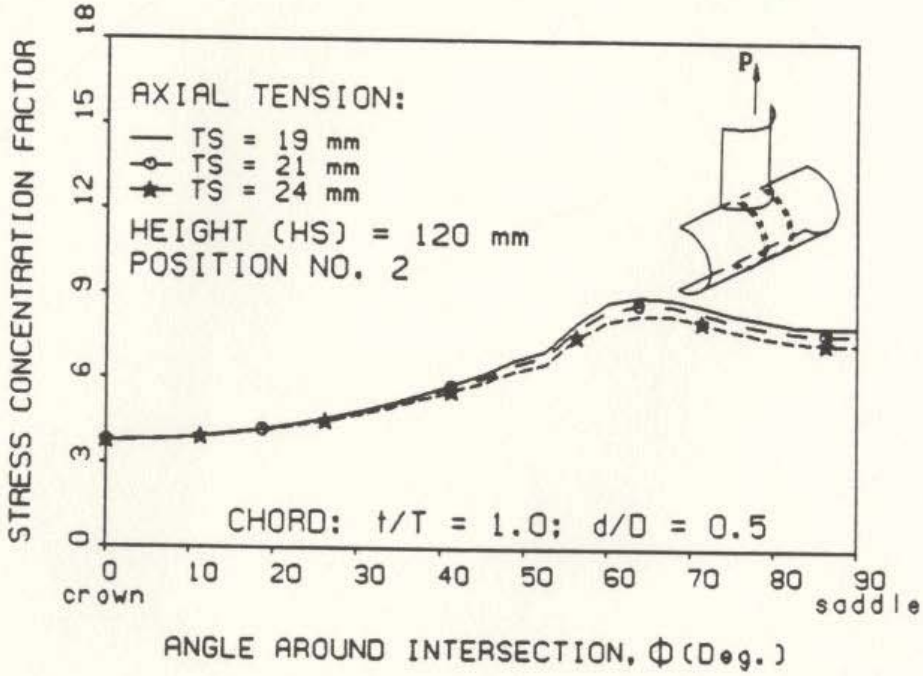

Figure 5.28: Effect of stiffener thickness (TS) on SCF in the chord (Axial) ($\alpha = 7.02$, $\gamma = 24$)

use of relatively thin stiffeners for stiffening tubular welded joints. One question that must be asked then is , what is the possible limit on minimum stiffener thickness? Other studies on this aspect have shown that the minimum thickness of the stiffener could be the same as the brace thickness when only few stiffeners are used (Dharmavasan and Aaghaakouchak, 1988).

5.4.4 Effect of the Thickness (τ) and Thinness (γ) Ratios

Figures 5.29 to 5.34 show the effect of the ratio of the brace thickness to that of the chord on the stress concentration factor, around the stiffened joint, under axial, in-plane and out-of-plane bending load cases. It is shown in these figures that for a constant stiffener thickness, increase in the chord thickness or a decrease in brace thickness, smaller τ (= t/T) ratio results in the reduction of the stress concentration factor. This result validates one of the methods that has often been used to stiffened tubular joints in which the thickness of the chord, for a given length termed 'joint can', is increased.

The results of the parametric study on the influence of the thickness ratios τ (= t/T) and the thinness ratios γ (= D/2T) are presented in Figures 5.35 through 5.40. Figures 5.35 to 5.38 show that depending on the placement of the stiffener and the τ value, the maximum stress concentration factor can occur either in the brace or the chord. For instance when $\beta = 0.5$, and $\tau < 0.54$, the maximum SCF occurs in the brace under axial load (Figure 5.36). Similarly these ratios change to $\tau < 0.62$ for in-plane bending and $\tau < 0.48$ for out-of-plane bending cases. It is also evident from Figures 5.39 and 5.40, that the SCF of the stiffened joint is

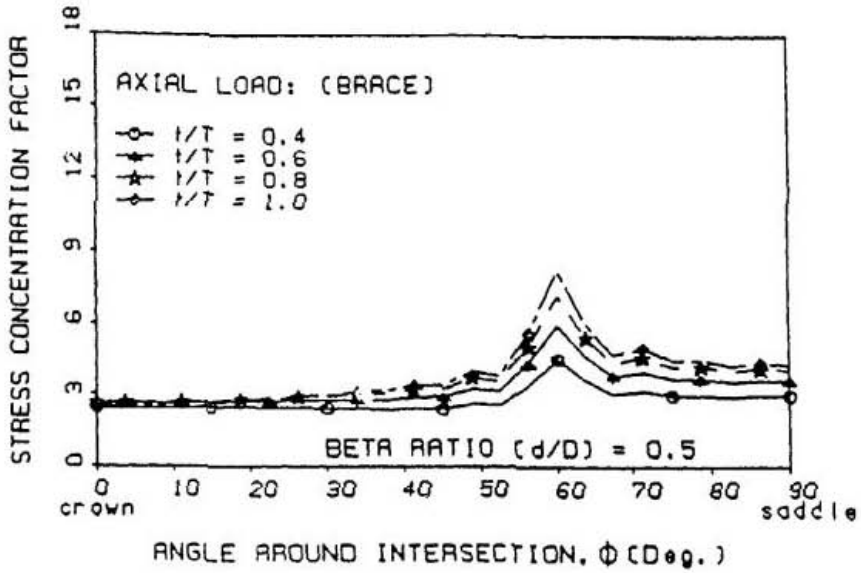

Figure 5.29: Variation of brace SCF with angle ϕ, showing the effect of τ ratio (Axial) (α = 7.02, γ = 24, Position No. 2, TS = 19mm, HS = 120mm)

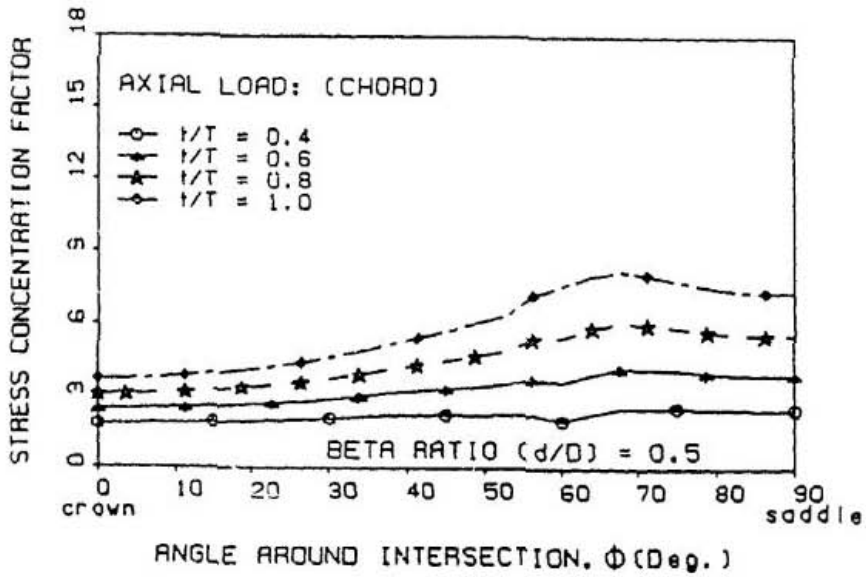

Figure 5.30: Variation of chord SCF with angle ϕ, showing the effect of τ ratio (Axial) (α = 7.02, γ = 24, Position No. 2, TS = 19mm, HS = 120mm)

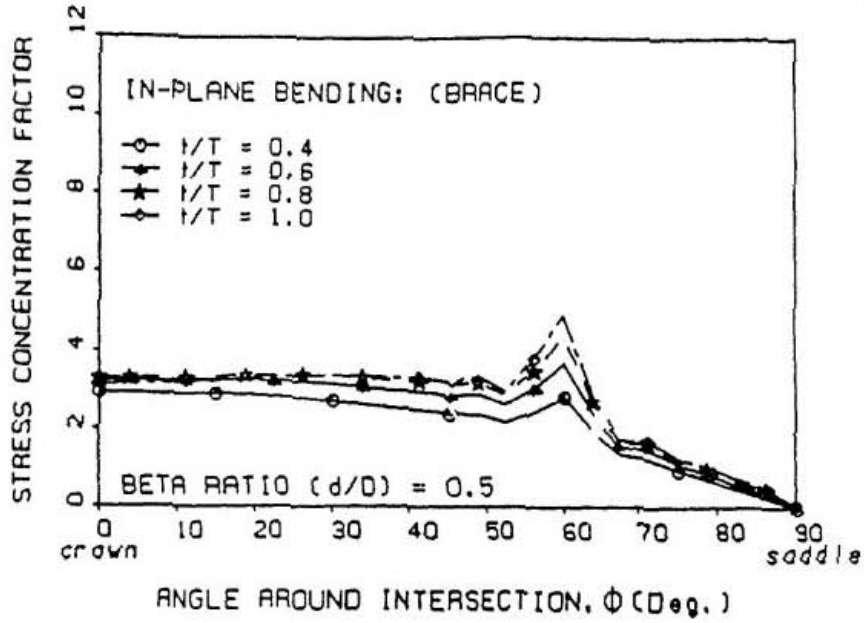

Figure 5.31: Variation of brace SCF with angle ϕ, showing the effect of τ ratio (IPB) (α = 7.02, γ = 24, Position No. 2, TS = 19mm, HS = 120mm)

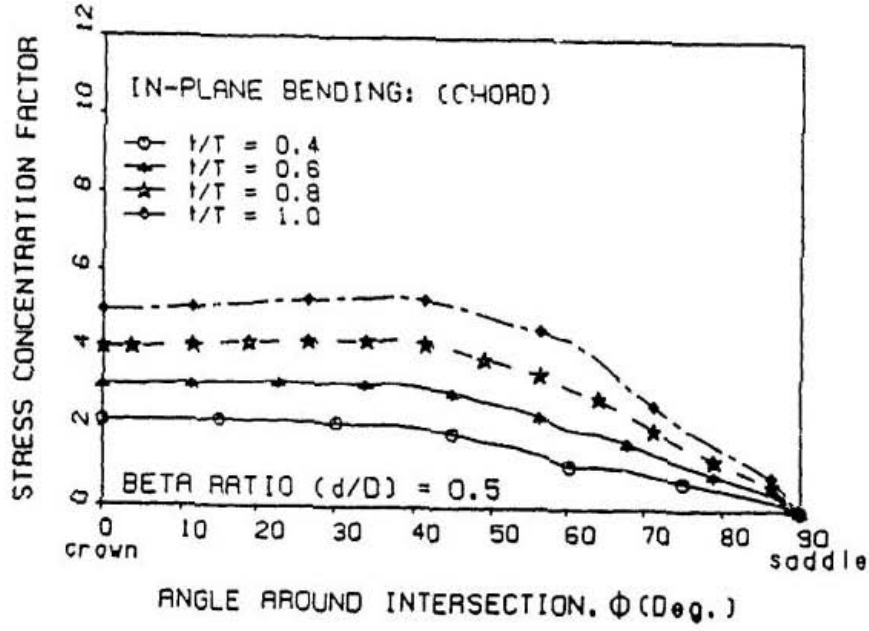

Figure 5.32: Variation of chord SCF with angle ϕ, showing the effect of τ ratio (IPB) (α = 7.02, γ = 24, Position No. 2, TS = 19mm, HS = 120mm)

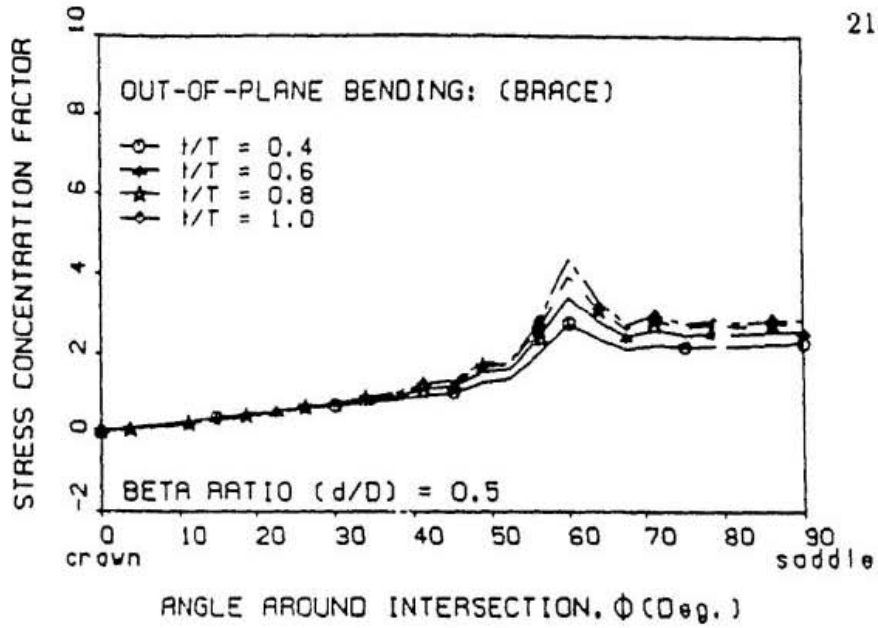

Figure 5.33: Variation of brace SCF with angle ϕ, showing the effect of τ ratio (OPB) (α = 7.02, γ = 24, Position No. 2, TS = 19mm, HS = 120mm)

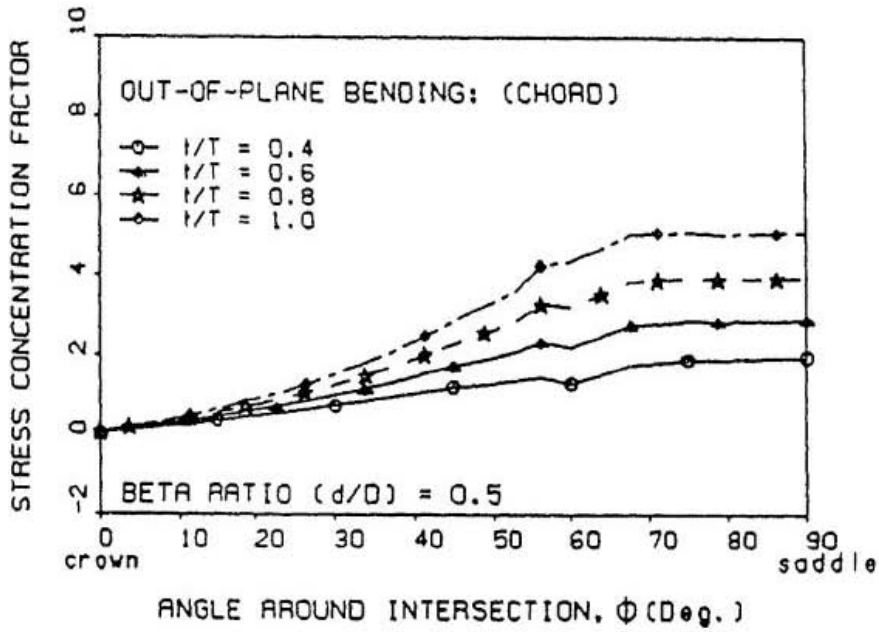

Figure 5.34: Variation of chord SCF with angle ϕ, showing the effect of τ ratio (OPB) (α = 7.02, γ = 24, Position No. 2, TS = 19mm, HS = 120mm)

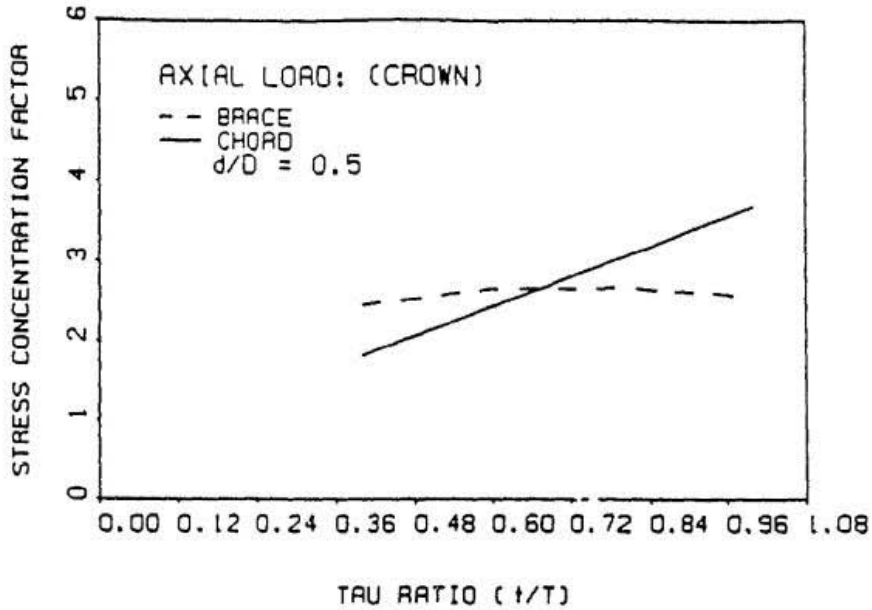

Figure 5.35: SCF vs. τ ratio at the crown (Axial) (α = 7.02, γ = 24, Position No. 2, TS = 19mm, HS = 120mm)

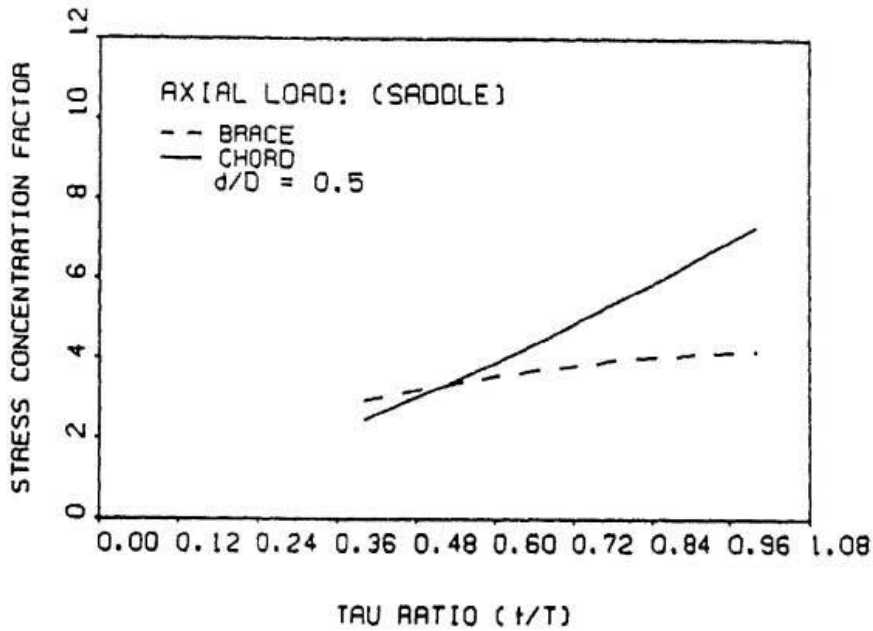

Figure 5.36: SCF vs. τ ratio at the saddle (Axial) (α = 7.02, γ = 24, Position No. 2, TS = 19mm, HS = 120mm)

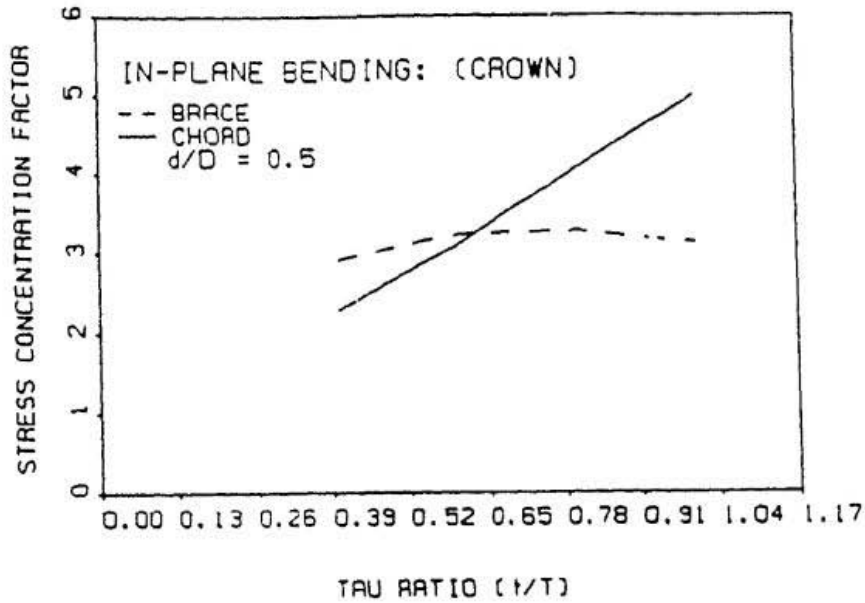

Figure 5.37: SCF vs. τ ratio at the crown (IPB) (α = 7.02, γ = 24, Position No. 2, TS = 19mm, HS = 120mm)

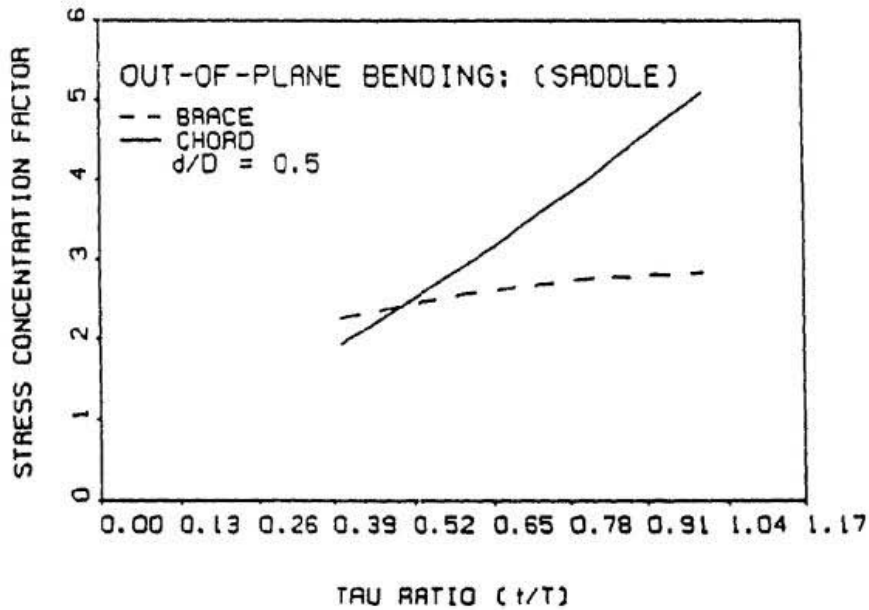

Figure 5.38: SCF vs. τ ratio at the saddle (OPB) (α = 7.02, γ = 24, Position No. 2, TS = 19mm, HS = 120mm)

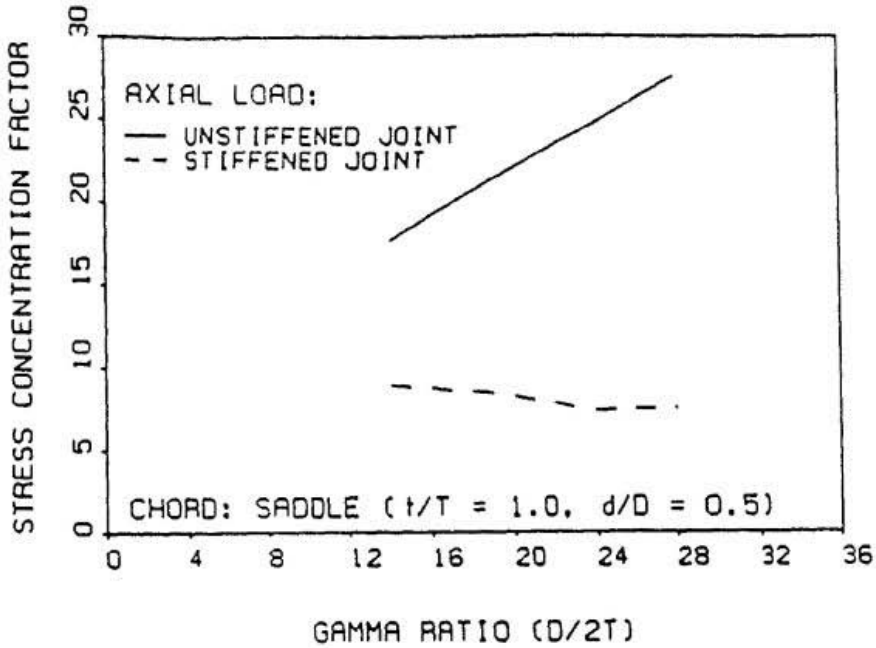

Figure 5.39: Effect of thinness ratio (γ) on chord SCFs in stiffened and unstiffened tubular joints at the saddle (Axial) ($\alpha = 7.02$, $\gamma = 24$, Position No. 2, TS = 19mm, HS = 120mm)

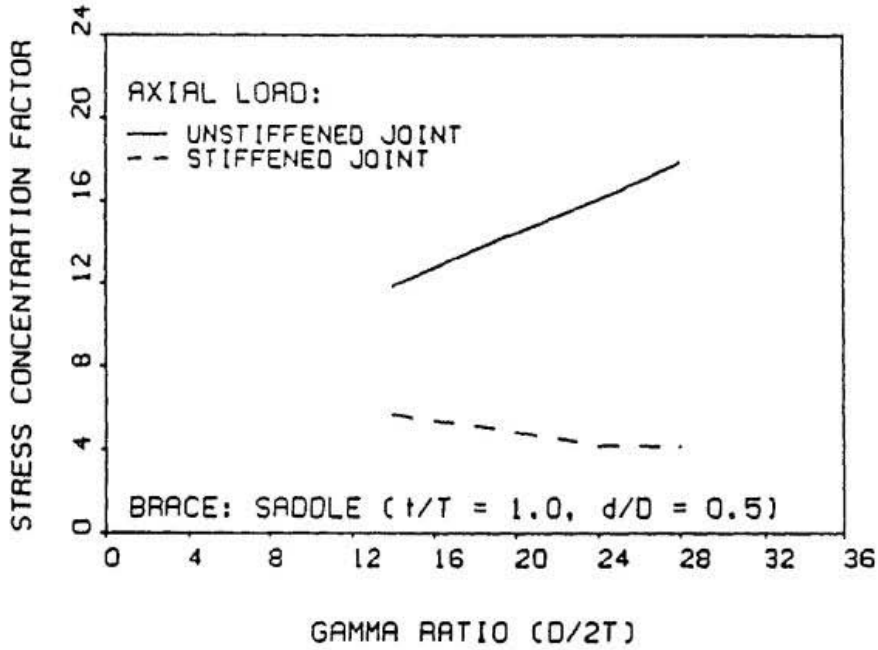

Figure 5.40: Effect of thinness ratio (γ) on brace SCFs in stiffened and unstiffened tubular joints at the saddle (Axial) ($\alpha = 7.02$, $\gamma = 24$, Position No. 2, TS = 19mm, HS = 120mm)

not very sensitive to the thinness ratio γ of the ring stiffened joints; the decrease in SCF is not significant when γ increases by a factor of 2.

5.4.5 Stress Concentration in the Stiffener

From the results obtained for the stress concentration in the stiffener, four regions were found to be susceptible to high stress concentration values as illustrated in Figure 5.41. The values of the stress concentration factor at these four locations, for a single stiffener, located at the saddle position for axial, in-plane bending and out-of-plane bending load cases are shown in Table 5.8. These regions may give some guidance to periodic non-destructive examination of the stiffened joints when they are in service. The stresses in regions B and D are compressive when the stiffener is subjected to tensile or out-of-plane loading in the brace; they will become tensile when the load is reversed (the brace load becomes compressive). From Table 5.8, it can be seen that all cases of axial loading exhibit maximum stress concentration in region C and all cases of the out-of-plane bending the maximum stress concentration factor occurs in region B. From a practical point of view, it may be concluded that Figure 5.41 and Table 5.8 suggest that positioning of welding lines of stiffeners in these regions, when stiffeners are fabricated by welding different pieces together, should be avoided. A comparison of the SCF values in stiffeners shows that they are comparable (but less than) the stress concentration factors in the brace and chord and as such they should be checked against fatigue failure. Since no large stress concentration points are present in the inner circumference of the ring stiffeners, the possibility of catastrophic development of fatigue cracks in stiffeners is rather rare.

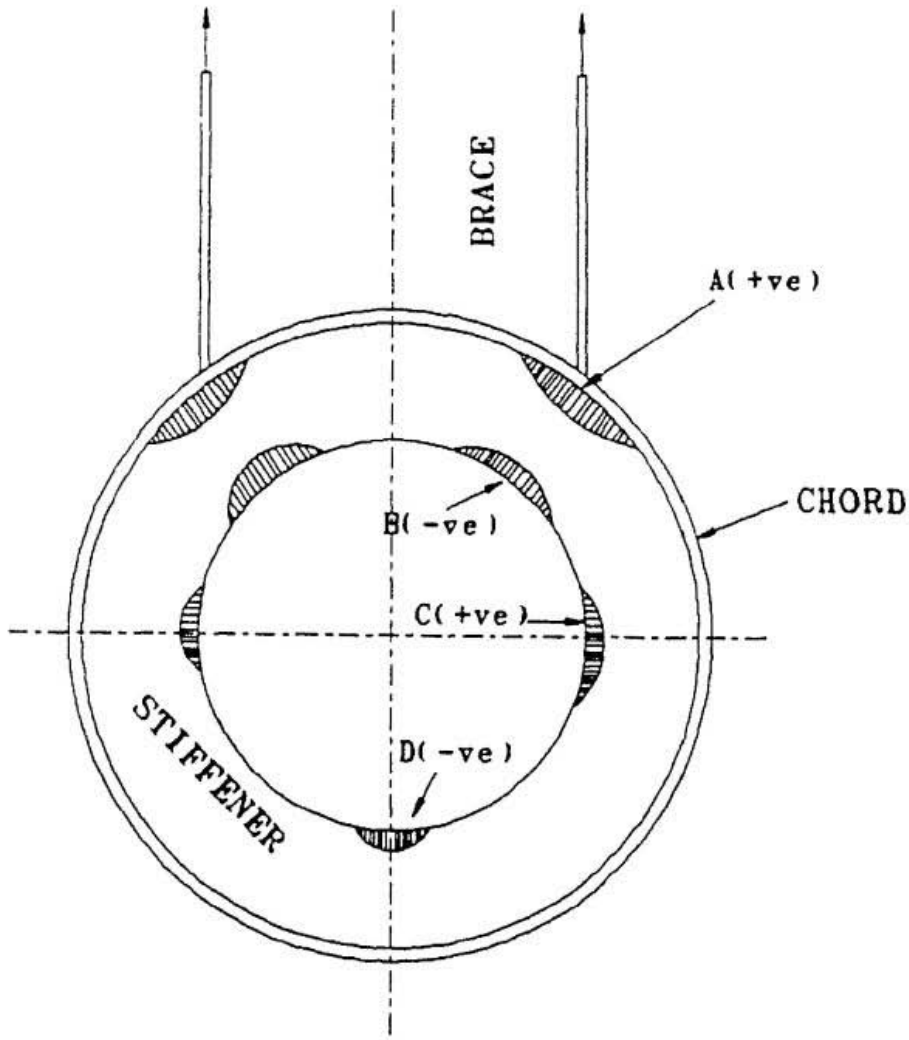

Figure 5.41: Four critical stress regions in the stiffener

Table 5.8: Stress analysis results of stiffened tubular joints subject to axial and out of plane bending loads; showing the values of SCFs at four critical point in the stiffener (α = 7.02, β = 0.5, γ = 24.0, τ = 1.0)

No. of Stiffener	Stiffener Position$^{\oplus}$	Location of the point on Stiffener*	Axial Loading	OPB Loading
1	saddle	A	6.45	4.17
1	saddle	B	-5.79	-5.37†
1	saddle	C	8.35†	1.69
1	saddle	D	-6.30	-0.02
2	1	A	4.28	2.81
2	1	B	-4.74	-4.29 †
2	1	C	5.20†	1.18
2	1	D	-4.05	-0.02
2	2	A	4.24	2.69
2	2	B	-4.31	-4.20†
2	2	C	5.15†	1.19
2	2	D	-4.00	-0.02
2	3	A	4.22	2.66
2	3	B	-4.00	-4.11†
2	3	C	5.14†	1.20
2	3	D	-3.97	-0.03
2	4	A	4.10	1.66
2	4	B	-3.65	-2.59†
2	4	C	5.18†	0.78
2	4	D	-4.07	-0.02

$\oplus$ - Figure 5.2

$\star$ - Figure 5.42

$\dagger$ - High stress region

5.5 Summary

Fatigue cracks in stiffened tubular joints which often initiate at the weld toe of the joints, close to the hot spot location, are the result of inherent welding defects resulting in high stress concentration factors around the intersection of the tubes. From the results of the foregoing analysis, it is shown that stiffening tends to reduce the hot spot stresses to a third or less of the original values, which may imply a significant increase in the fatigue life of the joint (for the same brace load). Reasoning from another point of view, the stiffeners may be used to reduce the thickness of the tubes and consequently reduce the total weight of the structure. However, in order to achieve the maximum benefit from the stiffening and thereby avoid the crack initiation and growth in undesired parts of a tubular joint, it could be seen that the position of the stiffener is of great importance.

Stiffening results in a more uniform stress distribution around the intersection of the tubes, especially on the chord side. This is due to the reduction of the local bending in the tube walls and changes in the local stiffness of the chord. As a consequence, stiffened tubulars support very large applied loads. Stiffening may introduce a higher SCF on the brace side depending on the τ and γ ratios. It is also observed that the SCFs in stiffeners are comparable to the chord or brace SCF (but less) and as such care should be taken to avoid the presence of stiffener weld lines in the zones of high SCFs; as a consequence of these results, there is a possibility that fatigue cracks could start in the stiffener and they must be periodically checked for fatigue cracks.

The following conclusions could be presented from the above study:

- The ratio of SCFs between unstiffened and stiffened joints were found to be 3.4 for axial, 1.33 for in-plane bending and 4.23 for out-of-plane bending load cases (α = 7.02, β = 0.5, τ = 1.0 and γ = 24.)

- The optimum positions of the stiffener locations were found to be the middle half of the plug region for axial and out-of-plane loads; for in-plane loads the outer quarters of the plug region were optimum positions for the stiffener locations.

- The increase in the number of stiffeners used reduces the SCF of the chord. It is observed that for in-plane loads, the stiffeners effects were found to be grouped in pairs of (0,1) and (2,3) stiffeners.

- The height (HS) of the stiffener has a greater influence on reducing the SCFs than the thickness (TS) of the stiffeners. Relatively deeper and thicker stiffeners are found to be better than deeper and slender stiffeners.

- Smaller thickness (τ) ratios (with unchanging HS and TS values for the stiffeners) give lower SCFs than larger thickness ratios. For $\tau < 0.54$ (β = 0.5, α = 7.07, γ = 24) the SCF is larger in the brace than chord for axial load; for in-plane load the ratio is $\tau < 0.62$ and for out-of-plane load the ratio is $\tau < 0.48$.

- Larger thinness ratio (γ = D/2T) tend to reduce the chord and brace SCFs.

Chapter 6

Fatigue Crack Initiation Life Prediction

6.1 General

The knowledge of the local stress and strain distribution around the welded tubular joint, is one of the common requirements to any fatigue life estimation. In addition, the accurate estimation of the local stress and strain, around intersection, is an important step towards the location of the problem sites at the intersection. These problem sites give an indication as to where the crack will start to initiate. The fatigue life of offshore welded tubular joints, consists of two parts: the crack initiation and the crack propagation lives. In this chapter, the estimation of the crack initiation life using strain-life concept, for offshore tubular welded joints, is presented.

The strain-life concept is based on the observation, that in many components, the response of the material in critical locations (notches) is strain or deformation dependent. Most engineering structures, such as the tubular joints dealt with in this study, are designed such that for nominal loads, the structure remains elastic,

but the presence of stress concentrations will often cause plastic strains to develop in the vicinity of the notches. The constraints imposed by the elastically stressed material surrounding the plastic region at the hot spot, make the deformation in this region (notch root) to be considered as strain-controlled. The strain-life method has often been considered 'initiation' life estimate, because crack growth is not explicitly accounted for: failure is assumed to occur when the equally stressed volume of material fails.

The strain-life approach in its simplest term assumes that the fatigue crack initiation, at a notch root, is due to the fracture of a fatigue element located at the notch root (in case of a tubular joint, this notch root region is located all around the weld toe region). The number of cycles required for a crack to initiate, at the notch root, can be related to the fatigue of strain-controlled unnotched laboratory specimens. In welded tubular joints, small crack initiating defects are always present at the weld toe, and as a result of this, fatigue life of welded tubular joints have been determined for several years with the notion that the fatigue life of the joints is dominated by the crack propagation; however, recent experimental studies, have shown that the number of cycles required to initiate a crack, large enough to be detected and treated by the modern linear fracture mechanics approach, is of the order of 10 to 40% of the total fatigue life. Hence estimation of the total life of a tubular welded joint, employing both crack initiation and and crack propagation aspects, seems to provide the most accurate estimate for the fatigue life of tubular joints.

6.2 Initiation Life Prediction Procedure

In the present study the first step was to calculate the stresses and strains, along the welded toe, in order to compute the theoretical stress concentration factor K_t for the joints. This process was essential to identify the likely crack initiation locations; also required is the fatigue stress concentration factor K_f. These stresses and strains and the corresponding SCFs, K_t, for unstiffened and stiffened joints, have already been obtained in the analyses and results given earlier in Chapters 4 and 5.

6.2.1 Weld Toe Strain Analysis

The relation between the far-field stress ΔS, far-field strain $\Delta\epsilon$, the weld toe stress $\Delta\sigma$, and weld toe strain ranges were obtained using the Neuber's rule in its modified form:

$$K_t = \sqrt{K_\sigma K_\epsilon} \tag{6.1}$$

where K_σ and K_ϵ are the local stress (SCF) and strain (SNCF) concentration factors obtained from the stress analysis of the joint (Chapters 4 and 5). Considerable effort has been spent, in trying to relate the theoretical stress concentration, K_t, to the fatigue stress concentration factor, K_f. Whereas the theoretical concentration factor, K_t, is dependent on the joint geometry and the mode of loading, the fatigue stress concentration factor, K_f, is also dependent on material type. In order to account for these additional effects, a sensitivity factor, q, which relates the stress

concentration i. fatigue to the theoretical stress value is used. This relation is given as

$$q = \frac{K_f - 1}{K_t - 1} \tag{6.2}$$

The sensitivity factor, q, ranges from zero (for no notch effect, K_f=1) to unity (for full theoretical effect, K_f=K_t). In the present study, a full theoretical effect is assumed, hence K_t in Eqn. (6.1) is taken equal to K_f. When Eqn. (6.1) is expressed in terms of ranges of stresses and strains, the modified Neuber's rule is obtained:

$$K_f \, \Delta S = (\Delta\sigma \, \Delta\varepsilon \, E)^{1/2} \tag{6.3}$$

6.2.2 Stress-Strain and Manson-Coffin Equations

The information needed for crack initiation life estimation also consists of the material's fatigue properties, i.e., (a) cyclic stress-strain relationship, and (b) strain-life relationship or Manson-Coffin curves. The cyclic stress strain relationship is given by:

$$\frac{\Delta\varepsilon}{2} = \frac{\Delta\sigma}{2E} + \left(\frac{\Delta\sigma}{2K'}\right)^{1/n'} \tag{6.4}$$

In the present study, the non-linear Eqns. (6.3) and (6.4) were combined together to give

$$\frac{(K_f\,\Delta S)^2}{2E} = \frac{\Delta\sigma^2}{2E} + \Delta\sigma\left(\frac{\Delta\sigma}{2K'}\right)^{1/n'} \tag{6.5}$$

$\Delta\sigma$ was determined by solving Eqn. (6.5) using an iterative technique (Newton' iterative technique) and then $\Delta\varepsilon$ was obtained from Eqn. (6.4). The final step in this prediction used the values, obtained from the above calculation, in the Manson-Coffin equation given below to arrive at the crack-initiation life, N_f. This equation takes into account, the contributions from both elastic and plastic weld toe strain ranges and obtains the crack initiation life as,

$$\frac{\Delta\varepsilon}{2} = \frac{(\Delta\varepsilon_e + \Delta\varepsilon_p)}{2} = \frac{\sigma'_f}{E}\,(2N_f)^b + \varepsilon'_f\,(2N_f)^c \tag{6.6}$$

where $2N_f$ gives the crack initiating life of the joint. Eqn. (6.6) is the basis of the strain-life method and is termed the *strain-life relation*. It contains both the elastic and the plastic portions. These portions can be plotted on a log-log plot separately and the total strain amplitude, $\Delta\varepsilon/2$, obtained by summing the elastic and the plastic portion values. The transition fatigue life, $2N_t$ which represents the life at which the elastic and the plastic curves intersect could be obtained by equating the elastic and plastic terms as

$$\frac{\Delta\varepsilon_e}{2} = \frac{\Delta\varepsilon_p}{2}$$

$$\frac{\sigma'_f}{E}\,(2N_f)^b = \varepsilon'_f\,(2N_f)^c \quad \text{at } N_f = N_t$$

$$2N_i = \left(\frac{\varepsilon'_f E}{\sigma'_f}\right)^{1/(b-c)} \tag{6.7}$$

6.2.3 Determination of Fatigue Properties

From Eqn. (6.6) it is evident that the crack initiation prediction requires four empirical constants ($b, c, \sigma'_f, \varepsilon'_f$). Extensive studies related to these constants have shown that the exponent c ranges from about -0.5 to -0.7, with -0.6 as a representative value and the exponent b ranges from about -0.06 to -0.14, with -0.1 as the representative value (Bannantine et al., 1990). Initial computations were performed using the range of constants from the numerous experimental studies. From these initial computations, it was observed that the exponents b and c play an important role in the initiation life. The range of initiation lives, obtained from this preliminary computation, using these published constants of b and c, showed no correlation to the experimental crack initiation life values. Hence, as a starting point, the values K' (1,500 MPa) and n' (0.19) reported by Bhuyan and Vosikovsky (1987) due to Lieurade et al. (1982), for HAZ of E355 steel (chemical and mechanical properties are equivalent to those of Canadian Grade 350 offshore steel), were assumed. Then from the experimental values of Iida (1987), who has given the range of crack initiation lives for different types of tubular welded joints at different strain levels, the plastic and the elastic portions of the Manson-Coffin's equation were solved iteratively to obtain b and c. In addition Eqns. (6.4) and (6.6) were combined to obtain the following relationships (Bannantine, 1990):

$$K' = \frac{\sigma'_f}{\left(\varepsilon'_f\right)^{n'}} \tag{6.8}$$

$$n' = \frac{b}{c} \tag{6.9}$$

which were in turn used to obtain suitable combinations for b and c.

6.3 Results and Discussion

The crack initiation lives have been evaluated, for all the three loading cases, viz., axial, in-plane bending and out-of-plane bending loads. The fatigue crack initiation life, was defined in this study, as the total number of cycles ($2N_f$) spent in generating an approximate initial crack depth, a_i, of 0.5 mm. A computer program, based on Newton's iterative technique was written, to solve the nonlinear Manson-Coffin equation [Eqn. (6.6)]. From this the initiation life was obtained for stress levels ranging from 160 MPa to 260 MPa. The total strain life was separated into the elastic and plastic components.

The summary of the results of the initiation lives, obtained for the three load cases, viz., axial, in-plane and out-of-plane bending loading, is given in Table 6.1, for different stress levels. The values within the brackets, in the tabular column for stress ranges, indicate the actual stress range at the weld toe due to the development of plastic strains at the weld toe region. Table 6.2 shows comparison of the lives obtained from the present study and the experimental results on tubular T-joints at the Memorial University of Newfoundland and the University of Waterloo laborato-

ries. It is obvious from the table that the values of initiation life obtained from the local stress strain approach employed in this study compares favorably with these experimental values. The elastic and plastic components of the initiation lives are shown in Tables 6.3, 6.4 and 6.5 for the three load cases.

The variation of strain amplitude at different stress range with the number of cycles to crack initiation, are given in Figures 6.1, 6.2 and 6.3 for axial, in-plane and out-of-plane bending load cases. From this figure, it is obvious, that the contribution of the plastic components to the total initiation life could be neglected.

Figure 6.4, shows the variation of the strain amplitude with the crack initiation life for three values of the fatigue strength exponent, b, and the fatigue ductility exponent, c; these values were obtained from the ranges of crack initiation lives given for tubular joints by Iida (1987). The figure illustrates the upper and the lower bounds of the crack initiation life obtained in this study. Proper care was exercised in selecting the coefficients b and c required for crack initiation analysis. Since the crack initiation lives were scattered over a band of strain and life ranges, the pair of values that satisfied Eqn. (6.9) was chosen. In addition, the computed initiation life obtained using those coefficients was also checked to see whether it lies within the feasible experimental range.

6.3.1 Summary

The results presented herein, along with the information gathered from full-scale tubular tests on the crack initiation life and failure characteristics of actual offshore tubular joints (Iida, 1987), supports the use of the local strain approach to the

Table 6.1: Fatigue crack initiation life of tubular T-joints under Axial, In-plane and Out-of plane bending loads: K′ = 1,500 MPa, σ'_f = 1,262 MPa, ε'_f = 1.28, n′ = 0.19, b = -0.209, c = -1.10

Joint Geometry $\tau = 1.0$; $\beta = 0.5$; $\alpha = 7.02$; $\gamma = 24$								
Axial Loading			IPB Loading			OPB Loading		
Stress Range (MPa)	Strain Amplitude ($\Delta\varepsilon/2$) $\times 10^4$	Initiation Life k.cycles	Stress Range (MPa)	Strain Amplitude ($\Delta\varepsilon/2$) $\times 10^4$	Initiation Life k.ycles	Stress Range (MPa)	Strain Amplitude ($\Delta\varepsilon/2$) $\times 10^4$	Initiation Life k.cycles
160(148)	3.52	787	160(145)	3.46	859	160(150)	3.58	730
170(157)	3.74	590	170(154)	3.68	643	170(160)	3.80	547
180(166)	3.97	450	180(163)	3.89	490	180(169)	4.03	417
190(176)	4.19	348	190(173)	4.11	379	190(178)	4.25	323
200(185)	4.41	273	200(182)	4.33	297	200(188)	4.48	253
210(194)	4.63	217	210(191)	4.54	236	210(198)	4.70	201
220(203)	4.85	174	220(200)	4.76	189	220(207)	4.93	161
230(213)	5.07	141	230(209)	4.98	154	230(216)	5.15	131
240(222)	5.29	116	240(218)	5.20	126	240(225)	5.38	107
250(231)	5.51	96	250(227)	5.41	104	250(235)	5.60	89
260(240)	5.73	80	260(236)	5.63	87	260(245)	5.83	74

Table 6.2: Comparison between experimental results of University of Waterloo and Memorial University with the present study (Pates et al., 1989)

Loading mode	UW (Expt.) Initiation N_f k.cycles (Apparent crack depth $a \approx 0.5mm$)	MUN (Expt.) Initiation N_f k.cycles (Apparent crack depth $a \approx 0.5mm$)	PS (FEM) Initiation N_f k.cycles (Assumed crack depth $a \approx 0.5mm$)
Axial (Saddle)	-	103 (250 MPa)	96 (250 MPa)
IPB (Crown)	99 (248 MPa)	-	104 (250 MPa)
OPB (Saddle)	86 (256 MPa)	-	89 (250 MPa)

Table 6.3: Elastic and plastic strain amplitudes: K′ = 1,500 MPa, σ'_f = 1,262 MPa, ε'_f = 1.28, n′ = 0.19, b = -0.209, c= -1.10 (Axial).

Joint geometry $\tau = 1.0$; $\beta = 0.5$; $\alpha = 7.02$; $\gamma = 24$.				
		Axial loading		
Stress range (MPa)	Initiation life k.cycles	Total strain amplitude $(\Delta\varepsilon/2)$ $\times 10^4$	Elastic strain amplitude $(\Delta\varepsilon_e/2)$ $\times 10^4$	Plastic strain amplitude $(\Delta\varepsilon_p/2)$ $\times 10^4$
160	787	3.5242	3.5200	0.0042
170	590	3.7446	3.7389	0.0057
180	450	3.9652	3.9574	0.0077
190	348	4.1858	4.1755	0.0103
200	273	4.4065	4.3931	0.0134
210	217	4.6274	4.6101	0.0173
220	174	4.8483	4.8263	0.0220
230	141	5.0695	5.0418	0.0277
240	116	5.2908	5.2563	0.0345
250	96	5.5124	5.4698	0.0426
260	80	5.7342	5.6822	0.0520

Table 6.4: Elastic and plastic strain amplitudes: K′ = 1,500 MPa, σ'_f = 1,262 MPa, ε'_f = 1.28, n′ = 0.19, b = -0.209, c= -1.10 (IPB).

Joint geometry $\tau = 1.0$; $\beta = 0.5$; $\alpha = 7.02$; $\gamma = 24$.				
		IPB loading		
Stress range (MPa)	Initiation life k.cycles	Total strain amplitude $(\Delta\varepsilon/2)$ $\times 10^4$	Elastic strain amplitude $(\Delta\varepsilon_e/2)$ $\times 10^4$	Plastic strain amplitude $(\Delta\varepsilon_p/2)$ $\times 10^4$
160	859	3.4600	3.4565	0.0038
170	643	3.6800	3.6722	0.0052
180	490	3.8900	3.8868	0.0070
190	379	4.1100	4.1011	0.0093
200	297	4.3200	4.3155	0.0122
210	236	4.5400	4.5279	0.0157
220	189	4.7600	4.7431	0.0201
230	154	4.9800	4.9505	0.0252
240	126	5.2000	5.1625	0.0314
250	104	5.4100	5.3738	0.0388
260	87	5.6300	5.5780	0.0472

Table 6.5: Elastic and plastic strain amplitudes: $K' = 1{,}500$ MPa, $\sigma'_f = 1{,}262$ MPa, $\varepsilon'_f = 1.28$, $n' = 0.19$, b = -0.209, c= -1.10 (OPB).

Joint geometry $\tau = 1.0$; $\beta = 0.5$; $\alpha = 7.02$; $\gamma = 24$.				
		OPB loading		
Stress range (MPa)	Initiation life k.cycles	Total strain amplitude $(\Delta\varepsilon/2)$ $\times 10^4$	Elastic strain amplitude $(\Delta\varepsilon_e/2)$ $\times 10^4$	Plastic Strain amplitude $(\Delta\varepsilon_p/2)$ $\times 10^4$
160.	729.	3.5800	3.5771	0.0046
170.	547.	3.8000	3.7984	0.0062
180.	417.	4.0300	4.0201	0.0084
190.	323.	4.2500	4.2405	0.0111
200.	253.	4.4800	4.4626	0.0146
210.	201.	4.7000	4.6824	0.0188
220.	161.	4.9300	4.9047	0.0240
230.	131.	5.1500	5.1207	0.0301
240.	107.	5.3800	5.3419	0.0376
250.	89.	5.6000	5.5516	0.0460
260	74.	5.8300	5.7699	0.0564

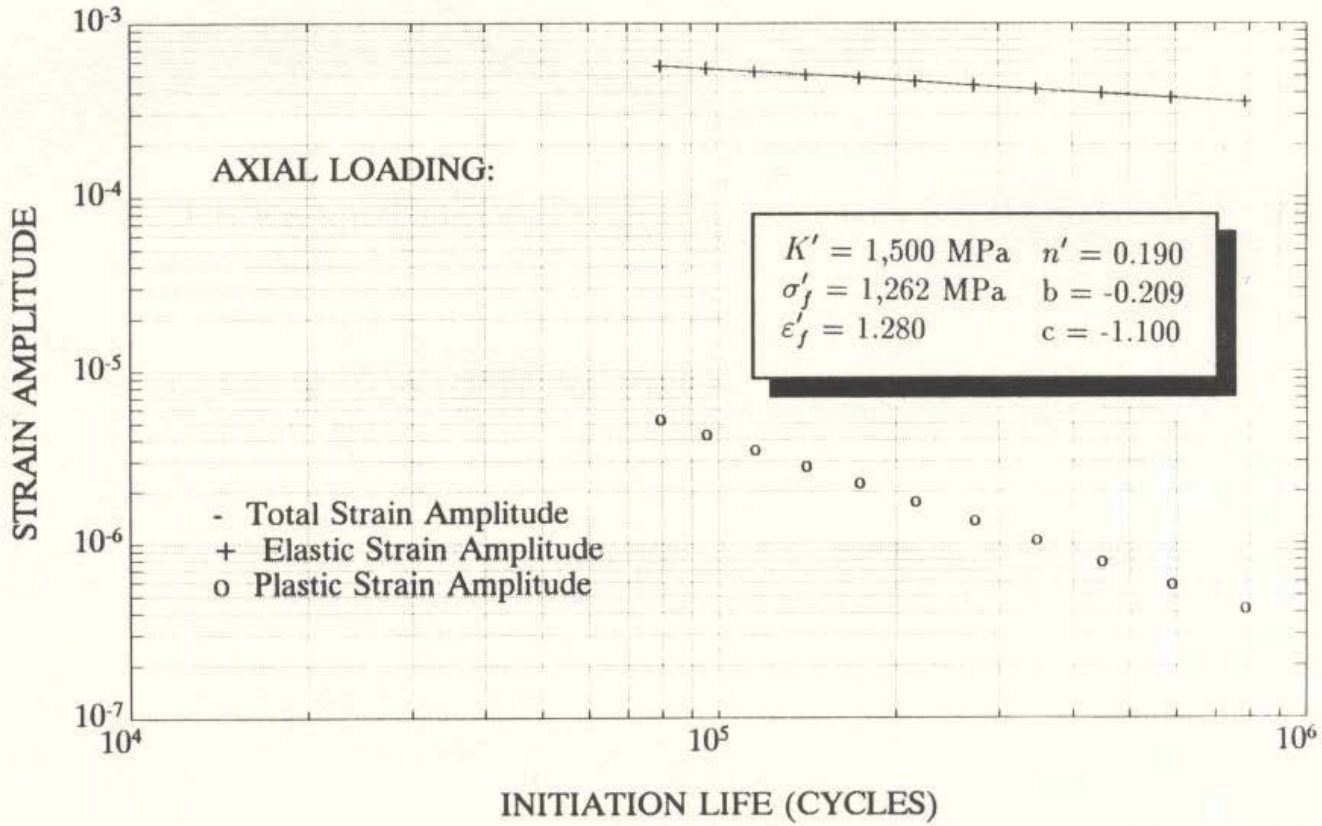

Figure 6.1: Strain-life curves showing total, elastic and plastic strain components for axial loading.

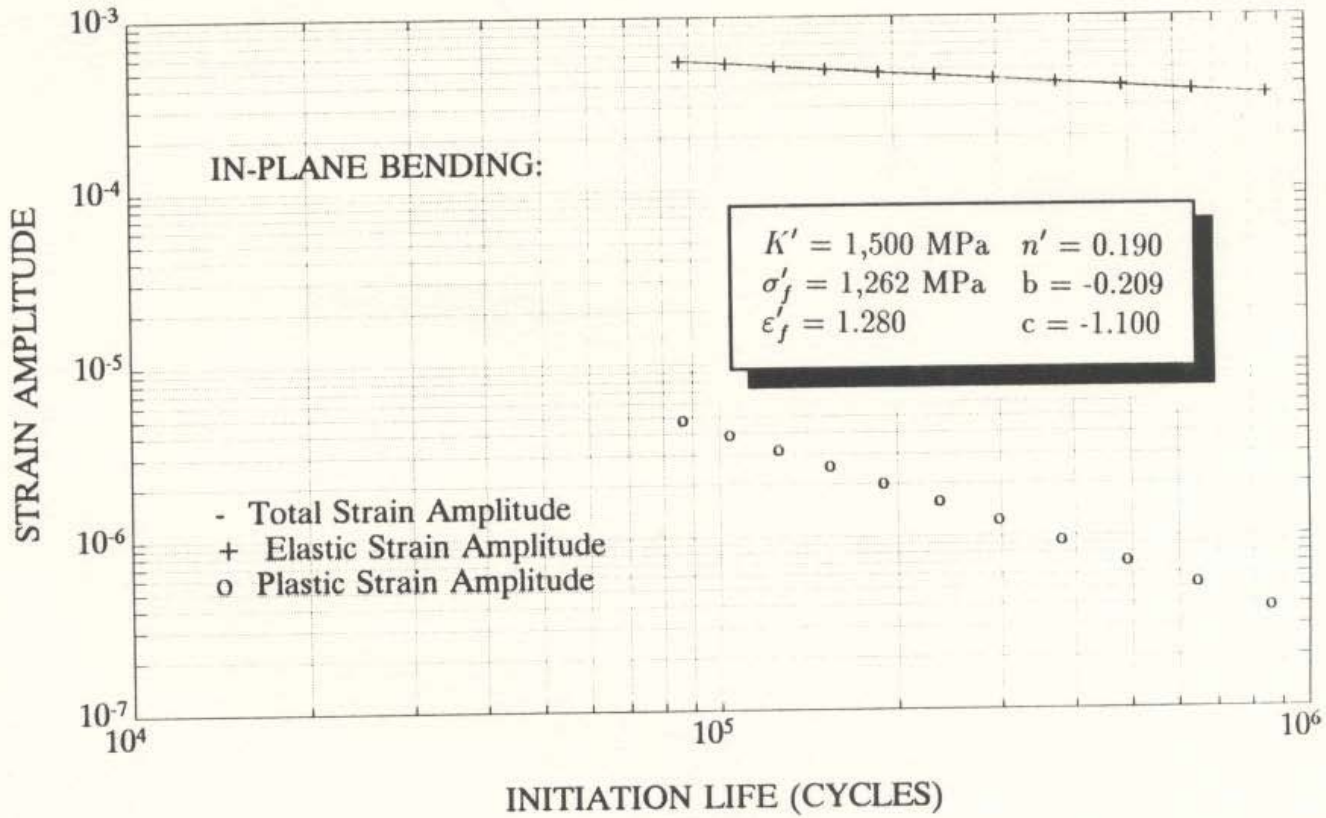

Figure 6.2: Strain-life curves showing total, elastic and plastic strain components for in-plane bending load.

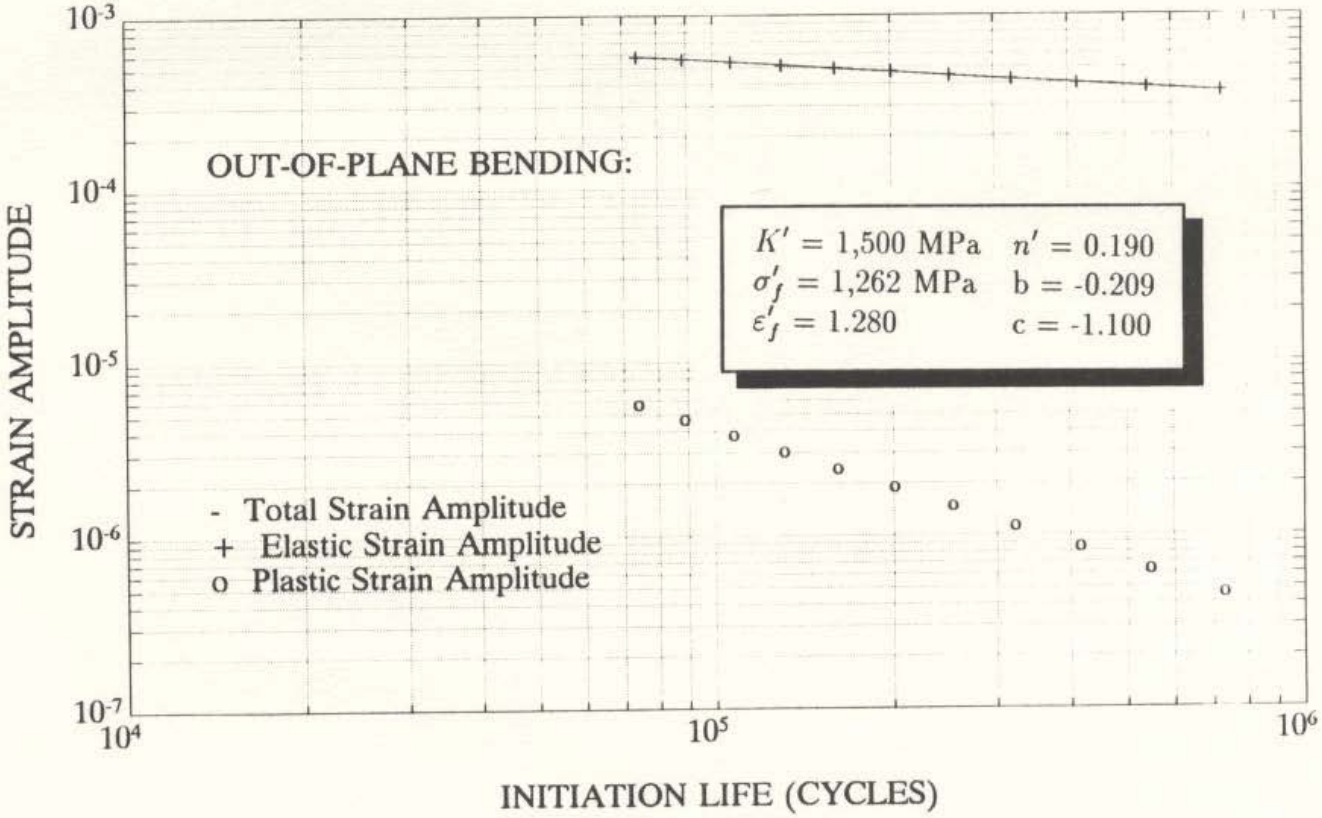

Figure 6.3: Strain-life curves showing total, elastic and plastic strain components for out-of-plane bending load.

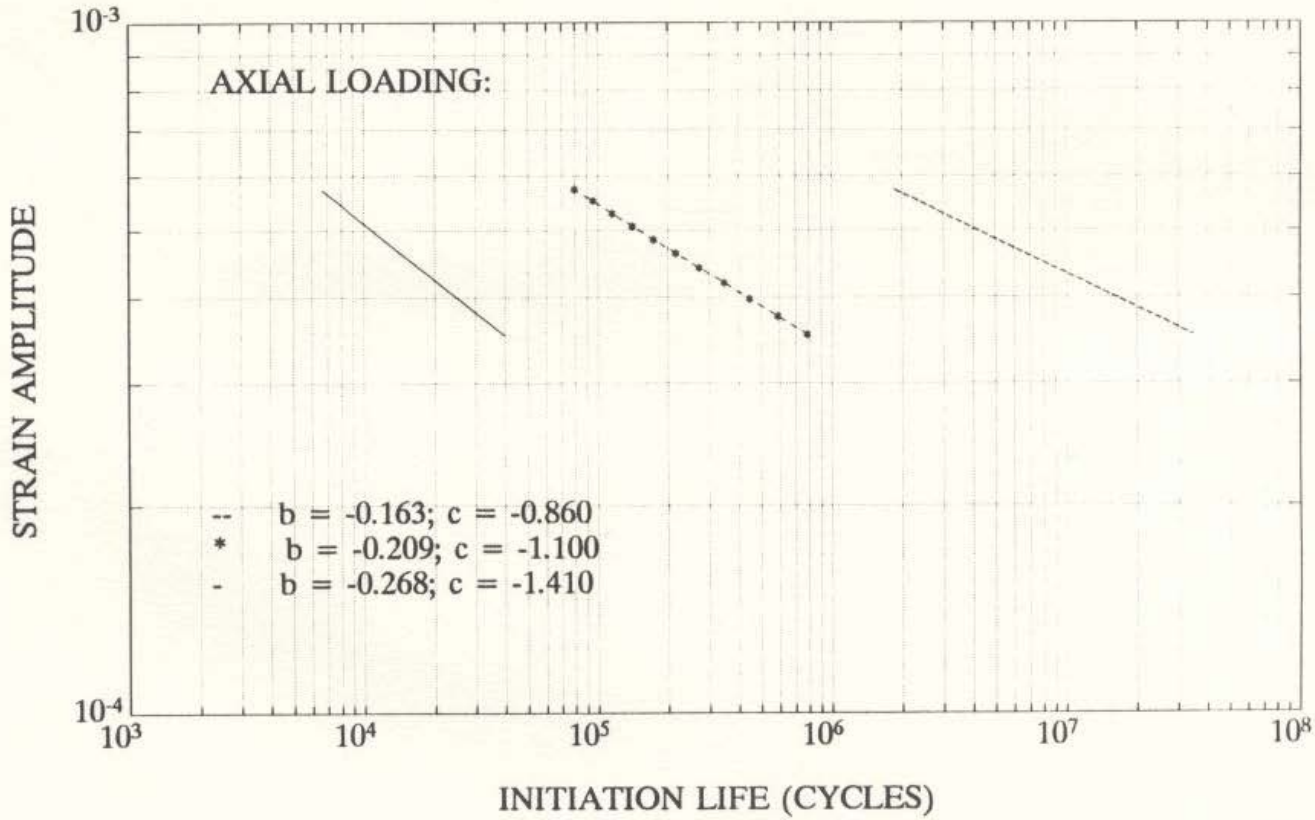

Figure 6.4: Strain-life curves showing the upper and lower bounds of exponents b (fatigue stength exponent) and c (fatigue ductility exponent) used in this study

prediction of fatigue crack initiation life of offshore tubular welded joints. On the average, the results obtained confirms the trends observed in experimental studies. However lack of adequate data concerning the fatigue strength exponent, b and fatigue ductility exponent, c, for tubular joints having large SCF or SNCF, led to an overly large fatigue crack initiation life during the preliminary computations, using already available values for these exponents. Furthermore, it appears that the use of these values for tubular joints do not compare favourably with experimental results. It does not seem realistic to assume that these exponents (b and c), obtained from small laboratory specimens having smaller SCF, SNCF and large strain amplitudes, could be used for tubular welded joints having very large SCF and SNCF and smaller strain amplitudes. In addition, the mode of tubular joint response to applied load is quite different from those of the small laboratory specimens from which the coefficients were obtained. Because of the preliminary analyses results and the foregoing discussion, the exponents (b and c) utilized in this study were obtained using the experimental data from fatigue crack initiation lives given for large scale tubular welded joints (Iida, 1987). Using this empirically computed exponents b and c, the analytically computed crack initiation life seems to give a very close fit to the experimental crack initiation life. It must be pointed out that this close fit of analytical values to experimental values is only an arbitrary one since the coefficients b and c were selected from the obtained range (Figure 6.4) to give values close to the experimental ones. More studies and experiments need to be carried out to correlate the analytical and experimental crack initiation lives of tubular joints.

Chapter 7

Fatigue Crack Growth Life Prediction

7.1 General

Fatigue as already emphasized in previous chapters, has been established as a primary cause of failure of offshore jacket structures used for the extraction of oil and gas in the major seas of the world. Majority of them are fabricated from tubular welded joints which experience fatigue damage, primarily due to the combination of high stress concentrations at the welded joint, small defects that result from welding and the variations in the load caused by sea wave or structural resonance. Conventionally structures of this type have been designed on the basis of the experimental stress-life curves (S-N curves). This curve relates the hot-spot stress range $\Delta\sigma_{HS}$, to the number of cycles that cause failure. In the context of tubular joints, this is generally taken to be the through thickness cracking life. Although the S-N curve approach could be used to predict the total fatigue life of tubular joints, this approach ignores the mechanics of fatigue failure; in addition, it also requires a large experimental data base. Moreover, the applicability of the experimental

results obtained from tests on small or medium scale tubular joints, to larger prototype tubular joints may not be correct or useful. Hence, an analytical procedure that can estimate the fatigue crack propagation life would be of great advantage. This could be important for tubular joints where much of the fatigue life may be taken up by crack growth. Hence an appropriate model that can explicitly take account of all influencing factors and at the same time separate the effect of each of these factors is needed. A model based on fracture mechanics would be more appropriate to meet such needs.

The advent of Linear Fracture Mechanics (LEFM) has made it possible for all variables (loading, geometrical properties, etc.) to be separated out and analyzed independently to determine their influence on the fatigue process. Thus complex stress fields such as those present around the intersection of tubular joints could be easily handled by LEFM. The resistance of the intersection, against fatigue cracking, is substantially affected by the presence of defects. One obvious and reasonable way to model the surface defects, that initiate at the weld toe of tubular joint intersection area and propagate under the influence of loading through the thickness and along the surface, is to represent them as cracks. In addition, the stress intensity factor, K, is introduced, to characterize the stress field in a small region around the leading edge of these cracks. However, the use of a full fracture mechanics approach would require the solution to a three dimensional problem which incorporates all the effects of the complex tubular joint stress distribution on the local stresses and strains ahead of the crack tip.

This chapter illustrates a numerical procedure to predict the crack growth rates of

tubular joints using fracture mechanics approach. A comprehensive crack analysis is carried out to determine the stress intensity factors along the crack front and these values are used in a crack growth law to compute the fatigue crack growth life.

7.1.1 Finite element Model of the Cracked Joint

The finite element idealization of the joint (Figures 7.1 and 7.2) for inclusion of the crack, follows a modification of the previous mesh to accommodate a larger number of elements at the critical regions where the cracks are expected to initiate and grow. The mesh for the shell stress analysis given in Chapter 4 was modified. The mesh consists mainly of isoparametric 8-noded, reduced integration shell elements. The modification to the mesh in Chapter 4, for use in the crack analysis, was achieved by using multi-point constraints to refine the elements. The multi-point constraints represent forced boundary conditions and as such were not used in the regions with high stress and deformation gradients and near positions where local quantities (stresses and stress intensity factors for example) are of interest. In the generated mesh, as shown in Figures 7.1 and 7.2, the multi-point constraints were not used nearer than three rows of elements from the intersection in the present study. This procedure allows a relatively fine mesh with 72 elements around the chord-brace intersection, to be used in the investigation; for axial and out-of-plane load cases, the finer mesh was concentrated around the saddle point (Figure 7.1), and for in-plane bending the finer mesh was used around the crown (Figure 7.2). These meshes were tested for convergence before the cracks were introduced.

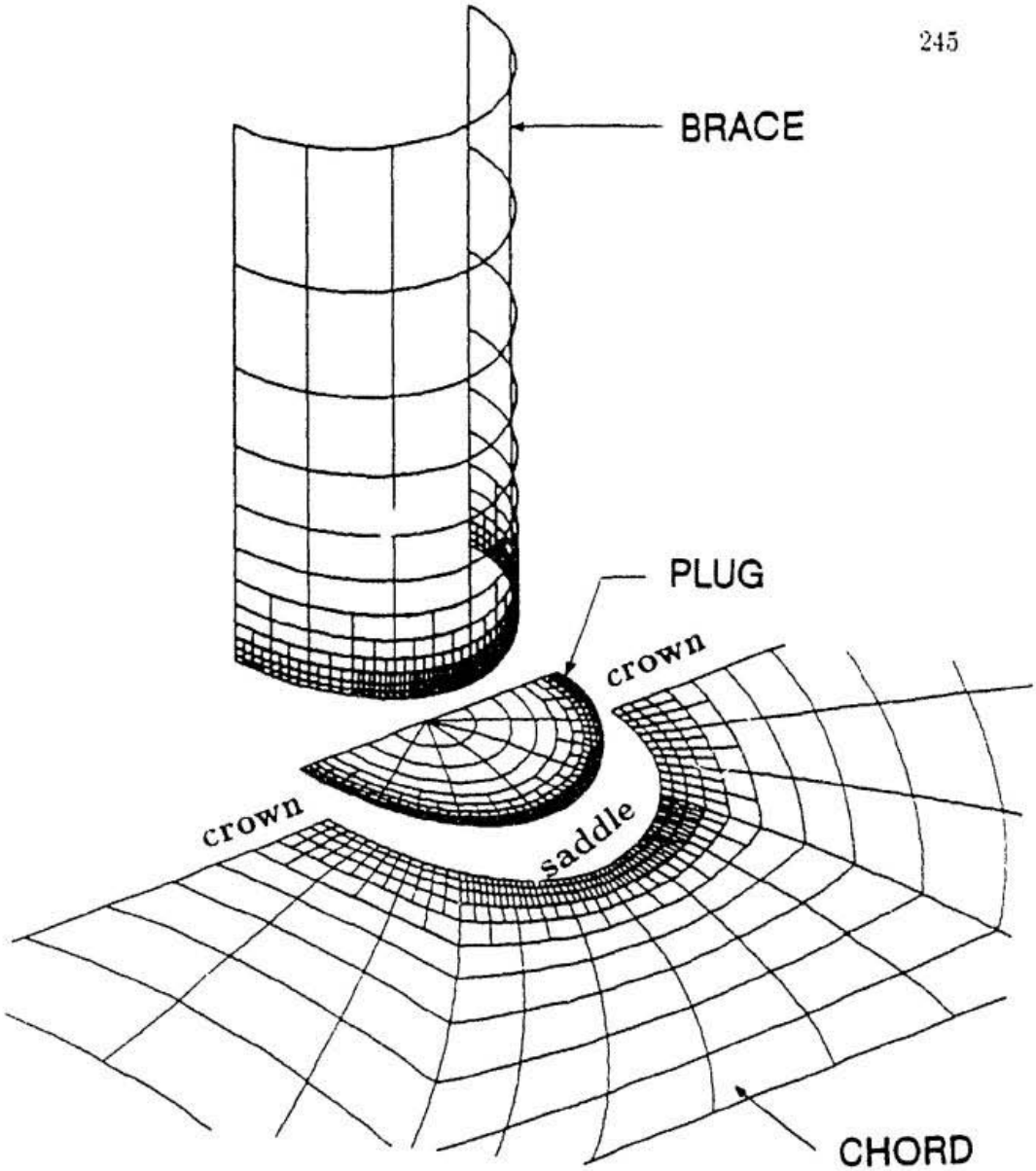

Figure 7.1: Typical computer generated mesh for crack growth analysis of the tubular joint under the action of brace axial and out-of-plane bending loads.

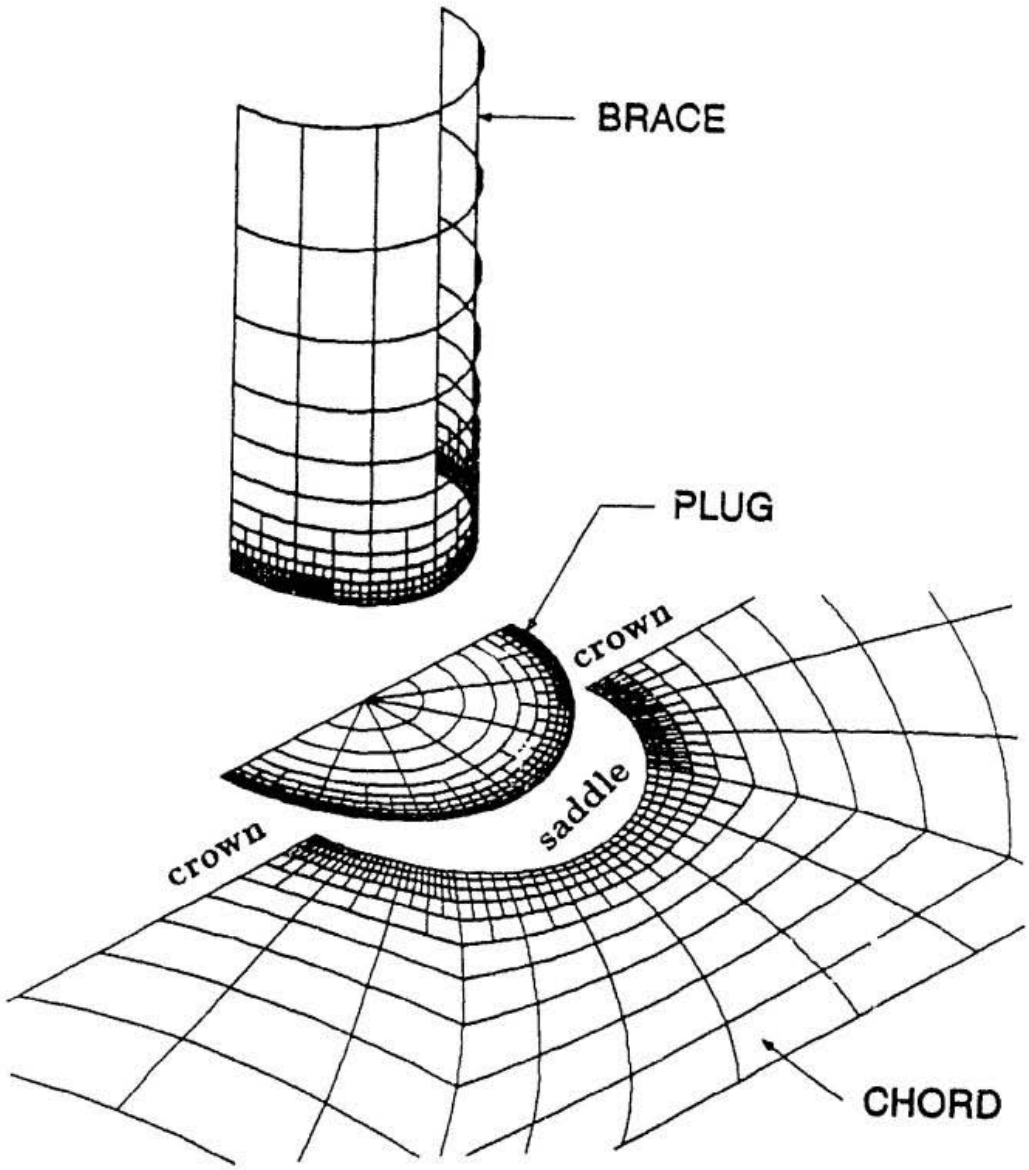

Figure 7.2: Typical computer generated mesh for crack growth analysis of the tubular joint under the action of brace in-plane bending load.

7.1.2 Joint Modelling for Crack

Specifically at this stage of the study, more attention was focused on the fatigue life of tubular joints under axial loading. Nonetheless, the essential results for other loading conditions, that is in-plane and out-of-plane bending loads, are given whenever necessary for comparison purposes. From the results presented in Chapter 4 and from related literature reviewed in Chapter 2, it is clear that for axial load and out-plane bending load cases the critical region (hot spot) for a tubular T-joint is the saddle point. For in-plane bending load, though most of the literature reported the critical region to be at the crown, contrary result was observed from this study. The critical region was observed to occur some distance away from the crown point (37.5°). To make comparisons on a common basis with experimental observations, the crack is assumed to initiate and grow at the crown position for in-plane bending load in the present study. Hence, the cracks are modelled at the saddle point for axial and out-of-plane bending loads and at the crown for in-plane bending load.

7.1.3 Tubular Joint Crack Shape

Previous studies have shown that fatigue crack growth, in tubular joints, generally occurs at the weld toe. For these class of joints, especially when they are employed in an environment that generates a fluctuating load, the shape of a growing weld toe surface flaw, under fatigue loading, is governed both by the loading conditions and by the geometrical configuration of the growing crack. In general, the flaw tends to grow along the brace-chord intersection along the surface and into the chord

thickness. Based on field and laboratory results the crack shape, of this type in tubular joints, has been described as a semi-elliptical one (Figure 7.3). Based on the above observations, the crack shape was accordingly, modelled as a semi-elliptical part-through thickness crack. It has also been observed during fatigue testing of tubular joints (Dover and Holbrook 1979, Dover and Dharmavasan 1988, Gowda 1983, Bhuyan 1986) that the part-through-thickness crack growth rate was almost constant. This observation, had led to the assumption, by some investigators, that the stress intensity factor for part-through-thickness crack growth rate could be obtained by modelling a 50% deep weld toe crack. This assumption was not made in this study. Rather, the part-through-thickness weld toe crack was modelled as a crack having a maximum depth equal to 90% of the chord thickness. Starting from an initial crack depth of about 0.5 mm to the final crack depth of 17.10 mm, five crack lengths, (= 2c), (from 62 to 188 mm) were investigated. For the crack length (2c) values, one symmetrical half of the crack extends over four, six, eight, ten and twelve elements, respectively.

7.2 Stress Intensity Factor Evaluation

The fatigue cracks, that develop at the weld toe of tubular joints, usually are of a semi-elliptical shape. A detailed fatigue life prediction of these tubular joints, on the basis of fracture mechanics, require the stress intensity factors for different crack sizes, crack shapes and crack front positions. The three dimensional stress state that exists around the crack front dictates that a solid (3-D) finite element model, which also incorporates the stress singularity at the crack tip, should be used in the study. The effective mesh generation for such elements, is laborious

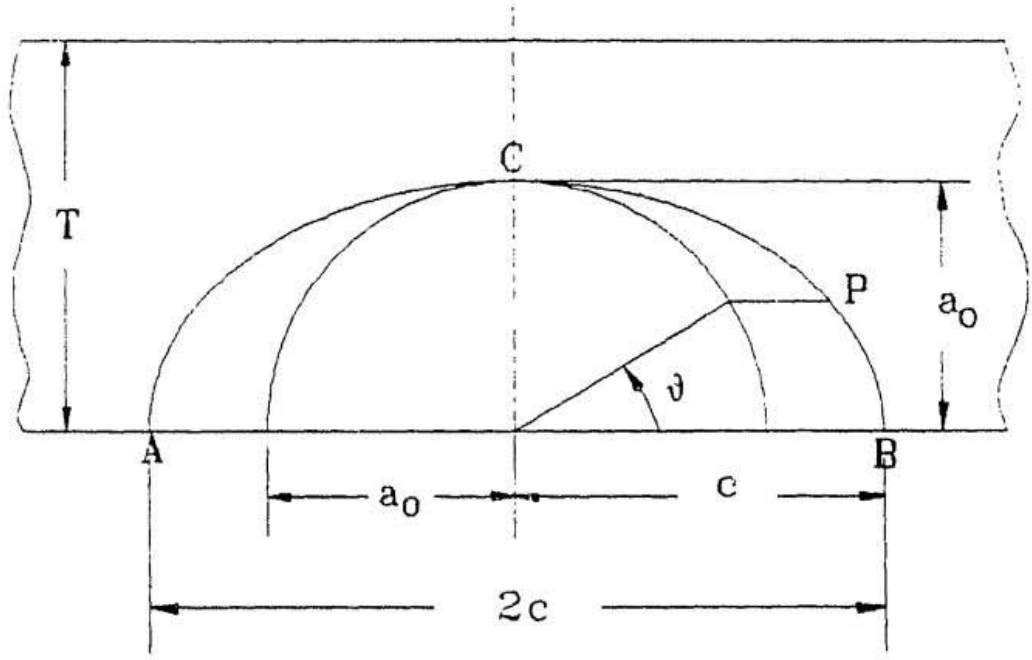

Figure 7.3: Schematic illustration of a semi-elliptical surface crack. A point P on the semi-elliptical crack front is located by the angle ϑ on the inscribed circle.

and cumbersome; also computationally according to the present state of computer facilities in the Faculty of Engineering Memorial University, St. John's, this is beyond our capabilities.

The use of line spring elements (Parks, 1981), which can be incorporated in the shell models, for the analysis of the surface cracks is less expensive and computationally feasible from the point of view of input data generation and analysis. In this study, the stress intensity factor calculation is based on the line spring model. The stiffness formulation for this element has already been given in Chapter 3.

The line spring elements (see Figure 7.4), representing the surface crack, were arranged at a position representative of the weld toe at the chord-brace intersection. This was chosen in this study to be one brace wall thickness away from the center-line intersection. Calculations by Huang (1987a), and Huang and Hancock (1987b) on cracked two-dimensional joints, under plane strain conditions, have shown that this placement of the line spring elements gives a good agreement between calculations using plane strain continuum elements and shell analysis with a line spring representation of the crack. This assumption has also been used for tubular T-joint by Du and Handcock (1989), in the finite element calculations of stress intensity factors for semi-elliptical cracks in a tubular welded joint using line springs and three-dimensional elements. In this study a Fortran program was written, to describe the semi-elliptical shape of the surface flaw. A mapping technique was used to ensure that the crack front points, in planar rectangular coordinates of the semi-ellipse, match with those of the curvilinear coordinates of the tubular joint surface where they will actually be located. The Fortran program uses the coordinates of

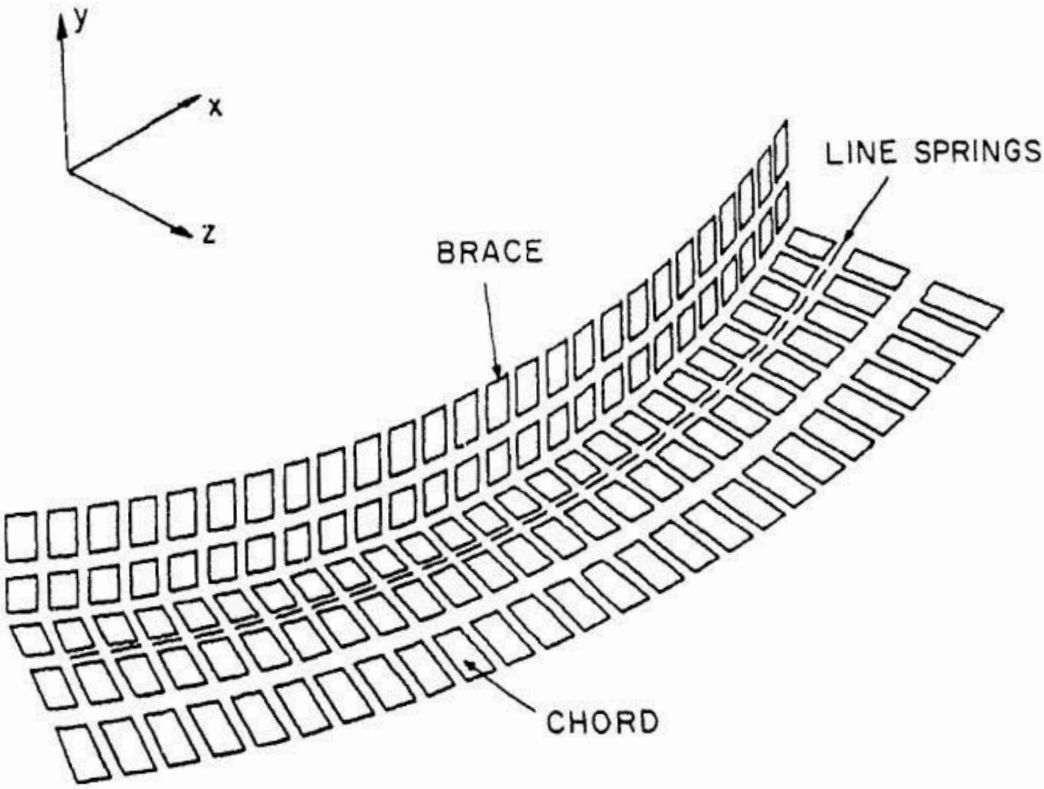

Figure 7.4: Location of the line spring elements in the tubular joint

two points at which the crack front meets the tubular surface (A and B, Figure 7.3),and the deepest flaw depth (point C), located at the middle point of the crack front. These three points (two surface points and the deepest point, Figure 7.3) are then mapped onto the planar semi-ellipse whose major and minor axes are defined by these three points. Once the semi-elliptical flaw is defined, it is then mapped back onto the tube surface through a coordinate transformation between the rectangular coordinates of the semi-ellipse and the curvilinear body coordinates of the tube. The curvilinear body coordinates are defined by the path of the crack tip on the tube surface, which is determined by the previously mentioned two surface points, and a coordinate along the depth (chord thickness) direction.

7.3 Fatigue Crack Growth Life Prediction

From the finite element line spring and shell element analysis results, the stress intensity factor range, is now available for fracture mechanics fatigue crack growth calculations using the Paris Law:

$$\frac{da}{dN} = C\,(\Delta K)^m \tag{7.1}$$

The crack propagation life of the joint is obtained by carrying out an integration of the above expression as follows:

$$\int_{N_i}^{N_f} dN = \int_{a_i}^{a_f} \frac{da}{C\,(\Delta K)^m} \tag{7.2}$$

where N is the number of cycles to grow the crack from the initial crack size a_i to final crack size a_f, and C and m are material constants. In the present study, a numerical integration technique based on incremental crack growth was adopted for the computation of the joint fatigue crack propagation life.

7.3.1 Fatigue Crack Growth Rate (da/dN) and the SIF Range (ΔK)

The derivation of relationship between the rate of propagation (da/dN) and the corresponding value of stress intensity factor range (ΔK) in this study was performed in two stages after the stress intensity factors were obtained. The first stage consists of obtaining the relation between the crack depth and the number of cycles applied. The second stage involves calculating the corresponding values of da/dN at several values of the crack depth.

From numerous investigations available to date, it has been shown that, although a law of the type defined by Eqn.(7.1) is applicable to a wide range of the values of ΔK, this does not represent the complete relationship. If for example the instantaneous rate of fatigue crack propagation is plotted against the corresponding value of ΔK on a log-log scale, the curve of the general form, shown in Figure 7.5 (repeated here for the sake of clarity, see Chapter 2), is obtained. The need for ΔK to exceed a threshold value ΔK_{th}, before any propagation can occur at all, has resulted in the presence of the lower point of inflection in this figure. Because of the presence of this threshold, it is possible, that, given the right combination of crack size and applied stress, some cracks may not propagate under fatigue loading. The transition from the threshold to the central region of the curve of log (da/dN)

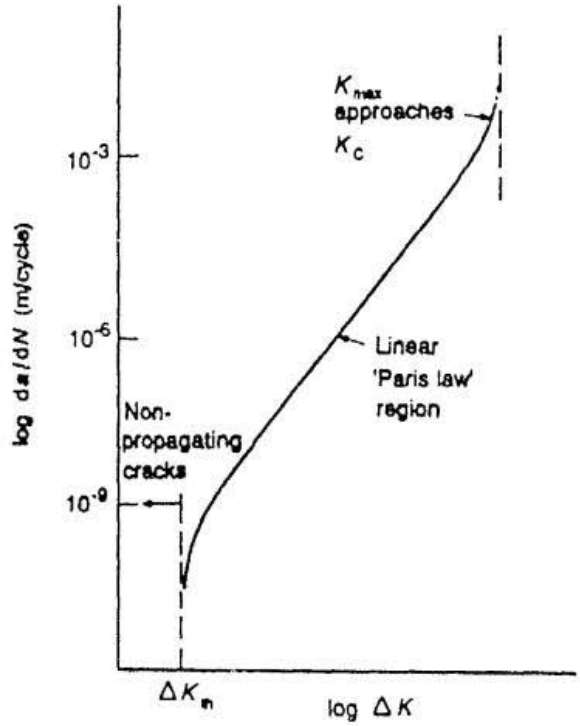

Figure 7.5: Idealized crack growth rate (da/dN) vs. stress intensity factor range (ΔK), (log-log scale)

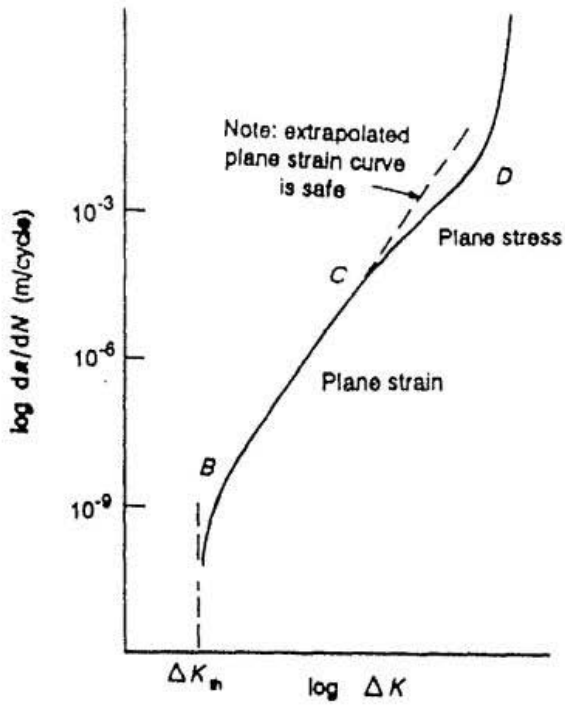

Figure 7.6: Typical crack growth rate (da/dN) vs. stress intensity factor range (ΔK) for thin specimens, (log-log scale)

against log ΔK is usually very steep; a very small increase in ΔK above ΔK_{th} will give rise to a very large increase in the values of da/dN. At the upper end of a curve the second point of inflection occurs representing maximum stress intensity reached, K_{max}, to the critical value (K_c) at which fast fracture would occur. The fatigue crack growth rate (da/dN) and stress intensity factor range (ΔK) relationship are in fact slightly more complicated than the idealized one shown in Figure 7.5, in that the 'linear' region can be composed of inflection points, as shown in Figure 7.6. The first linear portion (BC) corresponds to crack propagation under plane strain conditions, while the second linear portion (CD) is that of plane stress fracture. It has been reported by Gurney (1979), that this type of relation is obtained only if the specimen is sufficiently thin to permit relaxation to plane stress conditions before final rupture. However, in practical situations, the plane stress region is normally ignored. Because in welded joints, at least, fatigue cracks are usually either partly or fully embedded and grow in a plane strain mode for most of their lives. The percentage life which occurs under plane stress conditions is extremely limited. In addition, it can be seen from Figure 7.6, that it is safe, from calculation point of view, to assume that the plane strain relation also applies in the plane stress region, because extrapolation of the plane strain relation (BC) results in a faster rate of propagation for a given value of ΔK than the plane stress relation (CD). Also it will be safe to extrapolate the plane strain condition back into the threshold region of the curve. In conclusion, it is therefore apparent, that the Paris crack propagation law, Eqn. (7.1), can be applied with considerable confidence. However, this implies that the values of C and m must be known in order to use this equation successfully for fatigue crack growth life prediction. Some of the general trends in the available

data concerning C and m are briefly reviewed in the next section.

7.3.2 Material Constants C and m

Crack propagation data for wide range of material have been obtained for tests in air under pulsating tension loading. Gurney (1979b) has shown that log C is linearly related to m (see Figure 7.7) for steels under plane conditions. The relationship between C and m was given as

$$C = (1.315 \times 10^{-4})/(895.400)^m \tag{7.3}$$

If this is inserted into Eqn. (7.1) the following expression is obtained

$$\frac{da}{dN} = 1.315 \times 10^{-4} \left(\frac{\Delta K}{895.400}\right)^m \tag{7.4}$$

The above relationship, implies that da/dN versus ΔK relations for all steels pass through the point $da/dN = 1.315 \times 10^{-4}$ (when $\Delta K = 895.400\ N/mm^{3/2}$) as shown in Figure 7.8. It has since been the focus of attention of numerous investigators as to what defines the value of m (and hence of C) for any particular material. Barsom (1974) suggested that m should be taken as 2.25 for martensitic steels, 3.00 for ferrite pearlite steels and 3.25 for austenitic steels. One thing that does seem obvious, is that there is a tendency for m to decrease as the yield strength increases (Gurney, 1979b). Gurney suggested, a range of 2.40 to 3.60 for structural steels, with the value of $m = 3.0$ being frequently assumed for design purposes.

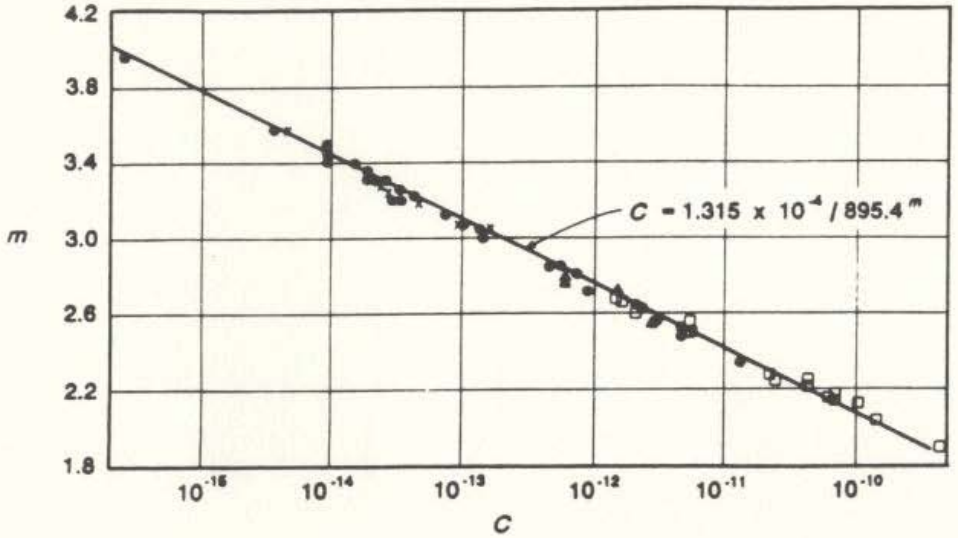

Figure 7.7: Relation between m and C for steels tested in air at $R \approx 0$: •, structural steels; □, high strength steels; ×, weld metal; △, HAZ [Gurney (1979b)]

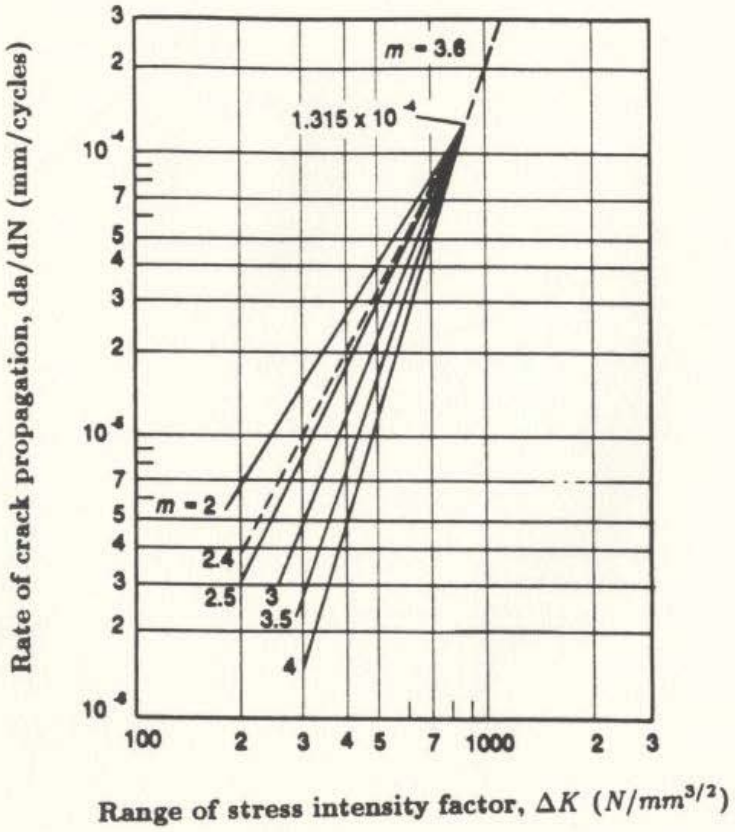

Figure 7.8: Influence of m on propagation rate. For structural steels, m usually lies between 2.4 and 3.6 [Gurney (1979b)]

Based on the foregoing observations by the mentioned investigators, the value of m and consequently C used in this study is based on that given by Gurney (1979b). A value of $m = 3.0$ was adopted for this study.

7.3.3 Fatigue Life Prediction

Although theoretical calculations suggest that K_I, K_{II} and K_{III} should be accounted for in the full fatigue life computations (Rhee, 1986), stress intensity factors obtained in the present study for all loading cases investigated, show that the weld toe crack propagation would be predominantly in the opening mode (mode I). Hence the crack propagation through the thickness was modeled using only the opening mode (mode I) stress intensity factors. The values for the deepest point along the crack front of a 94 mm crack half length (c) for all the three loading cases (axial, in-plane and out-of-plane bending loads) are given in the Tables 7.1 and 7.2 for two stress ranges (160 and 250 MPa). To illustrate the kind of results obtained at the surface of the tubular joint using line the spring element, stress intensity factors for the deepest and surface points of a saddle crack (under axial load) have been tabulated for different crack half lengths (c) and for different stress ranges; these tables are given in appendix C. It is worthwhile to point out at this stage,that because of the discrepancies obtained (in the SIF calculations) due to the inability of the line spring element to give meaningful results at the surface of the tube, the surface values (SIF) quoted in these tables are those obtained as a result of curve fitting. In order to incorporate the effect of load ratio, R, the stress intensity factor range (ΔK) was expressed in terms of the values of the stress intensity factors

Table 7.1: Stress intensity factors for the deepest points of saddle and crown cracks (160 MPa)

Crack depth (deepest point) a_o (mm)	SIFs at the deepest point on crack front Hot spot stress range = 160 MPa Crack half length (c) = 94 mm		
	SIF (KI) $\left[\frac{N}{mm^{3/2}}\right]$ Axial load	SIF (KI) $\left[\frac{N}{mm^{3/2}}\right]$ In-plane bending	SIF (KI) $\left[\frac{N}{mm^{3/2}}\right]$ Out-of-plane bending
1.00	252.12	311.85	262.40
2.50	377.40	462.98	389.87
3.80	444.69	531.14	472.62
5.70	506.99	597.25	527.03
7.60	545.46	642.62	575.74
9.50	557.79	668.35	573.91
11.40	537.68	667.71	577.52
12.54	508.15	651.33	546.92
14.25	432.83	598.21	464.71
16.00	314.78	501.50	321.59
17.10	206.68	513.54	189.42

Table 7.2: Stress intensity factors for the deepest points of saddle and crown cracks (250 MPa)

Crack depth (deepest point) a_o (mm)	SIFs at the deepest point on crack front Hot spot stress range = 250 MPa Crack half length (c) = 94 mm		
	SIF (KI) $\left[\frac{N}{mm^{3/2}}\right]$ Axial load	SIF (KI) $\left[\frac{N}{mm^{3/2}}\right]$ In-plane bending	SIF (KI) $\left[\frac{N}{mm^{3/2}}\right]$ Out-of-plane bending
1.00	393.94	487.27	410.00
2.50	589.69	723.40	609.17
3.80	694.83	829.90	738.47
5.70	792.17	933.20	823.48
7.60	852.28	1004.10	899.59
9.50	871.54	1044.30	896.73
11.40	840.12	1043.30	902.38
12.54	793.98	1017.70	854.56
14.25	676.30	934.70	726.11
16.00	491.85	783.60	502.49
17.10	322.94	802.40	295.97

obtained from the line spring finite element results of the tubular joint as

$$\Delta K_I = (1 - R)\, K_I \tag{7.5}$$

where R is the stress (or load) ratio, which is often introduced to indicate the relative proportions of the maximum and minimum stress and defined as

$$R = \frac{\sigma_{min}}{\sigma_{max}} \tag{7.6}$$

Eqn. (7.5) is valid for positive R only, which implies a tensile to tensile loading. The value of R negative implies that the loading is tensile to compressive, and this inevitably causes the crack to close during the compressive part of the loading cycle. Hence in this case only the tensile to tensile loading, which is responsible for the crack growth, is considered.

7.3.4 Propagation Life Calculation

The fatigue crack propagation life has been obtained in this study for the 94 mm crack half length (c) for all the three load cases, on an incremental crack growth integration of the Paris Law. The fatigue constants have been determined under conditions where only the applied load ratio, R, is known. The constants C and m used in the Paris law, for the present study are those developed by Gurney (1979b) for a variety of steels and weldment tested in air at R $\approx$ 0. For any value of R, the stress intensity factor range, ΔK, will automatically correct the crack growth rate to reflect this R-ratio effect using Eqn. (7.5).

7.3.5 Results and Discussions

The stress intensity factors used in the crack growth rate law, for the calculation of the fatigue crack growth life of the joint, have been obtained using the combination of line-spring elements and 8-node reduced integration degenerate shell elements. One important aspect of the modification to this approach, in the present study, was the prevention of crack surfaces from penetrating each other, which give rise to negative stress intensity factors. This modification was accomplished in the present study by writing a contact program that prevented the crack surfaces from penetrating each other. The essential aspects of this program consist of the inclusion of appropriate multi-point constraints applied in the form of linear equations on those nodes that lie along the crack front. It is worthwhile to mention at this point, that though this contact program gave promising results for most of the crack depths (a) and crack lengths considered the present study, it was observed that the prevention of the crack faces from penetrating each other (negative stress intensity factor) for the shortest crack length (c = 31.30 mm) and deepest crack depth (a = 17.10 mm, 90% of chord thickness) was somehow not possible. This suggests the probable dependence of stress intensity factor on the aspect ratio ($a/2c$) of the crack (Appendix C).

Figures 7.9 through 7.19 show normalized stress intensity factor (K_I) with respect to the brace nominal stress and crack depth versus the normalized crack front angle (ϑ) for relative depths a_o/T ranging from 0.05 to 0.9 for a crack half length (c) of 62.71 mm (axially load tubular T-joint). These figures illustrate the validity of the line spring elements in evaluating the stress intensity factors along the crack

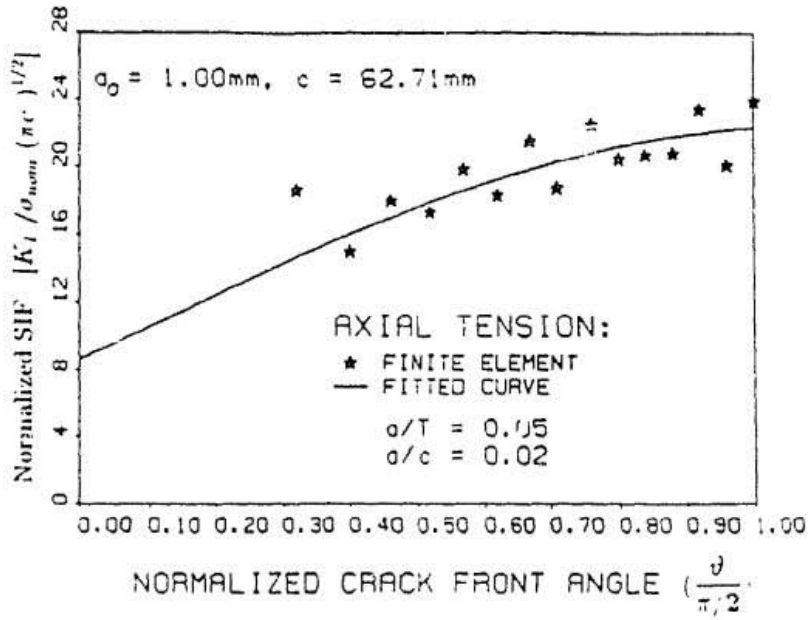

Figure 7.9: Normalized stress intensity factor dependence on the crack front position (Axial load) (a_o = 1.00 mm, c = 62.71 mm)

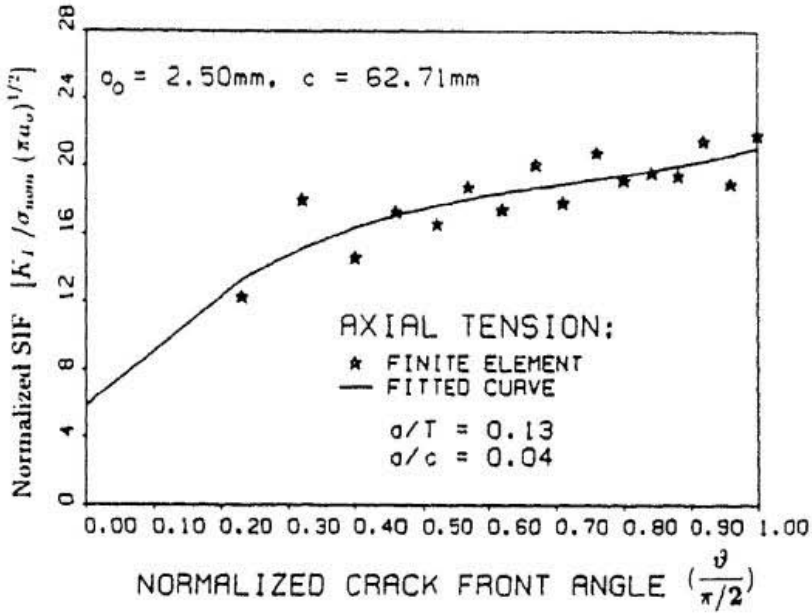

Figure 7.10: Normalized stress intensity factor dependence on the crack front position (Axial load) (a_o = 2.50 mm, c = 62.71 mm)

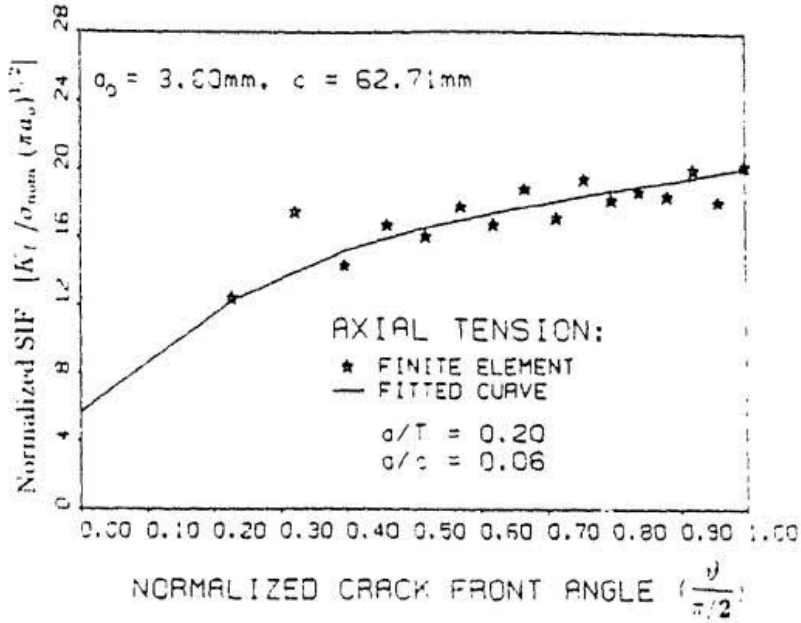

Figure 7.11: Normalized stress intensity factor dependence on the crack front position (Axial load) (a_o = 3.80 mm, c = 62.71 mm)

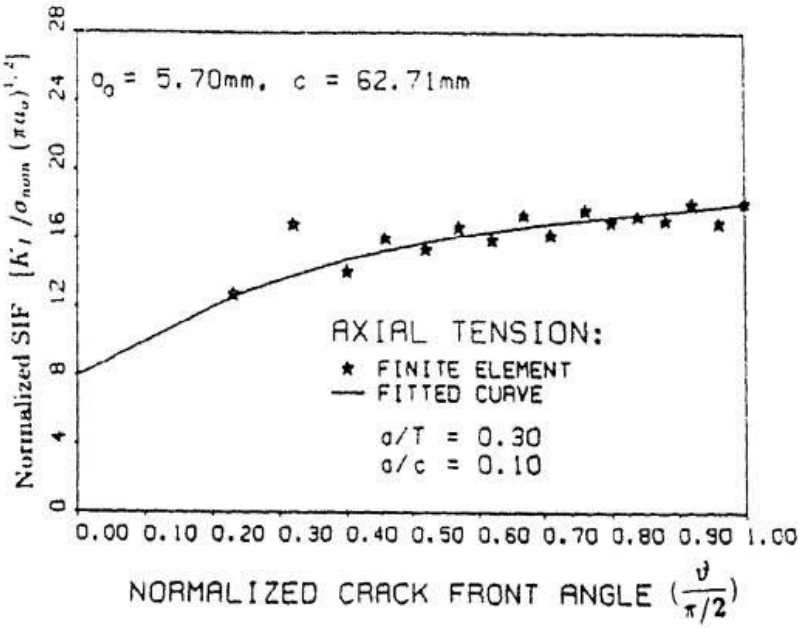

Figure 7.12: Normalized stress intensity factor dependence on the crack front position (Axial load) (a_o = 5.70 mm, c = 62.71 mm)

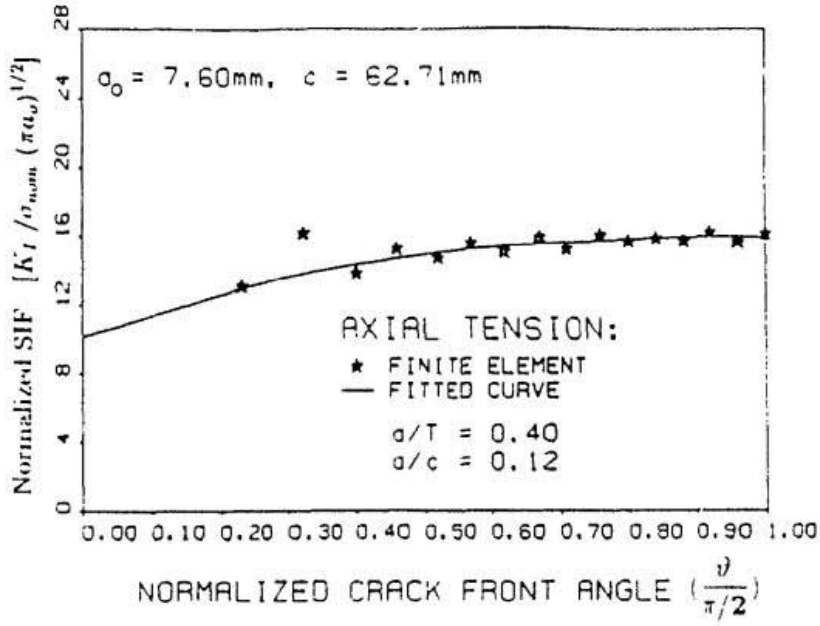

Figure 7.13: Normalized tress intensity factor dependence on the crack front position (Axial load) (a_o = 7.60 mm, c = 62.71 mm)

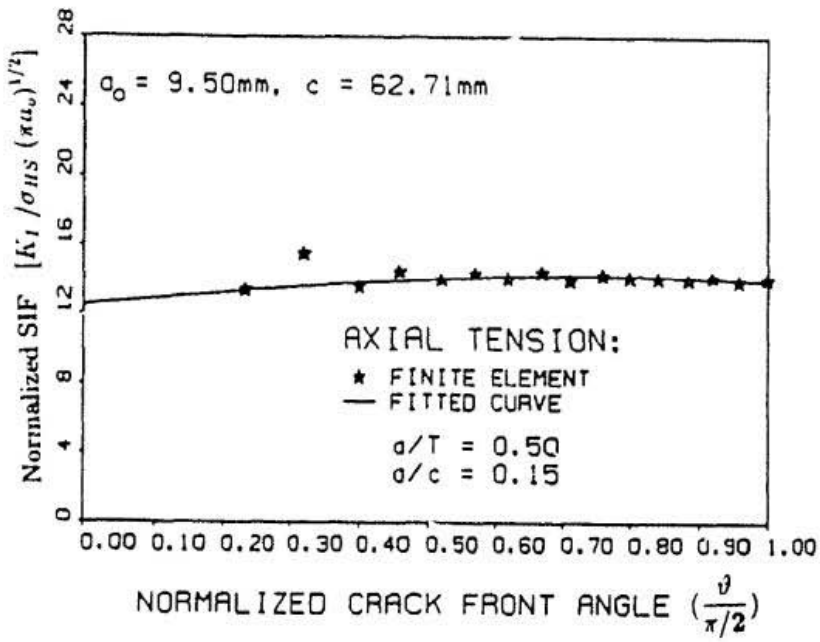

Figure 7.14: Normalized stress intensity factor dependence on the crack front position (Axial load) (a_o = 9.50 mm, c = 62.71 mm)

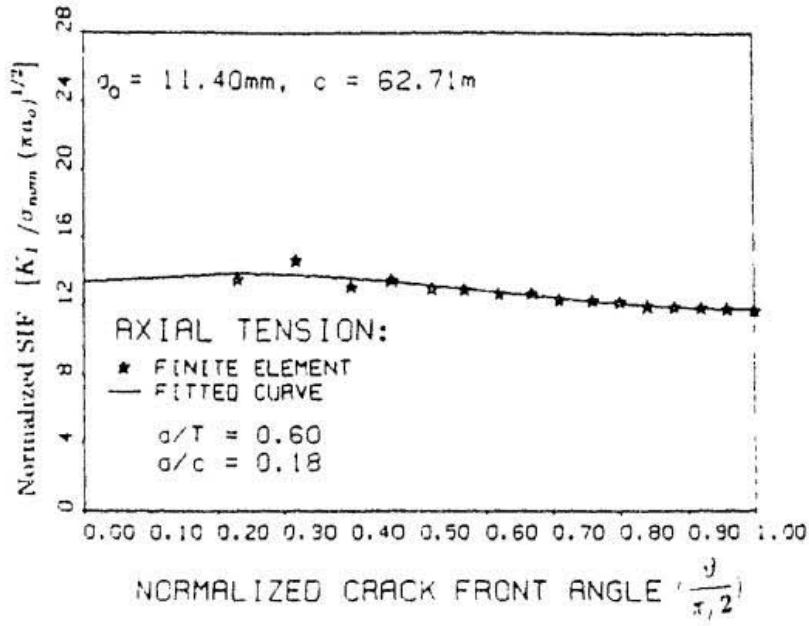

Figure 7.15: Normalized stress intensity factor dependence on the crack front position (Axial load) (a_o = 11.40 mm, c = 62.71 mm)

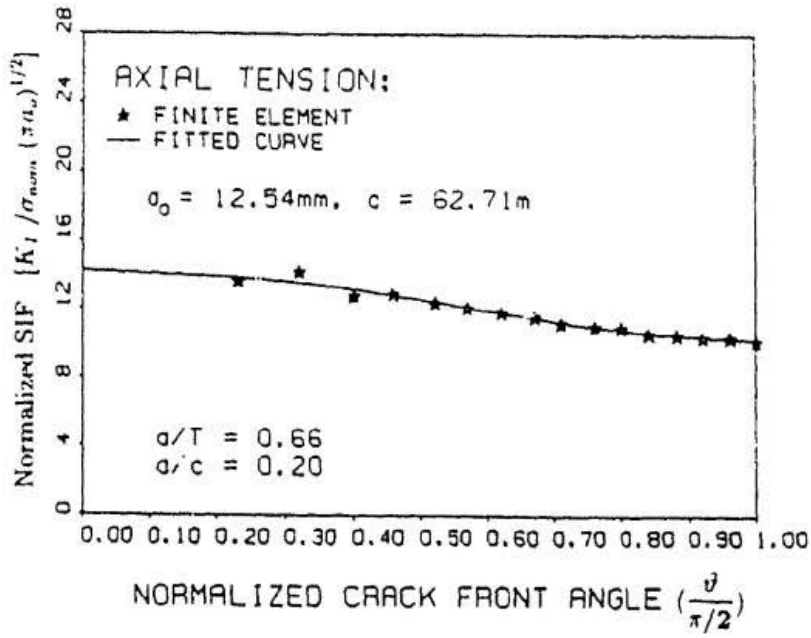

Figure 7.16: Normalized stress intensity factor dependence on the crack front position (Axial load) (a_o = 12.54 mm, c = 62.71 mm)

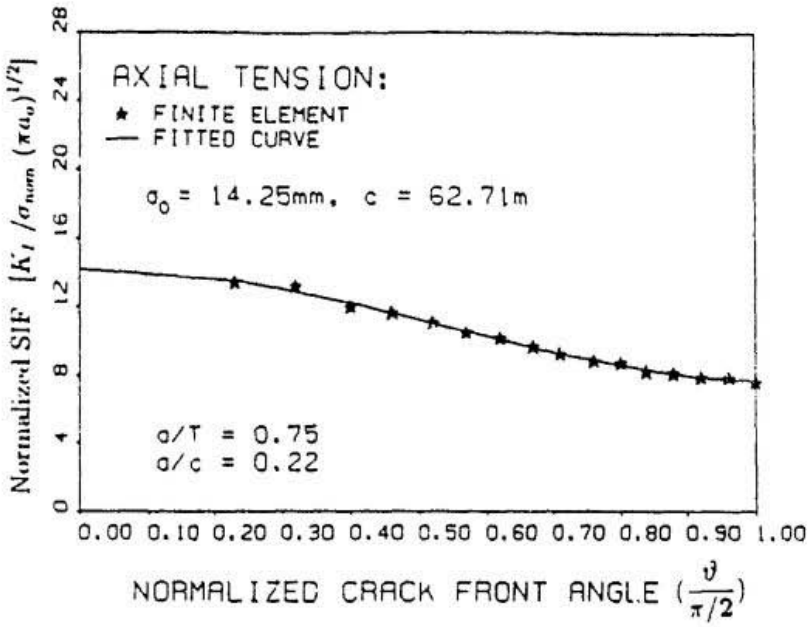

Figure 7.17: Normalized stress intensity factor dependence on the crack front position (Axial load) (a_o = 14.25 mm, c = 62.71 mm)

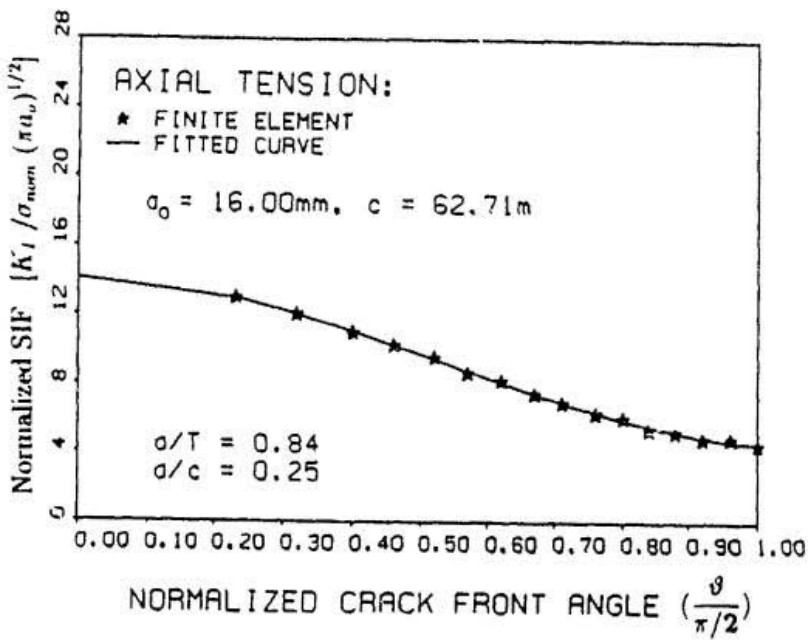

Figure 7.18: Normalized stress intensity factor dependence on the crack front position (Axial load) (a = 16.00 mm, c = 62.71 mm)

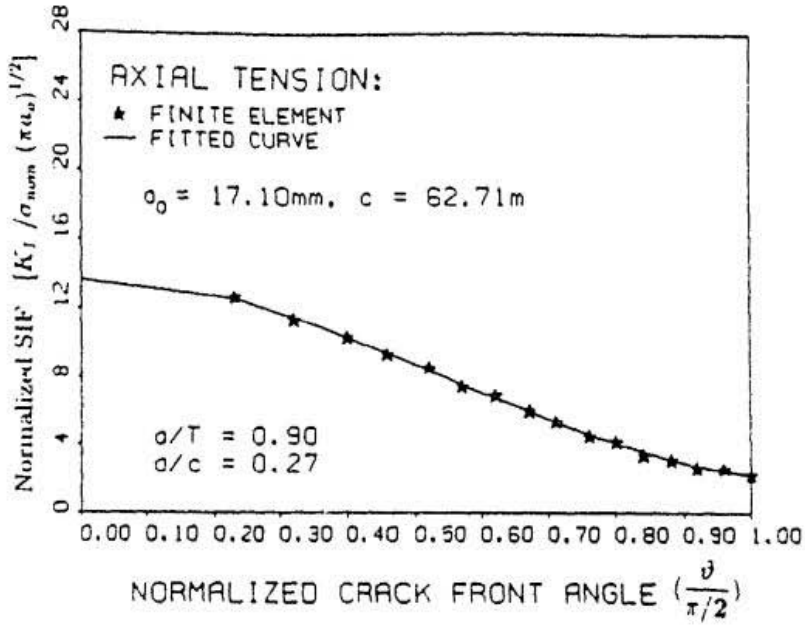

Figure 7.19: Normalized stress intensity factor dependence on the crack front position (Axial load) (a_0 = 17.10 mm, c = 62.71 mm)

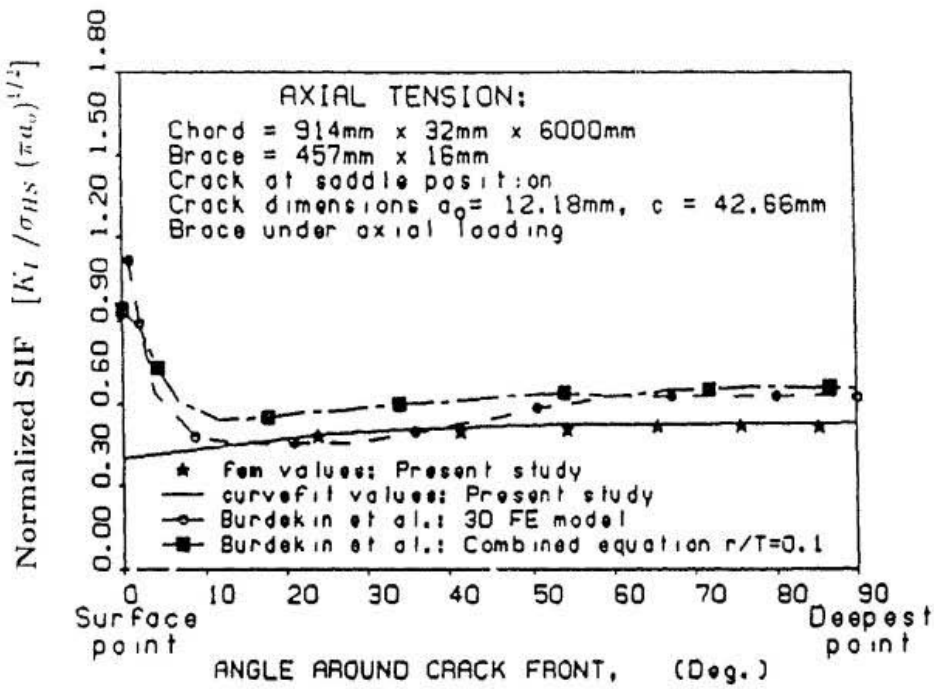

Figure 7.20: SIF vs. ϑ comparison between the present study and that of Burdekin et al. (1992) using 3-D FE and combined equation (axial load).

front of a semi-elliptical surface crack in tubular joints. The results obtained from the finite element analysis, along with the fitted curves, are shown in these figures. It is observed that the line spring element results for SIF oscillate as the free surface is approached, especially for the shallow crack depths. The percentage deviation of the fitted curve from the individual results are given in Table 7.3. The largest deviation of the line spring values from the fitted curve is -7.05% and this happens to be for the shallowest crack depth. From this table, it is observed that the line spring element gives a good result for deeper cracks than shallower cracks. The fitted curves have been extended to the intersection of the elliptical crack front with the tubular joint surface, based on the equation of the curve obtained for individual crack depth profile (from regresssion analysis). But it is important to state here, that the results obtained from the line spring elements closer to the surface of the tube, show that there is no physical basis for the line-spring model at the intersection of the crack front and the free surface. Although the fitted curve is extended to the surface of the tubular joint, it must be emphasized, that curve fitting utilizing the results of the line spring elements in this study, were performed using the values of stress intensity factors for $\vartheta/(\pi/2)$ equal to 0.3 to the deepest point ($\vartheta/(\pi/2) = 1.0$).

Figure 7.20 shows the comparison of the stress intensity factor distribution around the crack front of the present study with the 3-dimensional FE model and combined equation due to Burdekin et al. (1992). From this figure it is evident, that apart from the near surface SIF values, the results from the line spring element model show a good correlation with the SIFs obtained from three dimensional model and combined equation. The SIFs obtained from the present study seems to be a

Table 7.3: Normalized stress intensity factors at the deepest point of a saddle crack ($c = 62.71$ mm) under brace axial load

a [mm]	a/T	Actual Normalized SIF $\left[\frac{K_I}{\sigma_{nom}\sqrt{\pi a}}\right]$	Fitted curve $\left[\frac{K_I}{\sigma_{nom}\sqrt{\pi a}}\right]$	Deviation ‡ [%]
1.00	0.05	23.958	22.378	-7.05
2.50	0.13	21.870	21.121	-3.55
3.80	0.20	20.239	20.151	-0.59
5.70	0.30	18.137	18.089	-0.27
7.60	0.40	16.162	15.967	-1.22
9.50	0.50	14.073	13.941	-0.99
11.40	0.60	11.730	11.807	0.65
12.54	0.66	10.174	10.255	0.79
14.25	0.75	7.597	7.663	0.86
16.00	0.84	4.529	4.569	0.88
17.10	0.90	2.201	2.192	-0.41

‡ - Deviation of the fitted curve from the individual results

little lower than those given by Burdekin et al. (1992); thus the fatigue crack propagation life obtained from this study should tend to a higher value than those given by Burdekin et al.. It is important to note that the line spring element does not reflect both the weld toe effect and undershoot effect phenomena that have been observed in SIF's determined for both welded T-plates and tubular joints (Rhee 1988, Huang and Du et al. 1988 and Fu 1990) and also exhibited by Burdekin et al. in this figure. The probable absence of these phenomena in the present study may be due to (i) the line spring element being unable to give good results at the surface of the tube and (ii) the line-spring element is used in this context with a shell element and as such the weld toe is not modeled.

The results of the mode I stress intensity factors for the three load cases, viz., axial, in-plane and out-of-plane bending loads, normalized by the brace nominal stress (σ_{nom}), brace nominal stress (σ_{nom}) and $\sqrt{\pi a_o}$ and hot spot stress, σ_{HS} and $\sqrt{\pi a_o}$, respectively, plotted against the normalized crack depth (a_o/T), are shown in Figures 7.21, 7.22 and 7.23. Figure 7.21 shows that the normalized stress intensity factor increases as the crack depth increases, up to about 50% of tube wall thickness, and then decreases. Figures 7.22 and 7.23 show that the normalized SIF decreases as the crack depth increases. In Figure 7.22, the in-plane load curve gives much lower values than the out-of- plane or axial load cases since the SCF for in-plane loads is much lower than the axial or out-of-plane loads. Figure 7.23 gives the reason for the lower fatigue life of tubular joints subjected to in-plane loads since the normalized SIF for in-plane load is much higher than the axial or out-of-plane loads.

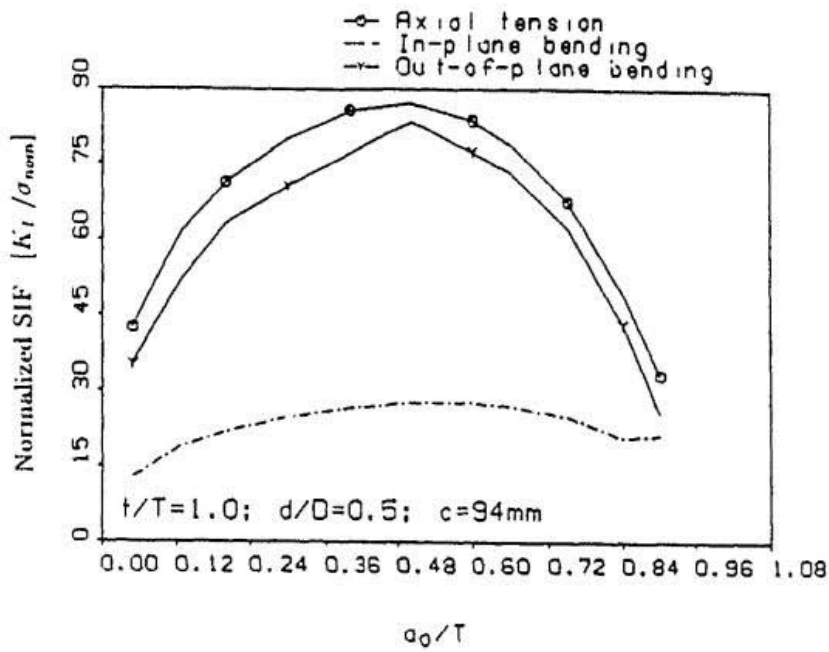

Figure 7.21: Normalized SIF (SIF/σ_{nom}) vs. a_o/T at the deepest points for axial, in-plane and out-of-plane bending loads.

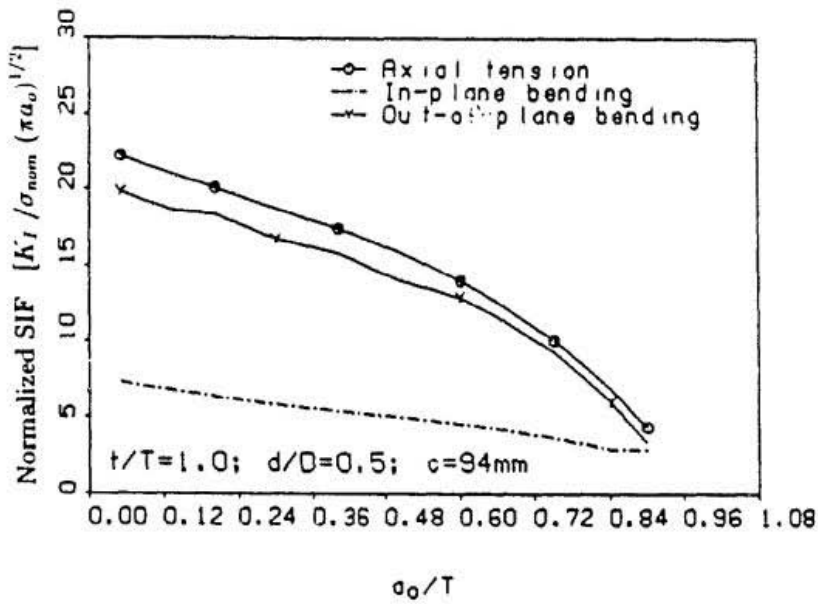

Figure 7.22: Normalized SIF (SIF/$\sigma_{nom}\sqrt{\pi a_o}$) vs. a_o/T at the deepest points for axial, in-plane and out-of-plane bending loads.

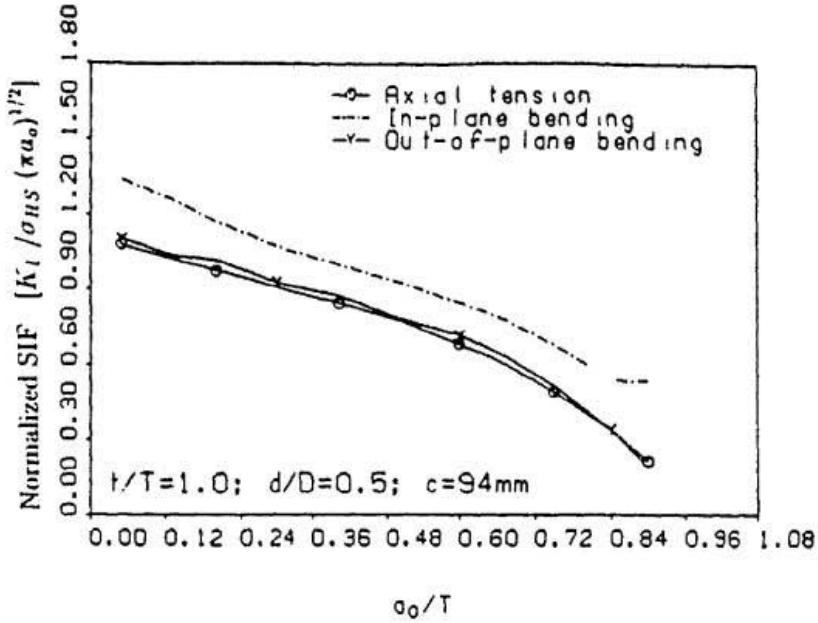

Figure 7.23: Normalized SIF (SIF/$\sigma_{HS}\sqrt{\pi a_o}$) vs. a_o/T at the deepest points for axial, in-plane and out-of-plane bending loads.

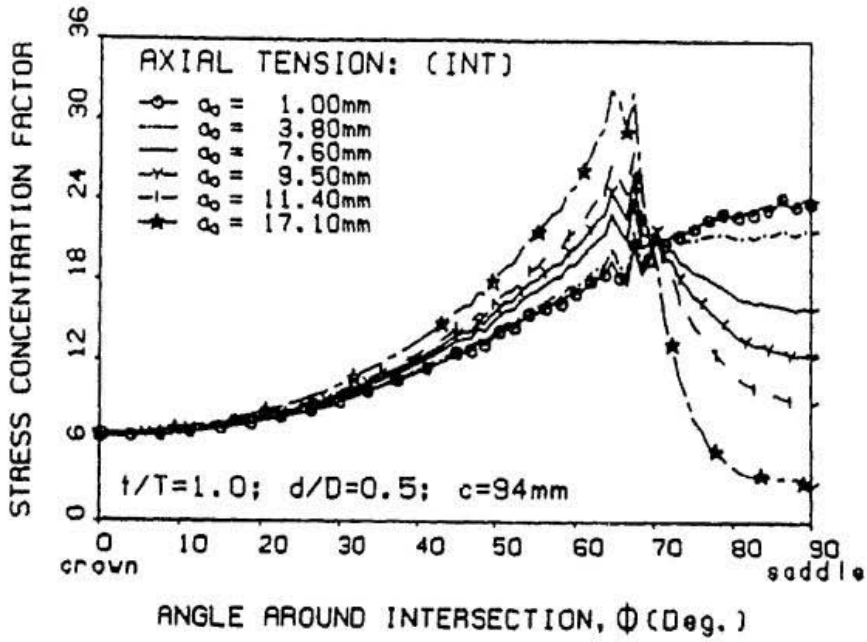

Figure 7.24: SCF variation around the joint intersection, at various crack depths. (axial load)

Figures 7.24 through 7.29 show the effect of the crack depth on the stress concentration around the brace/chord intersection (on the surface, near the crack) and along the crack line (along the crack front) for axial, in-plane and out-of-plane bending loads. The presence of the crack changes the SCF distribution around the intersection and the crack line. From all these figures, for all load cases, the SCF decreases as the crack depth increases at the location of the hot spot regions. But the decrease of the stress at these hot spot locations seems to cause a sharp rise in the SCF at the end of the crack front, near the surface.

The comparison of the fatigue life obtained in this study with the experimental study of an unstiffened tubular T-joint, carried out at Memorial University of Newfoundland (a/T vs. N) [Pates et al., (1989)], is shown in Figure 7.30. Although the present study overestimated the fatigue life, the trend of the present study is consistent with the experimental results. It appears that the crack growth during the earlier part of its penetration through the tubular wall thickness has a lower da/dN value due to its lower SIF value, as stated earlier in the discussions concerning Figure 7.20. Figure 7.31 shows the effect of stress range on the fatigue life of tubular T-joints used in this study.

Figure 7.32 shows the variation of the crack growth rate with crack depth. A comparison between the present study and MUN (axial loading) and UW (in-plane bending) experimental results is presented in this figure. There is a good agreement between the present study and the experimental values for deeper cracks; but for smaller crack depths the agreement is not good. This can again be explained by the inability of the line spring element to give good results at shallower depths.

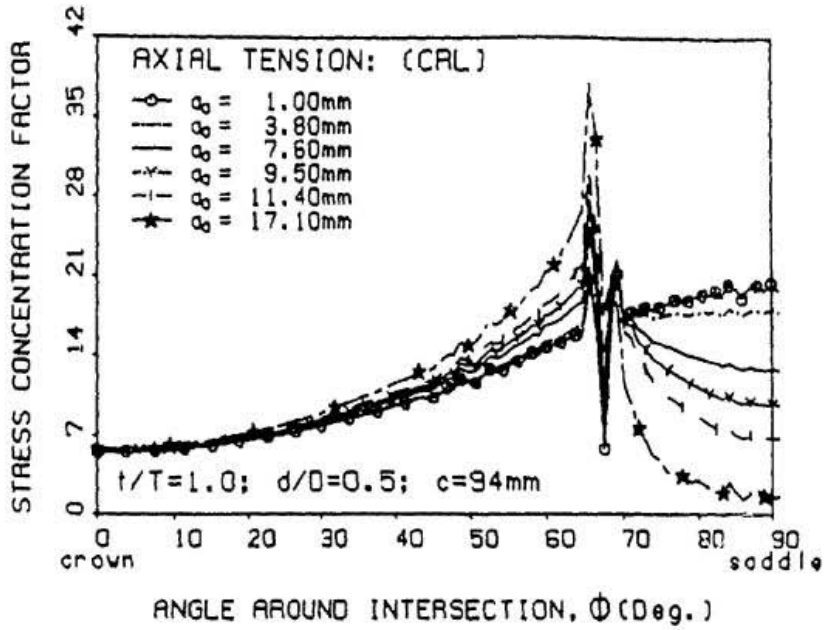

Figure 7.25: SCF variation along the crack line at various crack depth. (axial load)

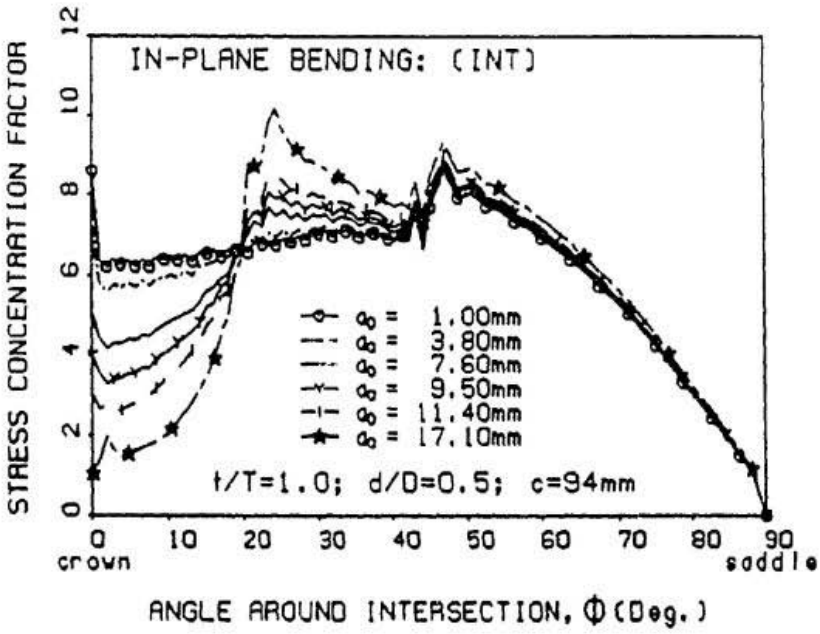

Figure 7.26: SCF variation around the joint intersection, at various crack depths. (IPB load)

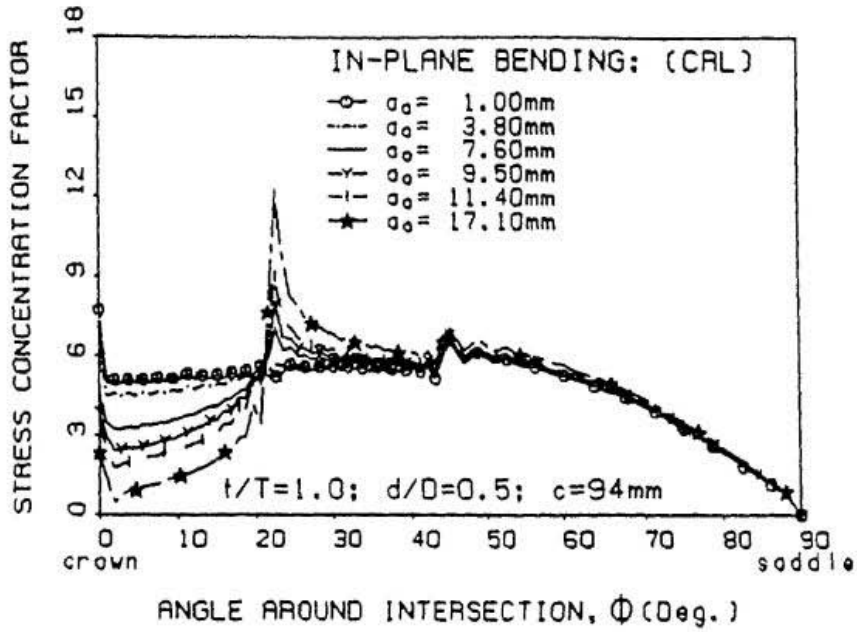

Figure 7.27: SCF variation along the crack line at various crack depths. (IPB load)

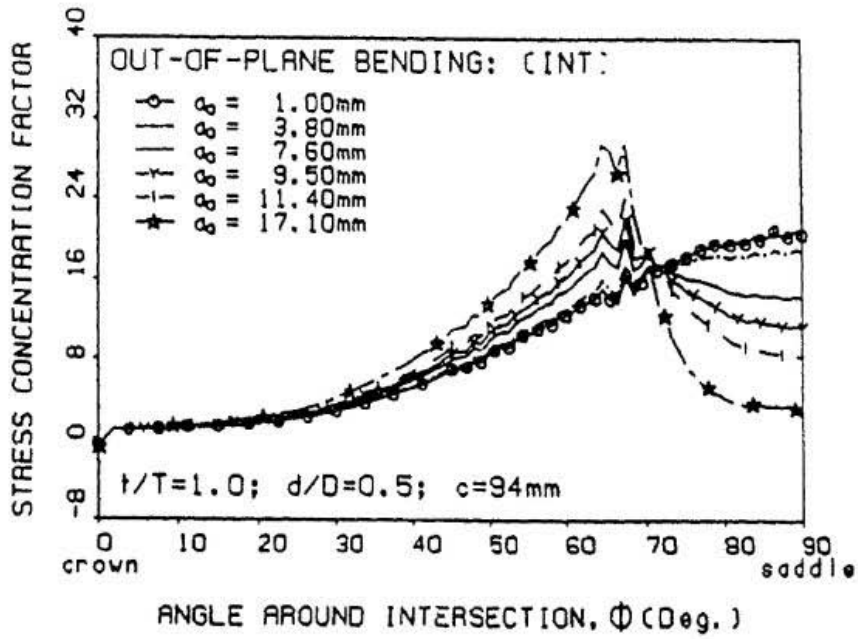

Figure 7.28: SCF variation around the joint intersection, at various crack depths. (OPB load)

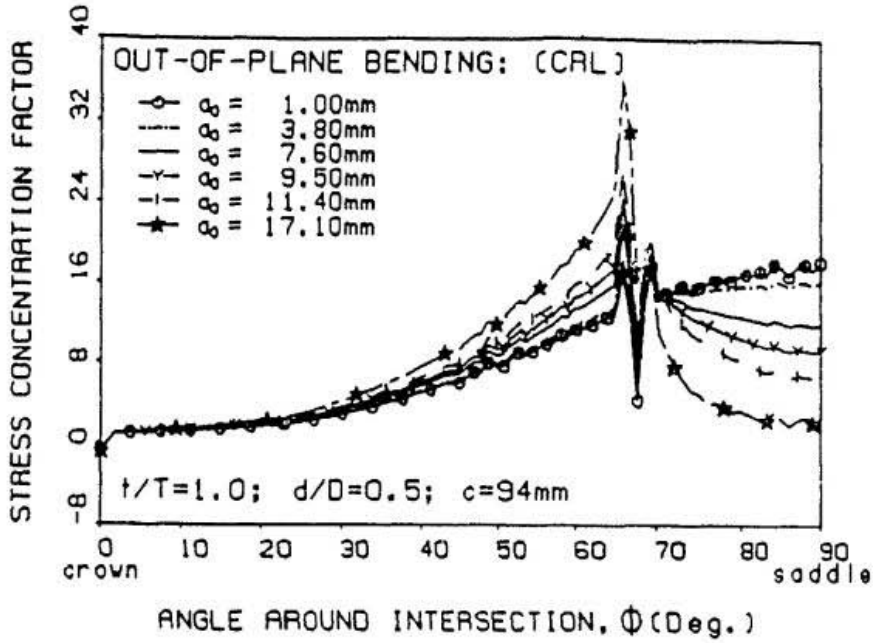

Figure 7.29: SCF variation along the crack line at various crack depths. (OPB load)

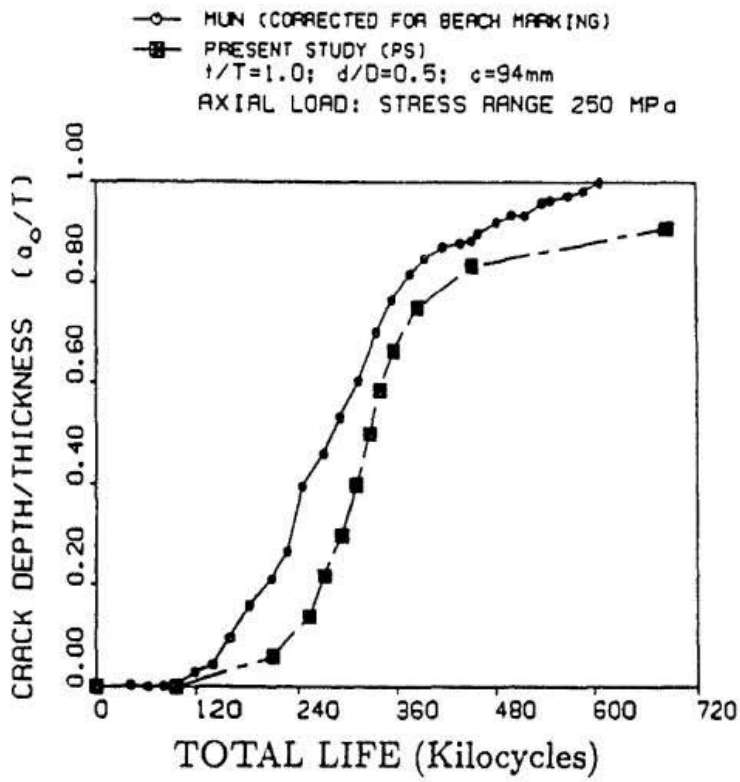

Figure 7.30: Crack depth vs cycles for propagating crack at saddle position; comparison between the present study (PS) and the earlier MUN experimental results (axial load)

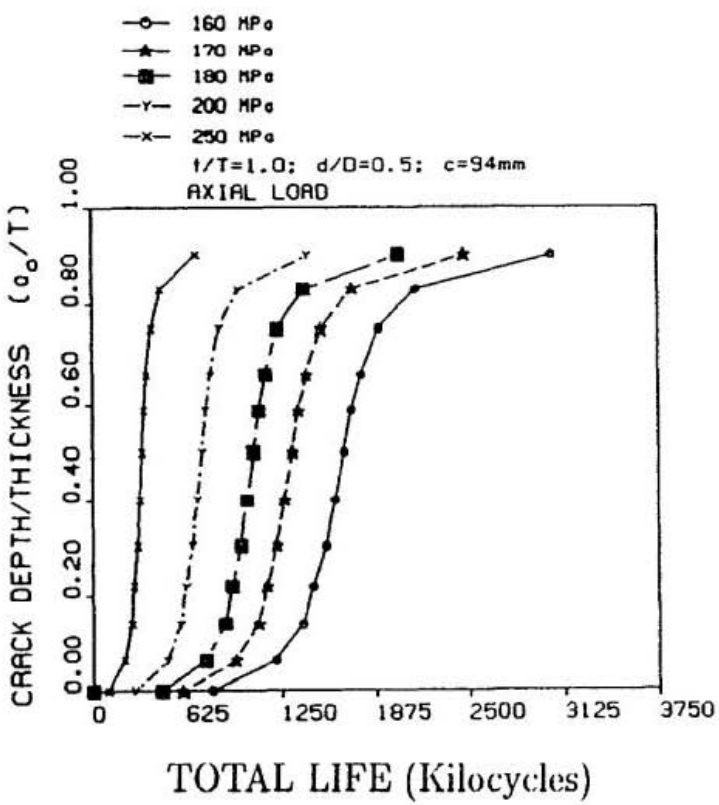

Figure 7.31: Crack depth vs. cycles showing the effect of stress range on the fatigue life of tubular T-joints (Axial load)

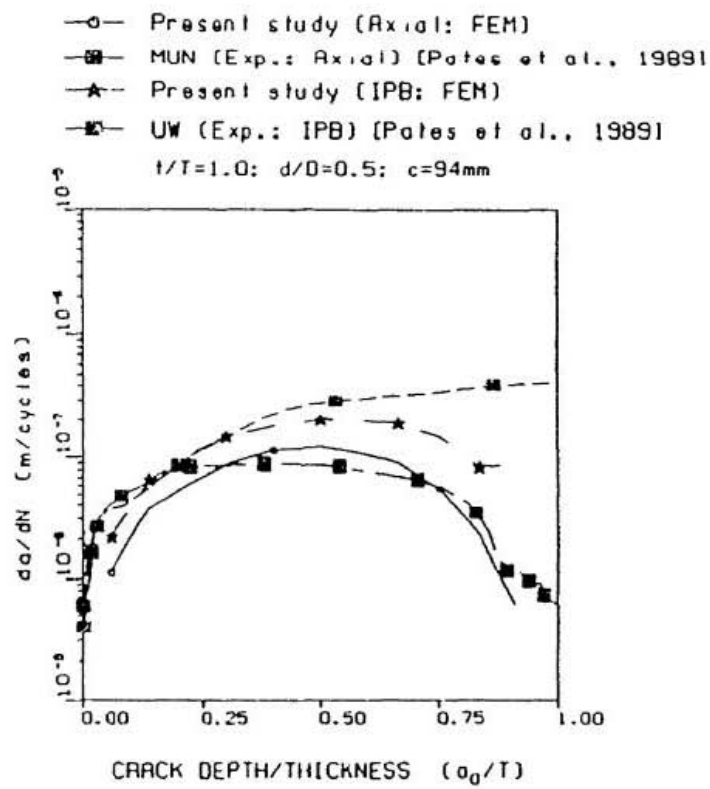

Figure 7.32: Crack growth rate vs. crack depth comparison between the present study (Axial: FEM) and MUN (Axial:Experiment) results [Pates et al., (1989)]; present study (IPB: FEM) and University of Waterloo results (Experiment: IPB) [Pates et al., (1989)]

Also for in-plane bending at large a_s/T values the experimental da/dN values of University Waterloo are much higher than the analytical da/dN values. This may be due to contribution from mode II and mode III stress intensity factors at deeper crack depths, a phenomenon that has been observed in many experimental investigations. However, the results of SIFs obtained in this study indicated that the crack growth was governed by mode I SIF.

Figure 7.33 shows influence of the load type on the fatigue life of the tubular joint under consideration. It is clear that for the same stress level, the axial load will have the highest life and the in-plane bending load the lowest with the out-of-plane bending load giving in between values. These results are consistent with the experimental results obtained in the fatigue strength study carried out under the Canadian Cooperation Fatigue Study program between Memorial and Waterloo Universities (Pates et al., 1989). The results of the fatigue life computation of the tubular T-joints (all three load cases) are shown in Tables 7.4, 7.5 and 7.6 with the percentage of crack initiation life for different stress ranges. The percentage crack initiation life for in-plane bending load case at lower stress ranges seems to be overestimated by the present calculations, but at higher stress ranges the results are consistent with experimental values. For the other two load cases, viz., axial and out-of-plane bending loads, the computed crack initiation lives exhibit good agreement with experimental values of MUN test. At 250 MPa, the axial load gives a crack initiation life of 14.0%, in-plane load gives an initiation life of 36.0% and the out-of-plane bending load gives an initiation life of 12.6%. From these results it appears that the load type is one of the important governing factors for the relative proportion of the crack initiation life to total life.

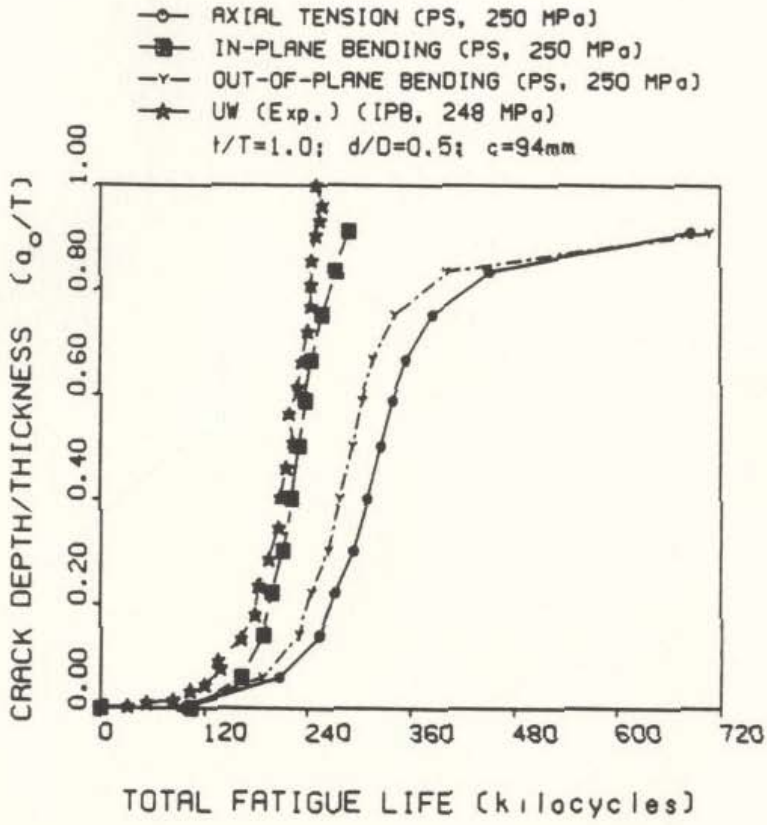

Figure 7.33: Comparison between the fatigue lives for axial, in-plane and out-of-plane bending loads for the present study (Note: University of Waterloo experimental results for in-plane bending load is also included).

Table 7.4: Fatigue lives at 90% chord thickness cracking (Axial tension).

Stress range MPa	Axial Tension (c = 94 mm)				
	N_f Kilo cycles	N_p Kilo cycles	N_T Kilo cycles	$\left[\frac{N_f}{N_T}\right]$ %	$\left[\frac{N_p}{N_T}\right]$ %
160	787	2254	3041	25.9	74.1
170	590	1879	2469	23.9	76.1
180	450	1583	2033	22.1	77.9
190	348	1346	1694	20.9	79.5
200	273	1154	1427	19.1	80.9
210	217	997	1214	17.9	82.1
220	174	867	1041	16.7	83.3
230	141	759	900	15.7	84.3
240	116	668	784	14.8	85.2
250	96	591	687	14.0	86.0
260	80	525	605	13.2	86.8

N_f = Initiation life
N_p = Propagation life
N_T = Total life

Table 7.5: Fatigue lives at 90% chord thickness cracking (IPB)

Stress range MPa	In-Plane Bending (c = 94 mm)				
	N_f Kilo cycles	N_p Kilo cycles	N_T Kilo cycles	$\left[\frac{N_f}{N_T}\right]$ %	$\left[\frac{N_p}{N_T}\right]$ %
160	859	706	1565	54.9	45.1
170	643	589	1232	52.2	47.8
180	490	496	986	49.7	50.3
190	379	422	801	47.3	52.7
200	297	362	659	45.1	54.9
210	236	312	548	43.1	56.9
220	189	272	461	41.0	59.6
230	154	238	392	39.3	60.7
240	126	209	335	37.6	62.4
250	104	185	289	36.0	64.0
260	86	165	251	34.3	65.7

N_f = Initiation life
N_p = Propagation life
N_T = Total life

Table 7.6: Fatigue lives at 90% chord thickness cracking (OPB).

Stress range MPa	Out-of-Plane (c = 94 mm)				
	N_f Kilo cycles	N_p Kilo cycles	N_T Kilo cycles	$\left[\frac{N_f}{N_T}\right]$ %	$\left[\frac{N_p}{N_T}\right]$ %
160	730	2362	3092	23.6	76.4
170	547	1969	2516	21.7	78.3
180	417	1959	2076	20.1	79.9
190	323	1410	1733	18.6	81.4
200	253	1209	1462	17.3	82.7
210	201	1049	1254	16.1	83.9
220	161	909	1070	15.0	85.0
230	131	795	926	14.1	85.9
240	107	700	807	13.3	86.7
250	89	619	708	12.6	87.4
260	74	550	624	11.9	88.1

N_f = Initiation life
N_p = Propagation life
N_T = Total life

7.4 Summary

The estimation of the crack propagation and total fatigue lives of the unstiffened tubular joints for axial, in-plane and out-of-plane loads has been presented in this chapter and compared with the experimental values obtained from the Memorial University and Waterloo University Cooperative Fatigue Testing programs. The comparison has been found to be good for the two types of loads considered by the respective Universities, viz., axial and in-plane bending loads. In addition to the fatigue lives the da/dN vs. normalized crack depth (a_o/T) curves and the stress variations along the surface of the intersection and along the crack front have been determined as the crack grows through the thickness. The stress (and strain) relief that occurs on the surface, the stress reduction along the crack depth and the stress concentration that occurs around the tip of the crack are clearly portrayed by these curves. The behaviour of the crack front is similar to the one expected as the crack grows through the thickness. The integration of the strain life procedure and the fracture mechanics concepts to arrive at the total crack-through life of an unstiffened tubular joint and the closeness of the numerically predicted values to the experimental ones could be claimed as the unique contribution from this study. It must be mentioned here that the method of using isoparametric shell elements, in conjuction with the line spring elements, for SIF computations did not consider the influence of the weld thickness at the toe. From an analysis (not included in the thesis) carried out earlier to determine the influence of the weld on the SCFs at the toe (by increasing the thickness of the corresponding two bottom layers of the brace), it was observed that the difference was marginal on the chord side where the line spring elements were used in the present study. Hence it was felt that there was no need for modelling the weld.

Chapter 8

Conclusions and Recommendations

8.1 Conclusions

In search for a possible numerical approach to solve the complex problem of the fatigue behaviour of offshore tubular welded joints, under the constant action of the cyclic wave loading, numerical studies were carried out using finite element method. The results were to be correlated with experimental results obtained earlier on unstiffened and stiffened tubular T-joints, fabricated from CSA G 40.2 M 350 WT steel, used in the Canadian Cooperative Offshore tubular joint experimental program carried out jointly at Memorial University of Newfoundland, St. John's, and the University of Waterloo, Waterloo. Three loading conditions, viz., axial, in-plane and out-of-plane bending loads were investigated. The axial load was applied as a tensile load on the brace, and the in-plane and out-plane bending loads were applied as transverse shear bending loads on the brace.

Extensive stress analysis was performed for both stiffened and unstiffened joints for different geometric parameters, using eight node degenerate isoparametric shell

elements with reduced Gaussian integration points. The choice of the element and the type of integration was designed to minimize the shear locking phenomenon encountered in the degeneration process as the shell thickness became smaller. The computation of stress and strain distribution around the intersection of chord and brace, and through the thickness of the joints was carried out for estimating their magnitudes and the locations of hot spot, which in turn gave an indication as to where the cracks were likely to initiate.

The local strain approach was used to estimate the fatigue crack initiation life. The line spring element was employed in the calculation of the stress intensity factors and the Paris crack growth law for the fatigue crack growth life estimation.

The results obtained from the entire analyses show that:

1. For the three loading cases of unstiffened tubular T-joints the maximum stress concentration factor (SCF) occurred at the saddle for the axial and out-of-plane bending loads, and at an angular distance of about 30 to 40 degrees, from the crown position, for the in-plane bending loads. There was an excellent correlation between experimental and analytical stress concentration factors for axial and out-of-plane bending loads; for in-plane bending loads the difference was significant. The maximum stress concentration location (hot spot location) could occur either in the brace or in the chord for the three loading cases, depending on the value of the thickness ratio τ. This ratio was observed to be smaller than 0.6 ($\beta = 0.5$, $\alpha = 7.02$ and $\gamma = 24.0$) for cracking to occur in the brace.

2. The differences between the present study and the experimental studies of Memorial University of Newfoundland (MUN) and the University of Waterloo (UW) could be attributed to the fact that the present study used a degenerate shell element and as such the weld was not modelled. Also the weld configuration at the crown, for the Waterloo University in-plane bending load tests, seems to exert a significant influence on the crown SCF. In addition the method of stress concentration computation could also have contributed to this difference since the experimental results (of MUN and UW) used radial stresses while the analytical study used the principal stresses for SCF computation.

3. The effect of chord end support was more obvious for the axial load case at the saddle point (10% difference between fixed and simply supported end cases), with very little difference at the crown location. For the in-plane bending loads a difference of 8% was observed at the crown; very little difference was observed for the out-of-plane bending loads.

4. The hot spot SCFs, for the unstiffened and stiffened tubular T-joints, varied considerably. The ratio of the SCF, for a specific unstiffened and stiffened tubular joint case study ($\beta = 0.5$, $\tau = 1.0$, $\alpha = 7.02$ and $\gamma = 24.0$), was obtained as 3.40 for axial loads, 4.16 for out-plane bending load and 1.33 for in-plane bending load. Hence the tubular joint could carry much higher axial and out-of-plane bending loads in the stiffened mode.

5. The results of the stress analysis in stiffened tubular joints suggest that the mechanism of the load transfer from the brace to chord is different when

compared with unstiffened joints. The load transmission from the brace to chord is better resisted by the greater in-plane stiffness of the ring stiffeners. Consequently the SCF of ring stiffened tubular joints is reduced considerably from that of unstiffened ones. In general, the higher the SCF distribution around the intersection (in unstiffened joints), the larger will be the effect of the ring stiffeners.

6. SCF was effectively reduced in stiffened joints by increasing the moment of inertia of the cross section of the ring stiffener. However, the hot spot would change from the chord or brace to the stiffener, if the sectional moment of inertia of the stiffener is large enough.

7. Although the location of the stiffener for effective reduction of SCF depended on the loading condition, results from the present study suggest the optimum locations to be middle half of the plug region for axial and out-plane loads and the outer quarters of the plug for in-plane bending loads.

8. The results presented in the present study show that the local strain approach can be successfully used to predict the fatigue crack initiation life of tubular welded joints

9. The use of fatigue strength exponent, *b*, and fatigue ductility exponent, *c*, obtained from small laboratory specimens having smaller SCF, SNCF and larger strain amplitudes, to tubular welded joints having very large SCF, SNCF and smaller strain amplitudes could lead to inaccurate and misleading results.

10. Empirically computed exponents b and c (from earlier experimental crack initiation life results for tubular T-joints) employed in this study, for crack initiation life computation, gave a very close fit to the experimental crack initiation life.

11. For semi-elliptical cracks at the weld toe of a tubular joint, it is possible to determine the correct stress intensity factors using full three-dimensional finite element analysis. This was achieved in this study by combining the line spring model with shell elements.

12. With suitable modifications and the correct contact algorithm, to prevent the crack surfaces from penetrating each other, the use of line spring elements was found to be suitable for evaluating the correct stress intensity factors along the crack front in complex structures like tubular welded joints.

13. Good comparison was obtained between the fatigue crack growth results of the present study and the experimental fatigue life results of MUN and UW.

14. The slight difference observed between the fatigue crack growth life estimation of the present study and that of MUN experimental results, for axial loads at shallower depths, is attributed to the inability of the line spring element to give accurate results at the intersection of the crack front and the tube surface.

15. The total life of tubular welded joints can be accurately predicted by combining the local stress-strain approach (to estimate the initiation life) with the fracture mechanics approach (to estimate the propagation life).

16. The assumption made by earlier researchers that the total fatigue life of tubular welded joints is governed primarily by the crack propagation life, can lead to inaccurate estimation of the fatigue life of tubular joints as shown in Tables 7.4, 7.5 and 7.6. It is observed that the ratios of the crack initiation life to total life range from 13 - 26% for axially loaded unstiffened tubulars, from 34 - 55% for in-plane bending loads and from 12 to 24% for out-of-plane bending loads.

8.2 Recommendations

As a consequence of the above study, many other areas that could be fruitfully explored have been opened up for subsequent researchers in this area. Even though extensive numerical studies have been reported on tubular joints by earlier researchers, the tying in together of the experiment and analysis starting from crack initiation to crack break-through has not been reported earlier (to the author's knowledge). As a result of the effort made in this study, the limitations present in the various methodologies suggested for this purpose have become evident. If greater attention is focused in this direction by other researchers, this would almost eliminate the need for expensive experimental testing of complex tubular joints (except in the case of a new design). Some studies that could assist in this process are:

(i) The conflict between the use of principal stress and the radial (to the brace) stress to compute the stress concentration factor in tubular joints should be resolved. Primarily this would be dependent on the question whether the crack

initiation and propagation are dependent on the principal stress or radial (to the brace) stress.

(ii) The accuracy of the SCFs obtained using 8-node degenerate isoparametric shell elements and 20-noded isoparametric three-dimensional elements (to model the tubular joint and intersection) should be examined and a judgement made on whether extrapolation to the weld toe is essential while using shell elements alone in the analysis. This becomes essential since the results obtained using the shell elements seems to lie very close to the experimental ones obtained using extrapolation to the weld toe.

(iii) More studies need to be carried out on the detailed stress analysis of unstiffened and stiffened tubular joints of other configurations, viz., Y, X, K and three-dimensional joints with a view to determine the hot spots, SCF distributions, principal plane orientations around the intersection (at the chord and brace – inside and outside – and in the stiffener) and the membrane and bending stress variations.

(iv) The nonlinear nature of the stress variation around the tubular joint intersection and the suitability of linear interpolation of the through-thickness bending and membrane stresses need be examined.

(v) Parametric equations should be developed for SCF distributions around the joint intersection taking into consideration the brace, chord and stiffener(s). Also parametric equations for SCF distribution for combination of various loads, viz., axial, in-plane bending and out-of-plane bending loads should be developed. The reliability of prediction, guidelines for mesh sizing around the intersection and size

of chord and brace lengths for proper SCF prediction need be examined and standardized.

(vi) The development of a suitable small-scale test to determine the strain-life material constants for high SCF/SNCF and low strain prototype structures should be examined.

(vii) The suitability of extending the line spring model SIF computations for surface penetration by considering the contiguity effects through small-scale CTS tests should be explored.

(viii) The suitability and accuracy of applying the results of the line spring elements to K_{II} and K_{III} cracking should be examined.

(ix) SIF computations, fatigue life calculations and comparison with experimental results should be extended to stiffened tubular joints.

(x) The detailed stress relief (on either side of crack) and stress concentration (around the tip of surface crack) observed in the numerical computations, reported above, should be suitably verified by experiments to validate the line spring elements.

REFERENCES

Aaghaakouchak, A.A and Dharmavasan, S., 1990. *Stress analysis of unstiffened and stiffened tubular joints using improved finite element model of intersection*, Proceedings of the Ninth International Conference of Offshore Mechanics and Arctic Engineering, Vol. III, Part A, Houston, Texas, pp. 321–328.

ABAQUS User's Manual. 1989. Hibbitt, Karlsson and Sorensen Inc. Providence, R. I. USA.

Ahmad, S., Iron, B.M., and Zienkiewicz, O.C., 1970. *Analysis of thick and thin shell structures by curved finite elements*, International Journal for Numerical Methods in Engineering, 2: pp. 419–451.

Barsoum, R.S., 1976. *A degenerated solid element for linear fracture analysis of plate bending and general shells*, International Journal for Numerical Methods in Engineering, Vol. 10, No. 1, pp. 551–564.

Barsoum, R.S., 1976. *On the use of isoparametric finite elements in linear fracture mechanics*, International Journal for Numerical Methods in Engineering, Vol. 8, No. 1, pp. 25–37.

Becker, J.M., Gerberich, W. and Bouwkwamp, J.G. 1970., *Fatigue failure of welded tubular joints*, Proceedings of Second Offshore Technology Conference, Paper No. OTC 1228, Dallas, Texas, pp. II-22 to II-29.

Bell, R., Vosikovsky, O., Burns, D.J and Mohaupt, U.H., 1987. *A fracture mechanics model for life prediction of welded plate joints*, Proceedings of the Third International Offshore Conference on Steel in Marine Structures (SIMS), Delft, The Netherlands, June 15–18, Paper TS53, pp. 901–910.

Berge, S., 1983. *Effect of plate thickness in fatigue of cruciform welded joints*, Report MK/R 67, Department of Marine Technology, Norwegian Institute of Technology, University of Trondheim.

Bhuyan, G.S., 1986. *Fatigue life prediction of offshore tubular T-joints using fracture mechanics approach*, A Ph. D. thesis, Faculty of Engineering and Applied Science, Memorial University of Newfoundland, Canada, pp. 182–189.

Bhuyan, G.S. and Vosikovsky, O., 1987. *Prediction of Fatigue crack initiation lives for welded plate T-joints, based on local stress-strain approach*, Physical Metallugy Research Laboratories Report: PMRL 87-51 (J), pp. 1–15.

Booth, G.S., 1987. *Constant amplitude fatigue tests performed on welded steel joints in air*. Proceedings of the European Offshore Steels Research Seminar, Cambridge. Paper 1, Session 3.

Borst, R.de, Kustres, G.M.A., Nauta, P. and Wilte, F.C.de, 1985. *DIANA - A comprehensive but flexible finite element system*. Finite Element System Handbook, ed. C.A. Brebbia. Springer Verlag, Berlin.

Chan, S.K., Tuba, I.S. and Wilson, W.K., 1970. *On the finite element method in linear fracture mechanics*. Engineering Fracture Mechanics, Vol. 2, pp. 1–17.

D. En., 1984. *Offshore installations: Guidance on design and correction*. Third Edition. U.K. Department of Energy, Her Majesty Stationary Office, London.

Delale, F. and Erdogan, F., 1981. *Line-spring model for surface cracks in a Reissner plate*. International Journal of Engineering Science, Vol. 19, pp. 1331–1340.

Dharmavasan, S. and Aaghaakouchak A.A., 1988. *Stress concentration factors in tubular by stiffened internal ring stiffeners*. Proceedings of the Seventh International Conference of Offshore Mechanics and Arctic Engineering, Vol. III, Part A, Houston, Texas, pp. 141–148.

Dhamarvasan, S., and Dover, W.D., 1984. *Stress distribution formulae and comparison of three stress analysis techniques for tubular joints*. Proceedings of the third International Conference on Offshore Mechanics and Arctic Engineering, Louisiana, U.S., pp. 421–432.

Dijkstra, O.D. and Hartog, J., 1978. *Dutch part of the large scale tubular joint fatigue test programme*. Proceedings, European Offshore steels Research Seminar, Cambridge. Paper 35, Session 10.

Dijkstra, O.D., Snijder, H.H. Overbeeke, J.L. and Wildshebut, H., 1987. *The calculation of fatigue crack growth for welded tubular joints using stress intensity factors determined by finite element method calculations*. Proceedings of the Conference on Steel in Marine Structures, Delft, The Netherlands, pp. 885–889.

Dijkstra, O.D., Snijder, H.H., and van Straalem, I.J., 1989. *Fatigue crack growth calculations using stress intensity factors for welded tee geometries*. Proceedings of Eighth International Conference on Offshore Mechanics and Arctic Engineering, The Hague, The Netherlands, March 19-23, pp. 137–143.

Dover, W.D. and Holdbrook, S.J.S., 1979. *Fatigue crack growth in tubular welded connections*. Proceedings of Second International Conference on the behaviour of Offshore Structures, London.

Dover, W.D. and Dharmavasan, S., 1982. *Fatigue fracture mechanics analysis of T and Y joints*. Proceedings of Fourteenth Offshore Technology Conference, Paper No. OTC 4404, Houston, Texas, May 3–6, pp. 315–318.

Dover, W.D., Kare, R.F., and Hall, M.S., 1991. *The reliability of SCF predictions using parametric equations: A statistical analysis*. Proceedings of the tenth International Conference on Offshore Mechanics and Arctic Engineering, Stavenger, Norway, pp. 453–459.

Dowling, N.E., 1979. *Fatigue at notches and the local strain and fracture mechanics approaches*. ASTM STP 677, pp. 247–273.

Dowling, N.E., Brose, W.R. and Wilson, W.K., 1979. *Notched member fatigue life predictions by local strain approach*. In Advances in Engineering, Vol. 6 (Edited by R.M. Wetzel), Society of Automotive Engineers, SAE, pp. 55–84

Du, Z.-Z. and Handcock, J. W., 1989. *Stress intensity factors of semi-elliptical cracks in a tubular welded joint using line springs and 3D finite elements*. Journal of Pressure Vessel Technology, Vol. 111, pp. 247–251

Dundrova, V., 1976. *Stress at intersection of tubes: cross and T-joints*. Struc. Fat. Res. Lab., Report P550-5, University of Texas.

Efthymiou, M., and Durkin, F., 1988. Development of stress concentration factor formulae and generalized influence functions for use fatigue analysis. Offshore Tubular Joint Conference, London.

Forman, R.G., Kearney, V.E. and Engle, R.M., 1967. *Numerical analysis of crack propagation in cyclic-loaded structures*. Trans. ASME, Journal of Basic Engineering, Vol. 89, pp. 459–464

Frost, N.E. and Dugdale, D.S., 1958. *The propagation of fatigue cracks in sheet specimens*. Journal of the Mechanics and Physics of Solids, Vol. 6, No. 2, pp. 92–101

Fu, B., 1990. *An elastic finite lement analysis of shallow crack in welded T-butt plates*. British Gas Engineering Research Station Report, ERS R.4344.

Fuchs, H.O. and Stephens, R.I., 1980. *Metal fatigue in Engineering*. John Wiley and Sons, p. 76.

Fröhling, W., 1992. *A weight function procedure for the calculation of stress intensity factors at the deepest point of semi-elliptical surface cracks in welded tubular joints*. Proceedings of the Eleventh International Conference on Offshore Mechanics and Arctic Engineering, Vol. III, Part B, pp. 275–284

Gibstein, M.B., 1978., Parametric stress analysis of T-joints, European Offshore Steels Research Seminar, Paper 26, Cambridge, UK.

Gibstein, M.B., 1981. *Fatigue strength of welded tubular joints tested at Det Norske Veritas Laboratories*, International Conference on Steel in Marine Structures, Paper No. 1.3, Paris.

Gibstein, M.B., and Moe, E.T., 1981. *Numerical and experimental stress analysis of tubular joints with inclined braces*, International Conference on Steel in Marine Structures, paper No. 6.3, Paris.

Gibstein, M.B., 1987. *Stress concentration in tubular K-joints with diameter ratio equal to one*, International Offshore Conference on Steel in Marine Structures, Paper TS 10, Delft, The Netherlands, pp. 377–393

Glinka, G., 1985. *Energy density approach to calculation of inelastic strain-stress near notches and cracks*, Engineering Fracture Mechanics, Vol. 22, No. 3, pp. 485–508.

Gurney, T.R., 1975. *Finite element analysis of some joints with the weld transverse to the direction of stress*, Welding Research International, Vol. 6, N0. 4, pp. 40–72

Gurney, T.R., 1977. *Theoretical analysis of the influence of toe defects on the fatigue strength of fillet welded joints*, Welding Institute Research Report 32/1977/e.

Gurney, T.R., 1979a. *Influence of thickness on the fatigue strength of welded joints*, The Second International Conference on behaviour of Offshore Structures, BOSS'79, London.

Gurney, T.R., 1979b. *Fatigue of welded structures*, Cambridge University Press, Lodon.

Gurney, T.R., 1981. *Some comments on fatigue design rules for offshore structures*, Proceedings of Second International Symposium on Integrity of Offshore Structures, Edited by D. Faulkner, M.J. Cowling and P.A. Frieze, Applied Science Publishers, Barking, Essex, England, pp. 219–234.

Gurney, T.R., 1989. *The influence of thickness on fatigue of welded joints—10 years on* (A Review of British Work), Proceedings of the Eighth International Conference on Offshore Mechanics and Arctic Engineering, The Hague, The Netherlands, March 19–23, pp. 1–8.

Greste, O., 1970. *Finite element analysis of tubular K-joints*, Clearing House No. PB193-560, University of California No. SESM 70-11.

Griffith, A.A., 1920. *The phenomena of rupture and flaw in solids*, Transactions, Royal Society of London, Ser. A, Vol. 221, p. 163.

Gulati, K.C., Wang, W.J. and Kan, D.K.Y., 1982. *An analytical study of stress concentratio effects in multi-brace joints under combined loading*, Proceedings of Fourteenth Annual Offshore Technology Conference, Paper No. 4407, Houston, Texas, pp. 337–342.

Haibach, E., Oliver, R. and Ritter, W., 1978. *Fatigue strength of angled specimens with fillet weld produced from 50 mm plate*, Proceedings, European Offshore Steels Research Bulletin, Vol. 13, No. 1, pp. 15–17

Haswell, J.V., 1992. *A general fracture mechanics model for a cracked tubular joint derived from the results of a finite element parametric study*, Proceedings of the Eleventh International Conference on Offshore Mechanics and Arctic Engineering, Vol. III, Part B, Calgary, Canada, pp. 267–271

Hellier A.K., Connolly, M.P., and Dover, W.D., 1990. Stress concentration factors for tubular Y and T joints, International Journal of Fatigue, Vol. 1, pp. 13–23.

Henshell, R.D., and Shaw, K.G., 1975. *Crack tip elements are unnecessary*, International Journal for Numerical Methods in Engineering, Vol. 9, 1975, pp. 495–509.

Hibbitt, Karlson and Sorensen Inc, 1989. *ABAQUS User Manual*

Hoffman, R.E., and Sharifi, P. 1980. *On the accuracy of different finite element types for the analysis of complex, welded tubular joints*, Proceedings, Offshore Technology Conference, Paper 2853, Houston, Texas, pp. 127–140

Huang, X. and Du, Z-Z. and Hancock, J.W., 1988. *A finite element evaluation of the stress intensity factors of the surface cracks in a tubular joint*, OTC Paper 5665, pp.

Huang, X. and Hancock, J.W., 1987. *The stress intensity factors of semi-elliptical cracks in a tubular welded T-joint under axial loading*, Engineering Fracture Mechanics, Vol. 30, pp. 25–35.

Hunter, M.S. and Ficke, W.G., 1957. *Cracking of notched fatigue specimens*, Proceedings of the American Society of Testing and Materials, Vol. 57, pp. 643–654.
Hutchinson, J.W., 1968. *Singular behaviour at the end of a tensile crack in a hardening material*, Journal of Applied Mechanics and Physics of Solids, Vol. 16, pp. 13–31.

Inglis, C.E., 1913. *Stresses in a plate due to the presence of cracks and sharp corners*, Proceedings, Institute of Naval Architects, Vol. 60.

Irwin, G.R., 1948. *Fracture dynamics*, in Fracturing of Metals, American Society of Metals, Cleveland.

Irwin, G.R., 1957. *Analysis of stresses and strains near the end of a crack traversing a plate*, Transactions, ASME, Journal of Applied Mechanics, Vol. 24.

Irvine, N.M., 1981. *Comparison of tubular joint stress analysis methods in the near weld region*, Proceedings of International Conference on Steel in Marine Structures, Paper 1.2, Paris.

Johnson, C.P., 1967. *The analysis of thin shells by a finite element procedure*, Report No. 67–22, University of California, Structures and Material Research Laboratory., Berkeley.

Johnston, G.O., 1978. *The influence of plate thickness on the fatigue strength of welded joints*, Welding Institute Report 3549/3/78 (unpublished).

Kathiresan, K., 1976. *Three-dimensional linear elastic fracture mechanics analysis by a displacement hybrid finite element model*, Ph.D. Thesis, Georgia Institute of Technology.

Kellog, M.W., 1956. *Design of piping systems.*, Second Edition, Wiley.

Kobayashi, A.S., Polvanich, N., Emery, A.F., and Love, W., 1975. *Surface flaws in a plate in bending*, Proc. 12th Annual Meeting Soc. Engng. Sc., Austin, Texas.

Kobayashi, A., Maiden, D., Simon, B. and Iida, S., 1969. *Application of the method of finite element analysis to two-dimensional problems in fracture mechanics*, Paper 69 WA-PVP-12, ASME Winter Annual Meeting.

Kuang, J.G., Potvin, A.B., Leick, R.D., and Kahlich, J.L., 1977. *Stress concentration in tubular joints*, Petroleum Engineering Journal, pp. 287–299.

Kuang, J.G., Potvin, A.B. and Leick, R.D., 1975. *Stress concentration in tubular joints*. Proceedings of Seventh Annual Offshore Technology Conference, Paper No. OTC 2205, Houston, Texas, pp. 593-612.
Lawrence, F.V., Jr., 1978. *Estimating the fatigue crack initiation life of welds*. Fatigue Testing of Weldments, ASTM STP 648, D. W. Hoeppner, Ed., pp. 134-158.

Lawrence, F.V., Jr., 1980. *Predicting the fatigue resistance of welds*. Fracture Control Program Report No. 36, College of Engineering, University of Illinois at Urbana-Champaign.

Lekhniskii, S.G., 1963. *The theory of elasticity of an anisotropic body*, Holder-Day, San Francisco.

Liaw, C.Y, Litton, R.W. and Reimer, R.B., 1976. *Improved finite elements for analysis of welded tubular joints*. Proceedings of Eighth Offshore Technology Conference, Paper No. OTC 2642, Houston, Texas, pp. 267-274.

Lieurade, H., and Maillard-Salin, C., 1982. *Low-cycle fatigue behaviour of welded joints in high-strength steels*. ASTM STP 770, pp. 311-336.

Liu, H.W., 1964. *Fatigue crack propagation and stresses and strains in the vicinity of crack*. Applied Material Research, October, pp. 229-237.

Miller, M.S. and Gallagher, J.P., 1981. *An analysis of several fatigue crack growth rate (FCGR) descriptions*. ASTM 738.

Mohaupt, U.H., Burns, D.J., Kalbfleisch, J.G. and Bell, R., 1987. *Fatigue crack development, thickness and corrosion effects in welded plate to plate joints*, International Conference on Steel in Marine Structures, Paper TS 3, The Netherlands, pp. 269-280.

Munaswamy, K., Bhuyan, G.S., and Swamidas, A.S.J., 1986. *Experimental and analytical studies on the fatigue of stiffened and unstiffened tubular t-joints*, Proceedings Offshore Technology Conference, Paper 5308, Houston, Texas, pp. 153-161.

Munaswamy, K., Williams, P., and Swamidas, A.S.J., 1987. *Fatigue tests of unstiffened tubular T-joints*, Progress Report AMCA-DSS Project DS6 File No. 235Q.23440-4-9276 Serial No. 05Q84-00431, Submitted to Material Technology Centre, AMCA, Ottawa, 122 p.

Neuber, H., 1969. *Theory of stress concentration for shear-strained prismatic bodies with arbitrary nonlinear stress-strain law*, Journal of Applied Mechanics, Vol. 28, pp. 544-551.

Niu, X. and Glinka, G., 1987. *The weld profile effect on stress intensity factors weldments*, International Journal of Fracture, Vol. 35, pp. 3–20.

Panagiotopoulos, G.D., 1986. *A finite element procedure for the stress analysis of tubular joint connection*, International Journal for Numerical Methods in Engineering, 23: pp. 318–329.

Paris, P.C. and Erdogan, F., 1963. *A critical analysis of crack growth laws*, Trans. ASME, Journal of Basic Engineering, Vol. 85, December, pp. 528–534.

Parks, D.M., Lockett, R.R., and Brockenbrough J.R., 1981a. *Stress-intensity factors for surface-cracked plates and cylindrical shells using line-spring finite elements*, Advances in Aerospace Structures and Materials, pp. 279–285.

Parks, D.M., 1981b. *Inelastic analysis of surface flaws using the line-spring model*, Advances in fracture research (Fracture 1981), Ed. D. Francois, Vol. 5, Pergamon, Oxford, pp. 2589–2598.

Parks, D.M. and White, C., 1982. *Elastic plastic line-spring finite elements for surface cracked plates and shells.*, Transactions of the American Society of Mechanical Engineering, Journal of Pressure Vessel Technology, Vol. 104, pp. 287–292.

Pates, M.J., Burns, D.J., Mohaupt, U., Swamidas, A.S.J., and Munaswamy K., 1989. *Fabrication and fatigue evaluation of welded t-joints for structures in marine environment*, Project Report DSS Contract No. 23SQ.23440-4-9276, Contract Serial No. 0SQ84-00431, Fabrication and Fleet Tech. (Kanata) - MTL (CANMET, EMR, Ottawa) Project: 166 p.

PDA Engineering, 1989. *PATRAN Plus User Manual, Vols. I and II.*

Peterson, R.E., 1974. *Stress concentration factors*, John Wiley and Sons, New York.

Petroski, H.J. and Achenbach, I.O., 1978. *Computation of the weight function from stress intensity factor*, Engineering Fracture Mechanics, Vol. 10., pp. 257–266.

Newman, J.C., 1977. *Improved method of collocation for the stress analysis of cracked plates with various shaped boundaries*, NASA TN D-6376.

Raju, I.S., and Newman, J.C., Jr., 1977. *Improved stress intensity factors for semi-elliptical surface cracks in finite thickness plates*, NASA TM X-72825.

Raju, I.S., and Newman, J.C., Jr., 1979. *Stress intensity factors for a wide range of semi-elliptical surface cracks in finite thickness plates*, Engineering Fracture Mechanics, Vol. 11, No. 4, pp. 817–829.

Raju, I.S., and Newman, J.C., Jr., 1981. *An empirical stress-intensity factors equations for surface crack*, Engineering Fracture Mechanics, Vol. 15, No. 1–2, pp. 185–192.

Raju, I.S., and Feichter, W.B., 1989. *A finite-element alternating method for two dimensional mode I crack configurations*, Engineering Fracture Mechanics, Vol. 33, No. 4, pp. 525–540.

Ramachandra, M.D.S., Madhava, R.A.G., Gandhi, P., Thandavamoorthy, T.S., Pant, P.K. and Murty, V.S.R., 1991. *Analytical and experimental investigations on internally ring stiffened steel tubular joints*, International Symposium on Fatigue and Fracture in Steel and Concrete Structures, Vol. 2, Mandras, India, pp. 715–718.

Rhee, H.C., 1986. *The behaviour of stress intensity factors of welded toe surface flaw of tubular X-joint*, Proceedings of Eighteenth Offshore Technology Conference, Paper No. OTC 5136, Houston, Texas, pp. 461–464.

Rhee, H.C. and Tyson, J.A., 1987. *Fatigue life calculation for offshore tubular joint using fracture mechanics crack growth analysis*, Proceedings of Nineteenth Offshore Technology Conference, Paper No. OTC 5557, Houston, Texas, pp. 1–7.

Rhee, H.C., 1989. *Fracture mechanics investigation of thickness effect on fatigue life*, Proceedings of the Eighth International Conference on Offshore Mechanics and Arctic Engineering, The Hague, The Netherlands, March 19-23, pp. 127–131.

Rhee, H.C., 1989. *Stress intensity factor evaluation from displacement along arbitrary crack tip radial lines for warped surface flaws*, Engineering Fracture mechanics, Vol. 32.

Rhee, H.C., 1991. *Reliability of solution method and empirical formulas of stress intensity factors for weld toe cracks of tubular joints*, Proceedings of the Tenth International Conference on Offshore Mechanics and Arctic Engineering, Vol. III, Part B, pp. 441–452.

Rice, J.R., 1972a. *Some remarks on elastic crack tip stress fields*, International Journal of Solids and Structures, Vol. 8, pp. 751–758.

Rice, J.R., and Levy, N., 1972b. *The part-through surface crack in a elastic plate*, Journal of Applied Mechanics, Vol. 39, pp. 185–194

Rice, J. and Tracey, D., 1973. *Computational fracture mechanics in numerical and computer methods in structural mechanics*. S.J. Fenves et al., Eds., Academic Press. New York, pp. 555-621.

Saxena, A., Hudak, S.J., Jr. and Jouris, G.M., 1979. *A three component model for representing wide-range fatigue crack growth rate behaviour*. Engineering Fracture Mechanics, Vol. 12, pp. 103-115.

Scordelis, A.C. and Bouwkamp, J.G., 1970. *Analytical study of tubular T-joints*. Proc. ASCE J. Struct. Div., Vol. 96 (ST1), No. 1070, pp. 65-87

Smith, F.W., and Alavi, M.J., 1971. *Stress intensity factors for a penny shaped cracked in a half space*. Engineering Fracture Mechanics, Vol. 3, No. 3, pp. 241-251

Socie, D.F., Morrow, J. and Chen, W.C., 1979. *A procedure for estimating the total fatigue life of notched and cracked members*. Journal of Engineering Fracture Mechanics, Vol. 11, N0. 4, pp. 851-860.

Tada, H., Paris, P.C. and Irwing, G.R., 1973. *The stress analaysis of cracks handbook*. Del Research Corporation, Hellertown, Pennsylvania.

Toprac, A. A., Johnston, L.P. and Noel, J., 1966. *Wleded tubular connections: an investigation of stresses in T-joints*. Weld. Res. Suppl., Vol. 31, No. 1, pp. 1-12s.

Toprac, A.A. and Louis, B.G., 1970. *The fatigue behaviour of tubular connections*. SFRL technical Report, P550-13.

Tracey, D.M. 1971. *Finite elements for determination of crack tip elastic stress intensity factors*. Engineering Fracture Mechanics, Vol. 3, pp. 255-266.

TUSTRA, 1985. *Tubular joint structural analysis module A*, User's Manual, RN 83 6150, Veritec, Oslo Norway.

Underwater Engineering Group, 1985. *Design of tubular joints for offshore structures*, UEG Publication VR-33, 1: pp. A49.

Visser, W., 1974. *On the structural design of tubular joints*. Proceedings. Offshore Technology Conference, OTC Paper 2117, pp. 881 - 894Texas.

Vosikovsky, O., Bell, R., Burns, D.J. and Mohaupt, U.H., 1985. *Fracture mechanics assessment of fatigue life of welded plate T-joints, including thickness effect*., Behaviour of Offshore Structural Steels, pp. 453-464.

Vosikovsky, O., Bell, R., Burns, D.J. and Mohaupt, U.H., 1987. *Effects of cathodic protection and thickness on corrosion of fatigue life of welded plate T-joints*, International Offshore Conference on Steel in Marine Structures, Paper TS 44, The Netherlands, pp. 787-798.

Walker, T.J., 1974. *A quantitative strain-and-stress state criterion for failure in the vicinity of sharp cracks*, Nuclear Technology, Vol. 23, pp. 189--203.

Westergaard, H.M., 1939. *Bearing pressures and cracks*, Transactions, ASME, Journal of Applied Mechanics.

Wildschut, H., 1978. *Fatigue behaviour of welded joints in air and sea water*, Proceedings, European Offshore Steels Research Seminar, Cambridge, Paper 5, Session 3.

Wordsworth, A.C., and Smedley, G.P., 1978. Stress concentration at unstiffened tubular joints. European Offshore Steels Research Seminar, Paper 31, Cambridge, UK.

Wylde, J.G. and McDonald, A., 1981. *Modes of fatigue crack development and stiffness measurements in welded tubular joints*, Fatigue in Offshore Structural Steel, Institution of Civil Engineers, Westminster, London, pp. 65-74.

Yamamoto, Y. and Tokuda, N., 1973. *Determination of stress intensity factor in cracked plates by finite element method*, International Journal for Numerical Methods in Engineering, Vol. 6, No. 3, pp. 127-439.

Yamamoto, Y., Tokuda, N. and Sumi, Y., 1983. *Accuracy considerations for finite element calculations of the stress intensity factor by the method of superposition*, in Hybrid and Mixed Finite Element Methods, Eds.: S.N. Atluri, R.H. Gallagher, and O.C. Zienkiewicz, F.R.S., Wiley, New York, pp. 361-379.

Yoshida, K., Inui, T., and Iida, K., 1977. *behaviour analysis and crack initiation prediction of tubular T-connections*, Proceedings Offshore Technology Conference,Paper No. 2854, Houston, Texas.

Zienkiewicz, O.C., 1977. The Finite Element Method., Third ed. McGraw-Hill, New York.

Zienkiewicz, O.C., Taylor, R.L. and Too, J.M., 1971. Reduced integration technique in general analysis of plates and shells. International Journal for Numerical Methods in Engineering, 3: pp 275-290.

Appendix A

Shape Function Generation

i	N_i	$\frac{\partial N_i}{\partial \xi}$	$\frac{\partial N_i}{\partial \eta}$
1	$1/4(1-\xi)(1-\eta)(-\xi-\eta-1)$	$1/4(2\xi+\eta)(1-\eta)$	$1/4(1-\xi)(2\eta+\xi)$
2	$1/4(1+\xi)(1-\eta)(\xi-\eta-1)$	$1/4(2\xi-\eta)(1-\eta)$	$1/4(1+\xi)(2\eta-\xi)$
3	$1/4(1+\xi)(1+\eta)(\xi+\eta-1)$	$1/4(2\xi+\eta)(1+\eta)$	$1/4(1+\xi)(2\eta+\xi)$
4	$1/4(1-\xi)(1+\eta)(-\xi+\eta-1)$	$1/4(2\xi-\eta)(1+\eta)$	$1/4(1-\xi)(2\eta-\xi)$
5	$1/2(1-\xi^2)(1-\eta)$	$-\xi(1-\eta)$	$-1/2(1-\xi^2)$
6	$1/2(1+\xi)(1-\eta^2)$	$1/2(1-\eta^2)$	$-(1+\xi)\eta$
7	$1/2(1-\xi^2)(1+\eta)$	$-\xi(1+\eta)$	$1/2(1-\xi^2)$
8	$\frac{1}{2}(1-\xi)(1-\eta^2)$	$-1/2(1-\eta^2)$	$-(1-\xi)\eta$
9	$(1-\xi^2)(1-\eta^2)$	$-2\xi(1-\eta^2)$	$-2\eta(1-\xi^2)$

Introducing new variables

$$\xi_0 = \xi\xi_i, \qquad \eta_0 = \eta\eta_i \tag{A.1}$$

the form

$$N_i = \frac{1}{4}(1+\xi_0)(1+\eta_0) \tag{A.2}$$

allows all shape functions to be written down in one expression as follows:

1. Corner nodes with $\xi_i = \pm 1$ and $\eta_i = \pm 1$

$$N_i = \frac{1}{4}(1 + \xi_0)(1 + \eta_0)(\xi_0 + \eta_0 - 1) \tag{A.3}$$

2. Mid-side nodes with (ξ_i, η_i) equate to $(0, \pm 1)$ and $(\pm 1, 0)$

$$N_i = \frac{1}{2}(1 + \xi_0)(1 - \eta^2) \tag{A.4}$$

and the shape function for the central ninth node is the bubble function,

$$N_i = (1 - \xi^2)(1 - \eta^2) \tag{A.5}$$

The systematic generation of these shape functions is illustrated in Figure A.1 for the serendipity family. As a starting point it is observed that for the mid-side nodes a Lagrange interpolation of a quadratic by linear type suffices to determine N_i at nodes 5 and 8. N_5 and N_8 are shown at Figures A.1 (a) and (b). For a corner node, such as Figure A.1 (c), a bilinear $\hat{N}_1$ is employed as a staring point, and it is immediately noted that while $\hat{N}_1 = 1$ at node 1, it is not zero at nodes 5 or 8, violating the finite element rule for shape function (Step 1). Successive subtraction of $\frac{1}{2}N_5$ (Step 2) and $\frac{1}{2}N_8$ (Step 3) ensures that a zero value is obtained at this node. By using an identical process the shape functions for other corner nodes are generated.

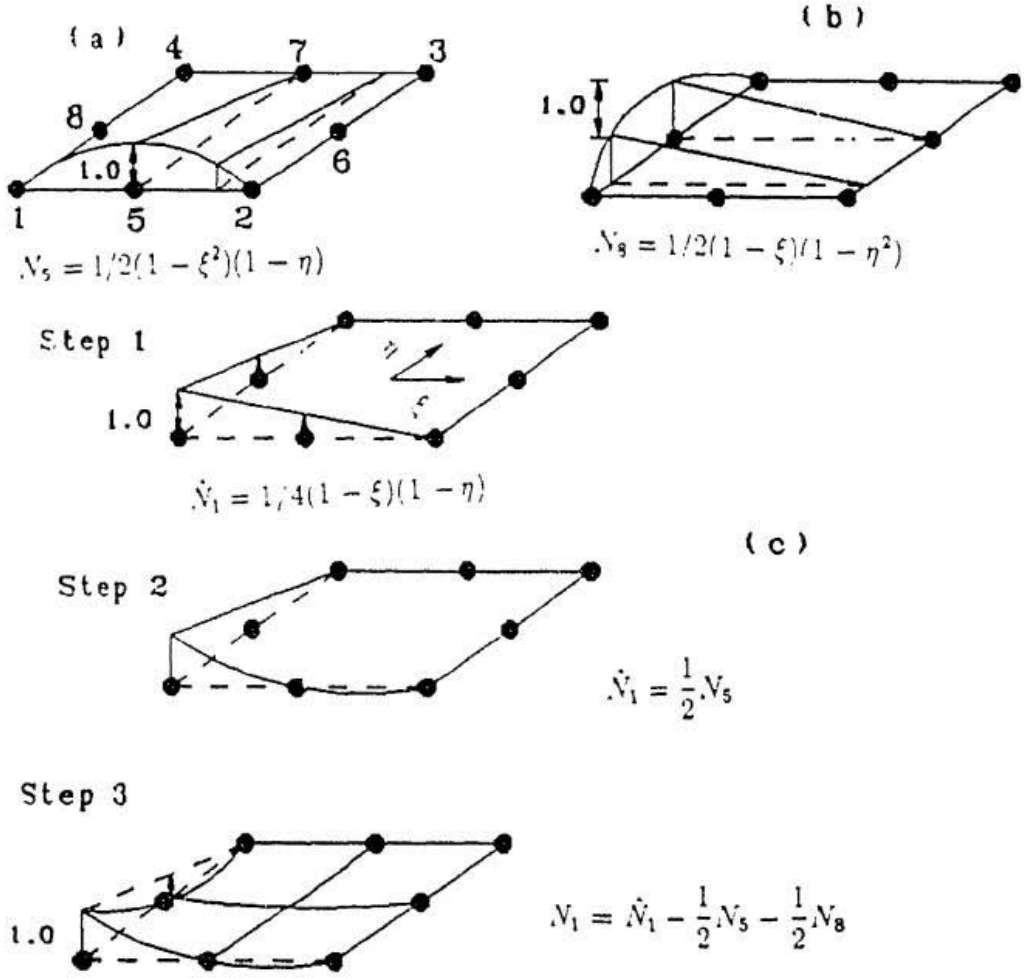

Figure A.1: Systematic generation of 'serendipity' shape functions

Appendix B

Elastic Constitutive Relationships

B.1 The Generalized Hooke's law

For the general cases of anisotropy the number of independent elastic constants in the [D] matrix is 21; this number is reduced considerably if the internal composition of the material possesses symmetry of any kind (Lekhnitskii, 1963). If a state of anisotropy possessing three mutually orthogonal planes of symmetry is assumed, with the mid-surface being a symmetric plane at each point and i the reference system of orthogonal axes (x_i', y_i', z_i') being parallel to the principal material axes ($i = 1, 2, 3$), one obtains the following strain-stress relationships:

$$
\begin{aligned}
\varepsilon_1 &= C_{11}\sigma_1 + C_{12}\sigma_2 + C_{13}\sigma_3 \\
\varepsilon_2 &= C_{12}\sigma_1 + C_{22}\sigma_2 + C_{23}\sigma_3 \\
\varepsilon_3 &= C_{13}\sigma_1 + C_{23}\sigma_2 + C_{33}\sigma_3 \\
\gamma_{12} &= C_{44}\tau_{12} \\
\gamma_{13} &= C_{55}\tau_{13} \\
\gamma_{23} &= C_{66}\tau_{23}
\end{aligned}
\tag{B.1}
$$

where the nine components of C_{ij} can be expressed as functions of Young's moduli, Poisson's ratios and the shear moduli. Noting the zero normal stress assumption $\sigma_{z'} = \sigma_3 = 0$, we obtain the elasticity matrix $\left[\overline{\mathbf{D}}\right]$ relating stresses and strains for a plate/shell element to be

$$
\{\sigma\} = \left[\overline{\mathbf{D}}\right]\{\varepsilon\} \tag{B.2}
$$

where

$$
\begin{aligned}
\{\sigma\} &= \{\sigma_1, \sigma_2, \tau_{12}, \tau_{13}, \tau_{23}\}^T \\
\{\varepsilon\} &= \{\varepsilon_1, \varepsilon_2, \gamma_{12}, \gamma_{13}, \gamma_{23}\}^T \\
[\overline{\mathbf{D}}] &= \begin{bmatrix} \overline{D}_1 & \overline{D}_{12} & 0 & 0 & 0 \\ \overline{D}_{12} & \overline{D}_2 & 0 & 0 & 0 \\ 0 & 0 & \overline{D}_3 & 0 & 0 \\ 0 & 0 & 0 & \overline{D}_4 & 0 \\ 0 & 0 & 0 & 0 & \overline{D}_5 \end{bmatrix}
\end{aligned}
\tag{B.3}
$$

and

$$
\begin{aligned}
\overline{D}_1 &= E_1/(1-\nu_{12}\nu_{21}) & \overline{D}_3 &= G_{12} \\
\overline{D}_2 &= E_2/(1-\nu_{12}\nu_{21}) & \overline{D}_4 &= K_1 * G_{13} \\
\overline{D}_{12} &= E_2\nu_{12}/(1-\nu_{12}\nu_{21}) & \overline{D}_5 &= K_2 * G_{23}
\end{aligned}
\tag{B.4}
$$

The terms K_1 and K_2 are the shear correction factors in the $\overline{13}$ and $\overline{23}$ planes.

In the case where the principal axes of anisotropy 1,2 do not coincide with the reference axes x', y', but are rotated by a certain angle, say θ, the new elasticity matrix $[\mathbf{D}]$ is determined by using the transformation as follows:

$$
\begin{aligned}
\{\sigma\} &= [\mathbf{T}]\{\sigma\} \\
\{\varepsilon\} &= [\mathbf{T}']\{\sigma\}
\end{aligned}
\tag{B.5}
$$

where

$$[\mathbf{T}] = \begin{bmatrix} [\mathbf{T}_1] & 0 \\ 0 & [\mathbf{T}_2] \end{bmatrix} \tag{B.6}$$

in which

$$[\mathbf{T}_1] = \begin{bmatrix} cos^2\theta & sin^2\theta & 2sin\theta cos\theta \\ sin^2\theta & cos^2\theta & -2sin\theta cos\theta \\ -sin\theta cos\theta & cos\theta sin\theta & (cos^2\theta - sin^2\theta) \end{bmatrix} \tag{B.7}$$

$$[\mathbf{T}_2] = \begin{bmatrix} cos\theta & sin\theta \\ -sin\theta & cos\theta \end{bmatrix}$$

and

$$[\mathbf{T}'] = \begin{bmatrix} [\mathbf{T}'_1] & 0 \\ 0 & [\mathbf{T}_2] \end{bmatrix} \tag{B.8}$$

in which

$$[\mathbf{T}'_1] = \begin{bmatrix} cos^2\theta & sin^2\theta & sin\theta cos\theta \\ sin^2\theta & cos^2\theta & -sin\theta cos\theta \\ -2sin\theta cos\theta & 2sin\theta cos\theta & (cos^2\theta - sin^2\theta) \end{bmatrix} \tag{B.9}$$

From Eqns. (B.2) and (B.5) it is possible to write

$$\{\sigma\} = [\mathbf{D}]\{\varepsilon\} \tag{B.10}$$

where $[\mathbf{D}]$ is the general elasticity matrix and $[\mathbf{T}]^{-1} \equiv [\mathbf{T}']^T$, hence

$$[\mathbf{D}] = [\mathbf{T}']^T \left[\overline{\mathbf{D}}\right] [\mathbf{T}'] = \begin{bmatrix} D_{11} & D_{12} & D_{13} & 0 & 0 \\ D_{12} & D_{22} & D_{23} & 0 & 0 \\ D_{13} & D_{23} & D_{33} & 0 & 0 \\ 0 & 0 & 0 & D_{44} & D_{45} \\ 0 & 0 & 0 & D_{45} & D_{55} \end{bmatrix} \tag{B.11}$$

Appendix C

Stress Intensity Factors

In order to show the values of the stress intensity factor obtained using the line spring element, the complete values of mode I behaviour are given in the following tables for axial tension load. SIF values for five crack lengths, considered in the present study, are given. The values are tabulated for the deepest and the surface points on the crack line. Note that these surface values were obtained by fitting a curve to the rest of values at points located below the surface of the tube. The unit of stress intensity factor is $\frac{N}{mm^{3/2}}$.

Table C.1: Stress Intesity Factors at Deepest and Surface points (Axial Load)

	SIFs at Deepest and Surface Points Stress Level = 160 MPa ($N/mm^{3/2}$)									
	c = 31.30mm		c = 47.06mm		c = 62.71mm		c = 78.57mm		c = 94.42mm	
a_o	$K_{I_{dpt.}}$	$K_{I_{spt.}}$	$K_{I_{dpt.}}$	$K_{I_{spt.}}$	$K_{I_{dpt.}}$	$K_{I_{spt.}}$	$K_{I_{dpt.}}$	$K_{I_{spt.}}$	$K_{I_{dpt.}}$	$K_{I_{spt.}}$
1.00	271.49	196.28	275.14	8.50	268.62	311.04	264.56	190.72	252.12	142.08
2.50	388.89	238.78	378.21	31.36	394.47	190.72	381.61	98.56	377.40	123.52
3.80	434.32	290.50	441.20	90.69	445.59	121.60	445.04	163.84	444.69	166.40
5.70	449.56	368.00	472.22	197.12	489.89	214.40	493.14	236.80	506.99	233.60
7.60	422.37	425.60	466.47	374.40	499.32	316.64	524.63	314.24	545.46	302.72
9.50	371.17	425.60	442.17	443.52	487.44	437.83	531.03	391.04	557.79	370.56
11.40	353.84	478.08	420.25	506.56	452.22	513.05	497.36	463.36	537.68	435.84
12.54	267.25	559.28	342.06	548.79	411.94	427.58	465.41	503.68	508.15	472.96
14.25	178.09	646.40	257.31	591.36	328.16	606.49	382.36	553.60	432.83	520.96
16.00	121.87	696.96	137.69	607.36	207.32	637.31	263.83	589.44	314.78	558.72
17.10	-39.20	705.28	39.31	595.84	102.82	638.56	154.87	597.76	206.68	571.52

Table C.2: Stress Intesity Factors at Deepest and Surface Points (Axial Load)

	SIFs at deepest and surface points Stress Level = 170 MPa $(N/mm^{3/2})$									
	c = 31.30mm		c = 47.06mm		c = 62.71mm		c = 78.57mm		c = 94.42mm	
a_o	$K_{I_{dpt.}}$	$K_{I_{spt.}}$	$K_{I_{dpt.}}$	$K_{I_{spt.}}$	$K_{I_{dpt.}}$	$K_{I_{spt.}}$	$K_{I_{dpt.}}$	$K_{I_{spt.}}$	$K_{I_{dpt.}}$	$K_{I_{spt.}}$
1.00	288.46	208.54	292.33	9.03	285.41	330.48	281.10	202.64	267.88	150.96
2.50	413.20	253.71	401.85	33.32	419.12	202.64	405.46	104.72	400.99	131.24
3.80	461.47	308.65	468.78	96.36	473.44	129.20	472.86	174.08	472.48	176.80
5.70	477.66	391.00	501.73	209.44	520.51	227.80	523.96	251.60	538.68	248.20
7.60	448.77	452.20	495.62	397.80	530.53	336.43	557.42	333.88	579.55	321.64
9.50	394.37	452.20	469.81	471.24	517.90	465.19	564.22	415.48	592.65	393.72
11.40	375.95	507.96	446.52	538.22	480.48	545.12	528.45	492.32	571.28	463.08
12.54	283.95	594.23	363.44	583.09	437.69	454.30	494.50	535.16	539.91	502.52
14.25	189.22	686.80	273.39	628.32	348.67	644.40	406.25	588.20	459.88	553.52
16.00	129.49	740.52	146.30	645.32	220.28	677.14	280.32	626.28	334.46	593.64
17.10	-41.65	749.36	41.77	633.08	109.24	678.47	164.55	635.12	219.60	607.24

Table C.3: Stress Intesity Factors at Deepest and Surface points (Axial Load)

	SIFs at Deepest and Surface points Stress Sevel = 180 MPa $(N/mm^{3/2})$									
	c = 31.30mm		c = 47.06mm		c = 62.71mm		c = 78.57mm		c = 94.42mm	
a_o	$K_{I_{dpt.}}$	$K_{I_{spt.}}$	$K_{I_{dpt.}}$	$K_{I_{spt.}}$	$K_{I_{dpt.}}$	$K_{I_{spt.}}$	$K_{I_{dpt.}}$	$K_{I_{spt.}}$	$K_{I_{dpt.}}$	$K_{I_{spt.}}$
1.00	305.42	220.81	309.53	9.56	302.20	349.92	297.63	214.56	283.64	159.84
2.50	437.50	268.63	425.48	35.28	443.78	214.56	429.31	110.88	424.58	138.96
3.80	488.61	326.81	496.35	102.02	501.29	136.80	500.67	184.32	500.28	187.20
5.70	505.76	414.00	531.24	221.76	551.13	241.20	554.78	266.40	570.36	262.80
7.60	475.17	478.80	524.78	421.20	561.74	356.22	590.21	353.52	613.64	340.56
9.50	417.57	478.80	497.44	498.96	548.37	492.56	597.41	439.92	627.51	416.88
11.40	398.07	537.84	472.78	569.88	508.74	577.18	559.53	521.28	604.89	490.32
12.54	300.66	629.19	384.82	617.39	463.44	481.02	523.59	566.64	571.67	532.08
14.25	200.35	727.20	289.48	665.28	369.18	682.30	430.15	622.80	486.94	586.08
16.00	137.10	784.08	154.90	683.28	233.24	716.97	296.81	663.12	354.13	628.56
17.10	-44.10	793.44	44.22	670.32	115.67	718.38	174.23	672.48	232.52	642.96

Table C.4: Stress Intesity Factors at Deepest and Surface Points (Axial Load)

	SIFs at Deepest and Surface Points Stress Level = 190 MPa $(N/mm^{3/2})$									
	c = 31.30mm		c = 47.06mm		c = 62.71mm		c = 78.57mm		c = 94.42mm	
a_o	$K_{I_{dpt.}}$	$K_{I_{spt.}}$	$K_{I_{dpt.}}$	$K_{I_{spt.}}$	$K_{I_{dpt.}}$	$K_{I_{spt.}}$	$K_{I_{dpt.}}$	$K_{I_{spt.}}$	$K_{I_{dpt.}}$	$K_{I_{spt.}}$
1.00	322.39	233.08	326.72	10.09	318.99	369.36	314.17	226.48	299.39	168.72
2.50	461.81	283.56	449.12	37.24	468.43	226.48	453.16	117.04	448.16	146.68
3.80	515.76	344.96	523.93	107.69	529.13	144.40	528.49	194.56	528.07	197.60
5.70	533.85	437.00	560.76	234.08	581.75	254.60	585.60	281.20	602.05	277.40
7.60	501.57	505.40	553.93	444.60	592.94	376.01	622.99	373.16	647.73	359.48
9.50	440.77	505.40	525.08	526.68	578.83	519.92	630.59	464.36	662.37	440.04
11.40	420.18	567.72	499.05	601.54	537.01	609.25	590.62	550.24	638.49	517.56
12.54	317.36	664.14	406.20	651.68	489.18	507.75	552.68	598.12	603.42	561.64
14.25	211.48	767.60	305.56	702.24	389.69	720.21	454.05	657.40	513.99	618.64
16.00	144.72	827.64	163.51	721.24	246.19	756.80	313.29	699.96	373.81	663.48
17.10	-46.55	837.52	46.68	707.56	122.09	758.29	183.91	709.84	245.43	678.68

Table C.5: Stress Intesity Factors at Deepest and Surface Points (Axial Load)

	SIFs at Deepest and Purface Points Stress Level = 200 MPa $(N/mm^{3/2})$									
	c = 31.30mm		c = 47.06mm		c = 62.71mm		c = 78.57mm		c = 94.42mm	
a_o	$K_{I_{dpt.}}$	$K_{I_{spt.}}$	$K_{I_{dpt.}}$	$K_{I_{spt.}}$	$K_{I_{dpt.}}$	$K_{I_{spt.}}$	$K_{I_{dpt.}}$	$K_{I_{spt.}}$	$K_{I_{dpt.}}$	$K_{I_{spt.}}$
1.00	339.36	245.34	343.92	10.62	335.78	388.80	330.70	238.40	315.15	177.60
2.50	486.11	298.48	472.76	39.20	493.09	238.40	477.01	123.20	471.75	154.40
3.80	542.90	363.12	551.50	113.36	556.98	152.00	556.30	204.80	555.86	208.00
5.70	561.95	460.00	590.27	246.40	612.37	268.00	616.42	296.00	633.74	292.00
7.60	527.97	532.00	583.09	468.00	624.15	395.80	655.78	392.80	681.82	378.40
9.50	463.97	532.00	552.71	554.40	609.30	547.29	663.78	488.80	697.23	463.20
11.40	442.30	597.60	525.31	633.20	565.27	641.31	621.70	579.20	672.10	544.80
12.54	334.06	699.10	427.58	685.98	514.93	534.47	581.77	629.60	635.18	591.20
14.25	222.61	808.00	321.64	739.20	410.20	758.11	477.94	692.00	541.04	651.20
16.00	152.34	871.20	172.11	759.20	259.15	796.63	329.78	736.80	393.48	698.40
17.10	-49.00	881.60	49.14	744.80	12[illegible]2	798.20	193.59	747.20	258.35	714.40

Table C.6: Stress Intesity Factors at Deepest and Surface Points (Axial Load)

	SIFs at deepest and surface points Stress Level = 210 MPa $(N/mm^{3/2})$									
	c = 31.30mm		c = 47.06mm		c = 62.71mm		c = 78.57mm		c = 94.42mm	
a_o	$K_{I_{dpt.}}$	$K_{I_{spt.}}$	$K_{I_{dpt.}}$	$K_{I_{spt.}}$	$K_{I_{dpt.}}$	$K_{I_{spt.}}$	$K_{I_{dpt.}}$	$K_{I_{spt.}}$	$K_{I_{dpt.}}$	$K_{I_{spt.}}$
1.00	356.33	257.61	361.12	11.16	352.56	408.24	347.24	250.32	330.91	186.48
2.50	510.42	313.40	496.40	41.16	517.74	250.32	500.86	129.36	495.34	162.12
3.80	570.05	381.28	579.08	119.03	584.83	159.60	584.12	215.04	583.66	218.40
5.70	590.05	483.00	619.79	258.72	642.99	281.40	647.25	310.80	665.42	306.60
7.60	554.37	558.60	612.24	491.40	655.36	415.59	688.57	412.44	715.92	397.32
9.50	487.17	558.60	580.35	582.12	639.76	574.65	696.97	513.24	732.09	486.36
11.40	464.41	627.48	551.58	664.86	593.54	673.38	652.79	608.16	705.70	572.04
12.54	350.77	734.05	448.95	720.28	540.67	561.20	610.86	661.08	666.94	620.76
14.25	233.74	848.40	337.72	776.16	430.71	796.02	501.84	726.60	568.09	683.76
16.00	159.95	914.76	180.72	797.16	272.11	836.46	346.27	773.64	413.15	733.32
17.10	-51.45	925.68	51.59	782.04	134.95	838.11	203.27	784.56	271.27	750.12

Table C.7: Stress Intesity Factors at Deepest and Surface Points (Axial Load)

	SIFs at deepest and surface points Stress Level = 220 MPa $(N/mm^{3/2})$									
	c = 31.30mm		c = 47.06mm		c = 62.71mm		c = 78.57mm		c = 94.42mm	
a_o	$K_{I_{dpt.}}$	$K_{I_{spt.}}$	$K_{I_{dpt.}}$	$K_{I_{spt.}}$	$K_{I_{dpt.}}$	$K_{I_{spt.}}$	$K_{I_{dpt.}}$	$K_{I_{spt.}}$	$K_{I_{dpt.}}$	$K_{I_{spt.}}$
1.00	373.30	269.88	378.31	11.69	369.35	427.68	363.77	262.24	346.67	195.36
2.50	534.72	328.33	520.04	43.12	542.40	262.24	524.71	135.52	518.93	169.84
3.80	597.19	399.43	606.65	124.70	612.68	167.20	611.93	225.28	611.45	228.80
5.70	618.15	506.00	649.30	271.04	673.60	294.80	678.07	325.60	697.11	321.20
7.60	580.76	585.20	641.40	514.80	686.57	435.38	721.36	432.08	750.01	416.24
9.50	510.36	585.20	607.98	609.84	670.23	602.02	730.16	537.68	766.96	509.52
11.40	486.53	657.36	577.84	696.52	621.80	705.44	683.87	637.12	739.31	599.28
12.54	367.47	769.01	470.33	754.58	566.42	587.92	639.94	692.56	698.70	650.32
14.25	244.87	888.80	353.80	813.12	451.22	833.92	525.74	761.20	595.14	716.32
16.00	167.57	958.32	189.32	835.12	285.07	876.30	362.76	810.48	432.83	768.24
17.10	-53.90	969.76	54.05	819.28	141.37	878.02	212.95	821.92	284.19	785.84

Table C.8: Stress Intesity Factors at Deepest and Surface Points (Axial Load)

	SIFs at deepest and surface points Stress Level = 230 MPa $(N/mm^{3/2})$									
	c = 31.30mm		c = 47.06mm		c = 62.71mm		c = 78.57mm		c = 94.42mm	
a_o	$K_{I_{dpt.}}$	$K_{I_{spt.}}$	$K_{I_{dpt.}}$	$K_{I_{spt.}}$	$K_{I_{dpt.}}$	$K_{I_{spt.}}$	$K_{I_{dpt.}}$	$K_{I_{spt.}}$	$K_{I_{dpt.}}$	$K_{I_{spt.}}$
1.00	390.26	282.15	395.51	12.22	386.14	447.12	380.31	274.16	362.42	204.24
2.50	559.03	343.25	543.67	45.08	567.05	274.16	548.56	141.68	542.51	177.56
3.80	624.34	417.59	634.23	130.36	640.53	174.80	639.75	235.52	639.24	239.20
5.70	646.24	529.00	678.81	283.36	704.22	308.20	708.89	340.40	728.80	335.80
7.60	607.16	611.80	670.55	538.20	717.77	455.17	754.15	451.72	784.10	435.16
9.50	533.56	611.80	635.62	637.56	700.69	629.38	763.35	562.12	801.82	532.68
11.40	508.64	687.24	604.11	728.18	650.06	737.51	714.96	666.08	772.91	626.52
12.54	384.17	803.96	491.71	788.88	592.17	614.64	669.03	724.04	730.46	679.88
14.25	256.00	929.20	369.89	850.08	471.73	871.83	549.64	795.80	622.20	748.88
16.00	175.19	1001.88	197.93	873.08	298.02	916.13	379.25	847.32	452.50	803.16
17.10	-56.35	1013.84	56.51	856.52	147.80	917.93	222.63	859.28	297.10	821.56

Table C.9: Stress Intesity actors at Deepest and Surface Points (Axial Load)

	SIFs at deepest and surface points Stress Level = 240 MPa ($N/mm^{3/2}$)									
	c = 31.30mm		c = 47.06mm		c = 62.71mm		c = 78.57mm		c = 94.42mm	
a_o	$K_{I_{dpt.}}$	$K_{I_{spt.}}$	$K_{I_{dpt.}}$	$K_{I_{spt.}}$	$K_{I_{dpt.}}$	$K_{I_{spt.}}$	$K_{I_{dpt.}}$	$K_{I_{spt.}}$	$K_{I_{dpt.}}$	$K_{I_{spt.}}$
1.00	407.23	294.41	412.70	12.75	402.93	466.56	396.84	286.08	378.18	213.12
2.50	583.33	358.18	567.31	47.04	591.71	286.08	572.41	147.84	566.10	185.28
3.80	651.48	435.74	661.80	136.03	668.38	182.40	667.56	245.76	667.04	249.60
5.70	674.34	552.00	708.33	295.68	734.84	321.60	739.71	355.20	760.48	350.40
7.60	633.56	638.40	699.71	561.60	748.98	474.96	786.94	471.36	818.19	454.08
9.50	556.76	638.40	663.25	665.28	731.16	656.75	796.54	586.56	836.68	555.84
11.40	530.76	717.12	630.37	759.84	678.33	769.57	746.04	695.04	806.52	653.76
12.54	400.88	838.92	513.09	823.18	617.91	641.37	698.12	755.52	762.22	709.44
14.25	267.13	969.60	385.97	887.04	492.24	909.73	573.53	830.40	649.25	781.44
16.00	182.80	1045.44	206.53	911.04	310.98	955.96	395.74	884.16	472.18	838.08
17.10	-58.80	1057.92	58.96	893.76	154.22	957.84	232.31	896.64	310.02	857.28

Table C.10: Stress Intesity Factors at Deepest and Surface Points (Axial Load)

	SIFs at deepest and surface points Stress Level = 250 MPa ($N/mm^{3/2}$)									
	c = 31.30mm		c = 47.06mm		c = 62.71mm		c = 78.57mm		c = 94.42mm	
a_o	$K_{I_{dpt.}}$	$K_{I_{spt.}}$	$K_{I_{dpt.}}$	$K_{I_{spt.}}$	$K_{I_{dpt.}}$	$K_{I_{spt.}}$	$K_{I_{dpt.}}$	$K_{I_{spt.}}$	$K_{I_{dpt.}}$	$K_{I_{spt.}}$
1.00	424.20	306.68	429.90	13.28	419.72	486.00	413.38	298.00	393.94	222.00
2.50	607.64	373.10	590.95	49.00	616.36	298.00	596.26	154.00	589.69	193.00
3.80	678.63	453.90	689.38	141.70	696.23	190.00	695.38	256.00	694.83	260.00
5.70	702.44	575.00	737.84	308.00	765.46	335.00	770.53	370.00	792.17	365.00
7.60	659.96	665.00	728.86	585.00	780.19	494.75	819.73	491.00	852.28	473.00
9.50	579.96	665.00	690.89	693.00	761.62	684.11	829.73	611.00	871.54	579.00
11.40	552.87	747.00	656.64	791.50	706.59	801.64	777.13	724.00	840.12	681.00
12.54	417.58	873.87	534.47	857.48	643.66	668.09	727.21	787.00	793.98	739.00
14.25	278.26	1010.00	402.05	924.00	512.75	947.64	597.43	865.00	676.30	814.00
16.00	190.42	1089.00	215.14	949.00	323.94	995.79	412.23	921.00	491.85	873.00
17.10	-61.25	1102.00	61.42	931.00	160.65	997.75	241.99	934.00	322.94	893.00

Table C.11: Stress Intesity Factors at Deepest and Surface Points (Axial Load)

	SIFs at deepest and surface points Stress Level = 260 MPa $(N/mm^{3/2})$									
	c = 31.30mm		c = 47.06mm		c = 62.71mm		c = 78.57mm		c = 94.42mm	
a_o	$K_{I_{dpt.}}$	$K_{I_{spt.}}$	$K_{I_{dpt.}}$	$K_{I_{spt.}}$	$K_{I_{dpt.}}$	$K_{I_{spt.}}$	$K_{I_{dpt.}}$	$K_{I_{spt.}}$	$K_{I_{dpt.}}$	$K_{I_{spt.}}$
1.00	441.17	318.95	447.10	13.81	436.51	505.44	429.92	309.92	409.70	230.88
2.50	631.95	388.02	614.59	50.96	641.01	309.92	620.11	160.16	613.28	200.72
3.80	705.78	472.06	716.96	147.37	724.08	197.60	723.20	266.24	722.62	270.40
5.70	730.54	598.00	767.35	320.32	796.08	348.40	801.35	384.80	823.86	379.60
7.60	686.36	691.60	758.01	608.40	811.40	514.54	852.52	510.64	886.37	491.92
9.50	603.16	691.60	718.53	720.72	792.08	711.47	862.92	635.44	906.40	602.16
11.40	574.98	776.88	682.91	823.16	734.85	833.71	808.22	752.96	873.72	708.24
12.54	434.28	908.82	555.85	891.78	669.41	694.81	756.30	818.48	825.74	768.56
14.25	289.39	1050.40	418.13	960.96	533.26	985.55	621.33	899.60	703.35	846.56
16.00	198.04	1132.56	223.75	986.96	336.90	1035.62	428.72	957.84	511.52	907.92
17.10	-63.70	1146.08	63.88	968.24	167.08	1037.66	251.67	971.36	335.86	928.72